Correlated Ab Initio Approaches to Metal-Metal Bonding in the Tricobalt Extended Metal Atom Chains

Thesis submitted for the degree of

Doctor of Philosophy

Department of Physical and Theoretical Chemistry

May 4, 2020

James Alexander Lamb

Brasenose College

University of Oxford

Abstract

The extended metal atom chains are a family of complexes with a linear, metallic chain surrounded by four equatorial polydentate ligands and capped by two axial ligands. The tricobalt extended metal atom chains studied in this work have a trimetallic core with halide axial ligands: the fluoride, chloride, bromide and iodide complexes. In this work we adopt correlated ab initio approaches (DFT and MCSCF) to the study of the metal-metal bonding between the cobalt atoms in the chain.

The literature surrounding the tricobalt series is extensive, reflecting the vast array of experimentally observed phenomena. X-ray crystallography has been used to determine crystal structures at a range of temperatures, and has shown the structure of the tricobalt chain can vary continuously between two extremes: symmetric with equal Co-Co bond lengths and unsymmetric with one Co-Co bond markedly lengthened. Magnetic measurements show an increase in temperature initiates a spin crossover in all known instances of the complex, in both the solution- and crystalline-phase. The data reported in the literature is consistent with a low-spin doublet ground state at low temperatures, however resolution of the high-spin state multiplicity is complicated by a lack of saturation in the effective magnetic moments at the highest available temperatures. In Chapter 1 we present a detailed review of the entire literature regarding the tricobalt extended metal chains such that the reader can put into context the entire range of remarkable behaviours.

In Chapter 2 we discuss the theoretical techniques underpinning this thesis, while Chapter 3 describes the specific computational methodologies used.

In Chapter 4 we undertake a comprehensive and systematic study of the symmetric form of the bromide complex. We detail electronic configurations of potential low-lying excited states that arise from the low-energy excitations within the ground state. The properties of the ground and excited states are used to explain the experimentally observed spin crossover and structural temperature dependence. We identify a symmetric sextet state, the thermal population of which is found to be consistent with the behaviour of those crystals that remain symmetric in their observed temperature ranges. In Chapter 5 we adopt the same systematic approach to study the unsymmetric form, again focusing on the bromide complex, and identify a quartet state that fits the behaviours seen in those crystals that show a transition between the symmetric and unsymmetric limits in their observed temperature ranges. In Chapter 6 we describe the electronic mechanisms by which the tricobalt bromide system makes this transition, examining low energy distortions in the symmetric low-spin state structures and the effect of the high-spin state population on the X-ray crystal structure. In Chapter 7 we extend the analysis developed in the first three chapters to study the complexes with the other axial halide ligands. Our results agree with the experimental findings of a decreasing spin crossover temperature going down the group VII halides F $>$ Cl $>$ Br $>$ I, and we present a re-evaluation of the link between the experimental structures and the spin crossover process.

Acknowledgements

I would first like to express my sincerest gratitude to my supervisor, Prof. John McGrady. His perspective, expertise and ability to explain and provide insight to even the most complicated subject matters in a straightforward manner have been invaluable throughout my time under his guidance. I would also like to extend my thanks to my friends and colleagues in the McGrady group, the TMCS CDT cohort, lecturers and staff, and fellow members of Brasenose College.

I want to give a special thank you to my wife, Annabel, who has been a constant source of support, positivity and encouragement. To my family, for your continued optimism and faith in me, and to my friends for the endless source of respite. Cameron for your help proofreading and Grandpat for your relentless quest to get me over the line.

Finally I am grateful to and acknowledge funding from EPSRC (EP/L015722/1).

Contents

Abstract **i**

Acknowledgements **iii**

1 Introduction **1**

1.1 A Short Review of Metal-Metal Bonding 1

1.2 The Extended Metal Atom Chains 5

1.3 The Tricobalt Chloride EMACs 14

1.3.1 Structure 15

1.3.2 Magnetism 26

1.3.3 Bonding 33

1.3.4 $Co_3(dpa)_4X_2$ [X = F, Br, I] 42

1.3.5 Summary 43

1.4 This Thesis 46

2 Theoretical Techniques **49**

2.1 The Schrödinger Equation 49

2.2 Quantum Chemistry 54

2.3 The Born-Oppenheimer Approximation 56

2.4 The Form of the Wavefunction 59

2.5 The Variational Method 60

2.6 Matrix Mechanics and Dirac Notation . . . 64
2.7 Hartree-Fock Theory . . . 66
2.8 Post-Hartree-Fock Methods . . . 79
2.9 Density Functional Theory . . . 89
2.10 Basis Sets . . . 97
2.11 Wavefunction Analysis . . . 102
2.12 Theoretical Studies of Transition Metal Complexes . . . 105
2.13 Concluding Remarks . . . 111

3 Computational Methodologies 114

3.1 ADF . . . 114
3.2 OpenMolcas . . . 119
3.3 ORCA . . . 121

4 A DFT and MCSCF Study of the $Co_3(dpa)_4Br_2$ Symmetric Form 123

4.1 Introduction . . . 123
4.2 Aims and Objectives . . . 126
4.3 Results and Discussion . . . 128
4.3.1 DFT Analysis: BP86 . . . 128
4.3.2 DFT Analysis: Functional Dependence . . . 138
4.3.3 MCSCF Analysis . . . 143
4.4 Conclusions . . . 151

5 A DFT and MCSCF Study of the $Co_3(dpa)_4Br_2$ Unsymmetric Form 152

5.1 Introduction . . . 152
5.2 Aims and Objectives . . . 154
5.3 Results and Discussion . . . 155

5.3.1 DFT Analysis: BP86 . . . 155
5.3.2 DFT Analysis: Functional Dependence . . . 168
5.3.3 MCSCF Analysis . . . 171
5.4 Conclusions . . . 176

6 The Symmetric-Unsymmetric Transition of $Co_3(dpa)_4Br_2$ 178

6.1 Introduction . . . 178
6.2 Aims and Objectives . . . 181
6.3 Results and Discussion . . . 182
6.3.1 Fractional Occupation Number Model . . . 182
6.3.2 Potential Energy Surfaces . . . 186
6.3.3 Spin Equilibrium Model . . . 188
6.4 Conclusions . . . 196

7 Influence of the Axial Ligand on $Co_3(dpa)_4X_2$ [X = F, Cl, Br, I] 198

7.1 Introduction . . . 198
7.2 Aims and Objectives . . . 200
7.3 Results and Discussion . . . 201
7.3.1 Spin State Splitting Analysis . . . 201
7.3.2 Structure and Wavefunction Analysis . . . 204
7.3.3 Re-evaluation of the Structure-Spin Crossover Relationship . . . 207
7.4 Conclusions . . . 210

8 Conclusions 211

Bibliography 215

Chapter 1

Introduction

1.1 A Short Review of Metal-Metal Bonding

Bonding in chemistry is driven by the interactions between the electrons and nuclei in a molecule. Metal-metal bonding occurs in transition metal (TM) complexes with multiple metal centres, and was first recognised in the $[Re_3Cl_{12}]^{3-}$ cluster by Cotton and colleagues in 1963 (Figure 1.1a). [1] Compared to metallic rhenium, the Re-Re bond lengths in the cluster are shorter (2.47 vs. 2.75 Å), and was shown to correspond to the formation of three Re-Re double bonds. [2] A year later Cotton and co-workers isolated the related $[Re_2Cl_8]^{2-}$ complex, which they showed to have a particularly short Re-Re bond length of 2.27 Å and an unexpected eclipsed structure (Figure 1.1b). [3] A valence shell electron pair repulsion (VSEPR) analysis would predict a staggered structure to minimise the repulsion between the Re-Cl bonding electrons. Using a valence bond (VB) theory and a molecular orbital (MO) treatment Cotton *et al.* characterised a metal-metal quadruple bond for the first time, which was used to explain the eclipsed structure.

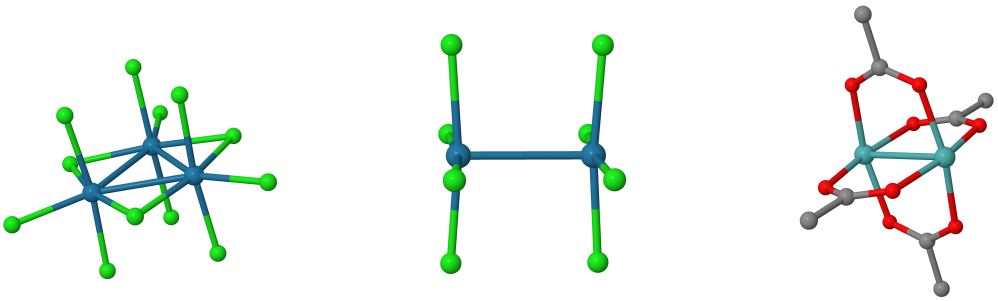

(a) (b) (c)

Figure 1.1: (a) $[Re_3Cl_{12}]^{3-}$, (b) $[Re_2Cl_8]^{2-}$ and (c) $Mo_2(OAc)_2$ structures from Cotton. [1, 3, 4]

In Figure 1.2 we show the d orbital framework of the $[Re_2Cl_8]^{2-}$ MO diagram. Each Re atom is in a local $ReCl_4$ square planar environment. The $5d_{x^2-y^2}$ orbitals are not shown as they have too high an energy due to a strong Re-Cl antibonding interactions. The $5d_{z^2}$ orbitals on each Re form a pair of bonding and antibonding orbitals with σ symmetry with respect to the Re-Re axis. The $5d_{xz}$ and $5d_{yz}$ orbitals form a doubly degenerate pair of π bonding and antibonding orbitals, and the $5d_{xy}$ a pair of δ bonding and antibonding orbitals. Each Re^{III} contributes four d electrons, which occupy the four bonding orbitals and give an overall bond order of four, with no antibonding orbital occupation. The δ occupation explains the experimentally observed eclipsed structure. If it were staggered there would be no overlap between the d_{xy} orbitals on the Re atoms and no delta bond. In the eclipsed structure, the stabilisation of the d_{xy} orbitals clearly overcomes the repulsion between the Re-Cl bonding electrons.

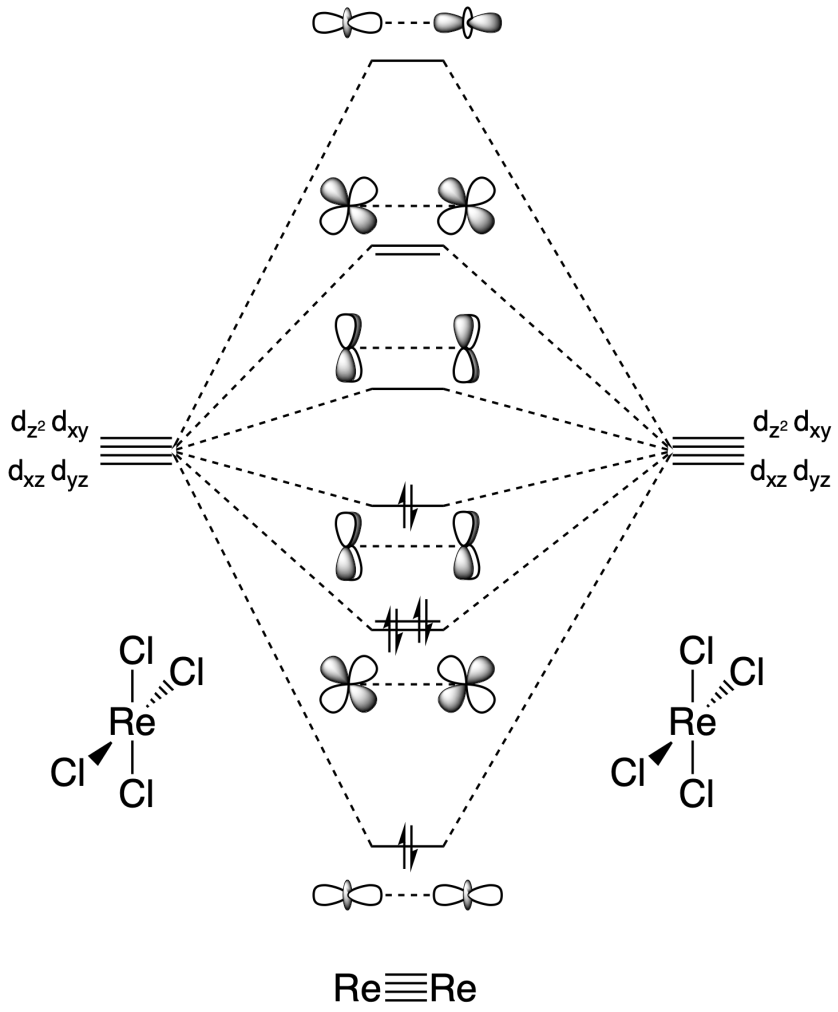

Figure 1.2: $[Re_2Cl_8]^{2-}$ MO diagram.

Cotton's pioneering work inspired a series of discoveries of complexes containing metal-metal quadruple bonds, for example the paddlewheel molybdenum (II) acetate complex in 1965 (Figure 1.1c). [4] By varying the number of d electrons within the same MO array, dimers with bond orders ranging from 0.5 – 4 have been found: 3.5 in $[Tc_2Cl_8]^{3-}$, [5] triple bonds in several molybdenum and tungsten complexes, [6] 2.5 in a Ru_2^{5+} paddlewheel complex [7], 1.5 in Ir_2^{5+} and Rh_2^{5+} paddlewheel complexes [8, 9] and 0.5 in a Pd_2^{5+} formamidinate species. [10] The bond order depends on the number of *d* electrons in the framework shown in Figure 1.2, where an increase in the number of electrons leads to an increased occupation of the antibonding orbitals and a decrease leads to an decreased

occupation of the bonding orbitals, both of which decrease the bond order.

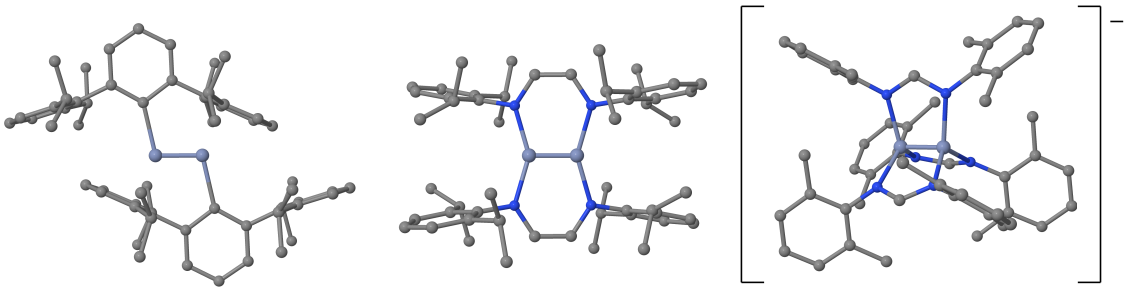

(a) (b) (c)

Figure 1.3: (a) Ar'CrCrAr' structure from Power, (b) $(^{H}L^{iPr})CrCr(^{H}L^{iPr})$ structure from Kreisel and (c) $[Cr_2(Ar^{Xyl}NC(H)NAr^{Xyl})_3]^-$ structure from Tsai. [11–13]

In the search for higher bond orders still, if the high energy $d_{x^2-y^2}$ orbitals can be lowered into the metal-metal bonding framework, systems with 10 d-electrons could potentially form a quintuple bond. To do so the number of ligands must be decreased to minimise interactions with the $d_{x^2-y^2}$ orbitals and maximise their availability for metal-metal bonding. Further, these ligands must provide enough steric bulk to prevent the metal atoms forming clusters. In 2005 Power and co-workers managed to isolate Ar'CrCrAr' (Ar' = 2,6-C_6H_3(2,6-C_6H_3iPr$_2$)$_2$, iPr = isopropyl) with a quintuple Cr-Cr bond with a bond length of 1.84 Å (Figure 1.3a) and a single metal-ligand bond on each Cr. [11] Similar structures with Cr-Cr quintuple bonds were later found by Kreisel *et al.* for $(^{H}L^{iPr})CrCr(^{H}L^{iPr})$ ($^{H}L^{iPr}$ = (2,6-C_6H_3iPr$_2$)NC_2N(2,6-C_6H_3iPr$_2$) [12] and Tsai *et al.* for $[Cr_2(Ar^{Xyl}NC(H)NAr^{Xyl})_3]^-$ (Ar^{Xyl} = 2,6-$C_6H_3(CH_3)_2$) [13] with Cr-Cr bond lengths of 1.80 and 1.74 Å, respectively (Figures 1.3b-c). They are both paddlewheel complexes, with two metal-ligand bonds in the former complex and three in the latter anionic complex.

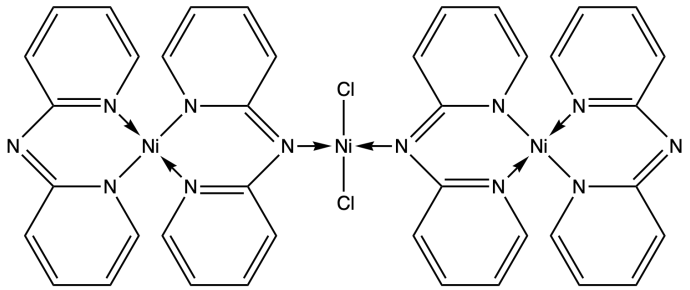

Figure 1.4: Schematic of the incorrect $Ni_3(dpa)_4Cl_2$ structure proposed by Hurley and Robinson. [14]

1.2 The Extended Metal Atom Chains

The focus of this thesis concerns TM complexes with metal-metal bonds between more than two metal centres: the extended metal atom chains (EMACs). The EMACs are a family of complexes whose defining feature is a central linear chain of metal atoms, from which their name is derived. Hurley and Robinson synthesised the first EMAC in 1968, $Ni_3(dpa)_4Cl_2$, where dpa is the deprotonated dipyridylamine anion, however their initial characterisation of the structure was incorrect (Figure 1.4). [14]

The true form, shown in Figure 1.5, was only later determined by Aduldecha and Hathaway using X-ray diffraction. [15] They recognised the chain of three Ni atoms forming a metallic core in a structure capped by the two axial chloride ligands with four tridentate dpa ligands coordinated to the equatorial positions of each Ni atom. The dpa ligands are not planar, even in isolation, and spiral down the metal chain with helical symmetry, as can be seen in Figure 1.5b. The innermost hydrogen atoms on the two pyridine moieties of the dpa ligand suffer a steric repulsion, which creates a dihedral angle of $\sim 54^\circ$ between the planes of the two pyridine rings within the EMAC.

The EMAC structure can be regarded as an extension of the bimetallic paddle-wheel complexes (Figures 1.1c and 1.3b-c) to include more metal centres. The structure belongs to the D_4 point group, whose symmetry operations are defined relative to the

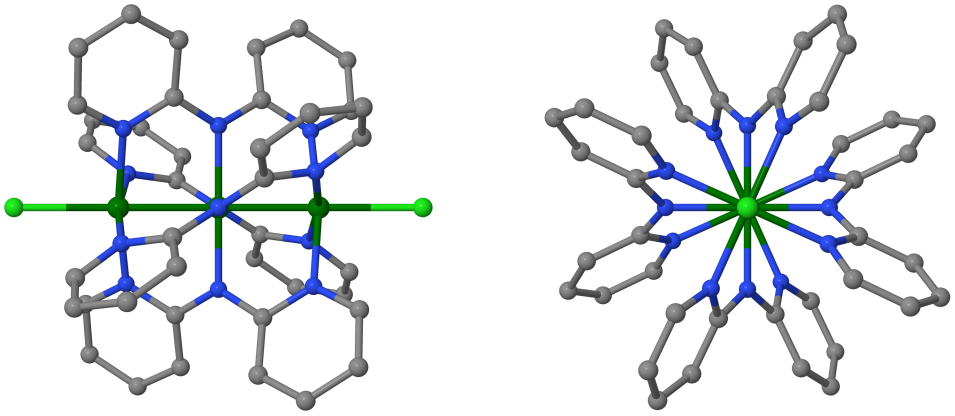

(a) (b)

Figure 1.5: The correct $Ni_3(dpa)_4Cl_2$ structure discovered by Aduldecha and Hathaway [15] viewed down the (a) x-axis and (b) z-axis.

principal C_4 axis that runs down the nickel chain. There are four C_2 axes that are perpendicular to the principal axis and go through the central nickel: two collinear with the central Ni-N bonds and two bisecting them. The helical twist in the dpa ligands gives the complex D_4 symmetry rather than D_{4h}, as would be the case if the ligands were rigorously planar. Like many of the TM complexes previously discussed, the EMACs have an inherent flexibility that allows the helical motif to accommodate a range of TMs in both homo- and hetero-metallic arrays with varying chain lengths, as well as substitution of the axial and equatorial ligands, although changes in the latter are more restricted as they must have a denticity that matches the number of metal atoms (i.e. tridentate in the trimetallic EMACs in Figure 1.5). Figure 1.6 presents a schematic of a general trimetallic EMAC. It shows the metal chain (M-M-M), both axial ligands (X) capping the chain and one of the four equatorial dpa ligands. The helical symmetry is not detailed and should be assumed. This style will be used throughout this thesis for simplicity when describing different EMACs, and can be straightforwardly extended to include more metal centres in the chain and substitutions of the metal and ligands.

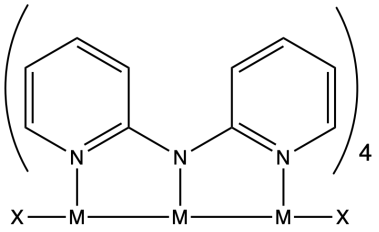

Figure 1.6: Schematic structure of the general trimetallic EMAC $M_3(dpa)_4X_2$.

The EMAC structure can be regarded as an extension of the bimetallic paddle-wheel complexes (Figures 1.1c and 1.3b-c) to include more metal centres. The structure belongs to the D_4 point group, whose symmetry operations are defined relative to the principal C_4 axis that runs down the nickel chain. There are four C_2 axes that are perpendicular to the principal axis and go through the central nickel: two collinear with the central Ni-N bonds and two bisecting them. The helical twist in the dpa ligands gives the complex D_4 symmetry rather than D_{4h}, as would be the case if the ligands were rigorously planar. Like many of the TM complexes previously discussed, the EMACs have an inherent flexibility that allows the helical motif to accommodate a range of TMs in both homo- and hetero-metallic arrays with varying chain lengths, as well as substitution of the axial and equatorial ligands, although changes in the latter are more restricted as they must have a denticity that matches the number of metal atoms (i.e. tridentate in the trimetallic EMACs in Figure 1.5). Figure 1.6 presents a schematic of a general trimetallic EMAC. It shows the metal chain (M-M-M), both axial ligands (X) capping the chain and one of the four equatorial dpa ligands. The helical symmetry is not detailed and should be assumed. This style will be used throughout this thesis for simplicity when describing different EMACs, and can be straightforwardly extended to include more metal centres in the chain and substitutions of the metal and ligands.

Depending on the extent of the metal-metal bonding, the electronic structures of the EMACs can be considered to lie between two extremes. When there is no bonding

the MOs can be considered as a set of localised d orbitals on each metal centre, where the central metal atom is in a local square planar environment and the two terminal atoms a local square pyramidal environment. The electronic structure of the $Ni_3(dpa)_4Cl_2$ complex is an example best described by this limit, with Ni-Ni distances of 2.443 Å. The central atom has all orbitals doubly occupied except a vacant $d_{x^2-y^2}$ orbital, which lies much higher in energy due to the local square planar environment. The two terminal atoms have unpaired electrons in the d_{z^2} and $d_{x^2-y^2}$ orbitals, where the local square pyramidal environment means the d_{z^2} and $d_{x^2-y^2}$ are closer in energy. We define the orientation of the orbitals in the EMACs locally at each metal atom, such that the d_{z^2} orbitals align the the principle M-M-M axis and the $d_{x^2-y^2}$ orbitals align with the local M-N bonds. On each terminal Ni the unpaired electrons have aligned spins, where both metal atoms interact antiferromagnetically through the low-spin central atom. [16, 17] The $Cu_3(dpa)_4Cl_2$ complex synthesised by Hathaway [18] and Pinkerton [19] has Cu-Cu distances of 2.47 Å, indicating the absence of covalent bonding, and magnetic properties that suggest antiferromagnetic coupling. It has a similar MO framework to the Ni_3 complex, where all the localised orbitals are doubly occupied except the three $d_{x^2-y^2}$. They are each singly occupied with the unpaired electron on the central Cu anti-aligned to the two terminal Cu, in agreement with the experimental magnetic measurements. [17, 20]

When there is metal-metal bonding each metal atom can be considered to exist in a local trans-octahedral environment, where the basic features of the MO array are summarised schematically in Figure 1.7. The d orbitals on each centre separate into distinct sets of σ, π and δ symmetry (with respect to the M-M-M axis), interacting to form bonding, nonbonding and antibonding linear combinations delocalised across the three metal atoms (although the nonbonding have no density on the central metal). Only one set of the π orbitals (xz) are shown in the schematic. The other π orbitals (yz) are also degenerate

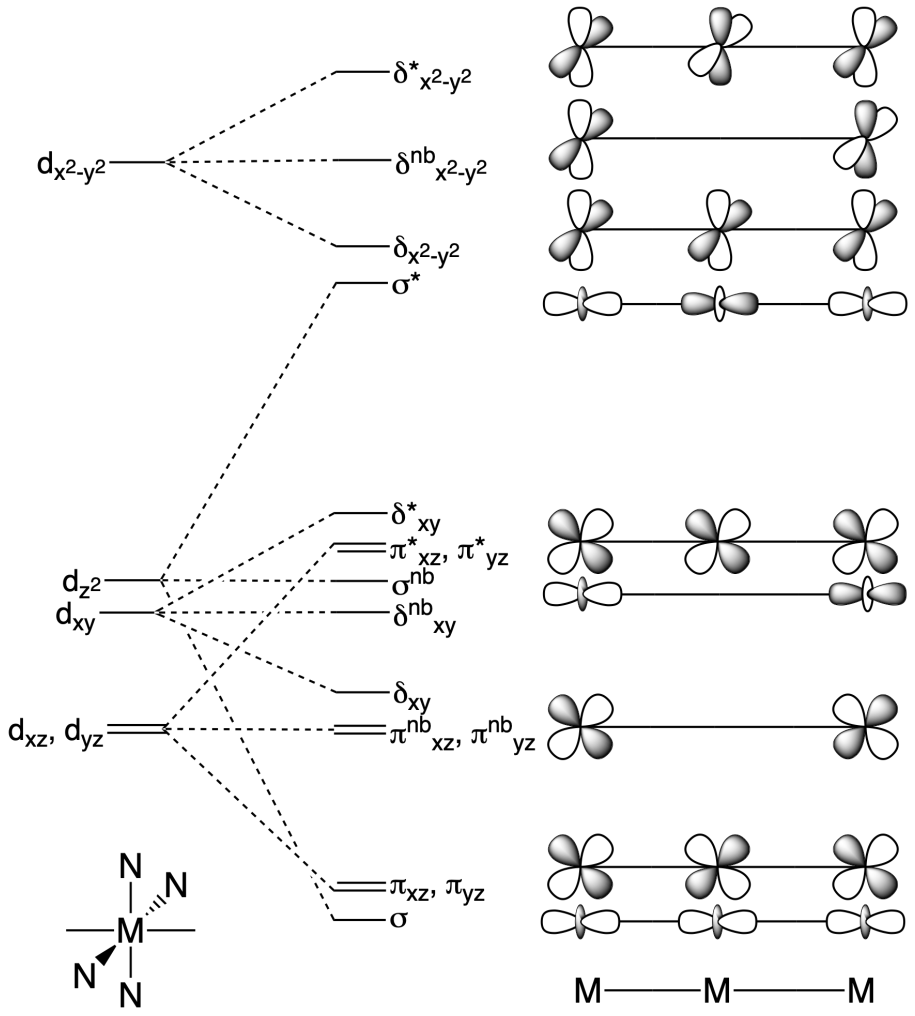

Figure 1.7: Schematic MO diagram of the general trimetallic EMAC $M_3(dpa)_4X_2$.

and related by a 90° rotation around the M-M-M axis. Similarly only one set of δ orbitals ($x^2 - y^2$) are shown. The other δ orbitals (xy) are related by a 45° rotation around the M-M-M axis. In Figure 1.2 we did not include the $\delta_{x^2-y^2}$ orbitals in the MO scheme, as the σ antibonding interactions with the ligand put them too high in energy. It should be noted that the $\delta_{x^2-y^2}$ orbitals in the EMACs have similar σ antibonding interactions with the nitrogen p orbitals on the dpa ligand, but these interactions are not depicted in the schematic, nor is the helical twist down the metal chain.

The electronic structures of the $Ru_3(dpa)_4Cl_2$ and $Rh_3(dpa)_4Cl_2$ complexes are best described by this limit, synthesised by Peng, [21] with shorter Ru-Ru and Rh-Rh

distances of 2.254 and 2.392 Å, respectively, indicating bond formation. The Ru(II) atoms each contribute six d electrons to the metal bonding framework and the Rh(II) atoms contribute seven d electrons. MO analyses predict a $(\pi^{nb})^4(\delta^{nb}_{xy})^2(\sigma^{nb})^2(\delta^*_{xy})^2$ configuration, where the δ^*_{xy} orbital lied below the π^* in $Ru_3(dpa)_4Cl_2$, [22] and a $(\pi^{nb})^4(\delta^{nb}_{xy})^2(\sigma^{nb})^1(\pi^*)^4(\delta^*_{xy})^2$ configuration in $Rh_3(dpa)_4Cl_2$, [23] where the bonding orbitals are all doubly occupied in both. These correspond to total bond orders of 3 and 1 across the trimer, and individual Ru-Ru and Rh-Rh bond orders of 1.5 and 0.5, respectively. In 1997 Cotton and co-workers synthesised $Cr_3(dpa)_4Cl_2$ with Cr-Cr distances of 2.3647 Å. Each Cr(II) contributes four d electrons, with an electronic configuration that is, somewhat surprisingly, quite similar to that of the trirhodium complex. The sigma framework can again be thought of as a three-centre three-electron bond in a $(\sigma)^2(\sigma^{nb})^1$ configuration, while the remaining nine electrons singly occupy each of the orbital in the π and δ_{xy} frameworks, rather than doubly occupying them as in $Rh_3(dpa)_4Cl_2$. A more recent multi-configurational analysis suggests a σ bond order close to one, a small π bonding contribution and negligible δ_{xy} bonding. [24]

The complexes discussed so far have all been shown to have a symmetric structure, with equal metal-metal bonds. The trichromium and tricobalt complexes have been shown to exhibit both symmetric structures and structures with an asymmetric trimetal core, with one metal-metal bond longer than the other, depending on the axial ligand. [25–27] The symmetric tricobalt complex has a similar electronic structure to the trirhodium complex, with each Co(II) contributing seven d electrons. The three-centre three-electron bond in the Cr_3 and Co_3 complexes is expected to play a role in the asymmetric distortion, [28, 29] suggesting a similarity with the distortion to the allyl radical, [30] which has a three-centre three-electron bond over the π framework. [31] The unsymmetric Cr_3 structures have a short Cr-Cr distance of ∼2.0 Å, which suggests the formation of a quadruple

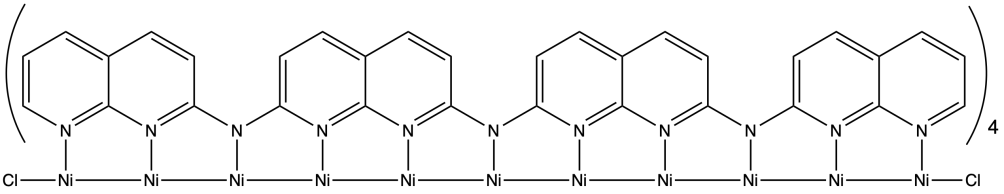

Figure 1.8: Schematic of the $[Ni_{11}(tentra)_4Cl_2]^{4+}$ structure from Peng. [39]

bond, while the long Cr-Cr distance of ∼2.6 Å is consistent with the absence of any significant Cr-Cr bonding. The axial ligand has been used to tune the asymmetry in the $Cr_3(dpa)_4X_2$ compounds, where strong sigma donor ligands (X = CN^- or $CCPh^-$) promote a symmetric structure and weak field ligands promote unsymmetric structures (X = NO_3^- or BF_4^-). [32–34] Even more remarkably, the structures of many members of the tricobalt series are markedly temperature dependent with single crystal samples exhibiting a continuous range of geometries between the symmetric and unsymmetric limits. [35–38] The tricobalt complex and its structure and bonding is the focus of this thesis and the literature surrounding it will be discussed in more detail in the next section.

Longer chain analogues represent a natural extension to the trimetallic EMACs. Chromium has been found to exhibit chains four, [40] five [41–43] and seven atoms long, [44] cobalt exhibits chains five [45, 46] and six [47] atoms long, while nickel exhibits chains of four, [48] five, [45, 49, 50] six, [51] seven, [52] nine [53] and most recently an EMAC eleven Ni atoms long, [39] synthesised almost 10 years after the nona-nickel complex. The formation of longer chains is hampered by the increased conformational flexibility in the equatorial dpa-type ligands, and Peng *et al.* found success using the more rigid, naphthyridine-based ligand 'tentra', which is detailed in Figure 1.8 showing the undeca-nickel EMAC $[Ni_{11}(tentra)_4Cl_2]^{4+}$ complex. The mixed valence chain can be separated into Ni^{2+} atoms bound to the amine moiety N on the tentra ligand and $(Ni_2)^{3+}$ dimers bound to the naphthyridine moiety. The nickel dimers at the ends of the chain behave differently to those at the centre due to the presence of the axial ligand, which weakens the

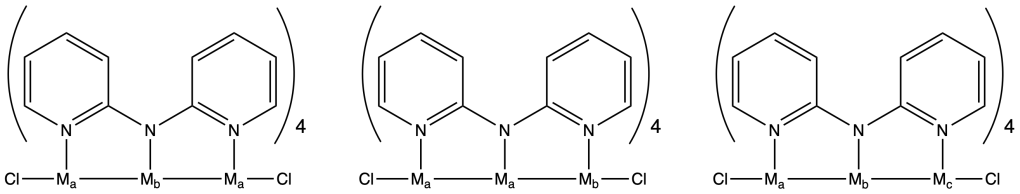

Figure 1.9: Schematic $M_3(dpa)_4Cl_2$ structures representing the three types of heterometallic systems (a) M_a-M_b-M_a, (b) M_a-M_a-M_b and (c) M_a-M_b-M_c.

terminal Ni-N and Ni-Ni bonds. More recently they have characterised two new undecanickel complexes using a new naphthyridine and pyridine based equatorial ligand 'bnatpya'. [54]

The examples presented thus far have all had homo-nuclear metallic cores. Many hetero-nuclear EMACs exist, and in general they can be classified as one of three types: M_a-M_b-M_a, M_a-M_a-M_b and M_a-M_b-M_c (Figure 1.9) for trimetallic chains. The first type were first found for $CoPdCo(dpa)_4Cl_2$ by Rohmer and co-workers in 2007. [56] Later that year the same group synthesised the $CuMCu(dpa)_4Cl_2$ (M = Pt , Pd) EMACs. [57] More recently the Peng group synthesised three manganese analogues, $MnMMn(dpa)_4Cl_2$ (M = Ni, Pt , Pd). [58] The synthesis of these complexes followed the same procedures used in the homo-metallic EMAC preparation. These are 'one-pot' processes where three separate metal centres exist in solution, offering no control over the final EMAC. Magnetic measurements showed a strong antiferromagnetic coupling between the metal atoms in all the compounds. The terminal atoms are predicted to exist in a local square pyramidal coordination, while the central hetero-metal ion always has a d^8 configuration, which is

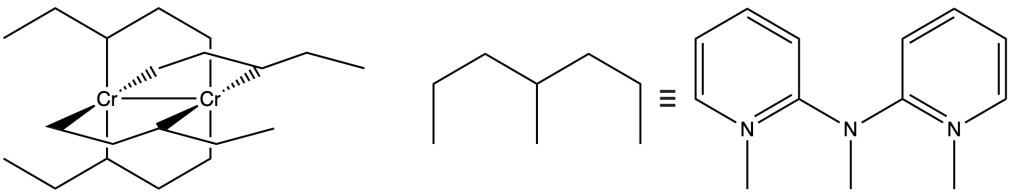

Figure 1.10: Schematic $Cr_2(dpa)_4$ precursor structure developed by Berry *et al.* [55]

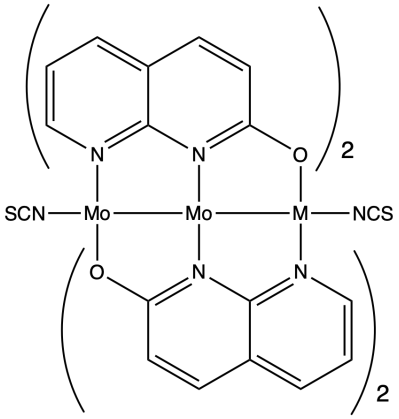

Figure 1.11: Schematic $Mo_2M(npo)_4(NCS)_2$ structure from Peng (M = Fe, Co or Ni). [59]

stabilised by a local square planar environment.

The second type of hetero-nuclear trimetalic EMACs, which take the form M_a-M_a-M_b, were not found through one-pot syntheses. To synthesise such an EMAC, a homo-di-nuclear precursor already containing the M_a-M_a bond needs to be used. In 2007 Berry and Nippe synthesised the first example of such a precursor, a quadruple bonded $Cr_2(dpa)_4$ (Figure 1.10), from the unsymmetric $Cr_3(dpa)_4Cl_2$, which reacts with $FeCl_2$ to form $Cr_2Fe(dpa)_4Cl_2$. [55] Adopting a similar scheme, in 2008 Peng and coworkers used a $Ru_2(OAc)_4Cl$ precursor to synthesise four new hetero-nuclear EMACs: the neutral and cationic forms of $Ru_2M(dpa)_4Cl_2$ (M = Cu, Ni). [60] Later that year Berry used $Cr_2(dpa)_4$ and its molybdenum analogue, $Mo_2(dpa)_4$, for the synthesis of two $M_2Co(dpa)_4Cl_2$ complexes (M = Cr, Mo), [61] and extended the series further in 2011 using $W_2(dpa)_4$ to synthesise two $W_2M(dpa)_4$ complexes (M = Fe [62] and Cr [63]). The current literature shows a range of M_a-M_a-M_b complexes with combinations of M_a = Cr, Mo and W and M_b = Fe, Mn, Zn, Ni and Co. [62, 64–66] In 2014 Berry presented the first example that did not contain any first row TMs, with M_a = Mo and W and M_b = Ru. [67] A full series of complexes with M_a = Ru and M_b = Co, Ag, Mn, Fe, Zn, Cd, Pd, Rh and Ir were found by Peng using $Ru_2(dpa)_4Cl$ in 2017, [68] who also developed a new precursor, $Mo_2(npo)_4$, binding it to M_b = Fe, Co and Ni (Figure 1.11) with terminal NCS ligands. [59]

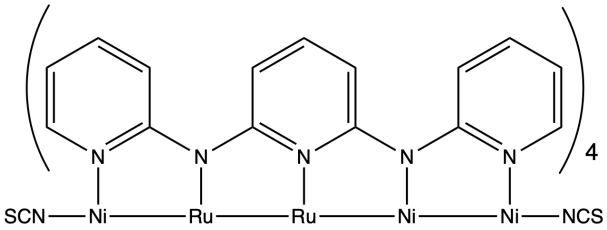

Figure 1.12: Schematic $NiRu_2Ni_2(tpda)_4(NCS)_2$ structure from Peng. [71]

The controlled synthesis of hetero-nuclear compounds is complicated by the presence of impurities that arise from the many ways the metal atoms can arrange. In the third and final type of complex, of the form M_a-M_b-M_c, there are 18 possible products ranging from the homo-nuclear complexes through to complexes with three different metals in different orders. In 2009, for the first time Berry synthesised a MoWCr backbone from a $MoW(dpa)_4$ precursor. [69] In 2013 Peng showed that the direct substitution of the terminal cobalt in $Co_2Rh(dpa)_4Cl_2$ by nickel provided a straightforward, one-pot synthesis of the neutral and cationic hetero-trimetallic $NiCoRh(dpa)_4Cl_2$ complex. [70] In 2014 Peng presented the only example of longer chain hetero-nuclear EMAC using nickel and ruthenium in $NiRu_2Ni_2(tpda)_4(NCS)_2$ (Figure 1.12), characterising a delocalised $(Ru_2)^{5+}$ dimer in a Ni^{+}–$(Ru_2)^{5+}$–Ni^{2+}–Ni^{2+} structure with a four-fold greater molecular conductance than its penta-nickel homo-nuclear counterpart. [71]

1.3 The Tricobalt Chloride EMACs

There is a wealth of experimental data surrounding the tricobalt EMACs that describes their varied structural and magnetic phenomena, as well as previous theoretical studies that search for the electronic mechanisms that govern those phenomena. The majority of the literature concerns the complexes with chloride terminal ligands, so this will be the focus of this review. The data is collated into three separate sections, examining the structures, magnetism and then bonding. The chloride complex exhibits all the known structural and

magnetic behaviours and has so far been the subject of all theoretical studies. Within each section we adopt a chronological format, such that the reader will be able to see the development of our understanding of the tricobalt EMAC. We will conclude by considering the tricobalt complexes of the other halides and a summary of the literature to put it into context as pertains to this thesis.

1.3.1 Structure

Motivation for investigating the tricobalt complexes originally derives from the chloride complex, first discovered in 1994 by Peng and co-workers. [26] When crystallised with a disordered dichloromethane and water solvate, unlike most EMACs, they found the tricobalt chains within the $Co_3(dpa)_4Cl_2{\cdot}2CH_2Cl_2{\cdot}H_2O$ crystal to have an asymmetric structure. This has become known in the literature as the unsymmetric structure after Peng *et al.* described an "unsymmetrical bonding formation." This will be discussed in more detail later but was quite different to the bonding scheme depicted in Figure 1.7 used to describe the symmetric structures. Using X-ray crystallography Peng observed distances of $Co_{(1)}$-$Co_{(2)}$ = 2.290 Å and $Co_{(2)}$-$Co_{(3)}$ = 2.472 Å, $Co_{(1)}$-N = 1.96 Å and $Co_{(3)}$-N = 2.12 Å, and $Co_{(1)}$-Cl = 2.432 Å and $Co_{(3)}$-Cl = 2.361 Å at 295 K. When reporting Co-N bond lengths we report the average of the four Co-N bonds at the respective cobalt atom, although the individual bond lengths may vary slightly due to the absence of rigorous 4-fold rotational symmetry in the crystal. We also introduce two values that allow us to compare the degree of asymmetry in different crystals of the tricobalt EMACs: ΔCo-Co = $Co_{(2)}$-$Co_{(3)}$ – $Co_{(1)}$-$Co_{(2)}$ and ΔCo-N = $Co_{(3)}$-N – $Co_{(1)}$-N. These will be used throughout this thesis, and for $Co_3(dpa)_4Cl_2{\cdot}2CH_2Cl_2{\cdot}H_2O$ are ΔCo-Co = 0.182 Å and ΔCo-N = 0.16 Å. The differences between the symmetric and unsymmetric structures are highlighted in the schematic in Figure 1.13. The asymmetry manifests primarily in the divergence of

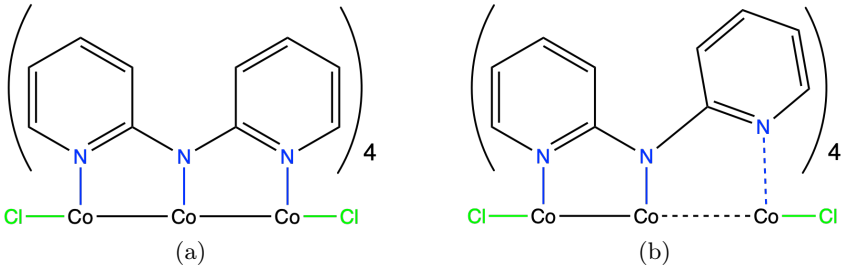

Figure 1.13: Schematic highlighting the key differences in the (a) symmetric and (b) unsymmetric structures of the chloride complex.

the Co-Co and terminal Co-N bonds, although they also found a divergence of the Co-Cl bonds. The cobalt atoms are labelled as $Co_{(1)}$, $Co_{(2)}$ and $Co_{(3)}$ to distinguish them, and throughout this thesis we define $Co_{(3)}$ as the cobalt atom with the longest Co-N bonds.

Peng *et al.* were only able to achieve a yield of 2-5% in their synthesis. Trying to improve on this, three years later the Cotton group crystallised the same tricobalt chloride complex with a dichloromethane solvate, $Co_3(dpa)_4Cl_2{\cdot}CH_2Cl_2$, in 42% yield. The structure was shown to be symmetric with identical Co-Co, terminal Co-N and Co-Cl distances, of 2.318, 1.991 and 2.520 Å, respectively, at 168 K. [27] The structure takes the same form as the trinickel complex shown in Figure 8, but with shorter metal-metal distances indicating a bonding interaction. Given the two distinct structures Cotton tentatively raised the prospect that the tricobalt chloride complex could represent a rare example of bond stretch isomerism. However, they originally dismissed this in their conclusions based on the lack of success of previous claims [72, 73] and because they were dubious of the unsymmetric nature of the structure put forward by Peng *et al.* due to the low yield, the disordered nature of the solvate and the fact that all other analogues known at the time (Ni, Cu, Rh, Re and Cr) had symmetric structures. [15, 18, 19, 21, 25] To clarify the legitimacy of the unsymmetric structure Cotton searched for further tricobalt chloride crystals. In 1997 he synthesised $Co_3(dpa)_4Cl_2{\cdot}Co(dpa)_2$, with an interstitial mononuclear $Co(dpa)_2$ molecule and an unsymmetric structure similar to that found by Peng. [74] This time they

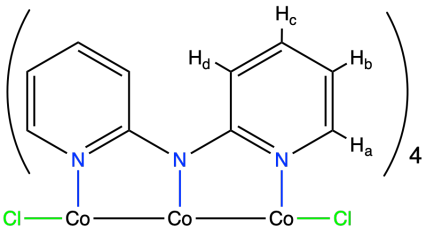

Figure 1.14: Schematic highlighting the four hydrogen chemical environments in the symmetric chloride complex.

concluded that the tricobalt chloride complex was indeed a bond stretch isomer, at least by the definition put forward by Parkin: "whereby molecules differ only in the length of one or more bonds." Specific bond lengths for $Co_3(dpa)_4Cl_2 \cdot Co(dpa)_2$ at 213 K are shown in Table 1.1, which contains bond lengths of all known crystals of the chloride complex and the temperature at which they were measured. When X-ray structures of the same crystal are reported at multiple temperatures in the same work, the highest and lowest temperature structures are given. Table 1.1 is further divided into two sections, with the upper section containing bond lengths of crystals with symmetric structures and the lower section containing bond lengths of crystals with unsymmetric structures.

In solution Cotton showed that only the symmetric structure existed over a range of temperatures. When either of the $Co_3(dpa)_4Cl_2 \cdot CH_2Cl_2$ or $Co_3(dpa)_4Cl_2 \cdot 2CH_2Cl_2$ crystals is dissolved ^{1}H NMR spectroscopy indicates that the structure is symmetric: in a CD_2Cl_2 solution, the spectra show exactly four peaks at a range of temperatures from 183 – 303 K. [75] The four peaks in question correspond to the four symmetry-distinct hydrogen atoms on the pyridine moiety of the dpa ligand, shown in Figure 17 – the equivalence of the 8 protons of each kind in the molecule is indicative of perfect D_4 symmetry, at least on the NMR timescale. The D_4 symmetric structure has four distinct bond lengths, with equal Co-Co, Co-Cl, central Co-N and terminal Co-N distances.

In 1999 the Cotton group discovered another crystal with an unsymmetric structure when re-examining their earlier work on the symmetric $Co_3(dpa)_4Cl_2 \cdot CH_2Cl_2$, notic-

	T / K	$Co_{(1)}$-$Co_{(2)}$	$Co_{(1)}$-$Co_{(2)}$	$Co_{(1)}$-Cl	$Co_{(3)}$-Cl	$Co_{(1)}$-N	$Co_{(2)}$-N	$Co_{(3)}$-N	ΔCo-Co	ΔCo-N
CH_2Cl_2[e]	20	2.344	2.344	2.508	2.445	1.981	1.904	1.987	0.000	0.006
CH_2Cl_2[b]	168	2.318	2.318	2.520	2.520	1.991	1.903	1.991	0.000	0.000
CH_2Cl_2[e]	296	2.337	2.337	2.488	2.488	1.997	1.907	1.997	0.000	0.000
THF[f]	120	2.311	2.311	2.440	2.440	1.982	1.898	1.982	0.000	0.000
THF[f]	295	2.348	2.348	2.423	2.423	2.020	1.907	2.020	0.000	0.000
Hexane[f]	120	2.313	2.325	2.438	2.446	1.983	1.900	1.990	0.013	0.007
Hexane[f]	295	2.362	2.362	2.422	2.422	2.032	1.912	2.032	0.000	0.000
Benzene[f]	170	2.316	2.328	2.469	2.484	1.981	1.904	1.986	0.012	0.005
Benzene[f]	316	2.342	2.367	2.461	2.450	2.006	1.906	2.016	0.025	0.010
Et_2O/CH_2Cl_2[f]	120	2.319	2.330	2.443	2.480	1.978	1.904	1.984	0.011	0.006
Et_2O/CH_2Cl_2[f]	296	2.323	2.367	2.446	2.456	1.987	1.910	2.021	0.044	0.034
Et_2O[g]	85	2.321	2.332	2.443	2.482	1.979	1.907	1.986	0.011	0.007
Et_2O[g]	350	2.340	2.396	2.441	2.435	2.003	1.916	2.051	0.057	0.048
$2CH_2Cl_2/H_2O$[a]	295	2.290	2.472	2.432	2.361	1.96	1.90	2.12	0.182	0.16
$Co(dpa)_2$[c]	213	2.285	2.459	2.386	2.353	1.965	1.907	2.125	0.174	0.160
$2CH_2Cl_2$[e]	20	2.304	2.385	2.428	2.440	1.978	1.901	2.040	0.081	0.062
$2CH_2Cl_2$[d]	213	2.294	2.466	2.432	2.369	1.973	1.906	2.115	0.172	0.142
$2CH_2Cl_2$[e]	296	2.299	2.471	2.434	2.363	1.978	1.910	2.119	0.172	0.141
Tol/Hex[f]	90	2.312	2.343	2.421	2.434	1.977	1.899	2.005	0.031	0.028
Tol/Hex[f]	298	2.311	2.457	2.414	2.357	1.979	1.907	2.108	0.146	0.129

Table 1.1: Co-Co, Co-Cl and Co-N bond lengths (Å) of all $Co_3(dpa)_4Cl_2$ crystals reported in the literature. [a] values from reference [26], [b] from [27], [c] from [74], [d] from [76], [e] from [35], [f] from [36] and [g] from [38].

ing that during its preparation another type of crystal was produced as a minor product: $Co_3(dpa)_4Cl_2{\cdot}2CH_2Cl_2$. [76] Despite the fact that these two crystals are obtained from the same solution and differ only in the number of interstitial dichloromethane molecules, the structures are very different, with the presence of a second CH_2Cl_2 molecule apparently favouring the unsymmetric geometry (see bond lengths in Table 1.1).

Building on the work of Cotton, in 2000 the Clérac group further investigated the $Co_3(dpa)_4Cl_2{\cdot}CH_2Cl_2$ and $Co_3(dpa)_4Cl_2{\cdot}2CH_2Cl_2$ crystals. [35] They discovered an even stronger interconvertability between the two crystals, whereby they produces $Co_3(dpa)_4Cl_2{\cdot}2CH_2Cl_2$ directly from $Co_3(dpa)_4Cl_2{\cdot}CH_2Cl_2$ by dissolving the latter in a mixture of CH_2Cl_2/hexane. They also showed a significant temperature dependence of

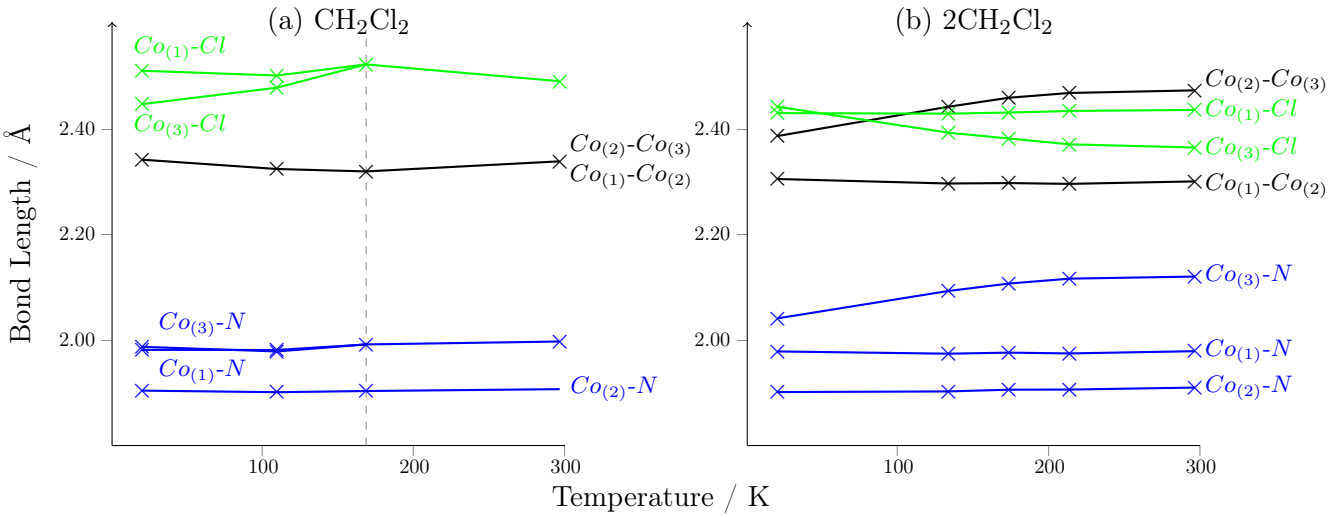

Figure 1.15: Bond lengths for the (a) $Co_3(dpa)_4Cl_2{\cdot}CH_2Cl_2$ and (b) $Co_3(dpa)_4Cl_2{\cdot}2CH_2Cl_2$ crystals from 20 – 296 K. [35]

both crystal structures. Figure 1.15 depicts the evolution of the Co-Co (black), Co-Cl (green) and Co-N (blue) distances of the symmetric $Co_3(dpa)_4Cl_2{\cdot}CH_2Cl_2$ and unsymmetric $Co_3(dpa)_4Cl_2{\cdot}2CH_2Cl_2$ crystals with temperature. A × marks bond lengths at specific temperatures, however it is important to note that bond lengths at intermediate temperatures have not been measured experimentally. The structural evolution is extrapolated from the measured values by joining the data points together by a straight line, and real values may differ should they be measured in the future. Error bars for each data point are not included in the figures. Maximum standard deviations reported in the literature for the tricobalt EMAC X-ray diffraction data are 0.002, 0.009 and 0.014 Å for Co-Co, Co-X (X = F, Cl, Br, I) and Co-N, respectively. We consider the error in the structures based on the 99% confidence interval of 3 standard deviations, such that the experimental interatomic distances are accurate to within 0.006, 0.027 and 0.042 Å for the Co-Co, Co-X and Co-N bonds, respectively.

The $Co_3(dpa)_4Cl_2{\cdot}CH_2Cl_2$ structure shown in Figure 1.15a is symmetric at 296 K, and remains symmetric as the temperature is to 168 K, with a slight decrease in the Co-Co and terminal Co-N distances of 0.019 and 0.006 Å, and a slight increase of 0.032

Å in the Co-Cl bonds. At these higher temperatures the CH_2Cl_2 molecules are disordered throughout the orthorhombic crystal, such that on average they interact with both ends of the EMAC equally. The low temperature behaviour sees the symmetry break, and between 168 – 109 K a phase transition occurs into a monoclinic form. A neutron diffraction study at 20 K revealed that in this phase the CH_2Cl_2 molecules are ordered and a weak hydrogen-bond is formed with the Cl at only one end of the EMAC. This results in the weakening of the corresponding $Co_{(1)}$-Cl bond and a divergence of the Co-Cl and terminal Co-N distances. As the temperature is decreased from 168 – 20 K both Co-Co distances increase by 0.022 Å, remaining symmetric through the full temperature range. On average the Co-Cl distances decrease by 0.044 Å from 168 – 20 K, while the terminal Co-N distances decrease by 0.012 Å from 168 – 109 K, then increase by 0.005 Å from 109 – 20 K. Low and high temperatures bond lengths are reported in Table 1.1. In crystals that undergo a phase transition in the observed temperature range, the phases are separated by a vertical dashed line (e.g. Figure 1.15a).

The unsymmetric $Co_3(dpa)_4Cl_2{\cdot}2CH_2Cl_2$ crystal structure was shown to have a stronger temperature dependence compared to the symmetric $Co_3(dpa)_4Cl_2{\cdot}CH_2Cl_2$, with a greater variation in the bond lengths over the temperature range (Figure 1.15b). At higher temperatures the structure shows a high degree of asymmetry, with large differences in the Co-Co and terminal Co-N distances of ΔCo-Co = 0.172 Å and ΔCo-N 0.141 Å at 296 K. As the temperature is decreased the structure appears to evolve towards a symmetric geometry. Figure 1.15b shows the temperature dependence of the bond lengths, and in particular the convergence of the $Co_{(1)}$-$Co_{(2)}$ and $Co_{(2)}$-$Co_{(3)}$ curves and the $Co_{(1)}$-N and $Co_{(3)}$-N curves at lower temperatures. Clérac notes that the contraction of the $Co_{(2)}$-$Co_{(3)}$ distance to 2.38 Å at 20 K does not represent a complete transition to the symmetric limit, with ΔCo-Co = 0.081. The bond is still significantly longer than in other $Co_{(2)}$ complexes

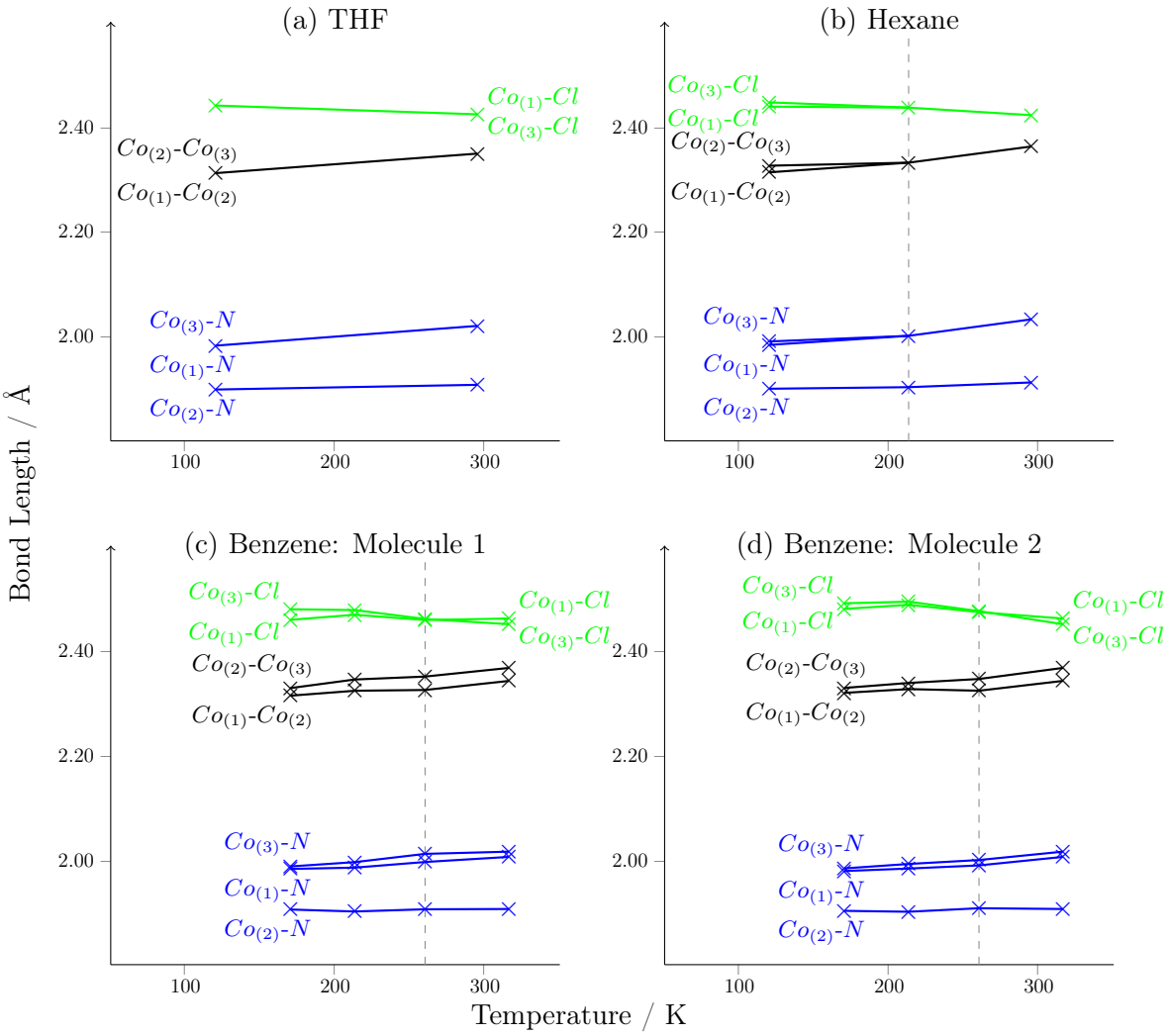

Figure 1.16: Bond lengths for the (a) $Co_3(dpa)_4Cl_2$·THF and (b) $Co_3(dpa)_4Cl_2$·2Hexane crystals from 120 – 295 K and the crystallographically independent (c) molecule 1 and (d) molecule 2 in the $Co_3(dpa)_4Cl_2$·Benzene crystal from 170 – 316 K. [36]

with a single Co-Co bond, which show distances in the range 2.265 - 2.302 Å. [77, 78]

Later in 2001 Clérac and co-workers published an extended series of tricobalt chloride complexes exhibiting a range of symmetric and unsymmetric structures. [36] They presented three crystals that maintain a symmetric structure through a range of temperatures. The temperature dependence of the structures are shown in Figure 1.16 and they all exhibit a broadly similar behaviour to one another. As the temperature decreases all three structures show a decrease in the Co-Co and terminal Co-N distances and an increase in the Co-Cl distances. With a tetrahydrofuran (THF) solvate ($Co_3(dpa)_4Cl_2$·THF) the EMAC

structure is rigorously symmetric at all temperatures with crystallographically equivalent terminal cobalt atoms. Both Co-Co and terminal Co-N distances decrease by 0.037 and 0.038 Å, and both Co-Cl increase by 0.017 Å as the temperature decreases from 295 – 120 K. With a hexane solvate ($Co_3(dpa)_4Cl_2$·Hexane) the EMAC is rigorously symmetric at 295 and 213 K and the crystal structure is isomorphous with $Co_3(dpa)_4Cl_2$·THF. Between 213 and 120 K there is a phase change and the symmetry is no longer enforced at lower temperatures, with ΔCo-Co = 0.013 Å at 120 K. On average the Co-Co and terminal Co-N distances decrease by 0.043 and 0.046 Å, and the Co-Cl increase by 0.020 Å as the temperature decreases from 295 – 120 K. With a benzene solvate ($Co_3(dpa)_4Cl_2$·Benzene) the symmetry is never enforced, and the $Co_{(1)}$-$Co_{(2)}$ and $Co_{(2)}$-$Co_{(3)}$ distances are never equal over the entire temperature range, however, the structure is always close to being symmetric. At 316 K the difference in the Co-Co and terminal Co-N distances are greatest with values of ΔCo-Co = 0.025 Å and ΔCo-N = 0.010 Å, which are smaller than the known unsymmetric structures (ΔCo-Co = 0.172 – 0.182 Å and ΔCo-N = 0.142 – 0.16 Å). Between 316 and 260 K there is a phase change, and from 260 – 170 K there are two crystallographically independent EMAC molecules in the unit cell, labelled Molecule 1 and Molecule 2 in Figure 1.16c-d. As the temperature is lowered, the degree of asymmetry decreases in both molecules with values for ΔCo-Co and ΔCo-N of 0.015 and 0.005 Å in molecule 1, respectively, and 0.009 and 0.005 Å in molecule 2 at 170 K. On average the Co-Co and terminal Co-N distances decrease by 0.032 and 0.028 Å, respectively, and the Co-Cl increase by 0.021 Å as the temperature decreases from 295 – 170 K. Where structures have two (or more) crystallographically independent molecules, the bond lengths given in Table 1.1 are the average of the two structures.

Clérac also identified a new unsymmetric crystal with a toluene and hexane solvate ($Co_3(dpa)_4Cl_2$·1.75Toluene·0.5Hexane). It has two crystallographically independent

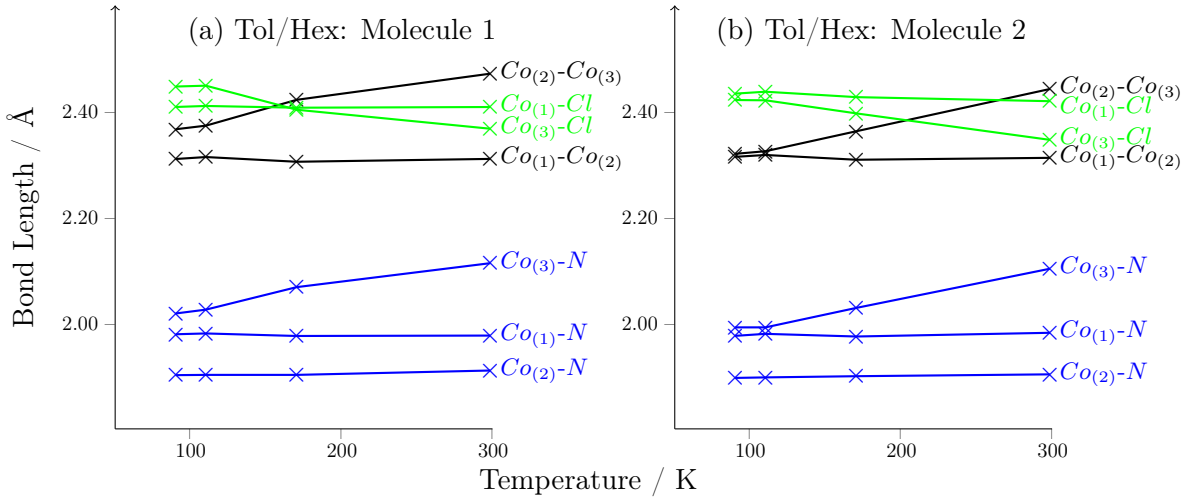

Figure 1.17: Bond lengths for the crystallographically independent (a) molecule 1 and (b) molecule 2 in the $Co_3(dpa)_4Cl_2$·1.75Toluene·0.5Hexane crystal [36] from 90 – 298 K.

EMAC molecules in the unit cell at all temperatures, similar to $Co_3(dpa)_4Cl_2$·Benzene below 260 K, and the temperature dependence is shown in Figure 1.17. Both are significantly unsymmetric at 298 K, with values for ΔCo-Co of 0.161 and 0.130 Å in molecules 1 and 2, respectively, and ΔCo-N values of 0.137 and 0.121 Å. As the temperature is lowered both molecules evolve towards the symmetric limit. Molecule 1 behaves very similarly to $Co_3(dpa)_4Cl_2$·$2CH_2Cl_2$, and maintains its asymmetry at low temperatures, with ΔCo-Co = 0.056 Å and ΔCo-N = 0.039 Å at 90 K. Molecule 2, in contrast, has essentially transitioned to the symmetric limit by 90 K, with ΔCo-Co = 0.006 Å and ΔCo-N = 0.016 Å.

The final crystal found by Clérac is solvated by diethyl ether and dichloromethane ($Co_3(dpa)_4Cl_2$·0.85Et2O·0.15CH_2Cl_2). At high temperatures the EMAC structure has a slight asymmetry, with ΔCo-Co = 0.044 Å and ΔCo-N = 0.034 Å at 296 K, but by 120 K the structure is almost symmetric, with ΔCo-Co = 0.011 Å and ΔCo-N = 0.006 Å. Unlike $Co_3(dpa)_4Cl_2$·Benzene, for which both terminal Co-N distances decrease as the temperature is lowered, $Co_{(1)}$-N distances are consistent across the temperature range as $Co_{(3)}$-N distances decreases. In $Co_3(dpa)_4Cl_2$·0.85Et2O·0.15CH_2Cl_2 the diethyl ether and

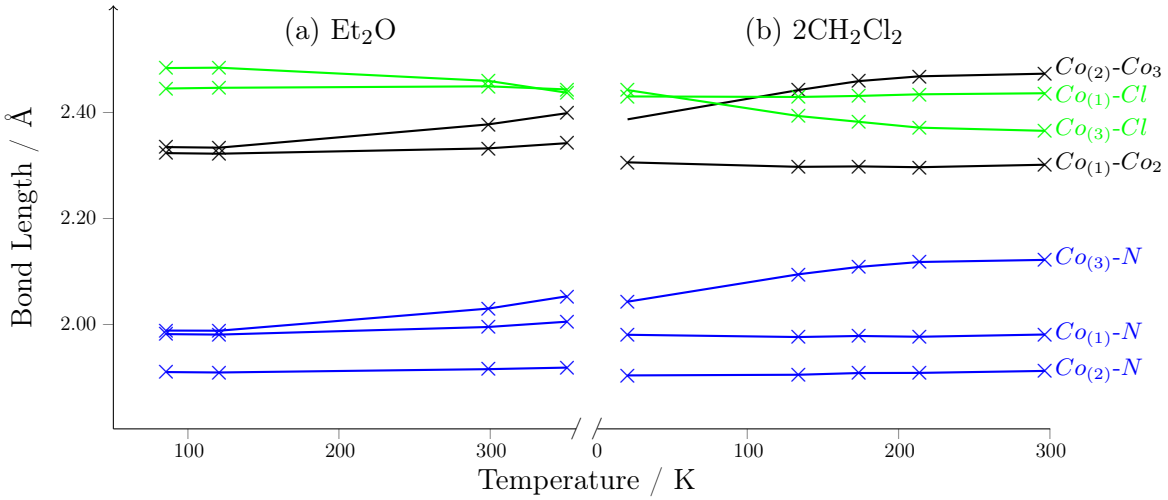

Figure 1.18: Bond lengths for the (a) $Co_3(dpa)_4Cl_2{\cdot}Et_2O$ crystal from 85 – 350 K [38] and (b) $Co_3(dpa)_4Cl_2{\cdot}2CH_2Cl_2$ crystal [35] from 20 – 296 K.

dichloromethane molecules occupy the same interstitial position with a ratio 0.85:0.15. In the latest work on the tricobalt EMAC series, in 2018 the Hillard group identify the isomorphic $Co_3(dpa)_4Cl_2{\cdot}Et_2O$ crystal with a pure diethyl ether solvate and no dichloromethane occupation of the interstitial position. [38] Both of the EMAC structures show very similar Co-Co, Co-Cl and Co-N distances over a range of temperatures (of the order 0.01 Å), and in Figure 1.18a we only present the temperature dependence of $Co_3(dpa)_4Cl_2{\cdot}Et_2O$ as the observed temperature range is greater. In their work, Hillard *et al.* present an intriguing discussion connecting the structural evolution of $Co_3(dpa)_4Cl_2{\cdot}Et_2O$ and $Co_3(dpa)_4Cl_2{\cdot}2CH_2Cl_2$, and both are shown in Figure 1.18 to highlight this. As previously discussed, at high temperatures $Co_3(dpa)_4Cl_2{\cdot}2CH_2Cl_2$ is very unsymmetric, and as the temperature is lowered the structure becomes more symmetric. Considered alongside $Co_3(dpa)_4Cl_2{\cdot}Et_2O$, the most striking feature across both of the temperature dependent structures is the apparent convergence of the low temperature $Co_3(dpa)_4Cl_2{\cdot}2CH_2Cl_2$ structure with the high temperature $Co_3(dpa)_4Cl_2{\cdot}Et_2O$ structure.

The vast majority of homo-metallic EMACs have a symmetric structure. The Cr_3 system is the only other EMAC known to exhibit an unsymmetric form, and this can

only be controlled through the substitution of the axial ligands. [34] In contrast, the Co_3 system can exhibit the symmetric and unsymmetric forms depending only on the solvate or temperature. The structural behaviour of the tricobalt series is therefore extremely unusual, and our understanding of its origins has evolved over time as more data has become available. Originally the two forms were thought to be distinct, and the origin of the asymmetry rooted in the effect of the crystalline environment. In the initial discovery of $Co_3(dpa)_4Cl_2{\cdot}2CH_2Cl_2$, both the symmetric and unsymmetric structures crystallised simultaneously under the exact same experimental conditions prompting Cotton *et al.* to suggest that the two forms of the EMAC must therefore have similar energies. [76] The first temperature dependent investigations showed $Co_3(dpa)_4Cl_2{\cdot}CH_2Cl_2$ remained symmetric at all temperatures, whilst $Co_3(dpa)_4Cl_2{\cdot}2CH_2Cl_2$ remained unsymmetric. Although the latter did become more symmetric at lower temperatures, it did not fully transition to the symmetric limit, suggesting that there exists a barrier between the two forms. However, $Co_3(dpa)_4Cl_2{\cdot}1.75Toluene{\cdot}0.5Hexane$ was later shown to contain an EMAC chain that does transition between the two structures. It was then noticed that this transition also appears to occur across the structures of two separate crystals. The current understanding, as put forward by Hillard *et al.*, is that the same mechanism governs the symmetric-unsymmetric transition across all these crystals, which implies the existence of some kind of continuum linking the two structural limits.

In the same work Hillard and co-workers also draw attention to the relatively poor understanding of the behaviour of those crystals that remain symmetric through the observed temperature ranges. In Table 1.1 we have separated the crystal structures that remain symmetric throughout the temperature range from those that exhibit an asymmetry. The low temperature structures of the THF, Hexane and Benzene solvates are all similar, as are their high temperature structures, suggesting a consistent electronic mech-

anism governing the structural changes. If we examine the data for the CH_2Cl_2 solvate, the structural behaviour between 296 and 168 K is similar to the other symmetric crystals, showing a decrease in the Co-Co and terminal Co-N distances and an increase in the Co-Cl distances. At higher temperatures the same electronic mechanism could be governing the structure. Below 168 K the structural changes are unlike the other symmetric crystals, where the phase change could affect the underlying electronic behaviour and prevent the structure from distorting at lower temperatures.

1.3.2 Magnetism

Alongside the extensive studies of structure, the effect of the temperature on the magnetic susceptibilities of the Co_3 EMACs has been scrutinised carefully. The magnetic susceptibility, χ, is the proportionality constant between the strength of a magnetic field, H, and the degree of magnetisation in a material, M.

$$M = \chi H \tag{1.1}$$

Paramagnetic compounds have at least one unpaired electron, and therefore a permanent magnetic moment. The Hamiltonian describing a magnetic moment interacting with a magnetic field has two eigenstates: a low-energy state aligned with the field and a high-energy state that is anti-aligned, with an energy difference ΔE. In a material containing multiple paramagnetic centres, like the crystals of the tricobalt chloride complex, at finite temperatures both states exist at the same time in equilibrium. The relative populations of the two states is given by the Boltzmann distribution, $\exp(\Delta E/kT)$ where k is the Boltzmann constant and T the temperature. The population of the low energy state increases as the temperature decreases, with more of the paramagnetic centres aligned with

the field. This is observed as an increase in the magnetic susceptibility. When $\Delta E << kT$ the magnetic susceptibility can be related to the temperature by the Curie law and C, the Curie constant.

$$\chi = C/T \tag{1.2}$$

By using the molar magnetic susceptibility, χ_M we can calculate the effective magnetic moment, μ_{eff}, of each paramagnetic centre, which is independent of the temperature and can in turn give an indication of the spin state. [79]

$$\mu_{eff} = \sqrt{3kT\chi_M/N\mu_B^2} = \sqrt{4S(S+1)}\mu_B = \sqrt{n(n+2)}\mu_B \tag{1.3}$$

N is Avogadro's number, μ_B the Bohr magneton, S the total spin quantum number and n the number of unpaired electrons, such that $S = n/2$. The spin only formula corresponds to μ_{eff} quite well, and best fits first row TMs with an orbital angular momentum, L, of zero. Deviations in μ_{eff} from the spin only value can be ascribed to contributions from a non-zero L and spin-orbit coupling. TM complexes can exist with a variety of magnetic moments depending on the number of metal atoms, their oxidation states, the nature of the ligands and the environment. Octahedral complexes with 4-7 d electrons can also exist in a low-spin (LS) or high-spin (HS) state. The relative energies of the states are given by the crystal field splitting, Δ_{oct}. The configuration depends on the pairing energy, P, which takes into account the increase in coulomb repulsion from having two electrons in the same orbital and the decrease in exchange energy after the spin flip.

In the experimental work, all the crystals of the tricobalt EMACs have been shown to exhibit a change in the effective magnetic moment as the temperature is increased, as do the chloride and bromide complexes in solution. [26, 27, 35–38, 74–76] This has been attributed to a spin crossover, or spin transition, which is a change in the spin state

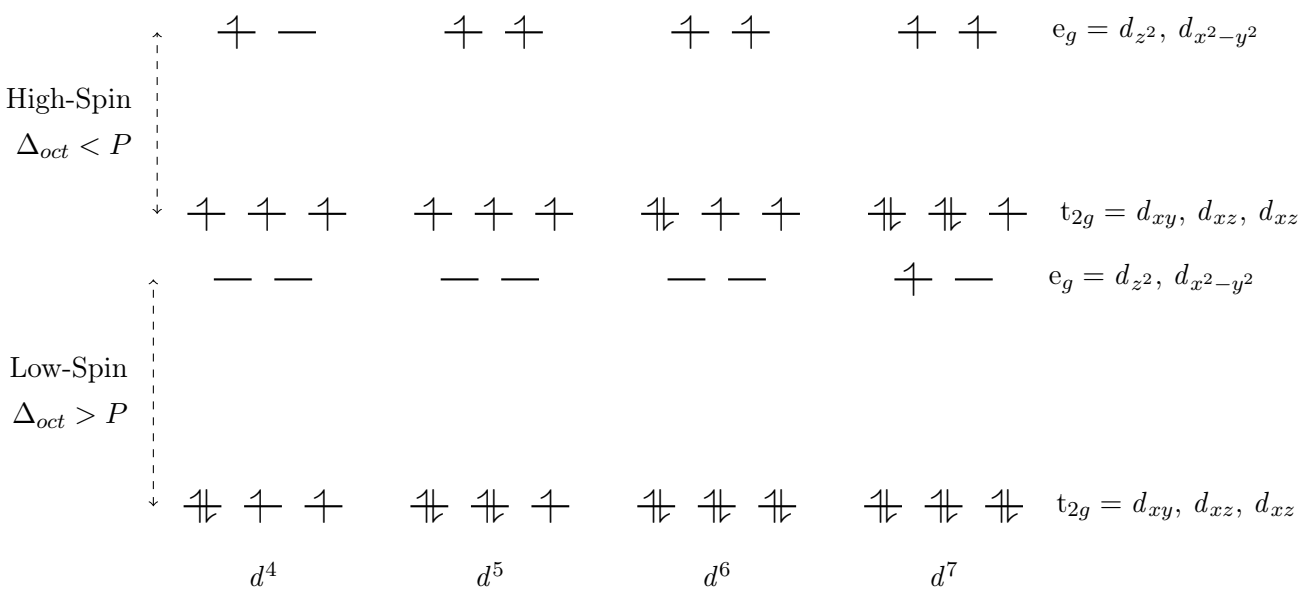

Figure 1.19: Low-spin and high-spin electron configurations of octahedral d^{4-7} complexes.

of a complex in response to an external stimulus, such as temperature, pressure or an electro-magnetic field. Most commonly the spin crossover is induced by a temperature change and occurs gradually, however, it can occur over a small temperature range. The profile of the spin crossover depends on the cooperativity between the centres, which is a measure of how the change in spin state is propagated through the material. When the cooperativity is low there is little interaction between the paramagnetic centres and the transition happens at different temperatures for different centres, which results in a slow change in the effective magnetic moment. When the cooperativity is high, the change is propagated quickly through the material and the spin crossover occurs abruptly, sometimes with hysteresis when the cooperativity is particularly high. [80, 81] Two-step spin crossovers are also possible; for crystals with two crystallographically independent centres, [82] or in bimetallic systems where two spin crossovers occur locally at each metal. [83] In both the occurrence at one centre hinders the transition at the second. Finally, the spin crossover can be incomplete, whereby not all the centres transition to the LS or HS state within the temperature range. The profile of a complete spin crossover shows a

plateau in the effective magnetic moment at both the high and low temperature limits, and the values at which it plateaus is used to determine the multiplicity of the spin states. Incomplete spin crossover processes can show a plateau at only one of the high or low temperature limits, or no plateau at either, and it is less straightforward to determine the multiplicity of the associated spin state or states.

In their original tricobalt chloride paper the Peng group observed an increase in μ_{eff} from 1.8 – 2.6 μ_B over the temperature range 150 – 300 K in the unsymmetric $Co_3(dpa)_4Cl_2{\cdot}2CH_2Cl_2{\cdot}H_2O$. [26] These values were considered to lie between what would be expected for an isolated LS and a HS Co(II) atom, whilst the μ_{eff} vs. T curve showed a similar shape to that of the $[Co(terpy)_2]X_2$ complex during a ^2E – $^4T_1$ spin crossover. [84] Peng *et al.* therefore attributed the change in μ_{eff} to a localised spin-crossover at the isolated cobalt with an energy difference of 1638 cm^{-1} (0.203 eV) between the ^2E and $^4T_1$ states, occurring independently of the Co_2 unit, which behaves diamagnetically.

In the work from the Cotton, Clérac and Hillard groups the magnetic susceptibilities are measured at a range of temperatures and the data was fit to an ideal model of a spin crossover process. In spin crossover complexes the LS and HS states are separated by a small energy difference, of the order kT, and both exist in equilibrium at finite temperatures. The ratio of the occupations of each state is again given by a Boltzmann distribution, which depends on the relative free energies of the states (their enthalpy and entropy differences, ΔH and ΔS) and the temperature. As the temperature increases, the occupation of the higher energy state increases. At any temperature the measured magnetic susceptibility, χ^T, is given by the weighted average of the LS and HS magnetic susceptibilities, χ^{LS} and χ^{HS}, defined by the occupations at that temperature. The experimental works use a least squares fitting of the magnetic data to the theoretical curve (Equation 1.4) to find ΔH and the spin crossover temperature, $T_{\frac{1}{2}} = \frac{\Delta H}{\Delta S}$. The spin crossover temperature

is the temperature at which half of the EMAC molecules in the crystal sample have been excited into the high spin state. The lower the spin crossover temperature, the smaller the energy difference between the high spin and low spin states. A complete derivation of an equivalent formula in the context of the structural temperature dependence is given in Chapter 6 following the method detailed by Kahn. [85]

$$\chi^T = \frac{(\chi^{HS} - \chi^{LS})}{\exp\left(\frac{\Delta H}{R}\left[\frac{1}{T} - \frac{1}{T_{1/2}}\right]\right) + 1} + \chi^{LS} \tag{1.4}$$

The model was first applied in their solution-based study, in which they noticed a temperature dependence of the chemical shifts "indicating the existence of a spin-state equilibrium in solution." [75] They observed a change in μ_{eff} from 2.78 to 4.48 μ_B between 193 – 308 K. Solution data were not available below the freezing point of 193 K, while the transition was incomplete at the 308 K, making the characterisation of the LS and HS states difficult. Unfortunately Mössbauer spectroscopy, which can differentiate LS and HS states, is not applicable to Co(II) systems. However, they were able to use electron paramagnetic resonance spectroscopy (EPR) at 5 K to measure a g value of 2.351, corresponding to a μ_{eff} of 2.04 μ_B and a LS doublet (S=1/2) ground state. At 308 K the value of μ_{eff} = 4.48 μ_B lies between the spin only values for a HS quartet (S = 3/2) and sextet (S = 5/2) state of 3.87 and 5.92 μ_B, respectively. The measured g value of 2.351 would correspond to HS μ_{eff} values of 4.55 μ_B for a quartet or 6.95 μ_B for a sextet state (assuming it remains constant at higher temperatures), while experimentally measured values for Co(II) quartet states fall in the range 4.3 – 5.2 μ_B, [79] suggesting the HS state could have S = 3/2 or 5/2. Cotton *et al.* used HS values of 4.55 and 6.95 μ_B to calculate the theoretical spin crossover behaviour, stating the latter gave a better fit to the experimental data and calculating ΔH = 7.7 kJ mol^{-1} (0.080 eV), ΔS = 20.8 J K^{-1} mol^{-1} and $T_{\frac{1}{2}}$ = 370 K for the corresponding

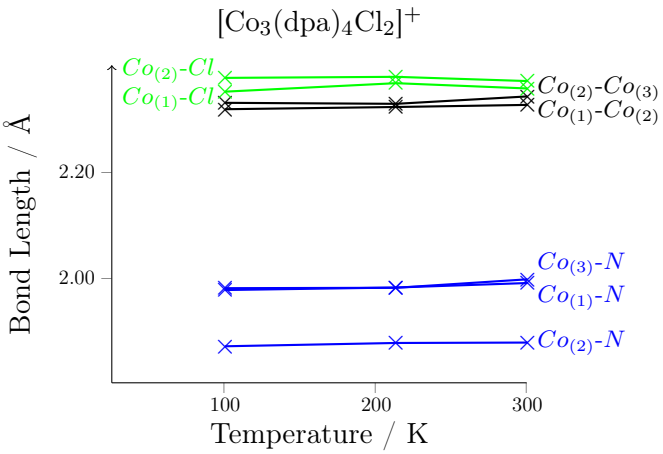

Figure 1.20: Bond lengths for the $[Co_3(dpa)_4Cl_2]^+$ crystal from 100 – 300 K. [86]

doublet ↔ sextet spin crossover.

In the crystal phase it is possible to measure μ_{eff} at lower temperatures, and Clérac and colleagues showed a similar behaviour for the symmetric $Co_3(dpa)_4Cl_2{\cdot}CH_2Cl_2$. [35] Between 8 – 160 K μ_{eff} plateaued at 2.07 μ_B, which corresponds to a doublet ground state (S=1/2) and a g value of 2.38. This was supported by fitting the magnetisation to a Brillouin function for a doublet, which gave a similar g value of 2.35, while EPR on a single crystal sample gave an average g value of 2.298. The spin crossover was again incomplete at the highest temperatures, and characterisation of the high temperature spin state was limited by the integrity of the crystal due to loss of the interstitial solvent molecules. This made fitting the experimental data to the theoretical model more sensitive to experimental error and changes in the g value with temperature. Their earlier work on the cationic $[Co_3(dpa)_4Cl_2]^+$ complex proposed a two step spin-crossover between three states: singlet ↔ triplet ↔ quintet. [86] If we examine the structural evolution of the cation (Figure 1.20), we see a similar profile to the neutral $Co_3(dpa)_4Cl_2{\cdot}CH_2Cl_2$ crystal in the same temperature range, which suggests a similar electronic mechanism could be at play. Clérac *et al.* argue that the extra electron in the neutral $Co_3(dpa)_4Cl_2{\cdot}CH_2Cl_2$ could therefore lead to a HS quartet or sextet state, and fit the data to models of both. For the quartet

they calculated ΔH = 18.0 kJ mol^{-1} (0.19 eV), ΔS = 54.7 J K^{-1} mol^{-1} and $T_{\frac{1}{2}}$ = 329 K and for the sextet ΔH = 13.7 kJ mol^{-1} (0.14 eV), ΔS = 29.2 J K^{-1} mol^{-1} and $T_{\frac{1}{2}}$ = 468 K. They found the sextet model fit the data slightly better, with regression coefficients of R^2 = 0.99803 and 0.99988 for the quartet and sextet, respectively.

For the unsymmetric $Co_3(dpa)_4Cl_2{\cdot}2CH_2Cl_2$ μ_{eff} is not saturated at either the low or high temperature limits. At 10 K μ_{eff} = 2.85 μ_B, which is high for a doublet, and increases to 4.47 μ_B at 300 K. To further investigate, Clérac *et al.* measured the magnetic susceptibilities of a single crystal, and found μ_{eff} to have a strong angular dependence with an anisotropic g factor. They were able to assign the ground state as a LS doublet and the HS state as a quartet, but the anisotropy and temperature dependence of the g factor meant they could not reasonably fit the data to the model. In their later study Clérac *et al.* were also able to assign a LS doublet ground state and HS quartet state to all the crystals they synthesised: $Co_3(dpa)_4Cl_2{\cdot}$THF, $Co_3(dpa)_4Cl_2{\cdot}$Hexane, $Co_3(dpa)_4Cl_2{\cdot}$Benzene, $Co_3(dpa)_4Cl_2{\cdot}0.85Et_2O{\cdot}0.15CH_2Cl_2$ and $Co_3(dpa)_4Cl_2{\cdot}1.75$Toluene$\cdot$0.5Hexane. [36] In the most recent work, Hillard and co-workers calculate the thermodynamic parameters, ΔH, ΔS and $T_{\frac{1}{2}}$, by refitting the previous magnetic data to the ideal solution model of a doublet $\leftrightarrow$ quartet spin crossover. [38] They also calculate these values for their new $Co_3(dpa)_4Cl_2{\cdot}Et_2O$ crystal, the previously undetermined $Co_3(dpa)_4Cl_2{\cdot}2CH_2Cl_2$ and include a recalculation for $Co_3(dpa)_4Cl_2{\cdot}CH_2Cl_2$. After a thorough examination of the entire spectrum of structural and magnetic data they are able to relate the experimental structure to the spin crossover behaviour, but only in the crystals that exhibit an unsymmetric structure, concluding that the greater the degree of asymmetry in the structure the lower the spin crossover temperature, Unfortunately such a relationship was not apparent in those structures that remain symmetric.

1.3.3 Bonding

In the first work on the tricobalt EMAC, Peng and co-workers proposed a bonding scheme for the unsymmetric structure in which they split the trimer into a diamagnetic $Co_{(1)}$-$Co_{(2)}$ dimer and an independent spin crossover square-pyramidal $Co_{(3)}N_4Cl$ chromophore. [26] The electronic structure of the dimer was straightforwardly described as a single $Co_{(1)}$-$Co_{(2)}$ sigma bond arising from a $(\sigma)^2(\pi)^4(\delta_{xy})^2(\delta^*_{xy})^2(\pi^*)^4$ configuration within an MO scheme equivalent to that of the Re_2Cl_8 dimer shown in Figure 1.2. The $Co_{(2)}$-$Co_{(3)}$ distance of 2.472 Å is similar to those observed for the Ni_3 and Cu_3 EMACs, which have a zero bond order, suggesting there is no bonding between the $Co_{(2)}$ and $Co_{(3)}$ atoms. The local structure of the $Co_{(3)}$ unit showed elongated $Co_{(3)}$-N and contracted $Co_{(3)}$-Cl distances compared to the cobalt atoms of the dimer, similar to other high-spin five-coordinate Co(II) complexes. [87] The structure of TM compounds can be related to their electronic structure and spin state. As previously described, in octahedral, square pyramidal and square planar complexes the metal $\delta_{x^2-y^2}$ orbitals lie high in energy due to strong σ antibonding interactions with the equatorial ligands. HS states have a greater occupation of the high energy $\delta_{x^2-y^2}$ orbitals compared to LS states, and the associated M-L distances are longer than in LS states. This behaviour has been observed in many spin crossover Co(II), Fe(II) and Fe(III) complexes. [88–100] In the case of the tricobalt EMACs, the Co $\delta_{x^2-y^2}$ orbitals interact with the nitrogen atoms of the pyridine/amine moieties of the dpa ligand. When considered alongside the observation of spin crossover process, the electronic structure of the CoN_4-Cl unit was described as an isolated Co(II) centre, existing in the HS state at higher temperatures with long Co-N bonds but undergoing a localised $^4T_1$ – ^2E crossover as the temperature was lowered. After distinguishing the symmetric and unsymmetric structures, Cotton and co-workers agreed with the bonding formation in the unsymmetric complex described by the Peng group. [74] Cotton *et al.* also recall their work

on the Cr_3 chains in further support, which as previously described shows a Cr quadruple bonded dimer coupled to a non-bonded square pyramidal CrN_4X unit in the unsymmetric structures. [25] Cotton also describes the bonding in the symmetric tricobalt structure as having "delocalised metal-to-metal bonds."

The first theoretical study from Bénard and Rohmer used DFT with the BP86 functional to search the isolated $Co_3(dpa)_4Cl_2$ potential energy surface (PES) for the separate minima characteristic of bond stretch isomers. [101] They used geometry optimisation with starting geometries of the experimental symmetric and unsymmetric structures. Both optimisations converged on the same symmetric minimum and they were unable to locate an unsymmetric structure. They attempted to trap the structure in an unsymmetric minimum by pre-optimising the geometry with Co-Co distances fixed to the experimental values but were again unsuccessful. The electronic configurations of the symmetric minima were found to all be equivalent and was assigned as the ground state. The energy of the structure with fixed Co-Co bonds was shown to lie only 6.7 kcal mol^{-1} (0.29 eV) above the symmetric minimum, showing the ground state PES to be quite flat. The bonding scheme can be considered equivalent to the one described for the Rh_3 complex earlier, where each Co(II) contributes seven d electrons to the MO array shown in Figure 1.7. The δ_{xy} and π frameworks are all completely filled, the sigma framework contains three electrons, with a doubly occupied bonding σ orbital, singly occupied σ^{nb} and vacant σ^*, while the $\delta_{x^2-y^2}$ framework is vacant. This is described as a three-centre three-electron bond over the σ framework with a frontier configuration of $(\pi^{nb})^4(\delta^{nb}_{xy})^2(\sigma^{nb})^1(\pi^*)^4(\delta^*_{xy})^2$.

Bénard and Rohmer also located two low-lying excited states. These arise from the excitation of a single electron from the π^* or δ^*_{xy} orbitals into the σ^{nb} hole, with relative energies of +0.24 and +0.35 eV and configurations of $(\pi^{nb})^4(\delta^{nb}_{xy})^2(\sigma^{nb})^2(\pi^*)^3(\delta^*_{xy})^2$ and $(\pi^{nb})^4(\delta^{nb}_{xy})^2(\sigma^{nb})^2(\pi^*)^4(\delta^*_{xy})^1$, respectively. Similar to the $\delta_{x^2-y^2}$ Co-N antibonding

interactions, the σ framework has antibonding Co-Cl interactions, and just as HS states with greater $\delta_{x^2-y^2}$ occupation have longer Co-N bonds, the increased occupation of the sigma framework leads to elongation of the Co-Cl bonds. This can be seen in the low-lying doublet excited states, with Co-Cl distances $\sim$0.1 Å longer than the ground state. They are both LS doublets, however, so their occupation would not explain the experimentally observed increase in μ_{eff}. The authors also note that the σ^* LUMO lies $\sim$1 eV above the HOMO and that the existence of a low-lying, thermally accessible HS quartet state is therefore improbable. They argue that these calculations, therefore, do not support the interpretation of the experimental work proposed by Peng *et al.* and there is no specific unsymmetric electronic structure. They instead propose the complex only exists on the flat ground state PES, and that the crystalline environment is responsible for the observed unsymmetric structure.

The work from Bénard and Rohmer did not include a specific search for a HS quartet state nor did it provide an explanation for the magnetic behaviour, and the characterisation of the unsymmetric tricobalt EMACs continued to prove problematic. Given this, Clérac *et al.* later insist that the original interpretation from the Peng group gives the best description of the bonding in the unsymmetric structure. [35] They support this with their calculation of an anisotropic g value, which they showed to be typical for mononuclear HS Co(II) complexes, and argue this would only arise from the coupling of a diamagnetic Co dimer with an isolated spin crossover Co(II) centre. They augment this with temperature dependent X-ray structure data, which can be related to the spin crossover process. As previously described, in a spin crossover process the individual complexes exist in equilibrium between the LS and HS states, with the occupation of each state defined by Equation 1.4 (page 30). We have also previously described how the structure of the complex is related to the spin state, in particular where the HS state has occupied $d_{x^2-y^2}$ orbitals and

longer M-L bonds (Co-N in the EMACs) than the LS state. The X-ray crystallography technique gives the average atomic positions over all the individual complexes in the whole crystal sample. The X-ray structure is therefore relatable to the spin crossover, and we can observe changes in the LS:HS ratio through changes in the structure, for example as an elongation of the M-L bonds as the HS fraction increases. In the case of the unsymmetric $Co_3(dpa)_4Cl_2{\cdot}2CH_2Cl_2$ we see an elongation of the $Co_{(3)}$-N bonds as the temperature, and therefore HS occupation, is increased concomitant with the magnetic data. This is characteristic of a localised spin crossover at the $Co_{(3)}$ centre. The change in Co-N distances are accompanied by a change in the Co-Co distances. At low temperatures the LS state dominates and the structure appears more symmetric, while the occupation of the HS state seems connected to the divergence in the Co-Co distances. This suggests the spin crossover process should also be able to be associated with the symmetric-unsymmetric transition as well as the Co-N elongation. In the same work, Clérac *et al.* propose the magnetic behaviour of the symmetric $Co_3(dpa)_4Cl_2{\cdot}CH_2Cl_2$ could indicate a spin crossover into a sextet state, and this was also suggested for the $Co_3(dpa)_4Cl_2$ complex in solution. [75] Both structures remain symmetric at higher temperatures, and these observations are inconsistent with an unsymmetric HS quartet state, and could indicate the existence of another low-lying HS state.

In 2001 Bénard, Rohmer and co-workers were finally able to find an unsymmetric HS quartet state using DFT (using BP86). [29] The optimised structure shows the same features as the experimental high temperature unsymmetric structures, with ΔCo-Co = 0.111 Å and ΔCo-N = 0.148 Å, and they assign the observed temperature dependent structure to the partial population of the unsymmetric quartet. The quartet state arises from the excitation of the δ^*_{xy} electron into the $\delta_{x^2-y^2}$ orbital (Figure 1.21c), and specific attention is drawn to the occupation of the $\delta_{x^2-y^2}$ orbital and its link to the structure.

At an unsymmetric geometry the $\delta_{x^2-y^2}$ orbital is lower in energy than the σ^* orbital due to the Co-N elongation. They could not locate an unsymmetric state from a symmetric starting geometry, where the σ^* orbital is the LUMO. They suggest that quartet states at the symmetric limit would have the σ^* orbital occupied preferentially over the $\delta_{x^2-y^2}$ orbital and a symmetric structure, although they were unable to explicitly optimise such a state. They calculated the energy of the unsymmetric quartet state to lie 18.3 kcal mol^{-1} (0.794 eV) above the ground state, which they considered too large to explain the observed spin crossover. They suggest the result could be influenced by a systematic error inherent to the method due to the comparison of states with different multiplicities. To test this they use B3LYP to calculate the single point energies at the BP86 ground state and unsymmetric quartet geometries, but the excitation energy was similar and they conclude that other methodologies should be considered. In their work they reiterate the shallowness of the ground state PES, and rule out the possibility of bond stretch isomerism, which should be associated with a single multiplicity, whereas here appears intrinsically linked to the doublet $\leftrightarrow$ quartet transition.

In 2006 McGrady and co-workers proposed a new, lower energy unsymmetric HS quartet state, with ΔCo-Co = 0.130 Å and ΔCo-N = 0.167 Å. [102] Rather than exciting a δ^*_{xy} electron, the new quartet state arises from the ground state through the excitation of a π^* electron into the $\delta_{x^2-y^2}$ orbital (Figure 1.21d). The symmetric ground state has been shown to have D_4 symmetry. The divergence of the Co-Co distances gives the unsymmetric quartet state found by Bénard *et al.* C_4 symmetry. The new quartet state has C_2 symmetry due to an additional Jahn-Teller distortion, which works to stabilise the doubly occupied orbital of the degenerate π^* pair through the divergence of the Co-N bonds at each Co. The work from McGrady *et al.* uses the lowest symmetry point group (C_2) to identify all the states, with the new quartet state referred to as ^{4}B, the original unsymmetric quartet

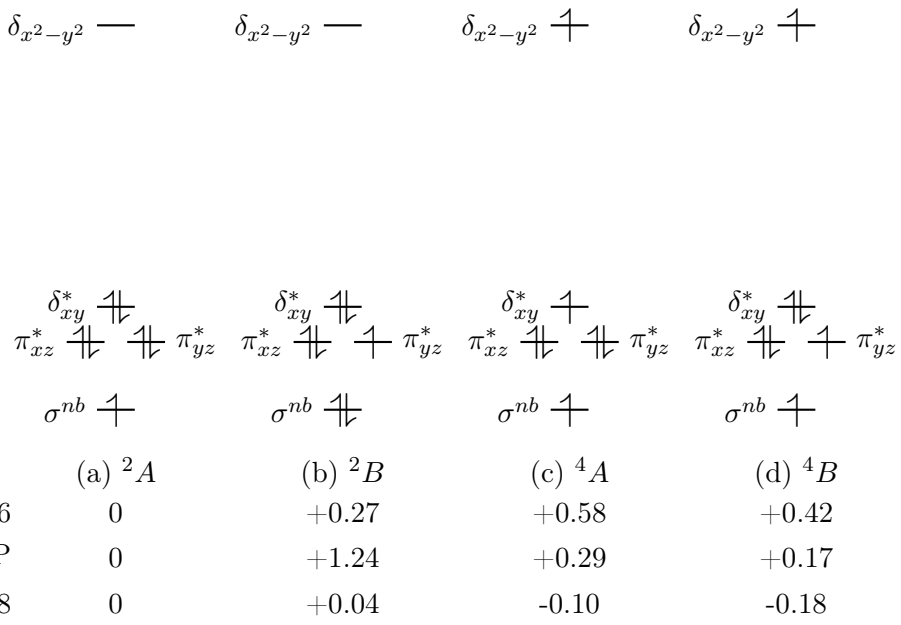

		(a) ^2A	(b) ^2B	(c) ^4A	(d) ^4B
	BP86	0	+0.27	+0.58	+0.42
E(rel) / eV	B3LYP	0	+1.24	+0.29	+0.17
	VS98	0	+0.04	-0.10	-0.18

Figure 1.21: Frontier electron configurations of the (a) ^{2}A ground state and low energy doublet and quartet states (b) ^{2}B, (c) ^{4}A and (d) ^{4}B with relative energies to the ^{2}A state for BP86, B3LYP and VS98 functionals.

as ^{4}A and the ground state symmetric doublet as ^{2}A. The configurations of the states are shown in Figure 1.21, along with the energies calculated with the BP86 (GGA), B3LYP (Hybrid) and VS98 (meta-GGA) functionals (all at the BP86 optimised geometries for each state). The ^{4}B state is shown to lie lower than the ^{4}A state with all the functionals. Interestingly, the VS98 functional actually predicts the ^{4}B state to be the ground state and both quartet states to have lower energies than the ^{2}A state. McGrady *et al.* separate the MOs of the ^{4}B state into a set localised on the isolated $Co_{(3)}$ and a set localised on the Co dimer, consistent with the description first proposed by Peng and co-workers. Their work does point out a significant degree of mixing between the two, however, and explain the separation should only be considered as a first approximation. In this work we present the same orbitals for $Co_3(dpa)_2Br_2$ (Chapter 4 Figure 4.2)

In the first theoretical work from Bénard *et al.* two low-lying doublet excited states were found, and McGrady and Pantazis suggest that one of these states, ^{2}B (Figure 1.21b), is of great importance to the behaviour of the tricobalt EMACs. They proposed that

it is the ^{2}B state that has the flat PES, and that it bridges a high-energy region between the ^{2}A and ^{4}B states, as shown in the potential energy diagram in Figure 1.22. The vertical axis represents the potential energy and the two base axes represent the asymmetry of the structure using ΔCo-Co and ΔCo-N. The symmetric ^{2}A and ^{2}B surfaces have minima at the origin where ΔCo-Co and ΔCo-N are zero, while the ^{4}B surface minimum is located at the unsymmetric limit with large values for ΔCo-Co and ΔCo-N. On the ^{2}B surface the EMAC would be able to explore unsymmetric geometries with little energetic cost. McGrady and Pantazis created a model to simulate the exploration of the ^{2}B potential energy surface using fractional occupation number (FON) DFT. [102] FON DFT allows occupations of molecular orbitals (or spin orbitals) to vary from 0 or 2 (or 0 or 1), and can be used to account for multi-reference effects, which are discussed in Chapter 2. [103–108] In the model McGrady and Pantazis used the fractional occupation of the δ_{xy} and $\delta_{x^2-y^2}$ orbitals in the ^{2}B state to slowly transfer electron density to the $\delta_{x^2-y^2}$. They showed that as the occupation of the $\delta_{x^2-y^2}$ orbital gradually increases the structure becomes more asymmetric, exhibiting an increase in ΔCo-Co and ΔCo-N similar to the experimental structural evolution $Co_3(dpa)_4Cl_2{\cdot}2CH_2Cl_2$ crystal. This model provides an electronic mechanism for the symmetric-unsymmetric transition that is not associated with a change in spin state, and could potentially explain the experimentally observed low temperature unsymmetric structures. It could also explain the convergence of the $Co_3(dpa)_4Cl_2{\cdot}Et_2O$ and $Co_3(dpa)_4Cl_2{\cdot}2CH_2Cl_2$ crystal structures, where it may be reasonable to suggest that the EMAC's lie on a common potential energy surface across many crystals. Under a regime like that described by Bürgi and Dunitz a flat PES can be distorted by small changes in the local environment. [109] This idea has been explored in many spin crossover complexes to investigate the influence of the crystalline environment on the LS and HS state energies. Acting like a perturbation to the PES, the magnitude of the effect can be of the same

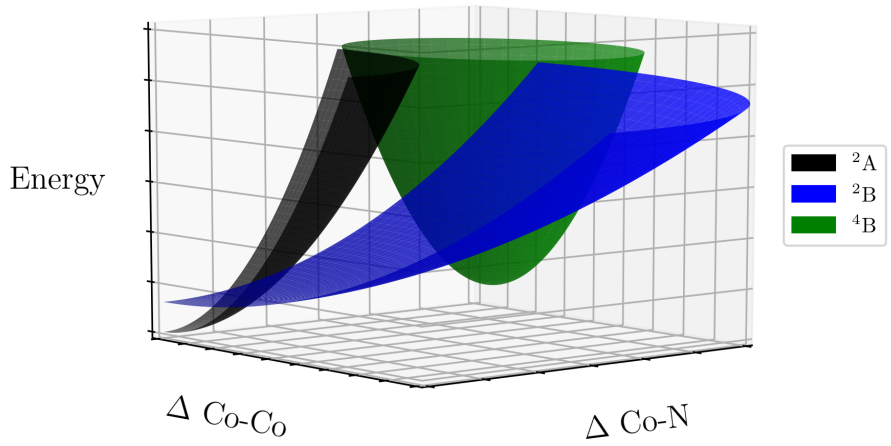

Figure 1.22: Schematic potential energy diagram showing surfaces for the ^{2}A, ^{2}B and ^{4}B states between the symmetric and unsymmetric limits.

order as the LS-HS state splitting energy. [98, 99, 110–112] These effects can be thought of more visually in terms of the LS and HS structures, where crystal packing forces can change the spin crossover properties by facilitating or impeding the associated structural changes. Cotton suggested such effects would play an important role in understanding the different structures in the different $Co_3(dpa)_4Cl_2$ crystals. [76] The energy differences between the ^{2}A, ^{2}B and ^{4}B states in the isolated molecule are sufficiently small that the crystalline environment could be expected to have a large effect on spin state splitting energies. This will affect the observed structures and magnetism of the different crystals through the relative stabilisation of symmetric or unsymmetric geometries.

The DFT calculations assume an isolated molecule in a vacuum at a temperature of absolute zero, and the effect of the crystalline environment and temperature are not taken into account explicitly in any of the theoretical work presented so far. This was rectified in 2009 when the most recent theoretical work from Murillo and co-workers presented a Hirshfeld surface analysis on the symmetric $Co_3(dpa)_4Cl_2{\cdot}CH_2Cl_2$ crystal and unsymmetric $Co_3(dpa)_4Cl_2{\cdot}2CH_2Cl_2$ crystal at different temperatures. [113] The electron density was determined from experimental X-ray diffraction data at multiple temperatures

using the Hansen-Coppens multipole model. [114] Their work focussed on investigating the differences in the weak intermolecular interactions between the EMAC complexes and the interstitial solvent molecules in the symmetric and unsymmetric crystals. The electron density at specific point in a crystal arises from the contribution of all the atomic densities in the crystal at that point. The Hirshfeld surface analysis defines a surface that encompasses a molecule within a crystal such that the electron density at the surface has equal contributions from the internal molecule and the rest of the crystal. [115] The surface is then coloured with a gradient to reflect the proximity of the internal and external atoms, and is a useful indicator of crystal packing forces, highlighting not only areas with close direct contacts, but also those that have multiple weaker contacts. The analysis from Murillo *et al.* showed that the Hirshfeld surface surrounding the EMAC in the symmetric $Co_3(dpa)_4Cl_2{\cdot}CH_2Cl_2$ looks very similar at both ends of the EMAC, even in the low temperature limit which sees the divergence in the Co-Cl bonds, with multiple close contacts to the other EMAC complexes and solvent molecules. This explains why the underlying $Co_3(dpa)_4$ core is relatively unaffected by the temperature. The Hirshfeld surface in the unsymmetric $Co_3(dpa)_4Cl_2{\cdot}2CH_2Cl_2$, however, looks quite different at either end of the EMAC showing more close contacts at one end, where the authors specifically highlight a strong and weak $Co_{(3)}$-Cl$\cdots$H-C hydrogen bonding interaction, but only a single weak $Co_{(1)}$-Cl$\cdots$H-C hydrogen bonding interaction at the other end.

The work also examines the electron densities of the two crystals from the X-ray diffraction data. Their analysis suggests that in the unsymmetric structure, although the $Co_{(1)}$-$Co_{(2)}$ is stronger there still exists a $Co_{(2)}$-$Co_{(3)}$ bond. This corresponds to the work from McGrady *et al.* which showed significant mixing between the Co dimer and isolated Co(II). Electron deformation and Laplacian maps suggest $Co_{(1)}$ and $Co_{(2)}$ exist in LS t_{2g} states, while $Co_{(3)}$ should be responsible for the change in spin state. They then calculate

the experimental d orbital occupations from the multipole parameters and show occupation of all orbitals at each centre, however a lower d_{xy} population and higher $d_{x^2-y^2}$ population on $Co_{(3)}$ compared to $Co_{(1)}$ and $Co_{(2)}$, suggesting those orbitals are responsible for the observed spin transition, corresponding to the FON analysis from McGrady and Pantazis.

1.3.4 $Co_3(dpa)_4X_2$ [X = F, Br, I]

The literature surrounding the tricobalt chloride complex is extensive, but it is not the only known tricobalt EMAC with axial halide ligands. The bromide analogue has been known since 2001, and has been shown to exhibit many of the behaviours observed for the chloride complex. $Co_3(dpa)_4Br_2$ has been shown to have a symmetric structure in crystals with CH_2Cl_2 and hexane solvates and an unsymmetric structure in $Co_3(dpa)_4Br_2 \cdot 1.75Toluene \cdot 0.5Hexane$, as well as ^1H NMR spectra that suggest a D_4 symmetric structure in solution. Similar magnetic behaviour was also observed for $Co_3(dpa)_4Br_2 \cdot CH_2Cl_2$, and whilst they cannot assign the HS state as a quartet or sextet due to the lack of saturation at higher temperatures, they do recognise a higher spin crossover temperature, indicative of a larger energetic separation of the LS and HS states. [37] The work also suggests that the similar structural and magnetic properties of the bromide and chloride complexes imply a similar underlying electronic structure.

Hillard *et al.* report the synthesis of $Co_3(dpa)_4Br_2 \cdot Et_2O$ in their recent experimental work with similar properties to the corresponding chloride complex with diethyl ether solvate, and extended the tricobalt series further to include the fluoride and iodide analogues: $Co_3(dpa)_4F_2 \cdot CH_2Cl_2$, $Co_3(dpa)_4I_2 \cdot Et_2O$ and $Co_3(dpa)_4I_2 \cdot C_2H_4Cl_2$. [38] This is the first time such complexes have been synthesised. In the work the authors suggest that the structures of the fluoride complex and those of other stronger field axial ligands favour a symmetric structure, even at high temperatures, and are less affected by the crys-

talline environment due to their large crystal field splitting energies. This has been shown in complexes with NCS^-, CN^- and $N(CN)_2^-$ axial ligands [116] and also in the cationic CH_3CN complex. [117] Meanwhile the geometry of complexes with weaker axial ligands could be more susceptible to crystal packing forces due to the smaller crystal field splitting energies. This may explain the behaviour of the complexes of the remaining halides, which show more examples of unsymmetric crystal structures at low temperatures.

They also examined the spin crossover process and magnetic data for the entire range of F, Cl, Br and I crystals. They showed that the temperature dependence of the magnetic susceptibilities varied depending on the axial halide ligand as well as the crystal structure. They recognised a general trend for a decreasing spin crossover temperature as the axial ligand descends the group F > Cl > Br > I. They were also able to show that the more unsymmetric crystals were likely to have lower spin crossover temperatures, an observation that holds across the crystals of the different halides.

1.3.5 Summary

The structural behaviours of the various crystals of the tricobalt series fall into one of three categories exemplified by: i) $Co_3(dpa)_4Cl_2{\cdot}CH_2Cl_2$ ii) $Co_3(dpa)_4Cl_2{\cdot}$Hexane and iii) $Co_3(dpa)_4Cl_2{\cdot}2CH_2Cl_2$. The first shows a low temperature symmetric structure that remains symmetric at higher temperatures, with an initial increase in the Co-X and decreases in the Co-Co and terminal Co-N distances, followed by decrease in the Co-X and increase in the Co-Co and Co-N distance as the temperature increases. This behaviour also occurs in the $[Co_3(dpa)_4Cl_2]^+$ cation, and appears to occur in the $Co_3(dpa)_4Br_2{\cdot}CH_2Cl_2$ although it only shows the initial structural changes within the observed temperature range. The second type of behaviour also shows a low temperature symmetric structure that remains symmetric at higher temperatures, but with a consistent increase in

the Co-Co and terminal Co-N distances and decrease in the Co-X distances. This behaviour is mirrored in $Co_3(dpa)_4Cl_2$·THF, $Co_3(dpa)_4Cl_2$·Benzene, $Co_3(dpa)_4Br_2$·Hexane and $Co_3(dpa)_4I_2$·$C_2H_4Cl_2$. The third type shows low temperature structures that tend to the symmetric ground state geometry and high temperature structures that tend towards an unsymmetric geometry. This behaviour occurs to varying degrees depending on the extent of the asymmetry at low temperatures. $Co_3(dpa)_4Cl_2$·Et_2O and $Co_3(dpa)_4Br_2$·Et_2O are very symmetric at low temperatures and only develop a slight asymmetry at high temperatures. $Co_3(dpa)_4Cl_2$·$2CH_2Cl_2$, $Co_3(dpa)_4Cl_2$·1.75Toluene·0.5Hexane, $Co_3(dpa)_4Br_2$·1.75Toluene·0.5Hexane and $Co_3(dpa)_4I_2$·Et_2O have a significant degree of asymmetry at low temperatures, which increases further with the temperature. The only crystal that does not seem to fit any of these behaviours seems to be the $Co_3(dpa)_4F_2$·$2CH_2Cl_2$, and will be investigated in more detail in Chapter 7.

The magnetic behaviour of the unsymmetric structures in category iii all appear to show a spin crossover into a HS quartet state from a LS doublet state. The category ii symmetric structures have all been modelled successfully as a spin crossover from a LS doublet into a HS quartet in the latest work from Hillard *et al.* The nature of the HS state in the category i symmetric structures is not fully determined, and has been suggested as either a quartet or a sextet. Theoretical calculations seem conclusive in the calculation of a symmetric doublet ground state, which is well understood and is characterised by a three-centre three-electron bond over the σ framework. The category iii complexes seem to be best described by an unsymmetric HS quartet state, which can be considered as a diamagnetic Co dimer coupled to an isolated spin crossover Co(II). Theoretical calculations appear to agree with this model, and they also highlight the importance of the isolated Co(II) $d_{x^2-y^2}$ orbital to the origin of the asymmetry. The optimised unsymmetric HS states do not explain the structural behaviour of those structures that remain symmetric

at high temperature but still exhibit a spin crossover, and in fact the latest work from Hillard *et al.* specifically calls for a new theoretical investigation to search for a symmetric HS quartet state. No such state has previously been found, nor has there been any attempt to locate any HS sextet states. Bénard *et al.* have previously suggested that occupation of the σ^* orbital in the symmetric limit could lead to a symmetric quartet state. [29] In the earlier work from Clérac *et al.* they presented a similar argument linking the elongation of the Co-Co bonds with the occupation of the σ^* orbital. However no such state has been found in the theoretical work, nor would such a state account for the category ii behaviour and the observed elongation of both terminal Co-N distances, which appears to be intrinsically linked to the occupation of the $\delta_{x^2-y^2}$ orbital. [36] They concede that the bonding in the tricobalt EMACs was still not fully understood, leaving the door open to further theoretical work.

In 2009 McGrady and Pantazis, working with Murillo, published a re-evaluation of the two-step spin crossover of the $Co_3(dpa)_4Cl_2$ cation. [118] In it they presented a methodical analysis of a range of excited states that could potentially explain the observed behaviour, and found results that disagreed with the previous electronic structures. In particular they found the δ^*_{xy} orbital in the neutral species to contain the redox active electron, and associated the HS quintet with the occupation of the $\delta_{x^2-y^2}$ orbital, as in their calculation of the 4B state. In this work we will apply a similar approach and conduct a systematic search over a range of electronic configurations in order to elucidate the broad spectrum of behaviours seen in the tricobalt complex.

The work from Hillard *et al.* formed the initial motivation for this thesis. We originally planned to investigate the effect of the axial ligand substitution on three state model proposed by McGrady and Pantazis. However, in light of the many behaviours described above it was clear that we would need to go beyond this model to fully understand

the tricobalt EMACs, and it became necessary to undertake a more comprehensive review. The amount of data collected quickly became vast, and trying to compare all the states for all the halides would hinder the clarity of this work. As such we will first focus on the tricobalt bromide EMAC, examining a range of states with symmetric (Chapter 4) and unsymmetric structures (Chapter 5), before considering the transition between the two (Chapter 6) and then extending the analysis to the fluoride, chloride and iodide complexes (Chapter 7). The bromide complex has not previously been studied theoretically, but still has a relatively large bank of experimental data for comparison with our calculations, as well as the potential for comparison with the theoretical work on the chloride complex. First understanding the bromide complex in detail will provide a platform to coherently describe the complexes of the other halides. A more detailed review of the literature surrounding the bromide, fluoride and iodide complexes will be given in the relevant chapters.

1.4 This Thesis

In modern computational chemistry we use a range of methods that describe how electrons in TM complexes interact and how metals bond with ligands and other metals. Using the linear combination of atomic orbitals, MOs are calculated and their occupations allow us to understand the interactions within the molecule and its bonding, and from that infer the molecular properties. Sometimes the bonding in a molecule is easily understood and it is obvious which orbitals are filled, however bonding between TMs is complicated by the nature of the valence atomic d shell. There can be many interactions between many near degenerate atomic orbitals. This leads to an array of MOs that all lie close in energy and the exact energetic profile, and therefore orbital occupations, cannot be determined straightforwardly. Depending on the choice of metals and their oxidation state the number of electrons in the metal-metal bonding framework can vary, whilst the multiplicity and

ligand interactions can further influence the bond order. The EMACs provide an ideal testing ground for quantum chemistry, exhibiting a wide range of interactions between a multitude of metal atoms, from exchange coupling through diamagnetic centres to the formation of multiple bonds, spin crossover behaviour and low-lying excited states in systems with strong static correlation. The intricate nature of their underlying electronic structures means that the EMACs also provide a significant challenge to modern theoretical techniques. They allow us to explore and push the boundaries of existing methods and to set benchmarks in the trials of new methods.

Further to this, many EMACs have been shown to conduct electricity and can be used to test our understanding of electron transport mechanisms. Electrical conductivity means the EMACs also have the potential to impact the electronics industry. Modern computer architectures rely on decreasing the size of transistors to increase computing power. Moore's law predicts that the number of transistors on a chip will double every two years increasing, which has so far been achieved through the miniaturization of the metal-oxide-semiconductor field-effect transistor (MOSFET) components. [119, 120] MOSFETs contain a source and drain electrode connected by a silicon semicoductor that is mediated by a gate electrode. They work by the application of a gate voltage over the component, which allows current to flow when it is high and in the on-state, and stops current flowing when it is low in the off-state. [121] However, as the distance between the source and drain electrodes decreases, quantum tunnelling effects take hold and the transistor leaks current and cannot be turned off. [122] Much of the scientific community's motivation and interest in EMAC research stems from their potential specification to suit a range of components in the field of molecular electronics. Rather than carving components out of bulk materials, molecular electronics is a bottom-up approach that builds components up from atoms and molecules, which could, in principal, allow atomic control over physical

properties, including the electron transport mechanisms through the component. [123] The metallic core and organic outer layer of the EMACs bears a strong resemblance to a conventional macro wire, and they have been proposed as molecular wires, [54, 124–126] [127] transistors, [128] spin filters [129] and as rectifiers that take advantage of asymmetric hetero-metallic Ru-Ru-Ni and Ru-Ru-Cu chains. [130]

In this thesis we present the first study of tricobalt bromide EMAC. The theoretical work has so far focused on the chloride analogue, however the experimental data shows a broadly similar behaviour for the bromide complex. In addition to this, the theoretical work is unable to explain the full range of experimentally observed behaviours, and as such we will present a more comprehensive, systematic search for excited states. This work also represents the first MCSCF analysis of the tricobalt system. CASPT2 has previosuly been used to trichromium system, but this did not include the $d_{x^2-y^2}$ orbitals, [24] which have been shown to be pivotal to understanding the tricobalt system in the DFT work so far, in particular the variable Co-N distances. [29, 102, 113, 118] Finally we develop and implement a novel model to simulate the structural temperature dependence of spin crossover compounds. We use the thermodynamic parameters extracted from the experimental magnetic data to calculate the temperature dependent HS population, and from that a thermally averaged temperature dependent structure.

Understanding the structure-function relationships of metal-metal bonded systems would offer control over a variety of properties. If the ultimate aim of electronic structure theories is to design molecules with specific properties, we first need to understand the electronic mechanisms that drive the properties of the molecules we already know. Indeed, as Clérac *et al.* state in some of the earliest experimental work "Our understanding of metal-metal bonding cannot be considered complete until it is able to deal with a case like this." [36]

Chapter 2

Theoretical Techniques

The foundations of quantum chemistry can be traced back to the 1920s when Schrödinger and Heisenberg formulated the theory of quantum mechanics. The theory set up a mathematical framework to describe the dynamics (positions and momenta) of systems of subatomic particles. It has become one of the most successful theories of all time, accurately predicting a multitude of phenomena that long perplexed classical mechanics.

2.1 The Schrödinger Equation

The central equation governing the motion of quantum particles is the time dependent Schrödinger equation. [131]

$$i\hbar\frac{\partial}{\partial t}\Psi\left(\mathbf{r},t\right)=\hat{H}\Psi\left(\mathbf{r},t\right) \tag{2.1}$$

This is a linear partial differential equation, where $\Psi\left(\mathbf{r},t\right)$ is a solution called a wavefunction, which describes a quantum state and its evolution it time. $\hat{H}$ is a linear operator called the Hamiltonian and $\hbar$ is Planck's constant divided by 2π. The Hamiltonian is a concept from classical mechanics, and is used to calculate the total energy of a system. It can be broken down into the sum of the kinetic energy, T and potential energy, V, of the

system, which are given by their respective linear operators

$$\hat{H} = \hat{T} + \hat{V} \tag{2.2}$$

The kinetic energy of a single particle system is related to the square of the particle's momentum, p, as shown below. The quantum operator $\hat{T}$ can be defined by replacing the value of the momentum with the quantum operator for the momentum, $\hat{p}$.

$$T = \frac{p^2}{2m} \tag{2.3}$$

$$\hat{p} = -i\hbar\nabla \tag{2.4}$$

$$\nabla = \frac{\partial}{\partial x} + \frac{\partial}{\partial y} + \frac{\partial}{\partial z} \tag{2.5}$$

$$\hat{T} = -\frac{\hbar^2}{2m}\nabla^2 = -\frac{\hbar^2}{2m}\left(\frac{\partial^2}{\partial x^2} + \frac{\partial^2}{\partial y^2} + \frac{\partial^2}{\partial z^2}\right) \tag{2.6}$$

The potential energy of a single particle system is related to the position of the particle and the time. The quantum operator for position is given by the vector operator $\hat{\mathbf{r}}$ $(\hat{x}, \hat{y}, \hat{z})$. Unlike the momentum operator, its relationship to the classical position is straightforward and its operation yields the position vector of the particle $\mathbf{r}$ with components (x, y, z).

$$\hat{V} = V(\mathbf{r}, t) \tag{2.7}$$

For a system of N particles the kinetic energy is given by the sum of the kinetic energies of all the individual particles, while the potential energy is a function of the positions of

all the particles and time.

$$\hat{H} = -\sum_{n=1}^{N} \frac{1}{2m_n} \nabla_n^2 + V\left(\mathbf{r}_1, \mathbf{r}_2, ..., \mathbf{r}_N, t\right) \tag{2.8}$$

For a system of charged particles in the absence of an external potential, the potential energy is given by the sum of the Coulomb interaction energies between each pair of particles (with charges q_1 and q_2).

$$V\left(\mathbf{r}_1, \mathbf{r}_2, ..., \mathbf{r}_N, t\right) = \sum_{n<m}^{N} \frac{q_n q_m}{4\pi\epsilon_0 |r_n - r_m|} \tag{2.9}$$

$V\left(\mathbf{r}_1, \mathbf{r}_2, ..., \mathbf{r}_N, t\right)$ depends on the positions of all the particles and the interactions between them. Each time a new particle is added to a system, it interacts with all of the particles already in the system. This is the essence of the so-called many-body problem. For all but a few ideal systems, finding a wavefunction that describes a system with many particles (three or more) is extremely complicated. If we assume the wavefunction is separable into the product of a time dependent function, $f\left(t\right)$, and a space dependent function, $\psi\left(\mathbf{r}\right)$, such that $\Psi\left(\mathbf{r}, t\right) = \psi\left(\mathbf{r}\right) f\left(t\right)$, then Equation 2.1 (page 49) can be reformulated.

$$i\hbar \frac{\partial}{\partial t} \psi\left(\mathbf{r}\right) f\left(t\right) = \hat{H} \psi\left(\mathbf{r}\right) f\left(t\right) \tag{2.10}$$

If we also assume that that the potential in the Hamiltonian has no time dependence, $V\left(\mathbf{r}, t\right) = V\left(\mathbf{r}\right)$ then we can separate the time and space dependencies. The Hamiltonian operator, $\hat{H}$, takes the partial derivative with respect to the spatial coordinates (Equation 2.9). Taking the partial derivative with respect to the spatial coordinates of the right and side and the partial derivative with respect to time of the left hand side and dividing

through by $\psi(\mathbf{r}) f(t)$

$$i\hbar\psi(\mathbf{r})\frac{\partial f(t)}{\partial t} = -\frac{\hbar^2}{2m} f(t)\nabla^2\psi(\mathbf{r}) + V(\mathbf{r})\psi(\mathbf{r}) f(t) \tag{2.11}$$

$$i\hbar\frac{1}{f(t)}\frac{\partial f(t)}{\partial t} = -\frac{\hbar^2}{2m}\frac{1}{\psi(\mathbf{r})}\nabla^2\psi(\mathbf{r}) + V(\mathbf{r}) \tag{2.12}$$

The two sides of the equation are equal, but as the left hand side is a function of t only and the right hand side a function of $\mathbf{r}$ only, they have no common variables and must therefore both be equal to a constant, E. Equating this constant to to the right hand side yields the time independent Schrödinger equation (Equation 2.15). [132]

$$-\frac{\hbar^2}{2m}\frac{1}{\psi(\mathbf{r})}\nabla^2\psi(\mathbf{r}) + V(\mathbf{r}) = E \tag{2.13}$$

$$-\frac{\hbar^2}{2m}\nabla^2\psi(\mathbf{r}) + V(\mathbf{r})\psi(\mathbf{r}) = E\psi(\mathbf{r}) \tag{2.14}$$

$$\hat{H}\psi(\mathbf{r}) = E\psi(\mathbf{r}) \tag{2.15}$$

This is an eigenvalue equation. The spatial wavefunction $\psi(\mathbf{r})$ can be one of a set of solutions called eigenfunctions. When an operator, $\hat{H}$, acts on one of its eigenfunctions, $\psi_i(\mathbf{r})$, the result is the original eigenfunction multiplied by a constant, E_i, called the eigenvalue. Equation 2.15 can be more generally expressed as

$$\hat{H}\psi_i(\mathbf{r}) = E_i\psi_i(\mathbf{r}) \tag{2.16}$$

This equation has no time dependence, and the resultant eigenfunctions are as such called stationary states, or eigenstates. The eigenvalue, E_i, corresponds to the energy of the eigenstate described by $\psi_i(\mathbf{r})$. The eigenstate with the lowest eigenvalue (and therefore lowest energy) is called the ground state and the higher energy states are called excited

states. The eigenstates of the Hamiltonian form a complete set of orthonormal states. The linear combination of these eigenstates can be used to describe any possible state of the system. [132, 133]

$$\psi(\mathbf{r}) = \sum_i c_i \psi_i(\mathbf{r}) \tag{2.17}$$

Experimental observables can be represented by different quantum operators. Each operator has its own complete set of orthonormal eigenstates and eigenvalues which can be used to represent any quantum state. When a measurement of a quantum system is made, a different result can occur each time. This demonstrates the probabilistic nature of quantum events. The coefficients, c_i, are complex numbers called amplitudes. When multiplied by their complex conjugate they give the probability the system is measured to be in the corresponding eigenstate $\psi_i(\mathbf{r})$.

$$c_i^* c_i = |c_i|^2 \tag{2.18}$$

The sum of all these probabilities necessarily equals one.

$$\sum_i |c_i|^2 = 1 \tag{2.19}$$

The expectation value of an operator acts like a weighted average over the eigenstates of the operator that contribute to a quantum state. It corresponds physically to the average of a repeated set of measurements of the observable represented by that operator. It may not be possible to actually measure the expectation value, as only an eigenvalue of the operator may be observed. The expectation value of $\hat{H}$ in the state $\psi(\mathbf{r})$ is given by

$$\left\langle \hat{H} \right\rangle = \int \psi^*(\mathbf{r}) \hat{H} \psi(\mathbf{r}) \, d\mathbf{r} \tag{2.20}$$

We can understand the time dependence of a solution of the time independent Schrödinger equation (Equation 2.15) by re-examining Equation 2.12 and setting the left hand side equal to the constant E, just as we did for the right hand side in Equations 2.13-2.15.

$$i\hbar \frac{1}{f(t)} \frac{\partial f(t)}{\partial t} = E \tag{2.21}$$

$$\frac{\partial f(t)}{\partial t} = \frac{-iE}{\hbar} f(t) \tag{2.22}$$

The solution to Equation 2.22 has the form

$$f(t) = e^{\frac{-iEt}{\hbar}} \tag{2.23}$$

and can be used to create a set of solutions to the time dependent Schrödinger equation (Equation 2.1) of the form

$$\Psi_i(\mathbf{r}, t) = e^{\frac{-iE_i t}{\hbar}} \psi_i(\mathbf{r}) \tag{2.24}$$

$e^{\frac{-iE_i t}{\hbar}}$ is the time dependent phase, which is an oscillating complex number with a frequency proportional to the energy, E_i, of the stationary state, $\psi_i(\mathbf{r})$. Each solution, $\Psi_i(\mathbf{r}, t)$, corresponds to a time dependent quantum eigenstate, of which their linear combination describes any possible time dependent quantum state. [132]

$$\Psi(\mathbf{r}, t) = \sum_i c_i e^{\frac{-iE_i t}{\hbar}} \psi_i(\mathbf{r}) \tag{2.25}$$

2.2 Quantum Chemistry

The essence of quantum chemistry is to solve the time independent Schrödinger equation for the electrons and nuclei that compose chemical systems, such as molecules, collections

of molecules or crystals. The general form of the molecular Hamiltonian contains the kinetic energies of the nuclei , $\hat{T}_n$, and electrons , $\hat{T}_e$, and the potential energies from the nuclear-nuclear, $\hat{V}_{nn}$, electron-nuclear, $\hat{V}_{en}$, and electron-electron, $\hat{V}_{ee}$, interactions.

$$\hat{H} = \hat{T}_n + \hat{T}_e + \hat{V}_{nn} + \hat{V}_{en} + \hat{V}_{ee} \tag{2.26}$$

The kinetic energies take the same form as in Equation 2.8 page 51, and the potentials take the form of the Coulomb interaction between two charged particles as in Equation 2.9 page 51. From this point we will use Hartree atomic units, which set $\hbar = m_e = e = 4\pi\epsilon_0 = 1$, a convention that simplifies the form of the equations and will be used throughout this thesis. [134] M_A and Z_A are the mass and charge of nucleus A. $R_{AB} = |R_A - R_B|$, $r_{Ai} = |R_A - r_i|$, and $r_{ij} = |r_i - r_j|$ are the scalar distance between nuclei A and B, nucleus A and electron i, and electrons i and j, where R_A are the coordinates of nucleus A and r_i are the coordinates of electron i. For a system of M positively charged nuclei and N negatively charged electrons and, the Hamiltonian takes the following form

$$\hat{H} = -\sum_{A}^{M} \frac{1}{2M_A}\nabla_A^2 - \sum_{i}^{N} \frac{1}{2}\nabla_i^2 + \sum_{A<B}^{M} \frac{Z_A Z_B}{R_{AB}} - \sum_{A}^{M}\sum_{i}^{N} \frac{Z_A}{r_{Ai}} + \sum_{i<j}^{N} \frac{1}{r_{ij}} \tag{2.27}$$

This is the exact non-relativistic molecular Hamiltonian. It has solutions of the form $\psi(\mathbf{r}, \mathbf{R})$, where $\mathbf{r} = \{\mathbf{r}_1, \mathbf{r}_2, ..., \mathbf{r}_N\}$ is the set of electronic coordinates and $\mathbf{R} = \{\mathbf{R}_1, \mathbf{R}_2, ..., \mathbf{R}_M\}$ is the set of nuclear coordinates. If we were able to solve this exactly then we would know the ground state and all excited state wavefunctions and therefore all the properties of the system, as well as how they evolve in time using Equation 2.25 page 54. [132] We would also be able to solve for interactions with external potentials, for example an electro-magnetic field (radiation). Unfortunately for anything more than two particles the many-body problem takes effect and an exact analytic solution becomes intractable.

As soon as we reach the realm of even small molecules we must use approximations to solve the Hamiltonian.

2.3 The Born-Oppenheimer Approximation

One such approximation is the Born-Oppenheimer (BO) approximation. [135] When an electron and a nucleus interact through the Coulomb potential, they both exert an equal and opposite force on each other. This force causes an acceleration on both particles inversely proportional to their masses. A proton (the lightest possible nucleus) is about 1836 times the mass of an electron, meaning the acceleration of a nucleus is about 1836 times slower than an electron. [136] When we solve the Schrödinger equation the ground state gives the lowest energy arrangement of the electrons and nuclei. As the electrons move so much faster than the nuclei, the electrons would appear to relax to an "instantaneous ground state" for each coordinate of the nuclear motion. By separating the nuclear and electronic motion, the BO approximation allows the solution to be separated into an electronic and a nuclear term

$$\psi\left(\mathbf{r},\mathbf{R}\right)=\psi_e\left(\mathbf{r}\right)\psi_N\left(\mathbf{R}\right) \tag{2.28}$$

Fixing the nuclear coordinates, then $\psi_N\left(\mathbf{R}\right)$ becomes constant. By solving the Hamiltonian for $\psi_e\left(\mathbf{r}\right)$ we also solve for $\psi\left(\mathbf{r};\mathbf{R}\right)$, which depends only parametrically on $\mathbf{R}$. In this way, the molecular Hamiltonian in Equation 2.27 becomes an electronic Hamiltonian, $\hat{H}_e$. The terms involving only nuclear coordinates become an additive constant to the Hamiltonian, and only effect the eigenvalues, not the eigenfunctions. The terms involving derivatives of

the nuclear coordinates are zero.

$$\hat{H} = -\sum_{i}^{N} \frac{1}{2}\nabla_i^2 - \sum_{A}^{M}\sum_{i}^{N} \frac{Z_A}{r_{Ai}} + \sum_{i<j}^{N} \frac{1}{r_{ij}} \tag{2.29}$$

When we solve this at a single nuclear geometry this is called a single point calculation. The eigenvalues, $\epsilon(\mathbf{R})$, give the electronic energy parametrised by the nuclear coordinates. Taking the forces on all the nuclei due to the electrons in their "instantaneous ground state" and the other nuclei we can relax each nuclear coordinate using the Hellmann-Feynman theorem. [137] This forms the basis of a geometry optimisation. Adding the nuclear repulsion energy to the eigenvalues of the electronic Hamiltonion gives the total energy for the nuclear coordinates $\mathbf{R}$:

$$E(\mathbf{R}) = \epsilon(\mathbf{R}) + \sum_{A<B}^{M} \frac{Z_A Z_B}{R_{AB}} \tag{2.30}$$

We can build up a picture of the energy as a function of the nuclear geometry, which is called the potential energy surface (PES). The gradient of the PES is a vector with components corresponding to the partial derivative of the energy with respect to each nuclear coordinate. The components are equivalent to the negative of the force on each coordinate. Stationary points on the PES, where the gradient is zero, correspond to geometries where the net force on each nuclei is zero (or with the convergence criteria) and the geometry is stable. Geometry optimisation algorithms search for stationary points that correspond to minima on the PES. [138–141] The simplest approach is a univariate search, which uses only the energy and searches for a minimum in each coordinate one at a time. Multivariate approaches use the gradient of the PES to search for minima. The gradient vector points in the direction of steepest ascent. The steepest descent method searches for a minimum along the gradient vector, then recalculates the gradient and finds the new minimum in

that direction, repeating until the gradient goes to zero. Each time the gradient is recalculated it necessarily points in the perpendicular direction to the previous gradient, and the path is inefficient and oscillates around the minimum energy path. Conjugate gradient methods improve the efficiency by searching for minima along a vector formed by taking a linear combination of the gradients at the current and previous points.

Newton-Raphson methods further improve efficiency by using the second derivative of the PES to estimate a more accurate step along the PES. Taylor expanding the PES to second order around the starting geometry gives the energy at the geometry after the step. Taking the derivative with respect to the coordinates at the new geometry and setting the derivative of the new energy to zero allows the specific step to be calculated. [138–140] Were the PES quadratic and the second derivative calculated exactly, the calculated step would actually be exact, although this is never the case for even simple molecules. Unlike the steepest descent and conjugate gradient algorithms, Newton-Raphson methods can lead to the location of saddle points and maxima on the PES. This is because they search for points where the gradient is zero, rather than always following a descending path. It is therefore important to identify the nature of the stationary point found. The second partial derivatives of the PES form a matrix called the Hessian. Diagonalising the Hessian gives a matrix whose elements are the eigenvalues of the Hessian. The eigenvectors correspond to the normal vibrational modes, and each associated eigenvalue is proportional to the square of the frequency of the mode. [141] When all the frequencies are positive the stationary point corresponds to a minimum, and when they are all negative the stationary point is a maximum. Saddle points have both positive and negative frequencies. First order saddle points, which have a single negative frequency, correspond to transition states along reaction coordinates. It is important to recognise that these algorithms depend on the starting point of the optimisation, and may sometimes only find a local minimum. To locate the

global minimum a different starting geometry may be needed. The global minimum is the most stable geometry, which we expect to correspond to the structure found in nature, especially for small molecules at low temperatures. In larger molecules there can be many local minima with low energies, and these can all influence the thermodynamic properties of the molecule at at non-zero temperatures. [138]

2.4 The Form of the Wavefunction

Subatomic particles are divided into two subclasses; bosons and fermions. Bosons have integer spin, e.g. photons, and fermions have half integer spin, e.g. electrons. The many-body eigenstates that solve the electronic Schrödinger equation, $\psi(\mathbf{r};\mathbf{R})$, are functions of the spatial coordinates of electrons only. In order to describe an electron fully its spin must be taken into account. Ignoring the parameter R, an eigenstate of an individual electron is described by $\psi(\mathbf{x})$, where $\mathbf{x} = \{\mathbf{x}_1, \mathbf{x}_2, ..., \mathbf{x}_N\}$, $\mathbf{x}_i = \{\mathbf{r}_i, \sigma\}$ and σ is the electron spin; α for a spin up electron or β for a spin down electron. Identical subatomic particles are indistinguishable. So if we take a system of identical particles and the coordinates (position and spin) of two are swapped, it would not be possible to tell they had been swapped. Alternatively, comparing two snapshots of a system, it is not possible to discern which particle has moved where. This means a specific label cannot be assigned to each particle. This has important statistical consequences, described by Bose-Einstein and Fermi-Dirac statistics for bosons and fermions, respectively. The permutation operator, $\hat{P}_{ab}$, swaps the coordinates of two identical particles a and b, such that:

$$\hat{P}_{ab}\psi(\mathbf{x}_1, ..., \mathbf{x}_a, \mathbf{x}_b, ..., \mathbf{x}_N) = \psi(\mathbf{x}_1, ..., \mathbf{x}_b, \mathbf{x}_a, ..., \mathbf{x}_N) \tag{2.31}$$

If the same permutation operator, P_{ab}, operates twice, the second time swaps the particles back yielding the original wavefunction, and P_{ab} is idempotent ($P_{ab}^2 = 1$) and therefore has eigenvalues of ± 1. Bosonic systems are defined by their eigenvalue of $+1$ and have symmetric wavefunctions. Fermionic systems are defined by their eigenvalue of -1 and have antisymmetric wavefunctions. Antisymmetry refers to the change in sign of the wavefunction when two identical particles are swapped. The wavefunction itself is not measurable, only its square, so the negative sign after permutation has no effect on any observable and the permuted wavefunction describes the same state.

$$\psi\left(\mathbf{x}_1, ..., \mathbf{x}_a, \mathbf{x}_b, ..., \mathbf{x}_N\right) = -\psi\left(\mathbf{x}_1, ..., \mathbf{x}_b, \mathbf{x}_a, ..., \mathbf{x}_N\right) \tag{2.32}$$

2.5 The Variational Method

We know the electronic Hamiltonian and understand the antisymmetric nature of the solution, but we still have to solve the complicated many body problem to find the molecular wavefunction. The variational method is a technique used to find the wavefunction of the ground state. It involves taking a trial wavefunction with a set of parameters (can be just one) and minimising the energy of the state described by that wavefunction with respect to the parameter(s). Taking the expression for the expectation value for the energy, E, of any state, $\psi\left(\mathbf{x}\right)$, we can use Equation 2.17 page 53 to expand the state in the eigenstates, $\psi_i\left(\mathbf{x}\right)$, of the Hamiltonian, $\hat{H}$ where $\hat{H}\psi_i\left(\mathbf{x}\right) = E_i\psi_i\left(\mathbf{x}\right)$.

$$\langle E \rangle = \frac{\int \psi^*\left(\mathbf{x}\right) \hat{H} \psi\left(\mathbf{x}\right) d\mathbf{x}}{\int \psi^*\left(\mathbf{x}\right) \psi\left(\mathbf{x}\right) d\mathbf{x}} \tag{2.33}$$

$$\langle E \rangle = \frac{\int \sum_i c_i^* \psi_i^*\left(\mathbf{x}\right) \hat{H} \sum_j c_j \psi_j\left(\mathbf{x}\right) d\mathbf{x}}{\int \sum_i c_i^* \psi_i^*\left(\mathbf{x}\right) \sum_j c_j \psi_j\left(\mathbf{x}\right) d\mathbf{x}} \tag{2.34}$$

$$\langle E\rangle = \frac{\sum_{ij} c_i^* c_j \int \psi_i^* (\mathbf{x})\, \hat{H} \psi_j (\mathbf{x})\, d\mathbf{x}}{\sum_{ij} c_i^* c_j \int \psi_i^* (\mathbf{x})\, \psi_j (\mathbf{x})\, d\mathbf{x}} \tag{2.35}$$

$$\langle E\rangle = \frac{\sum_{ij} c_i^* c_j \int \psi_i^* (\mathbf{x})\, E_j \psi_j (\mathbf{x})\, d\mathbf{x}}{\sum_{ij} c_i^* c_j \int \psi_i^* (\mathbf{x})\, \psi_j (\mathbf{x})\, d\mathbf{x}} \tag{2.36}$$

$$\langle E\rangle = \frac{\sum_{ij} c_i^* c_j E_j \int \psi_i^* (\mathbf{x})\, \psi_j (\mathbf{x})\, d\mathbf{x}}{\sum_{ij} c_i^* c_j \int \psi_i^* (\mathbf{x})\, \psi_j (\mathbf{x})\, d\mathbf{x}} \tag{2.37}$$

The eigenstates ψ_i are orthonormal, so the overlap between any two is given by the Kronecker delta $\int \psi_i^* (\mathbf{x})\, \psi_j (\mathbf{x})\, d\mathbf{x} = \delta_{ij}$.

$$\delta_{ij} = \begin{cases} 1 & \text{if } i = j, \\ 0 & \text{if } i \neq j \end{cases} \tag{2.38}$$

Therefore any contribution to the sum which has $i \neq j$ goes to zero, and in all remaining terms $i = j$

$$\langle E\rangle = \frac{\sum_{ij} c_i^* c_j E_j \delta_{ij}}{\sum_{ij} c_i^* c_j \delta_{ij}} \tag{2.39}$$

$$\langle E\rangle = \frac{\sum_{i} c_i^* c_i E_i}{\sum_{i} c_i^* c_i} \tag{2.40}$$

Subtracting the ground state energy, E_0, from both sides

$$\langle E\rangle - E_0 = \frac{\sum_{i} c_i^* c_i \left(E_i - E_0\right)}{\sum_{i} c_i^* c_i} \tag{2.41}$$

we notice that all the terms on the right ($c_i^* c_i$ and $(E_i - E_0)$) are greater than or equal to zero, means $\langle E\rangle - E_0$ must be greater than or equal to zero, giving the Variational Theorem result.

$$\langle E\rangle \geq E_0 \tag{2.42}$$

Whatever state our trial function describes, the energy of that state provides an upper bound to the energy of the ground state. In the variational method, the energy of the

trial wavefunction is minimised to give the best estimate of the ground state wavefunction. The above derivation used the eigenstates of the Hamiltonian as a basis for our trial wavefunction as a proof of concept. In practice we are actually trying to find these eigenstates, and to do so we instead use the linear variational method. A trial eigenstate is created using the linear combination of the atomic orbitals (LCAO). The atomic orbitals (AO) correspond to the eigenstates of hydrogen like atoms (adjusting the charge for other elements). Centring these orbitals at each atomic coordinate gives the basis functions, ϕ_μ, for our trial eigenstate, $\psi_i = \sum_\mu c_{i\mu}\phi_\mu$. The energy, E_i, of the eigenstate is given by

$$\sum_{\nu\mu} c^*_{i\nu} c_{i\mu} \int \phi^*_\nu \hat{H} \phi_\mu d\mathbf{x} = E_i \sum_{\nu\mu} c^*_{i\nu} c_{i\mu} \int \phi^*_\nu \phi_\mu d\mathbf{x} \tag{2.43}$$

We assume $c_{i\nu}$ is real in the following, but the result holds for complex coefficients. [133] Taking the derivative with respect to $c_{i\nu}$ and using the notation $\int \phi^*_\nu \hat{H} \phi_\mu d\mathbf{x} = H_{\nu\mu}$ and $\int \phi^*_\nu \phi_\mu d\mathbf{x} = S_{\nu\mu}$.

$$\frac{\partial}{\partial c_{i\nu}} \left[\sum_{\nu\mu} c_{i\nu} c_{i\mu} H_{\nu\mu} = E_i \sum_{\nu\mu} c_{i\nu} c_{i\mu} S_{\nu\mu} \right] \tag{2.44}$$

$$\sum_{\mu} H_{\nu\mu} c_{i\mu} = E_i \sum_{\mu} S_{\nu\mu} c_{i\mu} \tag{2.45}$$

When we do this for each $c_{i\nu}$ then the set of equations, known as the secular equations, can be summarised by the following matrix equation.

$$\mathbf{H}\mathbf{c}_i = E_i \mathbf{S}\mathbf{c}_i \tag{2.46}$$

Where $\mathbf{H}$ and $\mathbf{S}$ are matrices with elements $H_{\nu\mu}$ and $S_{\nu\mu}$ and $\mathbf{c}_i$ is a vector with elements $c_{i\mu}$, the coefficients that define the ground state according to the trial wavefunction $\psi_i = \sum_\mu c_{i\mu}\phi_\mu$. When we choose a basis of orthonormal functions, $S_{\nu\mu} = \delta_{\nu\mu}$ and $\mathbf{S} = \mathbf{I}$, this is a standard eigenvalue problem $\mathbf{H}\mathbf{c} = E\mathbf{c}$. The AOs are not an orthonormal basis, and

Equation 2.46 is a generalised eigenvalue problem. If $\mathbf{S}$ is invertible then we can pre-multiply both sides by $\mathbf{S}^{-1}$, the inverse of $\mathbf{S}$, to transform the general eigenvalue problem to a standard eigenvalue problem of the matrix $\mathbf{H}' = \mathbf{S}^{-1}\mathbf{H}$, with the same eigenvectors and eigenvalues as the general problem.

$$\mathbf{H}\mathbf{c}_i = E_i\mathbf{S}\mathbf{c}_i \tag{2.47}$$

$$\mathbf{S}^{-1}\mathbf{H}\mathbf{c}_i = E_i\mathbf{S}^{-1}\mathbf{S}\mathbf{c}_i \tag{2.48}$$

$$\mathbf{H}'\mathbf{c}_i = E_i\mathbf{c}_i \tag{2.49}$$

More generally $\mathbf{S}$ is not invertible, in which case we can use Cholesky decomposition to factorise $\mathbf{S}$ such that $\mathbf{S} = \mathbf{L}\mathbf{L}^T$, where $\mathbf{L}^T$ is the transpose of $\mathbf{L}$. [142] This is similar to finding the square root of the matrix $\mathbf{S}$, and again transforms the general eigenvalue problem to a standard one, now of the matrix $\tilde{\mathbf{H}} = \mathbf{L}^{-1}\mathbf{H}\left(\mathbf{L}^T\right)^{-1}$ with eigenvectors $\tilde{\mathbf{c}}_i = \mathbf{L}^T\mathbf{c}_i$ and the same eigenvalues as the general problem.

$$\mathbf{H}\mathbf{c}_i = E_i\mathbf{S}\mathbf{c}_i \tag{2.50}$$

$$\mathbf{H}\mathbf{c}_i = E_i\mathbf{L}\mathbf{L}^T\mathbf{c}_i \tag{2.51}$$

$$\mathbf{L}^{-1}\mathbf{H}\mathbf{c}_i = E_i\mathbf{L}^{-1}\mathbf{L}\mathbf{L}^T\mathbf{c}_i \tag{2.52}$$

$$\mathbf{L}^{-1}\mathbf{H}\mathbf{I}\mathbf{c}_i = E_i\mathbf{L}^{-1}\mathbf{L}\mathbf{L}^T\mathbf{c}_i \tag{2.53}$$

$$\mathbf{L}^{-1}\mathbf{H}\left(\mathbf{L}^T\right)^{-1}\mathbf{L}^T\mathbf{c}_i = E_i\mathbf{L}^T\mathbf{c}_i \tag{2.54}$$

$$\tilde{\mathbf{H}}\tilde{\mathbf{c}}_i = E_i\tilde{\mathbf{c}}_i \tag{2.55}$$

The eigenvector with the lowest eigenvalue represents the variational ground state. The eigenvalue corresponds to the energy of the ground state of the general eigenvalue problem. The eigenvector can be transformed back to a solution to the general problem, such that the components of $\mathbf{c}_i = \mathbf{L}\tilde{\mathbf{c}}_i$. Excited states are represented by the remaining eigenvectors and eigenvalues of $\tilde{\mathbf{H}}$.

2.6 Matrix Mechanics and Dirac Notation

The linear variational result is essentially the same as Heisenberg's formulation of quantum mechanics; matrix mechanics. Schrödinger's wave mechanics uses differential calculus, where linear operators represent observables and functions, called wavefunctions, represent quantum states. Matrix mechanics uses linear algebra, where matrices represent observables and vectors represent quantum states. The space that the vectors live in is called a Hilbert space, which is a complex vector space on which an inner product is defined and is differentiable. The basis vectors of the Hilbert space correspond to the basis functions used to expand the wavefunction. A vector within the space is composed of a set of complex numbers that correspond to the coefficients in the wavefunction. Changing the basis set corresponds to rotating the basis vectors around the origin, preserving all of the inner products between them. The elements of the vectors and matrices depend on the basis, $H_{ij} = \int \phi_i^* \hat{H} \phi_j d\mathbf{x}$. Different basis sets yield different vectors and matrices, known as representations, of the same states and observables. The eigenvectors of any observable form a complete orthonormal set of basis vectors with real eigenvalues, just as the eigenstates do in wave mechanics. [132, 133] An observable in the representation of its own eigenvectors is then just a diagonal matrix with the eigenvalue corresponding to each eigenvector down the diagonal. Using matrices lends the powerful tools of linear algebra to the study of quantum systems, and is an extremely useful formulation for computational chemistry.

Writing computer software relies heavily on the use of linear algebra, so writing software to solve quantum chemistry problems becomes intuitive.

Dirac invented a convenient notation known as bra-ket notation. [143] In this quantum states are represented by kets, $|\psi\rangle$, and the corresponding complex conjugates are represented by bras, $\langle\psi|$. Operators can be represented by outer products, $|i\rangle\langle j|$, and more generally sums of outer products, within a basis set $\{|i\rangle\}$. Operators can be thought of as transformations from one state to another, e.g. $|i\rangle\langle j|$ acting on the state $|j\rangle$ would give the state $|i\rangle$ such that $|i\rangle \langle j|j\rangle = |i\rangle \mathbf{1} = |i\rangle$, where we assume an orthonormal basis ($\langle i|j\rangle = \delta_{ij}$). The projection operator is central in linear algebra and takes the form $\sum_i |i\rangle\langle i|$. This projects a quantum state onto the subspace spanned by the set of states $\{|i\rangle\}$. If $\{i\}$ is complete then it spans the whole space and it can be used to describe any quantum state. We can also project onto a continuous basis, for example in the position ($\mathbf{x}$) or momentum ($\mathbf{p}$) representations, where instead of the sum we use an integral such that in the position basis the projection operator takes the form $\int |\mathbf{x}\rangle \langle\mathbf{x}| \, d\mathbf{x}$. Dirac notation is useful for switching between Schrödinger's wave mechanics and Heisenberg's matrix mechanics depending on the choice of basis. Using a discrete basis, i, corresponds to matrix mechanics.

$$|\psi\rangle = \sum_i |i\rangle \langle i|\psi\rangle = \sum_i c_i |i\rangle \tag{2.56}$$

$c_i = \langle i|\psi\rangle$ are the elements of the vector representing $|\psi\rangle$ in the basis i. Here we notice $\sum_i |i\rangle \langle i| = 1$, which is known as the closure relation, and is true for any complete set of states i. Using a continuous basis, $\mathbf{x}$, corresponds to wave mechanics.

$$|\psi\rangle = \int |\mathbf{x}\rangle \langle\mathbf{x}|\psi\rangle \, d\mathbf{x} = \int \psi(\mathbf{x}) |\mathbf{x}\rangle \, d\mathbf{x} \tag{2.57}$$

$\psi(\mathbf{x}) = \langle\mathbf{x}|\psi\rangle$ is the wavefunction representing $|\psi\rangle$ in the position basis. The wavefunc-

tion can thus be thought of as a kind of vector with a continuous set of elements. Here $\int |\mathbf{x}\rangle \langle \mathbf{x}| \, d\mathbf{x} = 1$, which is the closure relation for a complete continuous basis.

2.7 Hartree-Fock Theory

After the BO approximation, solving the electronic Hamiltonian (Equation 2.29 page 57) is still a challenging many-body problem. For most molecules this will be impossible to do analytically as there are still a large number of electrons. We can instead imagine a single electron Hamiltonian.

$$\hat{h}_i \psi_a (\mathbf{x}_i) = \epsilon_a \psi_a (\mathbf{x}_i) \tag{2.58}$$

The eigenstates of the single electron Hamiltonian are single electron wavefunctions, known as molecular orbitals (MOs), $\psi_i (\mathbf{x})$, with eigenvalues ϵ_i. Each of the single electron wavefunctions can further be separated into a spatial and spin term, known as spin orbitals, $\chi_i (\mathbf{x})$. They are the product of a single electron spatial orbital, $\psi_i (\mathbf{r})$, and a spin function; α for spin up or β for spin down.

$$\chi_i (\mathbf{x}) = \begin{cases} \psi_i (\mathbf{r}) \, \alpha \\ \quad \text{or} \\ \psi_i (\mathbf{r}) \, \beta \end{cases} \tag{2.59}$$

Taking the sum $\hat{h}_i$ over all the electrons we can estimate the total electronic energy.

$$\hat{H} = \sum_i^N \hat{h}_i \tag{2.60}$$

The eigenstates of this Hamiltonian are products of the single electron wavefunctions. Many-body wavefunctions of this form are called Hartree products.

$$\psi\left(\mathbf{x}_1, \mathbf{x}_2, ..., \mathbf{x}_N\right) = \chi_1\left(\mathbf{x}_1\right)\chi_2\left(\mathbf{x}_2\right), ..., \chi_N\left(\mathbf{x}_N\right) \tag{2.61}$$

Assuming the solution is of this form is known as the Hartree approximation. The eigenvalues, E, are the sum of the single electron energies that form the Hartree product wavefunction.

$$\hat{H}\psi\left(\mathbf{x}_1, \mathbf{x}_2, ..., \mathbf{x}_N\right) = E\psi\left(\mathbf{x}_1, \mathbf{x}_2, ..., \mathbf{x}_N\right) \tag{2.62}$$

$$\sum_i^N \hat{h}_i \chi_1\left(\mathbf{x}_1\right)\chi_2\left(\mathbf{x}_2\right), ..., \chi_N\left(\mathbf{x}_N\right) = \left[\epsilon_1 + \epsilon_2, ..., \epsilon_N\right]\chi_1\left(\mathbf{x}_1\right)\chi_2\left(\mathbf{x}_2\right), ..., \chi_N\left(\mathbf{x}_N\right) \tag{2.63}$$

Much like the BO approximation separates the nuclear and electronic motion, the Hartree approximation separates the motion of each electron. Wavefunctions of this type are said to be uncorrelated as the single electron wavefunctions do not influence one another. Considering the probability density of a two particle Hartree product

$$P\left(\mathbf{x}_1, \mathbf{x}_2\right) = \left|\psi\left(\mathbf{x}_1, \mathbf{x}_2\right)\right|^2 \tag{2.64}$$

$$P\left(\mathbf{x}_1, \mathbf{x}_2\right) = \left|\chi_1\left(\mathbf{x}_1\right)\chi_2\left(\mathbf{x}_2\right)\right|^2 \tag{2.65}$$

The probability of finding electron 1 in $d\mathbf{x}_1$ and electron 2 in $d\mathbf{x}_2$ is separable into the product of finding them there when the system does not contain the other electron.

$$\iint \left|\psi\left(\mathbf{x}_1, \mathbf{x}_2\right)\right|^2 d\mathbf{x}_1 d\mathbf{x}_2 = \int \left|\chi_1\left(\mathbf{x}_1\right)\right|^2 d\mathbf{x}_1 \int \left|\chi_2\left(\mathbf{x}_2\right)\right|^2 d\mathbf{x}_2 \tag{2.66}$$

In reality each electron is constantly interacting with all the other electrons, and the Hartree approximation leads to a poor description of the molecular system. To improve on the

approximation we can consider the fermionic nature of electrons. Fermionic wavefunctions must be antisymmetric under the permutation of two particles. For a two electron system the Hartree product is

$$\psi\left(\mathbf{x}_1, \mathbf{x}_2\right) = \chi_1\left(\mathbf{x}_1\right)\chi_2\left(\mathbf{x}_2\right) \tag{2.67}$$

The action of the permutation operator swaps electrons one and two

$$\hat{P}_{12}\psi\left(\mathbf{x}_1, \mathbf{x}_2\right) = \psi\left(\mathbf{x}_2, \mathbf{x}_1\right) = \chi_1\left(\mathbf{x}_2\right)\chi_2\left(\mathbf{x}_1\right) \tag{2.68}$$

$\chi_1\left(\mathbf{x}_1\right)\chi_2\left(\mathbf{x}_2\right)$ is not antisymmetric and therefore cannot be a true fermionic wavefunction.

$$\chi_1\left(\mathbf{x}_1\right)\chi_2\left(\mathbf{x}_2\right) \neq -\chi_1\left(\mathbf{x}_2\right)\chi_2\left(\mathbf{x}_1\right) \tag{2.69}$$

If instead we take the following linear combination and apply the permutation operator we see it is antisymmetric and $\psi\left(\mathbf{x}_1, \mathbf{x}_2\right) = -\psi\left(\mathbf{x}_2, \mathbf{x}_1\right)$

$$\psi\left(\mathbf{x}_1, \mathbf{x}_2\right) = \frac{1}{\sqrt{2}}\left[\chi_1\left(\mathbf{x}_1\right)\chi_2\left(\mathbf{x}_2\right) - \chi_1\left(\mathbf{x}_2\right)\chi_2\left(\mathbf{x}_1\right)\right] \tag{2.70}$$

$$\hat{P}_{12}\psi\left(\mathbf{x}_1, \mathbf{x}_2\right) = \psi\left(\mathbf{x}_2, \mathbf{x}_1\right) = \frac{1}{\sqrt{2}}\left[\chi_1\left(\mathbf{x}_2\right)\chi_2\left(\mathbf{x}_1\right) - \chi_1\left(\mathbf{x}_1\right)\chi_2\left(\mathbf{x}_2\right)\right] \tag{2.71}$$

$$\psi\left(\mathbf{x}_2, \mathbf{x}_1\right) = -\frac{1}{\sqrt{2}}\left[\chi_1\left(\mathbf{x}_1\right)\chi_2\left(\mathbf{x}_2\right) - \chi_1\left(\mathbf{x}_2\right)\chi_2\left(\mathbf{x}_1\right)\right] = -\psi\left(\mathbf{x}_1, \mathbf{x}_2\right) \tag{2.72}$$

Wavefunctions of this form are known as Slater determinants, as $\psi\left(\mathbf{x}_1, \mathbf{x}_2\right)$ can be written in the form of a determinant. [144]

$$\frac{1}{\sqrt{2}}\begin{vmatrix} \chi_1\left(\mathbf{x}_1\right) & \chi_2\left(\mathbf{x}_1\right) \\ \chi_1\left(\mathbf{x}_2\right) & \chi_2\left(\mathbf{x}_2\right) \end{vmatrix} = \frac{1}{\sqrt{2}}\left[\chi_1\left(\mathbf{x}_1\right)\chi_2\left(\mathbf{x}_2\right) - \chi_1\left(\mathbf{x}_2\right)\chi_2\left(\mathbf{x}_1\right)\right] \tag{2.73}$$

A general Slater determinant takes the form shown below. The determinant gives $N!$ Hartree products which cover every possible distribution of N electrons within the set of spin orbitals $\chi_i(\mathbf{x})$ in an antisymmetrised combination. The indistinguishability of the electrons is also described as there is an equal probability of each spin orbital containing any of our labelled electrons.

$$\psi(\mathbf{x}_1, \mathbf{x}_2, ..., \mathbf{x}_N) = \frac{1}{\sqrt{N!}} \begin{vmatrix} \chi_1(\mathbf{x}_1) & \chi_2(\mathbf{x}_1) & \cdots & \chi_N(\mathbf{x}_1) \\ \chi_1(\mathbf{x}_2) & \chi_2(\mathbf{x}_2) & \cdots & \chi_N(\mathbf{x}_2) \\ \vdots & \vdots & \ddots & \vdots \\ \chi_1(\mathbf{x}_N) & \chi_2(\mathbf{x}_N) & \cdots & \chi_N(\mathbf{x}_N) \end{vmatrix} \tag{2.74}$$

One property of determinants is that swapping any of two rows or columns gives the negative of the same determinant. Swapping two rows is equivalent to swapping the coordinates of two electrons, thus Slater determinants preserve antisymmetry. A further property of determinants is that if any two rows or columns in a determinant are the same then the determinant equals zero. This is equivalent to the Pauli exclusion principle, and any wavefunction has a probability of zero for two electrons to occupy the same spin orbital. We can see this directly if we consider the two electron wavefunction from Equation 2.70 with $\chi_1(\mathbf{x}) = \chi_2(\mathbf{x})$:

$$\psi(\mathbf{x}_1, \mathbf{x}_2) = \frac{1}{\sqrt{2}} \left[\chi_1(\mathbf{x}_1)\chi_1(\mathbf{x}_2) - \chi_1(\mathbf{x}_2)\chi_1(\mathbf{x}_1)\right] = 0 \tag{2.75}$$

As previously discussed, the probability density of a Hartree product showed that the wavefunction has completely uncorrelated electrons. Considering the probability density

of a two particle Slater determinant we see this is no longer the case.

$$P\left(\mathbf{x}_1, \mathbf{x}_2\right) = \frac{1}{2}\left|\chi_1\left(\mathbf{x}_1\right)\chi_2\left(\mathbf{x}_2\right) - \chi_1\left(\mathbf{x}_2\right)\chi_2\left(\mathbf{x}_1\right)\right|^2 \tag{2.76}$$

$$\begin{aligned} P\left(\mathbf{x}_1, \mathbf{x}_2\right) = \frac{1}{2}\Big[&\left|\chi_1\left(\mathbf{x}_1\right)\right|^2\left|\chi_2\left(\mathbf{x}_2\right)\right|^2 + \left|\chi_1\left(\mathbf{x}_2\right)\right|^2\left|\chi_2\left(\mathbf{x}_1\right)\right|^2 \\ &- \chi_1^*\left(\mathbf{x}_1\right)\chi_2^*\left(\mathbf{x}_2\right)\chi_1\left(\mathbf{x}_2\right)\chi_2\left(\mathbf{x}_1\right) - \chi_1^*\left(\mathbf{x}_2\right)\chi_2^*\left(\mathbf{x}_1\right)\chi_1\left(\mathbf{x}_1\right)\chi_2\left(\mathbf{x}_2\right)\Big] \end{aligned} \tag{2.77}$$

The probability of finding electron 1 in $d\mathbf{x}_1$ and electron 2 in $d\mathbf{x}_2$ is no longer separable due to the cross terms containing the positions of both electrons. Examining the cross terms, if electron one and two have opposite spins, then due to spin orthogonality both cross terms equal zero, and the electron motion is uncorrelated.

$$\chi_1^*\left(\mathbf{x}_1\right)\chi_2^*\left(\mathbf{x}_2\right)\chi_1\left(\mathbf{x}_2\right)\chi_2\left(\mathbf{x}_1\right) = \chi_1^*\left(\mathbf{x}_2\right)\chi_2^*\left(\mathbf{x}_1\right)\chi_1\left(\mathbf{x}_1\right)\chi_2\left(\mathbf{x}_2\right) = 0 \tag{2.78}$$

Setting $\mathbf{r}_1 = \mathbf{r}_2$, there is a finite probability of finding electron one and two in the same position. After integrating out the spin coordinates to remove the cross terms and using the definition of a spin orbital in Equation 2.59 page 66

$$P\left(\mathbf{r}_1, \mathbf{r}_1\right) = \left|\psi_1\left(\mathbf{r}_1\right)\right|^2\left|\psi_2\left(\mathbf{r}_1\right)\right|^2 \tag{2.79}$$

If electron one and electron two have the same spin, then the two cross terms remain in the integral and the positions of the electrons are now correlated. This is called exchange correlation, as it derives from the antisymmetry of the wavefunction under the permutation, or exchange, of two electrons. Setting $\mathbf{r}_1 = \mathbf{r}_2$ for two same spin electrons, the probability

of finding both electrons in the same position actually goes to zero.

$$P(\mathbf{r}_1, \mathbf{r}_1) = \frac{1}{2}\Big[|\psi_1(\mathbf{r}_1)|^2 |\psi_2(\mathbf{r}_1)|^2 + |\psi_1(\mathbf{r}_1)|^2 |\psi_2(\mathbf{r}_1)|^2 - \psi_1^*(\mathbf{r}_1)\psi_2^*(\mathbf{r}_1)\psi_1(\mathbf{r}_1)\psi_2(\mathbf{r}_1) - \psi_1^*(\mathbf{r}_1)\psi_2^*(\mathbf{r}_1)\psi_1(\mathbf{r}_1)\psi_2(\mathbf{r}_1)\Big] = 0 \tag{2.80}$$

as

$$\psi_1^*(\mathbf{r}_1)\psi_2^*(\mathbf{r}_1)\psi_1(\mathbf{r}_1)\psi_2(\mathbf{r}_1) = |\psi_1(\mathbf{r}_1)|^2 |\psi_2(\mathbf{r}_1)|^2 \tag{2.81}$$

This zero probability is called the Fermi hole and highlights the correlated motion of same spin electrons in Slater determinants. The Hartree-Fock (HF) approximation builds on the Hartree approximation by assuming the solution to the electronic Hamiltonian in the form of a Slater determinant. This correctly describes the antisymmetric nature of the wavefunction of a collection of fermions. Using a Slater determinant as a trial wavefunction in the variational method, where the energy is a functional of that wavefunction, the Slater determinant that minimises the energy is the HF ground state, $|\psi_0\rangle$.

$$\langle\psi_0|\hat{H}|\psi_0\rangle = E_0[\psi_0] \tag{2.82}$$

E_0 is the ground state energy and $|\psi_0\rangle$ is the Slater determinant formed by the N lowest energy spin orbitals. A Slater determinant can also be described by the action of the antisymmetrizer operator, $\hat{A}$, which gives a normalised antisymmetric combination of the spin orbitals on which it acts. [145]

$$\hat{A} = \frac{1}{N!}\sum_{\hat{P}} \chi(\hat{P})\hat{P} \tag{2.83}$$

$$|\psi_0\rangle = \sqrt{N!}\hat{A}\,|\chi_1\chi_2, ..., \chi_N\rangle \tag{2.84}$$

The $\hat{P}$ operators form a group that describes all possible permutations of the N electrons in the spin orbitals and $\chi(\hat{P}) = (-1)^p$ depending on the number of permutations, p, needed for each $\hat{P}$ such that $|\psi_0\rangle$ is antisymmetric. Using $\hat{A}$ allows us to show how the energy of a Slater determinant is calculated. The electronic Hamiltonian can be split into one-electron and two-electron operators.

$$\hat{H} = -\sum_{i}^{N} \frac{1}{2}\nabla_i^2 - \sum_{A}^{M}\sum_{i}^{N} \frac{Z_A}{r_{Ai}} + \sum_{i<j}^{N} \frac{1}{r_{ij}} \tag{2.85}$$

The first two terms depend on only a single electron, i, and can be rewritten as the sum of the one-electron operators, $\hat{h}_i$.

$$\hat{h}_i = -\frac{1}{2}\nabla_i^2 - \sum_{A}^{M} \frac{Z_A}{r_{Ai}} \tag{2.86}$$

$$\sum_{i}^{N} \hat{h}_i = -\sum_{i}^{N} \frac{1}{2}\nabla_i^2 - \sum_{A}^{M}\sum_{i}^{N} \frac{Z_A}{r_{Ai}} \tag{2.87}$$

$\hat{h}_i$ only acts on electron i and will commute with anything that does not depend on electron i. The remaining term in the electronic Hamiltonian

$$\sum_{i<j}^{N} \frac{1}{r_{ij}} \tag{2.88}$$

is a two-electron operator. It acts on both electrons i and j and will commute with anything that does not depend on either electron i or j. The expression for the total energy is given by

$$E\left[\psi_0\right] = \langle\psi_0|\hat{H}|\psi_0\rangle = \sum_{i}^{N} \langle\psi_0|\hat{h}_i|\psi_0\rangle + \sum_{i<j}^{N} \langle\psi_0|\frac{1}{r_{ij}}|\psi_0\rangle \tag{2.89}$$

Considering the one-electron terms first, expanding the Slater determinant using the anti-symmetrizer operator $\hat{A}$ gives

$$\langle\psi_0|\sum_i^N \hat{h}_i|\psi_0\rangle = N!\,\langle\chi_1\chi_2,...,\chi_N|\hat{A}^\dagger\sum_i^N \hat{h}_i\hat{A}|\chi_1\chi_2,...,\chi_N\rangle \tag{2.90}$$

$\sum_i^N \hat{h}_i$ contains all N electrons so it commutes with $\hat{A}$, such that $\hat{A}^\dagger\sum_i^N \hat{h}_i\hat{A} = \sum_i^N \hat{h}_i\hat{A}^\dagger\hat{A}$. $\hat{A}$ is also Hermitian $\left(\hat{A} = \hat{A}^\dagger\right)$ and idempotent $\left(\hat{A} = \hat{A}^2\right)$, such that $\hat{A}^\dagger\hat{A} = \hat{A}^2 = \hat{A}$, and

$$\langle\psi_0|\sum_i^N \hat{h}_i|\psi_0\rangle = N!\,\langle\chi_1\chi_2,...,\chi_N|\sum_i^N \hat{h}_i\hat{A}|\chi_1\chi_2,...,\chi_N\rangle \tag{2.91}$$

Considering just a single term in the sum ($\hat{h}_1$) and partially expanding $\hat{A}$

$$\langle\psi_0|\hat{h}_1|\psi_0\rangle = N!\,\langle\chi_1\chi_2,...,\chi_N|\hat{h}_1\frac{1}{N!}\left[\hat{P}_0 + \sum_{\hat{P}\neq P_0}\chi(\hat{P})\hat{P}\right]|\chi_1\chi_2,...,\chi_N\rangle \tag{2.92}$$

Where $\hat{P}_0 = 1$ gives the contribution from the unpermuted set of spin orbitals and the energy of the first term is given by

$$\langle\chi_1\chi_2,...,\chi_N|\hat{h}_1|\chi_1\chi_2,...,\chi_N\rangle = \langle\chi_1|\hat{h}_1|\chi_1\rangle\langle\chi_2|\chi_2\rangle,...,\langle\chi_N|\chi_N\rangle = \langle\chi_1|\hat{h}_1|\chi_1\rangle \tag{2.93}$$

For the remaining permuted terms, there will always be a contribution from some $\langle\chi_i|\chi_j\rangle = 0$ taking the whole term to 0, leading to

$$\langle\psi_0|\hat{h}_1|\psi_0\rangle = \langle\chi_1|\hat{h}_1|\chi_1\rangle \tag{2.94}$$

We then extend the same treatment to all the other electrons and reintroduce all the terms in the sum of one-electron operators.

$$\langle\psi_0|\sum_i^N \hat{h}_i|\psi_0\rangle = \sum_i^N \langle\chi_i|\hat{h}_i|\chi_i\rangle \tag{2.95}$$

Now we consider the two-electron operator, which also commutes with $\hat{A}$ as we take the sum over all pairs i and j, by again taking a single term in the sum ($\frac{1}{r_{12}}$) and partially expanding $\hat{A}$

$$\langle\psi_0|\frac{1}{r_{12}}|\psi_0\rangle = N!\,\langle\chi_1\chi_2,...,\chi_N|\frac{1}{r_{12}}\frac{1}{N!}\left[\hat{P}_0 - \hat{P}_{12} + \sum_{\hat{P}\neq\hat{P}_0,P_{12}} \chi(\hat{P})\hat{P}\right]|\chi_1\chi_2,...,\chi_N\rangle \tag{2.96}$$

Where $\hat{P}_0 = 1$ gives the contribution from the unpermuted $|\chi_1\chi_2,...,\chi_N\rangle$ and $\hat{P}_{12}$ gives the contribution from the permuted $|\chi_2\chi_1,...,\chi_N\rangle$ with $\chi(\hat{P}_{12}) = -1$

$$\langle\psi_0|\frac{1}{r_{12}}|\psi_0\rangle = \langle\chi_1\chi_2,...,\chi_N|\frac{1}{r_{12}}\left[\hat{P}_0 - \hat{P}_{12}\right]|\chi_1\chi_2,...,\chi_N\rangle \tag{2.97}$$

$$\langle\psi_0|\frac{1}{r_{12}}|\psi_0\rangle = \langle\chi_1\chi_2,...,\chi_N|\frac{1}{r_{12}}|\chi_1\chi_2,...,\chi_N\rangle - \langle\chi_1\chi_2,...,\chi_N|\frac{1}{r_{12}}|\chi_2\chi_1,...,\chi_N\rangle \tag{2.98}$$

$$\langle\psi_0|\frac{1}{r_{12}}|\psi_0\rangle = \left[\langle\chi_1\chi_2|\frac{1}{r_{12}}|\chi_1\chi_2\rangle - \langle\chi_1\chi_2|\frac{1}{r_{12}}|\chi_2\chi_1\rangle\right]\langle\chi_3|\chi_3\rangle,...,\langle\chi_N|\chi_N\rangle \tag{2.99}$$

Again, for the remaining permuted terms, there will always be a contribution from some $\langle\chi_i|\chi_j\rangle = 0$ taking the whole term to 0, leading to

$$\langle\psi_0|\frac{1}{r_{12}}|\psi_0\rangle = \langle\chi_1\chi_2|\frac{1}{r_{12}}|\chi_1\chi_2\rangle - \langle\chi_1\chi_2|\frac{1}{r_{12}}|\chi_2\chi_1\rangle \tag{2.100}$$

Extending the same treatment to all the other electron pairs and combining with the result for the one-electron operator gives the total HF energy.

$$\langle\psi_0|\hat{H}|\psi_0\rangle = \sum_{i}^{N} \langle\chi_i|\hat{h}_i|\chi_i\rangle + \sum_{i<j}^{N} \langle\chi_i\chi_j|\frac{1}{r_{ij}}|\chi_i\chi_j\rangle - \langle\chi_i\chi_j|\frac{1}{r_{ij}}|\chi_j\chi_i\rangle \tag{2.101}$$

The first one-electron term gives the kinetic energy of the electrons and the attraction to the nuclei.

$$h_i = \langle\chi_i|\hat{h}_i|\chi_i\rangle \tag{2.102}$$

The final two two-electron terms are known as the Coulomb and exchange terms. The Coulomb term, $\mathcal{J}_{ij}$, describes the electrostatic repulsion between two electrons in orbitals χ_i and χ_j.

$$\mathcal{J}_{ij} = \langle\chi_i\chi_j|\frac{1}{r_{ij}}|\chi_i\chi_j\rangle \tag{2.103}$$

The exchange term, $\mathcal{K}_{ij}$, does not have a classical analogue and arises from the antisymmetric nature of the wavefunction under particle exchange.

$$\mathcal{K}_{ij} = \langle\chi_i\chi_j|\frac{1}{r_{ij}}|\chi_j\chi_i\rangle \tag{2.104}$$

The total energy is then a functional of the set of occupied spin orbitals.

$$E\left[\{\chi_i\}\right] = \sum_{i}^{N} h_i + \sum_{i<j}^{N} \left(\mathcal{J}_{ij} - \mathcal{K}_{ij}\right) \tag{2.105}$$

This energy can be minimised using the Lagrange's method of undetermined multipliers, which ensures the orbitals, χ_i, remain orthogonal. [133]

$$\mathcal{L}\left[\{\chi_i\}\right] = \sum_{i}^{N} h_i + \sum_{i<j}^{N} \left(\mathcal{J}_{ij} - \mathcal{K}_{ij}\right) - \sum_{i,j}^{N} \epsilon_{ij} \left(\langle\chi_i|\chi_j\rangle - \delta_{ij}\right) \tag{2.106}$$

Finding the set of orbitals that makes the functional derivative zero with respect to every orbital

$$\frac{\partial \mathcal{L}}{\partial \chi_i} = 0, \qquad \forall \chi_i \tag{2.107}$$

leads to a one-electron equation, and a one-electron operator, $\hat{f}_i$, which acts on a single electron, $\mathbf{x}_i$, in orbital χ_i.

$$\hat{f}_i \chi_i (\mathbf{x}_i) = \hat{h}_i \chi_i (\mathbf{x}_i) + \sum_{j \neq i}^{N} \hat{\mathcal{J}}_{ij} \chi_i (\mathbf{x}_i) - \sum_{j \neq i}^{N} \hat{\mathcal{K}}_{ij} \chi_i (\mathbf{x}_i) = \epsilon_i \chi_i (\mathbf{x}_i) \tag{2.108}$$

The total energy of the orbital χ_i is given by ϵ_i, where

$$\hat{\mathcal{J}}_{ij} \chi_i (\mathbf{x}_i) = \int \frac{\chi_j^* (\mathbf{x}_j) \chi_j (\mathbf{x}_j)}{r_{ij}} d\mathbf{x}_j \chi_i (\mathbf{x}_i) \tag{2.109}$$

and

$$\hat{\mathcal{K}}_{ij} \chi_i (\mathbf{x}_i) = \int \frac{\chi_j^* (\mathbf{x}_j) \chi_i (\mathbf{x}_j)}{r_{ij}} d\mathbf{x}_j \chi_j (\mathbf{x}_i) \tag{2.110}$$

are the one-electron Coulomb and exchange operators, which act on a single electron, i, but whose form depends on all the remaining orbitals j. The latter is only defined upon its action on an orbital $\chi_i (\mathbf{x}_1)$. If orbital i and j have different spins then $\hat{\mathcal{K}}_{ij} \chi_i (\mathbf{x}_i) = 0$ due to spin orthogonality. We notice that $\hat{\mathcal{J}}_{ii} \chi_i (\mathbf{x}_i) = \hat{\mathcal{K}}_{ii} \chi_i (\mathbf{x}_i)$ and the exchange term exactly cancels the Coulomb term when $i = j$. Therefore we can take the sum over all j in Equation 2.108, such that $\hat{f}_i$ is the same now for every electron.

$$\hat{f}_i = \hat{h}_i + \sum_{j}^{N} \left(\hat{\mathcal{J}}_{ij} - \hat{\mathcal{K}}_{ij} \right) \tag{2.111}$$

This form of $\hat{f}_i$ is known as the Fock operator, and we have derived the HF equation.

$$\hat{f}_i \chi_i (\mathbf{x}_1) = \epsilon_i \chi_i (\mathbf{x}_1) \tag{2.112}$$

When this is solved for every electron the variational energy is minimised. Each single electron Hamiltonian, $\hat{f}_i$, depends on the orbitals of each of the other electrons, j. The HF equations must therefore be solved iteratively. An initial guess of each orbital is made, which creates the repulsive potential. The equations are then solved for each electron to find a new set of orbitals, which creates a new repulsive potential etc. This procedure is repeated until there is no difference between the input and the output orbitals. This is known as the self-consistent field (SCF) method. When the difference between the input and the output falls below a certain threshold, the solution is said to have converged. The N electrons fill the spin orbitals with the lowest energies, and the Slater determinant they create is the HF ground state, ψ_0. These equations must be minimised with respect to the spin orbital functions, which is very difficult to solve simultaneously and self-consistently, even numerically, and for larger molecules was not possible. In 1951 Roothan and Hall incorporated the LCAO method, which redefines the problem in terms of matrices and is more suitable to solving with computer software. The spatial part of the spin orbital is formed using the LCAO method. [146, 147]

$$|\psi_i\rangle = \sum_{\mu} c_{i\mu} |\phi_\mu\rangle \tag{2.113}$$

These orbitals can be extended to spin orbitals with the appropriate spin function using Equation 2.59 page 66. The alpha and beta electrons therefore have the same spatial orbital, known as a restricted HF (RHF) calculation. This can be relaxed such that the alpha and beta orbitals are allowed unique orbitals, known as an unrestricted HF (UHF) calcu-

lation. Substituting the LCAO trial wavefunction into Equation 2.112 page 77 and using the linear varitaional method to minimise the energy gives a system of linear equations summarised by the matrix equation

$$\mathbf{F}\mathbf{C}_i = \epsilon\mathbf{S}\mathbf{C}_i \tag{2.114}$$

$\mathbf{F}$, the Fock matrix, has elements

$$\mathbf{F}_{\nu\mu} = \langle\phi_\nu|\hat{f}_i|\phi_\mu\rangle \tag{2.115}$$

$\mathbf{S}$ is the overlap matrix of the atomic orbital basis states, which needs to be Choleskey decomposed to find solutions of the generalised eigenvalue problem, with elements

$$\mathbf{S}_{\nu\mu} = \langle\phi_\nu|\phi_\mu\rangle \tag{2.116}$$

$\mathbf{C}_i$ is the eigenvector made from the coefficients $c_{i\mu}$. The eigenvectors with the N lowest energy eigenvalues corresponds to the occupied MOs in the HF ground state. In a closed shell system each MO can contain 0 or 2 electrons we use an RHF calculation. In an open-shell system with one or more unpaired electron, we can use UHF, where each MO contains 0 or 1 electrons, or we can use a calculation known as a restricted open-shell HF (ROHF), where each MO can contain 0, 1 or 2 electrons, in. UHF calculations result in a lower energy approximation to the ground state compare with ROHF, as there is more variational flexibility in the wavefunction. [133] However, the unrestricted wavefunction produced is no longer an eigenfunction of the $\hat{S}^2$ operator and is thus not the true wavefunction of a state. This leads to an incorrect $\hat{S}^2$ expectation value, known as spin contamination, and

is related to the overlap between the occupied alpha and beta orbitals.

$$\left\langle \hat{S}^2 \right\rangle_{\text{UHF}} = \left\langle \hat{S}^2 \right\rangle_{\text{Exact}} + N_\beta - \sum_{i,j}^{occupied} \left| \left\langle \psi_i^\alpha \middle| \psi_j^\beta \right\rangle \right|^2 \tag{2.117}$$

Where $\left\langle \hat{S}^2 \right\rangle_{\text{Exact}} = s(s+1)$. The amount of spin contamination gives an indication of the error in the wavefunction. It derives from the unrestricted Hamiltonian, which is different for α and β electrons. Spin contamination can lead to incorrect geometries and can effect the population analysis, which are discussed later. HS excited states usually contaminate the wavefunction, leading to an increase in both the energy and the $\hat{S}^2$ expectation value relative to the true wavefunction of the state. This further suggests that there exist HS states with low excitation energies, which indicates strong static correlation in the system and that a multi-configurational treatment is needed to describe it.

2.8 Post-Hartree-Fock Methods

The HF approximation assumes the wavefunction can be described by a single Slater determinant. This leads to an inaccurate description of the interelectronic repulsion. The difference in the true ground state energy and the HF energy is known as the correlation energy. The name arises from its failure to describe the fully correlated motion of the electrons due to the neglect of the instantaneous repulsion.

Configuration Interaction

The eigenstates of the Fock matrix form a complete orthonormal set of basis vectors, $\{|\chi_i\rangle\}$, and any state can be written as a linear combination of them.

$$|\psi\rangle = \sum_i c_i |\chi_i\rangle \tag{2.118}$$

If we take the projection onto the real axis, x_1, then we can see that any one dimensional function can be written

$$\langle x_1|\psi\rangle = \sum_i c_i \langle x_1|\chi_i\rangle \tag{2.119}$$

$$\psi(x_1) = \sum_i c_i \chi_i(x_1) \tag{2.120}$$

If we instead take the projection onto the plane spanned by the axes x_1 and x_2, then at fixed x_2 any two dimensional function can be written

$$\psi(x_1, x_2) = \sum_i c_i(x_2)\, \chi_i(x_1) \tag{2.121}$$

$c_i(x_2)$ is a one dimensional function parametrised by the fixed coordinate x_2, which itself can be written as a linear combination of the basis vectors, $\{|\chi_i\rangle\}$.

$$c_i(x_2) = \sum_j c_{ij} \chi_j(x_2) \tag{2.122}$$

Substituting this into the the two dimensional function

$$\psi(x_1, x_2) = \sum_{i,j} c_{ij} \chi_i(x_1)\, \chi_j(x_2) \tag{2.123}$$

In general any N dimensional function can be written

$$\psi(x_1, x_2, ..., x_N) = \sum_{i,j,...,N} c_{ij,...,N} \chi_i(x_1)\, \chi_j(x_2), ..., \chi_N(x_N) \tag{2.124}$$

In order to preserve the antisymmetry of the total wavefunction we use the Slater determinants formed by the orbitals. The full set of Slater determinants consist of all possible occupations of the complete set of spin orbitals, $\{|\chi_i\rangle\}$. These can be described in terms

of the HF ground state and its excitations. The ground state, $|\psi_0\rangle$, is the Slater determinant with the lowest energy orbitals occupied. We next then consider the states formed by single excitations from the ground state, $|\psi_i^a\rangle$. These correspond to the ground state occupation except the electron in orbital i is excited into orbital a. Double excitations, $\left|\psi_{ij}^{ab}\right\rangle$, correspond to the ground state occupation except the electrons in orbitals i and j are excited into orbitals a and b. Building on the HF approximation, which uses a single Slater determinant, creating a multi-configurational trial wavefunction from the linear combination of these determinants is known as the configuration interaction (CI) method. The CI method variationally minimises the energy associated with the CI wavefunction with respect to the coefficients, $c_{ij,...,N}$. When you consider all the possible excitations that describe every possible electronic configuration, creating a trial wavefunction from the linear combination of the full set of Slater determinants is known as a full CI (FCI) calculation, which can describe any electronic state exactly. In the limit where a complete atomic basis set is used, the exact wavefunction can be written as

$$|\Phi\rangle = c_0 |\psi_0\rangle + \sum_{i,a} c_i^a |\psi_i^a\rangle + \sum_{\substack{\mathrm{i<j} \\ \mathrm{a<b}}} c_{ij}^{ab} \left|\psi_{ij}^{ab}\right\rangle + \sum_{\substack{\mathrm{i<j<k} \\ \mathrm{a<b<c}}} c_{ijk}^{abc} \left|\psi_{ijk}^{abc}\right\rangle + , ..., \tag{2.125}$$

To illustrate the power of CI, we consider a hydrogen molecule with a minimal atomic basis set consisting of an S orbital on each atom, ϕ_A and ϕ_B. The eigenvectors are the bonding (σ_g) and antibonding (σ_u) combinations.

$$|\sigma_g\rangle = \frac{1}{\sqrt{2\,(1+S_{AB})}} \left[|\phi_A\rangle + |\phi_B\rangle\right] \tag{2.126}$$

$$|\sigma_u\rangle = \frac{1}{\sqrt{2\,(1-S_{AB})}} \left[|\phi_A\rangle - |\phi_B\rangle\right] \tag{2.127}$$

Where S_{AB} is the overlap between the atomic S orbitals centred at hydrogen A and B. If we take HF ground state, we get a Slater determinant with the two electrons in the system both in the bonding orbital (where the bar indicates spin β)

$$|\psi_0\rangle = \frac{1}{2\sqrt{2}\,(1+S_{AB})}\left[|\sigma_g\overline{\sigma}_g\rangle - |\overline{\sigma}_g\sigma_g\rangle\right] \tag{2.128}$$

Substituting in the equation for the bonding orbital gives

$$\begin{aligned}\frac{1}{2\sqrt{2}\,(1+S_{AB})}\Big[&\left|\phi_A\overline{\phi}_A\right\rangle + \left|\phi_A\overline{\phi}_B\right\rangle + \left|\phi_B\overline{\phi}_A\right\rangle + \left|\phi_B\overline{\phi}_B\right\rangle \\ &- \left|\overline{\phi}_A\phi_A\right\rangle - \left|\overline{\phi}_B\phi_A\right\rangle - \left|\overline{\phi}_A\phi_B\right\rangle - \left|\overline{\phi}_B\phi_B\right\rangle\Big]\end{aligned} \tag{2.129}$$

Here the first, fourth, fifth and eighth terms are called ionic terms. These have both electrons on one hydrogen and none on the other. This leaves one hydrogen negative and the other positive. These terms have an equal probability as the neutral terms where each hydrogen has one electron. This illustrates how the HF method can work well in some cases, but poorly in others. At equilibrium bond lengths we expect some contribution from terms like this as the electrons are still near both nuclei. However at the dissociation limit, we should not have any ionic contributions. If we look at the Slater determinant where the two electrons are in the anti-bonding orbital.

$$\left|\psi_{12}^{34}\right\rangle = \frac{1}{2\sqrt{2}\,(1-S_{AB})}\left[\sigma_u(1)\,\overline{\sigma}_u(2) - \sigma_u(2)\,\overline{\sigma}_u(1)\right] \tag{2.130}$$

Then when we substitute in the equation for the anti-bonding orbital we get the same result except the ionic terms now have the opposite sign.

$$\frac{1}{2\sqrt{2}\left(1-S_{AB}\right)}\left[\left|\phi_A\overline{\phi}_A\right\rangle-\left|\phi_A\overline{\phi}_B\right\rangle-\left|\phi_B\overline{\phi}_A\right\rangle+\left|\phi_B\overline{\phi}_B\right\rangle\right.$$
$$\left.-\left|\overline{\phi}_A\phi_A\right\rangle+\left|\overline{\phi}_B\phi_A\right\rangle+\left|\overline{\phi}_A\phi_B\right\rangle-\left|\overline{\phi}_B\phi_B\right\rangle\right] \tag{2.131}$$

If instead of describing the state with a single Slater determinant, we use a linear combination of the two determinants $|\psi_0\rangle$ and $\left|\psi_{12}^{34}\right\rangle$.

$$|\psi\rangle = c_0\,|\psi_0\rangle + c_{12}^{34}\left|\psi_{12}^{34}\right\rangle \tag{2.132}$$

It can then be shown that in the dissociation limit, as $\mathbf{r}_{HH}\to\infty$, that $S_{AB}\to 0$ and $\frac{c_0}{c_{12}^{34}}\to -1$, such that $c_0 = -c_{12}^{34} = \frac{1}{\sqrt{2}}$ and

$$|\psi\rangle = \frac{1}{2}\left[\left|\phi_A\overline{\phi}_B\right\rangle+\left|\phi_B\overline{\phi}_A\right\rangle-\left|\overline{\phi}_B\phi_A\right\rangle-\left|\overline{\phi}_A\phi_B\right\rangle\right] \tag{2.133}$$

Now there are no ionic terms and the dissociated hydrogen atoms can be described accurately. In general the number of determinants in the CI expansion increases dramatically with the number of HF orbitals and a FCI calculation is only realistic for small systems. To make the study of larger systems possible, the CI expansion is truncated. The most common truncation uses only the single and double excitations (CISD). In the FCI expansion the coefficients of the higher energy determinants with multiple excitations are smaller than the low energy determinants. The principle behind truncating the expansion is that the majority of the FCI correlation energy is recovered by the low energy excited determinants in the truncated wavefunction, but the expansion is small enough that calculations on larger systems become feasible.

Coupled Cluster

Coupled cluster takes a different approach to expanding the wavefunction in multiple Slater determinants. Using second quantisation the excited state determinants are described by a set of operators, $\{\hat{\tau}\}$, which act on the ground state.

$$|\Phi\rangle = c_0 |\psi_0\rangle + \sum_{i,a} c_i^a \, \hat{\tau}_i^a \, |\psi_0\rangle + \sum_{\substack{\mathrm{i<j} \\ \mathrm{a<b}}} c_{ij}^{ab} \, \hat{\tau}_{ij}^{ab} \, |\psi_0\rangle + \sum_{\substack{\mathrm{i<j<k} \\ \mathrm{a<b<c}}} c_{ijk}^{abc} \, \hat{\tau}_{ijk}^{abc} \, |\psi_0\rangle + , ..., \tag{2.134}$$

The operators $\{\hat{\tau}\}$ are defined in terms of the second quantisation creation and annihilation operators, $\hat{a}^\dagger$ and $\hat{a}$.

$$\hat{\tau}_i^a = \hat{a}_a^\dagger \hat{a}_i \tag{2.135}$$

$$\hat{\tau}_{ij}^{ab} = \hat{a}_a^\dagger \hat{a}_b^\dagger \hat{a}_i \hat{a}_j \tag{2.136}$$

$\hat{a}_i$ destroys an electron in orbital i and $\hat{a}_a^\dagger$ creates an electron in orbital a , such that $\hat{\tau}_i^a = \hat{a}_a^\dagger \hat{a}_i$ creates the excited state configuration where the electron in orbital i is excited into orbital a. Coupled cluster uses the exponential of the sum of the $\{\hat{\tau}\}$ operators. Examining the wavefunction expanded in only the single and double excitations we see the power of the coupled cluster technique.

$$|\Phi\rangle = \exp\left(\hat{T}_1 + \hat{T}_2\right) |\psi_0\rangle \tag{2.137}$$

Which uses the condensed terms

$$\hat{T}_1 = \sum_{i,a} c_i^a \, \hat{\tau}_i^a \tag{2.138}$$

$$\hat{T}_2 = \sum_{\substack{\mathrm{i<j} \\ \mathrm{a<b}}} c_{ij}^{ab} \, \hat{\tau}_{ij}^{ab} \tag{2.139}$$

Expanding the exponential as a Taylor series to second order

$$\exp\left(\hat{T}_1 + \hat{T}_2\right) = 1 + \hat{T}_1 + \hat{T}_2 + \frac{1}{2!}\left(\hat{T}_1 + \hat{T}_2\right)^2 \tag{2.140}$$

The squared term contributes higher energy excited states to the wavefunction, for example triple and quadruple excitations from the product of the single and double excitation operators, $\hat{T}_1\hat{T}_2$ and $\hat{T}_2\hat{T}_2$.

$$\exp\left(\hat{T}_1 + \hat{T}_2\right) = 1 + \hat{T}_1 + \hat{T}_2 + \frac{1}{2!}\left(\hat{T}_1\hat{T}_1 + \hat{T}_1\hat{T}_2 + \hat{T}_2\hat{T}_1 + \hat{T}_2\hat{T}_2\right) \tag{2.141}$$

Higher polynomial terms of the Taylor expansion give even higher energy Slater determinants. These give a better approximation to the full configuration interaction wavefunction. Truncating the expansion to include only single and double excitations, CCSD, with a perturbative correction for the energy contribution from the triple excitations, CCSD(T), is currently the gold standard in multi-configurational chemistry. Unfortunately, CCSD(T), is only tractable for system with about 1500 basis functions. [148] Recently Neese and co-workers have developed the first ever linear scaling CCSD(T) method with near DFT cost. It is expected that dynamic correlation is a short range effect, given that it tries to recover the energy of instantaneous electron repulsion. Therefore, rather than considering the full valence space, if each occupied orbital were assigned a set of local orbitals into which excitations could occur then computation of the correlation could become more efficient. These orbitals were defined by projecting the valence space onto the nearby AOs of the occupied orbital, creating a set of projected AOs (PAOs). [149, 150] Neese's method first expands the virtual space in a set of pair natural orbitals (PNOs), [151, 152] and then projects onto the local AOs of the original occupied orbital. This was first used for a CCSD expansion, giving the domain-based local pair natural orbital-CCSD (DLPNO-CCSD). [153] Later it has been used with CCSD(T) to give DLPNO-CCSD(T), allowing

CCSD(T) level calculations on far larger systems than ever before, recovering 99.8% of the total correlation energy. [154, 155]

Complete Active Space Self Consistent Field

The HF approximation does not account for the correlation energy recovered by the full configuration interaction method. It fails for two reasons. To understand the first we consider the coulomb operator in Equation 2.109 page 76, which acts on an electron in orbital i and gives the repulsion to the electron density due to an electron in orbital j. Each orbital j is fixed in the operator, and the operator is summed over all N orbitals. In the HF model each individual electron, therefore, only interacts with the electron density, or mean field, created by the other electrons. On average, the optimised wavefunction describes electrons that are allowed to approach one another too closely. It does not account for any instantaneous repulsion between them, which leads to a larger repulsive energy and a ground state with too high an energy compared to the true wavefunction. This energy is known as dynamic correlation, named for its relation to the electronic motion. Originally this was thought of as the sole contributor to the correlation energy. The second reason has already been discussed in the context of the dissociation of the hydrogen molecule. HF theory is based on the assumption that the solution to the Schrödinger equation can be approximated by a single Slater determinant. As the H-H bond length increases, the bonding and anti-bonding orbital energies converge and the configuration with the anti-bonding orbital occupied becomes increasingly important to the description of the dissociating molecule. In general, single determinant solutions break down when there are low-lying excited state configurations. The error in the predicted energy it causes is known as static (or nondynamic) correlation as it is not related to the electronic motion.

The correlation energy is often described using this separation of static and dy-

namic correlation, although there can be cases where the separation is not clear. In the HF model, all Coulomb electron correlation is completely unaccounted for (exchange correlation is accounted for by using an antisymmetric Slater determinant). The correct way to describe both static and dynamic correlation is actually the same - using the full configuration interaction method. Static correlation effects are associated with the low-lying excited state configurations, which have large coefficients in the multi-configurational wavefunction. Dynamic correlation effects are associated with high-lying excited state configurations where low-energy electrons are excited into high-energy valence orbitals. This allows them to properly avoid the other electrons in the high density core orbitals, leading to a lower energy wavefunction. There are many of these configurations but they tend to have small coefficients in the multi-configurational wavefunction. The distinction between the two types of correlation energy can become unclear when there are configurations between these two limits. A full configuration interaction calculation is a very expensive technique and only possible for the study of small systems. As discussed, the configuration interaction and coupled cluster methods truncate the expansion. As the complete expansion is approached the wavefunction gets more accurate, but computational costs increase dramatically. CI and CC are known as single-reference methods as they describe excited states using only the HF ground state as a reference. As the full space is not explored these methods can fail in the description of some systems. In particular when there are excited state configurations with large coefficients in the expansion. The problem arises because the reference state is optimised for the ground state, and it does not describe the excited states very well. For systems with small reference state coefficients (reference weights$<$90%) single reference methods are insufficient, and multi-configurational self consistent filed (MCSCF) techniques are needed.

One such technique is the complete active space self consistent field (CASSCF)

method developed by Roos and co-workers. [156–158] CASSCF curtails the number of excited determinants in a different manner. Rather than restricting the type of excitation, it restricts the orbitals that can be excited to and from. A full CI calculation is then performed within this small subspace of the system. Known as the active space, it is designed such that it accounts for the majority of the static correlation. It should therefore include the orbitals associated with the low-lying excited states. HF theory is used for the remaining orbitals not in the active space. The HF orbitals are all exactly doubly occupied or completely unoccupied, while the active space orbitals can take any occupation value between 0 and 2. A calculation predicting active orbitals with occupations close to 0 or 2 (<0.02 or >1.98) suggests they need not be included in the active space. The SCF step in MCSCF techniques means the calculation optimises the full set of orbitals (inactive, active and valence spaces) as well as the CI coefficients in each iteration. Importantly, this SCF step is under the influence of the multi-configurational active space wavefunction, and the orbitals can more accurately describe excited states that were poorly described by a single reference wavefunction.

Multi-Reference Perturbation Theory

Perturbation theories such as Møller-Plesset perturbation theory introduce a correlation potential as a small perturbation to the HF model. They calculate a corrected energy and wavefunction that incorporates the effect of excited states. For example second order Møller-Plesset perturbation theory (MP2) predicts the effect of double excitations. However perturbation theory only works for small perturbations to the Hamiltonian, which means these corrections must be small for the theory to work well, and it can fail when there are large excited state coefficients.

Although CASSCF can do very well calculating static correlation, the MP2, CI

and CC methods do a better job of calculating dynamic correlation. They perform better than CASSCF because they include excitations from any occupied orbital into the full valence space. In order to account for this the complete active space second-order perturbation theory (CASPT2) is used. [159] This is a multi-reference perturbation theory method that takes the CASSCF wavefunction as its reference and then calculates the perturbation corrections to the energy up to second order. This energy then includes the effect of excitations within the full occupied and valence space, and therefore both static and dynamic correlation. The CASPT2 result can also be useful in predicting the active space. Low-lying excited states with large coefficient cause spurious CASPT2 results as the large corrections are inappropriate for perturbation theory. However, these results can be used to indicate that the excited orbital should be included in the active space, and once it is the ensuing CASPT2 calculation will perform reliably.

2.9 Density Functional Theory

The HF and post-HF methods attempt to find solutions to the many-body molecular Hamiltonian through aproximations to the form of the wavefunction. Density functional theory (DFT) represents a different approach, whereby the Hamiltonian is approximated rather than its solution. In the limit where the approximate Hamiltonian becomes exact, so does the solution that solves it. In the derivation of the HF equation (Equation 2.112 page 77) we showed how the Coulomb term cancels the exchange term when the two electrons occupy the same orbital. We can rewrite the total HF energy for the set of occupied spin orbitals (Equation 2.105).

$$E\left[\{\chi_i\}\right] = \sum_{i}^{N} h_i + \frac{1}{2}\sum_{i,j}^{N}\left(\mathcal{J}_{ij} - \mathcal{K}_{ij}\right) \tag{2.142}$$

The Coulomb term for a single electron in orbital χ_1

$$\sum_j^N \mathcal{J}_{1j} = \sum_j^N \langle \chi_1 \chi_j | \frac{1}{r_{1j}} | \chi_1 \chi_j \rangle = |\chi_1(\mathbf{r})|^2 \int \frac{\sum_j^N |\chi_j(\mathbf{r})|^2}{r_{1j}} d\mathbf{r} \tag{2.143}$$

can be seen to contain the total electron density, $\rho(\mathbf{r})$.

$$\sum_j^N |\chi_j(\mathbf{r})|^2 = \rho(\mathbf{r}) \tag{2.144}$$

Reintroducing the sum over i, the total Coulomb energy can be written in terms of the total electron densities of electrons one and two.

$$\sum_i^N |\chi_i(\mathbf{r})|^2 \frac{\sum_j^N |\chi_j(\mathbf{r})|^2}{r_{ij}} = \frac{\rho(\mathbf{r}_1)\rho(\mathbf{r}_2)}{r_{12}} \tag{2.145}$$

The electron density naturally appears from the form of Coulomb energy. This provided the motivation behind DFT, where the underlying principle is that the exact energy can be written as a functional of the electron density. As for the Coulomb energy, the nuclear-electron attraction can be defined exactly in terms of the electron density. The problem facing DFT lies in the calculation of the kinetic and exchange energies. Theoretically there exists an exact functional that gives the exact energy, but its form has long escaped quantum chemists. The functional form can be separated into contributions from the kinetic energy, $T[\rho]$, electron-nuclear attraction energy, $V_{en}[\rho]$, and the electron-electron Coulomb, $J[\rho]$, and exchange, $K[\rho]$, energies.

$$E[\rho] = T[\rho] + V_{en}[\rho] + J[\rho] + K[\rho] \tag{2.146}$$

The functional form of the electron-nuclear attraction and Coulomb terms are known exactly, but in practice the form of kinetic and exchange energy functionals are approximated. The earliest functionals date back to 1927 and the Thomas-Fermi model, which calculates the kinetic energy based on the uniform electron gas and ignores the exchange contribution, treating the electron-nuclear and electron-electron interactions classically. [160–163]

$$E_{TF}\left[\rho\right] = \frac{3}{10}(3\pi^2)^{\frac{2}{3}} \int \rho^{\frac{5}{3}}\left(\mathbf{r}\right) d\mathbf{r} - \sum_{A}^{M} Z_A \int \frac{\rho\left(\mathbf{r}\right)}{r_{A1}} d\mathbf{r} + \frac{1}{2} \int\int \frac{\rho\left(\mathbf{r}_1\right)\rho\left(\mathbf{r}_2\right)}{r_{12}} d\mathbf{r}_1 d\mathbf{r}_2 \quad (2.147)$$

The initial success of DFT was limited and it did not begin to gain traction until 1964 with the work of Walter Kohn and Pierre Hohenberg. [164] They introduced two theorems, known as the Hohenberg-Kohn theorems: i) the energy is a unique functional of the electron density and ii) the density that minimises the energy is the ground state density. A year later Kohn and Sham presented a novel approach to finding the kinetic energy. [165] Previous approaches (e.g. the Thomas-Fermi model) took the total electron density and predicted the kinetic energy of all the contributing electrons from the kinetic energy of the uniform electron gas, which by definition has an unvarying density. This was, unsurprisingly, not accurate for systems with non-uniform electron densities. Rather than considering the total density of a system of interacting particles, Kohn and Sham suggested using a fictitious system of non-interacting particles moving in an effective potential. By correctly defining the effective potential the density of the interacting system can be recovered by the density generated by the non-interacting system. The non-interacting system is defined by a set of single electron wavefunctions, known as Kohn-Sham orbitals, χ_i^{KS}, for which the exact kinetic energies are known using Equation 2.6 page 50. The non-interacting kinetic energy, $T_S\left[\rho\right]$, is not the exact interacting kinetic energy, but the majority is recovered by the approximation. The non-classical components of the electron-

electron interactions, the exchange and correlation, are also still to be accounted for. As such Kohn and Sham introduce the exchange-correlation functional, $E_{xc}[\rho]$, to define the total energy of the interacting system.

$$E[\rho] = T_S[\rho] + V_{en}[\rho] + J[\rho] + E_{xc}[\rho] \tag{2.148}$$

The exchange-correlation functional is defined in terms of the true kinetic energy, $T[\rho]$, and true interacting electron-electron repulsion, $V_{ee}[\rho]$.

$$E_{xc}[\rho] = T[\rho] - T_S[\rho] + V_{ee}[\rho] - J[\rho] \tag{2.149}$$

Variationally minimising the energy with respect to the orbitals gives the Kohn-Sham equation, which defines the form of effective potential needed to generate the interacting density shown inside the square brackets. [162, 163]

$$\left(-\frac{1}{2}\nabla^2 + \left[-\sum_A^M \frac{Z_A}{r_{A1}} + \int \frac{\rho(\mathbf{r}_2)}{r_{12}} d\mathbf{r}_2 + V_{xc}(\mathbf{r}_1)\right]\right)\chi_i^{KS} = \epsilon_i \chi_i^{KS} \tag{2.150}$$

Where the exchange-correlation potential, $V_{xc}(\mathbf{r})$, is defined as the functional derivative of the exchange-correlation functional with respect to the density.

$$V_{xc} = \frac{\delta E_{xc}[\rho]}{\delta \rho} \tag{2.151}$$

In theory if we knew the form of V_{xc} and $E_{xc}[\rho]$ then we would know the exact ground state density and energy. In practice the form of the effective potential is not correct, and the density generated by the non-interacting system does not correspond to the true density. Compared to HF theory, DFT improves on the approximation to the energy

as the Coulomb correlation is taken into account to better describe the instantaneous electron-electron repulsion. The power of DFT lies in taking a $3N$-dimensional wavefunction problem (every electron moving in 3-dimensions) to a 3-dimensional density problem, facilitating computation compared with traditional post-HF methods. Using the density does create a problem, however, known as the self-interaction error. Considering an individual electron, as it both contributes to the total density and interacts with the total density, it is technically interacting with itself. In theory this should be exactly cancelled by the exchange-correlation potential, but given this is approximated this is not always the case. In addition, the approximation to the exchange energy is also inexact, whereas in HF theory the exchange energy is defined exactly. Despite its name, the exchange-correlation potential accounts for not only the exchange and correlation, but also the self interaction correction and the correction to the kinetic energy.

As previously stated, were the exact form of the exchange-correlation potential known DFT would be an exact theory. The form of the exchange-correlation potential identifies the central approximation of DFT. There have been many attempts to find the best approximation, the most simple of which is known as the local density approximation (LDA). The LDA exchange-correlation energy is defined using the local density and the exchange-correlation energy per particle of the uniform electron gas at that density, $\epsilon_{xc}(\rho(\mathbf{r}))$.

$$E_{xc}^{LDA}[\rho] = \int \rho(\mathbf{r})\,\epsilon_{xc}(\rho(\mathbf{r}))\,d(\mathbf{r}) \tag{2.152}$$

$\epsilon_{xc}(\rho(\mathbf{r}))$ has been calculated to a very high accuracy using quantum Monte-Carlo. [166] Equation 2.152 acts like the sum of the exchange-correlation energies per particle at each point in space, given by $\epsilon_{xc}(\rho(\mathbf{r}))$, where the contribution of each point is weighted by the number of electrons at that point, $\rho(\mathbf{r})$. DFT has proven to be a powerful tool

for quantum chemists. LDA, and the closely related Local Spin Density Approximation (LSDA), have had success in the study of systems with a slowly varying electron density, e.g. (non-molecular) crystals. For molecules, which have more rapidly changing densities, LDA/LSDA fails.

The development of the Generalised Gradient Approximation (GGA) in 1983 made the use of DFT applicable to chemistry. [167] DFT divides the density into a grid to calculate the total energy. Using the gradient of the density gives a better description of the elements on the grid, as it describes how the density varies within and between each element. This leads to a better estimate of the total energy for systems with a non-uniform density. Gradient-corrected methods outperform HF theory and often second order Møller–Plesset perturbation theory (MP2) for many molecules. The preference for DFT over MP2 is increased further when the computational cost of MP2 is considered. Before the use of GGA functionals became commonplace, few chemists were willing to take on the challenge of a theoretical study of transition metal complexes. The GGA approach made such studies far more accessible to chemistry and the wider community, and publication numbers increased. [168] In practice there are many GGA methods. They are all functionals of the density and the reduced density gradient, but differ in the exact form of their exchange-correlation functional. The majority separate the exchange-correlation functional into two separate functionals to account for the exchange and correlation.

$$E_{xc}^{GGA}[\rho] = E_{x}^{GGA}[\rho] + E_{c}^{GGA}[\rho] \tag{2.153}$$

Common exchange functionals are the B86 (developed by Becke in 1986) and PW86 (Perdew and Wang 1986) functionals. [169, 170] The former builds on the work of Langreth and Mehl, [167] fitting two parameters (one of which was introduced by Becke) to

the exactly known HF exchange energies of H through Ar, Kr, and Xe. The latter is free of any (semi) empirical parameters. Another exchange functional is the B88 (Becke in 1988) functional, which fits a parameter to the HF exchange energies of the noble gases. [171] Using a similar form to the B86 functional, Handy and Cohen developed the OPTX (optimised exchange) functional, which uses the HF exchange energies of the elements in the first two rows of the periodic table. [172] The two most common correlation functionals are the P86 (Perdew 1986) and LYP (Lee, Yang and Parr in 1988). [173, 174] They were formulated by fitting to the correlation energies of neon and helium atoms, respectively. Combining either of these with the B88 exchange functional gives two of the most widely used exchange-correlation functionals, BP86 and BLYP.

Rather than using experimental data to determine parameters in a functional, Perdew wanted to create a functional that satisfied a set of universal physical constraints, e.g. the exchange-correlation hole must integrate to -1. He developed a series of exchange and correlation functionals free of any empirical fitting starting with the previously mentioned PW86, followed by PW91 (Perdew and Wang 1991) [175] and culminating in the PBE functional (Perdew, Burke and Ernzerhof 1996).[176, 177] Such functionals should be appropriate to study any system, whereas heavily parameterised functionals may only work well on systems similar to the training set. With enough parameters any functional should be able to perform well for a certain set of molecules, but this does not necessarily reflect the accuracy of the functional.

Meta-GGA functionals extend the idea behind GGA functionals further and use second derivative of the electron density. Extending PBE into the meta-GGA realm, Perdew developed the TPSS functional in 2003, again without any empirical parameters. [178] More recently the SCAN functional has been developed, which satisfies all 17 known exact constraints (six for exchange, six for correlation and five for their sum) that a meta-

GGA can. [179]

In a push for greater accuracy in GGA functionals, in 1993 Becke proposed including a contribution from the exact exchange energy, creating the first of the so-called hybrid functionals. The exchange hole in GGA functionals is localised to the reference electron, whereas the exchange energy is an inherently non-local phenomenon. e.g. considering the H_2 molecule in unrestricted HF theory, the exact exchange hole is the σ_g orbital, and is completely independent of the position of the reference electron. GGA and, in particular, LSDA functionals tend to overbind electrons as the localised exchange hole prevents them approaching one another too closely. The electron repulsion energy term is therefore too small and the total energy too stable. Becke suggested that in order to create 'highly accurate' functionals, the exact exchange energy should be considered. [180–182] His functional took the form

$$E_{xc} = E_{xc}^{LSDA} + a_0(E_x^{exact} - E_x^{LSDA}) + a_x\Delta E_x^{B88} + a_c\Delta E_c^{PW91} \tag{2.154}$$

Where a_0, a_x and a_c were empirical coefficients found to be 0.20, 0.72 and 0.81 when fit to experimental data, E_{xc}^{LSDA} and E_x^{LSDA} are the LSDA exchange-correlation and exchange energies, E_x^{exact} is the exact exchange energy, ΔE_x^{B88} is the B88 gradient correction to the exchange energy and ΔE_c^{PW91} is the PW91 gradient correction to the correlation energy. In 1994 Frisch further honed the functional, replacing ΔE_c^{PW91} with the LYP gradient correction to the correlation energy and the LSDA correlation energy with the local VWN correlation functional of Vosko, Wilk and Nusair [183] to create the B3LYP functional. [184] B3LYP was remarkably successful and has since become probably the most widely used functional in electronic structure theory research.

The most recent addition to the set of density functional approximations are

known as double-hybrid functionals. Like hybrid functionals, double-hybrids also contain a contribution from the exact HF exchange energy to the exchange potential, but unlike hybrid functionals they also contain a contribution from the MP2 correlation energy to the correlation potential, e.g the B2-PLYP functional from Grimme. [185, 186]

2.10 Basis Sets

In the discussion of CI we remarked that a FCI calculation with a complete basis set (CBS) gives the exact solution to the electron Schrödinger equation. The FCI limit is out of reach due to the vast number of determinants, and we have detailed several approximations that make calculations on molecular systems tractable (CI, CC, CASSCF). These approximations made no attempt to limit the size of the basis set, which is only complete in the infinite limit. Quantum chemistry calculations approximate the CBS limit using the linear combination of atomic orbitals (LCAO) to describe the MOs that define the Slater determinant. The basis set describes all of the atomic orbitals in the molecule and resembles a set of local hydrogenic orbitals centred at the nuclear coordinates. Figure 2.1 shows the radial form of the hydrogen-like orbitals, which decay as e^{-r}, where r is the distance from the centre of the nucleus.

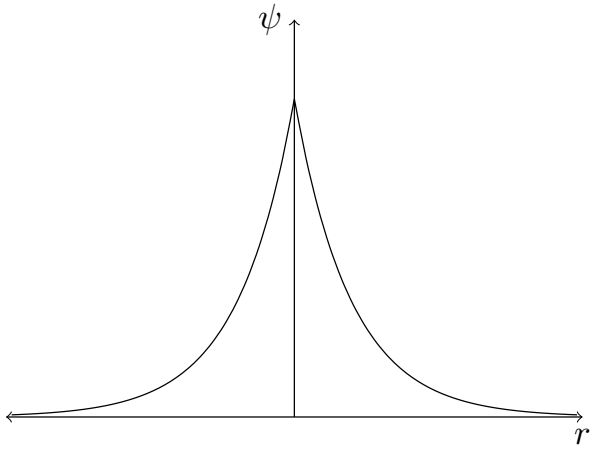

Figure 2.1: STO of the form in Equation 2.155 centred at $r = 0$.

$$\psi_{nlm}^{STO} = Nr^{n-1}e^{-\zeta r}Y_{lm}(\Theta, \Phi) \tag{2.155}$$

Slater type orbitals (STOs) emulate the hydrogen-like orbitals, showing the e^{-r} decay and the cusp at the nucleus in the radial part, given by the second and third terms of equation 2.155. This is then multiplied by the appropriate spherical harmonic function to give the angular behaviour (N is a normalisation constant). [187]

The simplest basis sets use a single STO to represent each atomic orbital. STOs represent atomic orbitals well, and are used in the Amsterdam Density Functional (ADF) package used in this thesis. As previously discussed, DFT calculates the energy by defining a grid and summing the energy due to the density at each point. This amounts to a numerical integration over the 3-dimensional space, where the accuracy is improved by defining a finer grid. The orbitals are only used to generate the total density at each point, and their specific form does not affect the calculation time. In wavefunction based methods, there are many multi-centre integrals (e.g. coulomb and exchange energies) for each pair of orbitals that need to be solved. Using STOs makes this an arduous process requiring each integral to be solved numerically, with each integral a similar difficulty to the entire DFT integral over the whole density. For this reason the use of hybrid functionals in ADF takes significantly longer than functionals without any HF component.

$$\psi_{ijk}^{GTO} = Nx^i y^j z^k e^{-\zeta r^2} \tag{2.156}$$

In contrast, using Gaussian functions in Gaussian type orbitals (GTOs) to describe orbitals (Equation 2.156) facilitates the calculation of these integrals. The radial part of the orbital is given by the exponential, and the angular part by the powers of x, y and z where the sum $i+j+k$ gives the total angular momentum (e.g. $i+j+k=0$ for an s-orbital, $i+j+k=1$ for p, $i+j+k=2$ for d etc.). The product of two Guassian functions centred at two

different nuclear coordinates is another Guassian function centred on the axis between the two nuclei. This allows the multi-centre integrals to be solved analytically. [188]

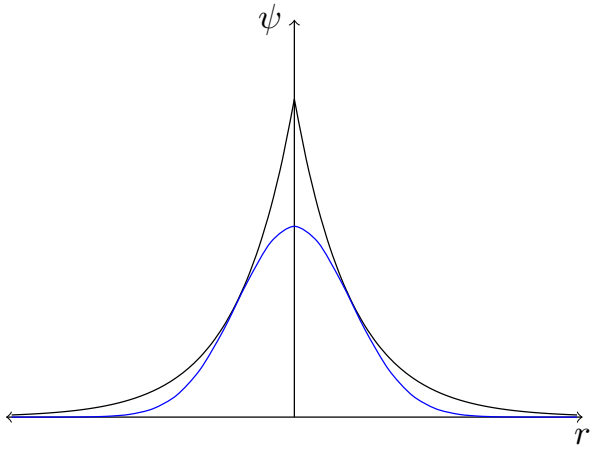

Figure 2.2: STO of the form in Equation 2.155 and GTO of the form in Equation 2.156 centred at $r = 0$.

The problem with using GTOs is that they do not represent the atomic orbitals as well as STOs. As can be seen in Figure 2.2 (blue), GTOs decay too quickly and do not have the cusp at the centre of the nucleus. To overcome this issue, a linear combination of GTOs (CGTOs) can be used. Figure 2.3 shows three GTOs (red, blue and green), the combination of which gives a better approximation to the STO in black. Using more GTOs further improves the approximations. The STO-nG (Slater type orbital approximated by n Gaussian functions) basis sets developed by Pople use a least squares fitting of the exponents and coefficients in the Gaussian expansion to STO atomic orbitals. They showed that as n increases the calculated values for atomization energies, atomic populations, and electric dipole moments converge on the values found using the STO basis set. [189]

Using a single STO or CGTO basis function is known as a minimal basis. They have been designed to describe atomic orbitals, rather than orbitals within a molecule. Minimal basis sets are not particularly flexible and do not allow electrons to respond to their chemical environment, for example the approach of another atom during bond

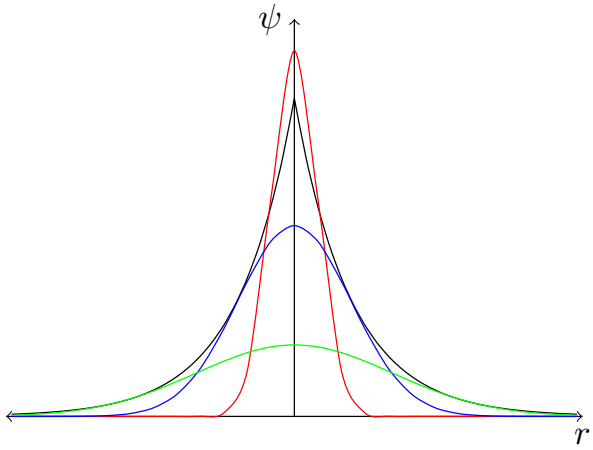

Figure 2.3: STO of the form in Equation 2.155 and three GTOs of the form in Equation 2.156 centred at $r = 0$.

formation. Instead, the basis set needs to contain multiple functions for each atomic orbital to allow them to deform. Using functions with different exponents (ζ) allows the orbitals to expand or contract depending on their local environment. Using two basis functions for each atomic orbital is known as a double zeta basis, three a triple zeta basis etc. A split-valence basis uses multiple basis functions to describe valence atomic orbitals that strongly interact with neighbouring atoms, and a single basis function to describe the core orbitals that only weakly interact with neighbouring atoms. Pople developed several split valence basis sets: the 3-21G, 4-31G, 5-31G and 6-31G are double split valence basis sets with core orbitals described by a single function that is the sum of three, four, five or six GTOs and valence orbitals by two functions, one the sum of two or three GTOs and the other a single GTO. [190–193]

Further to considering multiple basis functions for each atomic orbital, basis functions describing higher angular momentum atomic orbitals can also be added. Known as polarisation functions, they allow an improved description of directionality in chemical bonding within molecules. The 6-31G* basis set from Pople adds a set of d-orbitals to first row [194] and second row [195] elements while the 6-31G** also adds p-orbital polarisation

functions to hydrogen atoms to the double split valence basis sets. A valence triple zeta polarised basis set was also developed, known as 6-311G**. [196] Diffuse basis functions can also be added, as proposed by Clark *et al.*, and are essential for the description of anionic systems where the electron shell is significantly expanded. [197] Pople later developed even larger basis sets, which took 6-311G** and added diffuse *s*- and *p*-orbitals (+ indicates diffuse *s* and *p* only on heavy atoms and ++ indicates diffuse *s* on hydrogen atoms too), up to two extra polarising *d* orbitals and a polarising *f*-orbital, with hydrogen atoms allowed up to two extra polarising p-orbitals and a single d-orbital to give the 6-311^{++}G[3*df*,3*pd*] basis set. [198]

Another popular collection of basis sets is the split valence def2-nVP family from Ahlrichs, which span split, triple or quadruple zeta bases (n=S, TZ or QZ) with the optional inclusion of diffuse and polarisation functions. [199] They take advantage of small effective core potentials for elements heavier than krypton and have optimised auxiliary orbitals for the RI approximation of the Coulomb, [200] Coulomb and exchange, [201] and for use in MP2 and CC2 (second-order approximate coupled cluster) calculations. [202] The generally contracted atomic natural orbital (ANO) approach proposed by Almlöf and Taylor uses the natural orbitals of atomic CISD calculations, noting that the atomic orbitals calculated using HF with split valence basis sets are unsuitable for describing dynamic correlation. They presented a range of truncations depending on the natural orbital occupation numbers that showed a systematic improvement in the basis set error as higher radial and angular functions were added concurrently. [203] Inspired by this, Dunning and co-workers developed the correlation-consistent polarised basis sets (cc-pVnZ), which were specifically designed to converge on the CBS limit as the size of the basis increases through the valence double, triple, quadruple and quintuple zeta sets (n=D, T, Q, 5). The core orbitals are given by the HF atomic orbitals, while the valence exponents are optimised us-

ing CCSD calculations. Dunning then selected basis functions based on their contribution to the correlation energy rather than their natural orbital occupation numbers. [204–207] Taking a different approach, Roos and co-workers worked to improve the accuracy of the ANO basis sets, which were found to overstabilise the ground state. They constructed a new set of ANOs by averaging over several excited states, the ground state of the cation and anion as well as the atom in an electric field in the large ANO-L basis sets optimised to produce the results of the uncontracted set, [208–210] while the smaller ANO-S basis sets were averaged over some homonuclear diatomics as well, and were instead optimised to reproduce structural properties such as bond lengths, strengths and vibrational frequencies. [211] The ANO-Relativistic Core-Correlated (ANO-RCC) basis sets include relativistic effects through the Douglas–Kroll Hamiltonian and use CASPT2 to calculate the natural orbitals. They use the averaging techniques described for the ANO-L and ANO-S basis sets and contain functions that describe the correlation of semi-core electrons for atoms H-Cm. [212–216] More recently Widmark *et al.* created the compact relativistic ANO-eXtra Small basis set (ANO-XS) to limit the number of basis functions and allow calculations on larger molecules, in particular for metal complexes where an ANO-XS set can be used for ligand atoms in combination with an ANO-RCC set for metal atoms. [217]

2.11 Wavefunction Analysis

Once we have calculated the wavefunction that solves the Schrödinger equation for the electronic Hamiltonian (Equation 2.29 page 57) and optimised the geometry of a molecule, we can begin to understand its molecular properties. The MOs that underpin the theoretical techniques discussed in this chapter are interpreted as representing where each electron is likely to be found in space. However, when we describe molecular properties we use concepts like atoms with partial charges and electrons in single, double, triple etc. bonds

that hold molecules together. In order to translate the geometry and MOs into such a description, we need to be able to assign the electron density to specific nuclei within the molecule. The most straightforward of such analyses uses the basis functions to partition the electron density between atoms. [138, 139]. The electron density of an electron in MO ψ_i is given by $\rho_i(\mathbf{r}) = \psi_i^2(\mathbf{r})$. Each MO is defined using a LCAO, $\psi_i(\mathbf{r}) = \sum_{\mu}^{AOs} c_{i\mu}\phi_\mu(\mathbf{r})$, and so the density is given by $\rho_i(\mathbf{r}) = \sum_{\nu\mu}^{AOs} c_{i\nu}c_{i\mu}\phi_\nu(\mathbf{r})\phi_\mu(\mathbf{r})$. Taking the sum over all MOs, weighting the contribution by the occupation number, n_i, and integrating over space gives the total number of electrons.

$$\sum_{i}^{MOs}\sum_{\nu\mu}^{AOs} n_i c_{i\nu}c_{i\mu}\int \phi_\nu(\mathbf{r})\phi_\mu(\mathbf{r})d\mathbf{r} = \sum_{\nu\mu}^{AOs}\mathbf{D}_{\nu\mu}\mathbf{S}_{\nu\mu} = \mathrm{Tr}(\mathbf{DS}) = N \tag{2.157}$$

$\mathbf{S}$ is the overlap matrix has been seen before in the definition of the Fock matrix (Equation 2.115 page 78). $\mathbf{D}$ is the density matrix, where each element is defined by $\mathbf{D}_{\nu\mu} = \sum_{i}^{MOs} n_i c_{i\nu}c_{i\mu}$. The occupation numbers, n_i, are 0, 1 or 2 for single determinant methods (HF and DFT), but can be fractional for multi-configurational wavefunctions. The Mulliken population analysis uses products of elements in the ovelap and density matrices, $\mathbf{D}_{\nu\mu}\mathbf{S}_{\nu\mu}$, to assign the electron distribution. [218, 219] We can separate the sum over the AOs into the sum over the AOs on nucleus A and then summing over all nuclei.

$$N = \sum_{A}^{nuclei}\sum_{\mu\in A}^{AOs}\sum_{\nu}^{AOs}\mathbf{D}_{\nu\mu}\mathbf{S}_{\nu\mu} = \sum_{A} N_A \tag{2.158}$$

N_A therefore corresponds to the number of electrons on nucleus A. The sum $\sum_{\nu}^{AOs}$ be further split into two parts, one with $\nu = \mu$ and the other $\nu \neq \mu$, where we use $\mathbf{S}_{\nu\mu} = 1$.

$$N_A = \sum_{\mu\in A}^{AOs}\sum_{\nu}^{AOs}\mathbf{D}_{\nu\mu}\mathbf{S}_{\nu\mu} = \sum_{\mu\in A}^{AOs}\mathbf{D}_{\mu\mu} + \sum_{\mu\in A}^{AOs}\sum_{\nu\neq\mu}^{AOs}\mathbf{D}_{\nu\mu}\mathbf{S}_{\nu\mu} \tag{2.159}$$

The first term on the right hand side, $\mathbf{D}_{\mu\mu}$, straightforwardly corresponds to the number of electrons in atomic orbital $\phi_\mu(\mathbf{r})$. The second term represents half the number of electrons "shared" between atomic orbitals $\phi_\mu(\mathbf{r})$ and $\phi_\nu(\mathbf{r})$. The other half corresponds to an equivalent term, $\mathbf{D}_{\mu\nu}\mathbf{S}_{\mu\nu}$, where $\nu \notin A$ and is not assigned to N_A. The density is instead assigned to the nuclei containing $\phi_\nu(\mathbf{r})$, and the Mulliken population analysis is, therefore, equivalent to distributing the "shared" electron density equally between each pair of atomic orbitals. The charge density on an atom, Q_A, can then be calculated as $Q_A = Z_A - N_A$, where Z_A is the atomic charge. In a similar manner, we can also calculate spin densities, ρ_A, by calculating the number of α and β electrons on atom A, where $\rho_A = N_{A\alpha} - N_{A\beta}$. The Mulliken population analysis suffers from several problems: AOs can be assigned populations less than 0 or greater than 2 , which is unphysical, while splitting the "shared" electron density equally has no physical basis and does not account for differences in electronegativity between atoms. Also, when large, diffuse basis sets are used electron density can be assigned to nuclei far away, and atomic charges are dependent on the basis set size. Comparing charges that use different basis sets is therefore not possible.

The Mulliken population analysis is only one of a family of basis set population analyses, all of which partition the overlap matrix $\mathbf{S} = \mathbf{S}^{(1-x)}\mathbf{S}^x$. [220] Using the cyclic permutation property of traces, the total number of electrons can be written in a number of ways, $N = \mathrm{Tr}(\mathbf{DS}) = \mathrm{Tr}\Big(\mathbf{DS}^{(1-x)}\mathbf{S}^x\Big) = \mathrm{Tr}\Big(\mathbf{S}^x\mathbf{DS}^{(1-x)}\Big)$. The Löwdin population analysis uses $x = \frac{1}{2}$, and is equivalent to transforming the AOs into an orthonormal basis set, $\tilde{\phi} = \mathbf{S}^{-\frac{1}{2}}\phi$. [221, 222] This takes all the $\mathbf{D}_{\nu\mu}\mathbf{S}_{\nu\mu}$ terms to zero and prevents the unphyscial populations predicted by a Mulliken Analysis. Atomic charges still depend on the basis set size though, and these methods are most useful when small basis sets are used, and when they are only needed for comparing trends and substitution or conformation effects. [138]

The Atoms In Molecules (AIM) approach developed by Bader divides the molecule into atomic volumes, V_A, and atomic charges are given by the total electron density, $\rho(\mathbf{r})$, in that volume, $Q_A = Z_A - \int_{V_A} \rho(\mathbf{r}) d\mathbf{r}$. [223] Other methods aim to reproduce the molecular electrostatic potential (ESP) at multiple grid points by fitting partial charges to the nuclei. [224, 225] In general population analyses based on the basis functions are very quick, and while they can depend on the choice of basis set, they are often used because of the ease of their calculation. ESP analyses requires calculation of the potential at a large number of grid points and can take a long time, especially in large systems, while AIM evaluates the complete topology of the electron density, and can take more time than calculating the wavefunction. [139]

2.12 Theoretical Studies of Transition Metal Complexes

Given the size and number of electrons in TM complexes, most studies take advantage of the computational efficiency of density functional theory (DFT). When using DFT to study TM complexes, the form of the exchange-correlation functional can play an important role. It may seem sensible to use a functional designed to work for any system, like PBE or SCAN, however results are often better for hybrid functionals like B3LYP which have empirical parameters. In 2004 Swart combined the OPTX exchange functional with PBE correlation to create the OPBE functional. [226] It was shown to predict spin state orderings in various iron complexes correctly, and performed well for other TMs complexes. [227] The OPTX exchange functional is also often combined with the LYP correlation functional to give the OLYP functional, with improved results over BLYP, [228] including good spin state splitting energies. [229] Handy and Cohen also attempted to develop a correlation functional, OPTC, to use with OPTX but found better accuracy with OLYP. [230] In 2001 the Reiher group developed the B3LYP* functional, which uses 15% HF exchange

(compared to 20% in B3LYP) after optimising for iron based TM complexes. [231] They showed a linear dependence between LS-HS splitting energies and the proportion of exact exchange included in the functional, but found in general an optimum region of 10–15 % HF gave the correct ground state for their entire test set. Extending the study showed that B3LYP* improves upon B3LYP spin state splitting results, which already performs better than pure GGA functionals, [232] while a review of functional performance showed that it gives the best spin state splitting results out of a set of GGA and hybrid functionals. [233] More recently DFT studies have been extended to the solid state to try to include the effect of the crystalline environment using the DFT+U method based on the Hubbard model. [234–237] The strength of DFT has been reviewed in the context of TM spectroscopy, with a general consensus that there is no one functional that performs well for all types of system. [226, 227, 238–250]

DFT studies of transition metal complexes are often shown to be strongly functional dependent. That is, the structures and energies of the electronic states in a molecule vary depending on the choice of functional. This raises the question of which functional to choose. In 2001 Perdew described his "Jacob's ladder of Density Functional Approximations". [251] With LSDA at the bottom rung, climbing the ladder incorporates more ingredients into the functional going through GGA, meta-GGA, hybrid and double-hybrid functionals. In theory, the farther up the ladder the more accurate the results. However when considering transition metal complexes it is not always quite so simple. In this chapter we have already presented several papers that show the success of various functionals over others, where the accuracy does not always correlate with this functional hierarchy. It is therefore important to understand the strengths and weaknesses of the functionals and how the results may change dependent on their form.

We have already discussed how LSDA and GGA functionals suffer an over-

stabilisation error due to the form of the exchange-correlation functional. In general this occurs for delocalised states, where the localised approximation to the exchange hole does a poor job describing the exchange energy. [252] Even Perdew details that the modern SCAN functional is likely to perform less well for semi-local states, [179] while more recent studies show it still suffers many of the same problems of GGA functionals. [253] Meanwhile, hybrid functionals can suffer an over-stabilisation of high spin states. This is due to inclusion of exact HF exchange, which lowers the energy for pairs of same spin electrons. The exchange energy is inversely proportional to the distance between the electrons, which leads to overly localised wavefunctions when using hybrid functionals. [227, 254]

For this study this presents a particular problem, as the electronic-structure model reported in the literature involves a low-spin ground state that is delocalised across the three cobalt atoms and a low-lying high-spin excited state with significant localisation on one of the terminal cobalt atoms. We therefore have to calculate the wavefunctions of two states that will suffer very different errors for different functionals. A description of the exact spin state splitting energies is most likely more nuanced than the arguments presented above. E.g. the inclusion of exact exchange in the exchange-correlation functional will in turn lower the relative contribution of the LSDA/GGA exchange approximation, so there will be less over-binding error etc. Furthermore, as DFT is a single determinant method it is unlikely to describe static correlation well, which is likely to be different for high-spin and low-spin states as well. [255, 256] In this thesis, the protocol will be to investigate the phenomena of interest (energies and structures of various configurations) using a range of functionals (BP86, BLYP, OLYP, OPBE, B3LYP, B3LYP* and SCAN), which span a spectrum of know behaviour in the context of transition metal spin state splitting. We can then identify issues where functional choice is particularly critical.

This group has previously used DFT to study the tricobalt EMACs and the results

do show some functional dependence, which have been discussed in Chapter 1. DFT has also been used to study the trinickel [16] and the neutral and single electron oxidised tricopper [20] EMACs. [257] Both have high d electron counts and metal-metal bond orders of zero. They are described using the DFT Kohn-Sham results and a subsequent calculation of the exchange coupling using a Heisenberg Hamiltonian. The metal-metal interactions are characterised by an antiferromagnetic superexchange interaction between the localised spin states on the terminal metal atoms mediated by the central metal atom in the nickel and copper complex cation or by the dpa ligand in the neutral copper complex. A similar analysis has been applied to CuPtCu and CuPdCu, [57] Pd_3 and NiPdNi, [258] MnNiMn, MnPdMn and MnPtMn [58] and longer Ni_5 and Ni_7 chains. [259, 260] The analysis was also extended to use CASPT2 in the initial calculation of the Cu_3 and Ni_3 complexes, from which more accurate exchange coupling constants could be extracted. [17] Indeed, given the intricate nature of the d orbital interactions and the potential for low-lying excited states, higher-level methods like CASPT2 could be more appropriate when DFT fails to correctly predict spin state splitting energies, and has often been used as a benchmark when experimental data is lacking. [229, 235, 261–264] A recent review benchmarked the performance of DFT, CCSD(T), CASPT2 and MRCISD+Q against a set of experimental results and showed that in general CCSD(T) performs most reliably, noting no functional provides a consistent performance across the data set. [265]

CASPT2 has been used to study many TM complexes, but usually focuses on systems with a single metal centre due to the high computational costs. [266] The Fe(II) porphyrin system has been very popular in the past, where understanding the exact spin state energetics has proven particularly problematic and there is a strong biological interest in the enzymatic activity. [264, 267–269] Results can still be variable, but generally the size of TM systems means CASPT2 offers a better performance/cost ratio [270] compared

to more expensive CI [271] and CC [272] [273] methods, although the new linear scaling DLPNO-CCSD(T) method from Nesse described in the theoretical techniques may improve its applicability. [274] CASPT2 has also been used to study transition- and actinide- and lanthanide-metal bonded systems, [275–279] including the trichromium EMAC, investigating the origin of the symmetric structure with a CN^- axial ligand and unsymmetric structures with NO_3^- axial ligand. [24] DFT had previously failed to find an unsymmetric minima, which is captured by the CASPT2 study. The active space used had 12 electrons in the 12 σ, π and δ_{xy} orbitals: a CAS(12,12) calculation. As a full CI calculation is done within the active space, the computational cost scales exponentially with the size of the space. The active space in the tricobalt EMACs would potentially be similar, but would also need to include the $\delta_{x^2-y^2}$ orbitals given their importance to the structural behaviour as described in the previous section. This would constitute an active space with 21 electrons in 15 orbitals, and the accepted limit with modern computational architectures is CAS(18,18). [280] Although chemical intuition can be a useful tool in the selection of the active space, in practice active spaces can be very sensitive and the calculated orbitals may not appear as expected, often rotating with the inactive and valence spaces as the algorithm optimises the energy.

One of the first CASPT2 treatments of a TM was to calculate the excitation energies of atomic nickel. [281] This work showed that a second set of 3d orbitals should be included in the active space, referred to as 3d'. They resemble a set of expanded 3d orbitals and allow the 3d electrons 'breathing room', which is important for the correct description of the correlation between the concentrated 3d electrons. They also showed the 4p orbitals needed to be included to correlate with the 4s electrons. In TM complexes the 4s orbital is much higher in energy and unoccupied so it, along with its correlating 4p orbitals, is not needed in the active space. The bonding and antibonding pairs for d orbitals

with M-L σ interactions have also been shown to have important correlation effects, and as described by Pierloot and Roos, a general rule for active space selection is to included these with the full set of d and d' orbitals to accurately describe ground and excited states in TM complexes. [266, 282–284] In the tricobalt EMAC the Co d-orbitals all have antibonding interactions with the surrounding ligands, with those of σ character formed by the cobalt d_{z^2} and $d_{x^2-y^2}$ orbitals with the halogen and nitrogen p_z orbitals. Including the M-L σ bonding/antibonding pairs would increase the active space size to CAS(31,20), while including the d' shell as well would mean a CAS(31,35) active space, which are both intractable for both CASSCF and CASPT2. Even with these orbitals CASPT2 has been shown to stabilise HS states by up to 5 kcal mol^{-1} [264, 272, 285]. This arises for the same reasons it does in HF calculations and the incomplete expansion of the wavefunction in CASSCF. Tuning the IPEA shift [286] applied to the PT2 treatment has been shown to improve results, but care must be taken not to accidently create a parameterised method by adjusting the applied shift until you reach the desired result. [287] More recently Pierloot showed that the inclusion of the $3s$ and $3p$ TM orbitals can correct the HS stabilition error. [288] On top of these orbitals we could consider the dpa ligands in the EMACs, which have aromatic rings that often show large correlations between the π and π^* orbitals. One possibility to extend the active spaces is the restricted active space (RAS) technique, [289] on which a PT2 treatment can still be applied (RASPT2). [290] In a RASSCF calculation the active space is portioned into three subspaces: RAS1, RAS2 and RAS3. RAS1 and RAS3 would normally be doubly occupied or unoccupied orbitals, respectively. In the calculation you define a certain number of electrons that are allowed to leave RAS1 and enter RAS2 or RAS3. You also define a number of electrons that are allowed to enter RAS3 from RAS1 or RAS2. It effectively acts like a truncated CI calculation, where the most important excitations are included in the expansion but the number total determinants

is decreased, where the final expansion consist of a full CI within all three spaces for all possible RAS1 and RAS3 excitations.

Despite its successes CASPT2 is still out of reach for many systems, and still suffers from a heavy user dependence and takes many years of use to master. Automatic selection of the correct active space is currently an active area of research as the community strives for a black box CASSCF technique, which should maximise computational efficiency. [291] Another active area takes more of a brute force approach to the study of larger systems, through the generation of larger active spaces by approximating the calculation of the CI coefficients using density matrix renormalistation group theory (DMRG) [292–296] or full configuration interaction quantum Monte Carlo (FCIQMC) in the stochastic-CASSCF technique. [297] Recent work using FCIQMC showed that for a model Fe(II)-porphyrin system the ideal active space, CAS(32,34), contained the ten $3d$ and $3d$' orbitals, four $4s4p$ metal orbitals, the entire ligand π system and the four sigma M-L bonding orbitals to properly describe the complex and the metal-ligand charge transfer. [298] The Fe(II) work had just a single metal centre and a simplified π system. Such an approach with either DMRG or FCIQMC would still be out of reach for the EMAC systems, which have 30 $3d$ and $3d$' orbitals not including the bonding-antibonding pairs, metal $4s4p$ or ligand π system. Instead we will adopt a more traditional approach, where we use CASSCF and RASSCF to restrict the active space to the most important orbitals to the static correlation and try to capture the remaining correlation with a CASPT2/RASPT2 treatment.

2.13 Concluding Remarks

Understanding the spectroscopy of TM complexes has been a notoriously difficult problem for quantum chemists. The most widely available tool for their study is DFT. Theoretically there exists an exact functional for DFT that gives the true ground state energy and density,

however its form is currently not known, and unlikely to be found in the near future. DFT predictions of spin state energetics in the literature shows variable performance for different exchange correlation functional approximations for different systems, particularly when comparing spin states of different multiplicities. [178, 226–233, 238–250, 299–304] DFT can do well when the spin states have similar correlation energies, and therefore the error in the total energy is the same in the ground and excited states. When the spin states have different correlation energies using a single determinant leads to poor excitation energies. Although DFT does attempt to incorporate electron correlation through the exchange-correlation functional, DFT still uses a single determinant wavefunction to construct the density.

High level wavefunction based techniques, such as CI, CC and the CASSCF, account for the electronic correlation in the proper way by expanding the wavefunction as a linear combination of excited state determinants. This expansion accounts for static correlation due to low-lying excited state configurations and dynamic correlation due to states with core electrons excited into the valence orbitals. When we consider the spectroscopy of a transition metal complex both of these effects must be considered in the ground and excited states. The true correlation energy is found using a FCI calculation, which expands the wavefunction in the full set of excited state determinants of the ground state HF wavefunction. This is very expensive, and in practice the expansion is curtailed in order to study chemical systems. CI and CC do this using the entire space but limit the excitations considered, CASSCF does this by limiting the space but considering all excitations within that space. As the complete space is not fully explored by these techniques they can still fail, and it is important to understand their limitations. CI and CC methods can do poorly in systems with strong static correlation where the reference wavefunction has a small weight ($<90\%$) in the total expansion. CASSCF does not account for any of the

correlation in the orbitals outside the active space, which are only treated at the HF level such that CASSCF suffers similar errors to HF theory, such as overstabilising high spin states. However, this can be compensated for using CASPT2, which uses multi-reference perturbation theory to account for the remaining dynamic correlation in the system.

Chapter 3

Computational Methodologies

3.1 ADF

All DFT results presented in this thesis use the Amsterdam Density Functional (ADF) 2016 and 2018 packages. [305–307] ADF will be used primarily to optimise the structures of the ground state and of a range of excited states. ADF utilises molecular symmetry to improve efficiency of calculations. One of the benefits of using ADF is that it enables us to specify α and β electron occupations of each irreducible representation of the molecular point group. The symmetry of the tricobalt EMAC ground state has been shown to belong to the D_4 point group in the experimental and theoretical work, which has five irreducible representations that allow a high degree of control over the electronic configuration. The unsymmetric excited states have C_2 symmetry (two irreducible representations) in the theoretical work, with a linear Co-Co-Co chain, however the experimental work shows a bent chain and no molecular symmetry (the C_1 point group and one irreducible representation). We will continue to impose the C_2 point group in the optimisation of unsymmetric states in order to specify electronic configurations more accurately. This will also aid the convergence of calculations.

Several studies benchmarking DFT results against experimental data for transition metal complexes give typical mean unsigned errors (MUE) in bond lengths (both M-M and M-L bonds) of ∼0.002 - 0.05 Å, and are considered quite accurate in their prediction of geometries. However, DFT performs variably for the calculation of bond energies, with MUE values falling in the range ∼0.3 - 20 kcal mol^{-1} per bond (0.001 - 0.87 eV) over a range of test databases for functionals considered in this thesis. [239, 242–250] As discussed in Chapter 2 the problems with using DFT in the context of spin state splitting energies are well known, and they can fail to such an extent that even the energetic ordering is incorrect. [178, 226–233, 238–250, 299–304] The energy of a particular state is, therefore, likely to depend on the functional choice, and the lowest energy state may not always be the same. Without being able to specify occupations the optimisation procedure would converge on the lowest energy state of a given multiplicity, which can therefore vary depending on the functional used. When we can specify the occupations, however, we are able to investigate a wider array of states with a variety of functionals so we can assess both their energies and structures to see which best correlate with experiment. Locating the minimum energy geometries of the different states is of particular importance when considering spin crossover processes, where the thermal occupation of the states influences the X-ray crystallography data at non-zero temperatures.

Calculations are performed on the isolated molecule in a vacuum. The periodic nature of the crystal is not accounted for, and any interactions of the EMAC with the solvate and other EMAC molecules are not considered explicitly. We have decided this in order to focus on understanding the metal-metal bonding and the cobalt d electron interactions, as well as to allow computations within reasonable time frames. In ADF an SCF cycle is considered to converge based on the commutator of the Fock matrix and the density matrix of the previous iteration, $[F, P]$. Convergence is reached when the

maximum element of the $[F, P]$ matrix is below 10^{-6} and the norm of the matrix (the sum of the squares of the elements) is below 10^{-5}. A damping factor of 0.03 is applied when updating the Fock matrix to ensure smooth convergence and a level shift of 0.02 Eh (Hartree atomic units) is applied to prevent the oscillation of electron density between orbitals at the Fermi energy. Geometry optimisations use a quasi-Newton approach in ADF, which uses the Hessian to update the geometry. [308–310] The geometry is considered converged when the energy difference with the previous geometry is below 0.001 Eh, the maximum element of the gradient vector is below 0.001 Eh Å^{-1}, the root mean square (RMS) of the gradient vector is less than 0.00066 Eh Å^{-1}, the maximum change in any nuclear coordinate is 0.01 Å and the RMS of all changes in nuclear coordinates is less than 0.0066 Å. Structures are verified as minima by calculating frequencies analytically, however any imaginary frequencies corresponding to the bending motion and breaking of C_2 symmetry are ignored. [311–315] Dy default ADF performs a Mulliken population analysis on the wavefunction at the optimised geometry. We will use this to inform us on how the spin density changes between the ground and excited states and how the substitution of the axial ligand effects atomic charges in the tricobalt EMACs. As we are only comparing values for the same family of complexes relative to each other the Mulliken population analysis is sufficient to indicate weather charge/spin densities increase or decrease. We will not be using the Mulliken charges to calculate absolute atomic partial charges. As the tricobalt EMACs have an odd number of electrons the electron configuration is always open-shell, and we will use unrestricted DFT (UDFT) in our calculations. Spin contamination often arises in unrestricted calculations as a results of the difference in the α and β molecular orbitals. The deviation from the exact $\hat{S}^2$ value suggests a contribution to the wavefunction from other spin states, for example when there are low-lying excited states during bond dissociation or in TM complexes, and can indicate whether a single determinant method can

properly capture the static electron correlation. Spin contamination where $\left\langle \hat{S}^2 \right\rangle$ differs from $\left\langle \hat{S}^2 \right\rangle_{\text{Exact}}$ by ∼10% are thought to be significant. [316] There is, however, some debate as to whether spin contamination is meaningful in DFT. [317–321] DFT only uses the wavefunction as a tool to construct the density and spin contamination may arise from the approximation to the correlation energy in the exchange-correlation functional. In general UDFT results show lower amounts of spin contamination than corresponding UHF calculations. It is thought to derive from the exchange term, and hybrid functionals also typically show higher levels of spin contamination compared to calculations using pure LDA or GGA functionals.

ADF was originally developed as a DFT code, with no intention to use any wavefunction (HF and post-HF) methods. As DFT does not require the calculation of any complicated multi-centre integrals, CGTO basis sets were not deemed necessary, and ADF uses STO basis sets. The main benefit of this is that the basis sets bare a closer resemblance to the hydrogenic AOs they describe. Since this decision was made the use of hybrid functionals has become commonplace. Despite initial resistance, ADF has incorporated hybrid functionals into the package, however, calculation of the HF exchange energy requires the calculation of multi-centre integrals, which takes a long time using the STO basis sets. The computational cost of using hyrbid functionals with ADF is therefore much higher than pure functionals (LDA, GGA, meta-GGA). For hybrid functionals the resolution of the identity (RI) approximation is used for the calculation of the HF exchange energy. [322] The RI method uses a set of auxilary functions to fit the two-electron functions in the multi-centre integrals to approximate the HF exchange matrix more efficiently.

Frozen core basis sets are used in nearly all DFT calculations with ADF. Specifically we use double zeta polarised (DZP) basis set for hydrogen, DZP basis sets for carbon, nitrogen, fluorine, chlorine and bromine frozen up to 1s, 1s, 1s, 2p and 3p respectively and

triple zeta polarised (TZP) basis sets for cobalt and iodine frozen up to 2p and 4p, respectively (a TZP basis set is used for iodine as a DZP is not available). The only exception is when using the SCAN functional, which requires the use of all electron basis sets. SCAN also requires the use of the Zero Order Regular Approximation (ZORA) to treat relativistic effects, [323–327] which is used in combination with the ZORA all electron basis sets. [328] SCAN was only implemented into ADF in the 2018 package, and by this time we had already completed most of the DFT calculations without treating relativistic effects, with results comparable to experiment. Results for all functionals other than SCAN do not include relativistic effects. We have tested the effect by optimising the geometries of the symmetric doublet ground state and unsymmetric quartet excited state with BP86. The test calculations use ZORA with ZORA basis sets for the fluoride, chloride, bromide and iodide tricobalt EMACs. The ZORA basis sets use the frozen core approximation to match the original BP86 results without ZORA (H, C, N, F, Cl, Br, I, Co = DZP, DZP.1s, DZP.1s, DZP.1s, DZP.2p, DZP.3p, TZP.4p, TZP.2p). The structures show that there is a small contraction in nearly all bond lengths, with the exception of the Co-F distances. Both Co-Co distances decrease by ∼0.002 - 0.004 Å in the ground state, while in the unsymmetric excited state the shorter Co-Co distance decreases by ∼0.001 - 0.002 Å and the longer by ∼0.010 - 0.014 Å. Co-N bonds decrease by ∼0.005 - 0.013 Å, with the largest decreases on the isolated Co in the unsymmetric state. Variation in the Co-X (X = F, Cl, Br, I) distances are largest, decreasing by ∼0.011 - 0.026 Å for Co-X (X = Cl, Br I), but only increasing by ∼0.001 - 0.003 Å for Co-F. The energy difference between the two states increased when relativistic effects were included, by ∼0.035 - 0.048 eV.

To begin, as in the original theoretical work, I will use the BP86 functional to optimise geometries. BP86 is among the best performing functionals for predicting geometries of transition metal complexes, [243, 244, 246, 282] especially when considering

the performance/cost ratio, and indeed in previous studies of EMACS the agreement with experiment has been encouraging. [29, 102, 113, 118] However, BP86 struggles to reproduce bond energies with the same consistency as higher level functionals. Given the nature of this investigation, specifically into the nature of a change in spin state, the relative energies of the electronic states will be of vital importance. I will, therefore, also consider three other GGA functionals: BLYP, OLYP and OPBE, as well as one meta-GGA functional: SCAN, and two hybrid functionals: B3LYP and B3LYP*. Full geometry optimisations are performed with each functional to investigate the effect on the structure. This range of functionals has been chosen to represent different families of density functional that have shown success in transition metal-based systems in previous studies, as discussed in the Chapter 2. Other functionals were tested, including TPSS, M06-L and MN15-L, but they require tighter convergence criteria in ADF and the increased computational cost meant that we were unable to converge the majority of calculations within reasonable time. We also do not use any double-hybrid functionals for the same reason, with the cost of hyrbid functionals (B3LYP and B3LYP*) in ADF already quite high, often requiring multiple restarts in our calculations.

3.2 OpenMolcas

CASSCF [156–158] and CASPT2 [159] calculations were performed using the OpenMolcas package [329]. We use the DFT optimised geometries with ADF and calculate the single point energies of the ground and excited states. We use a combination of CASSCF and RASSCF to generate a multi-configurational wavefunction for each state, followed by CASPT2 to calculate the energy. CASSCF is a MCSCF method that is used to treat strong static correlation within a subspace of active orbitals, and is particularly important in systems with low-lying excited states. CASPT2 is a multi-reference method which is

applied to the multi-configurational CASSCF reference function to recover the dynamic correlation. As discussed in Chapter 2, CASSCF can be combined with the DMRG or stochastic FCIQMC techniques to allow the calculation of larger active spaces. However, such a reference wavefunction may still not include all the important correlating orbitals but would be too complex for a subsequent CASPT2 treatment.

MCSCF techniques combine a FCI expansion within the active space and an SCF cycle to update the orbitals. The orbital optimisation is performed using the super-CI method [330] with the Davidson method [331] to calculate the FCI wavefunction. Convergence of the FCI wavefunction is achieved when the norm of the residual (RNORM) is below 10^{-6}, where the residual is defined by the difference in the input and output coefficients of the CI expansion. CASSCF convergence occurs when the change in energy, the orbital rotation matrix and energy gradient values are below 10^{-8}, 10^{-4} and 10^{-4}, respectively. The CASPT2 energy also converges when RNORM is below 10^{-6}. The Douglas–Kroll–Hess Hamiltonian is used to include scalar relativistic effects, which is implemented in OpenMolcas over ZORA. [332] The two electron integral matrices are Cholesky decomposed, where any elements below the threshold value of 10^{-6} Eh are neglected. [333] An ionisation potential electron affinity (IPEA) shift of 0.25 Eh is imposed on the zeroth-order Hamiltonian in CASPT2 calculations of the first-order wavefunction and the second-order energy to correct the overestimation of the correlation energy in open-shell systems. [286] This also helps to prevent intruder states from causing energy divergences.

The atomic natural orbitals optimized for relativistic corrections and core correlation (ANO-RCC) basis set is used with the following contractions Co.21s15p10d6f4g2h.5s4p2d1f, Br.20s17p11d4f2g.5s4p2d, C.14s9p4d3f2g.3s2p, N.14s9p4d3f2g.3s2p and H.8s4p3d1f.2s. ANO-RCC is CGTO type basis set, and the contractions are equivalent to either DZ (Br, C, N, H) or DZP (Co) basis sets. OpenMol-

cas uses natural orbitals and natural occupation numbers, first introduced by Löwdin, to interpret the wavefunction. [334] The natural orbitals correspond to the eigenvectors or the first order reduced density matrix, and the occupation numbers to the eigenvalues. In a restricted wavefunctions occupation numbers take the values 0 or 2, while in unrestricted and multi-configurational wavefunctions occupation numbers can have values between 0 and 2, where larger occupations indicate a greater contribution to the wavefunction.

3.3 ORCA

MP2 and DLPNO-CCSD(T) [154, 155] calculations are carried out using the ORCA package. [335] Again we use structures optimised at the DFT level with ADF to perform single point calculations. MP2 and DLPNO-CCSD(T) are both single-reference methods, and DLPNO-CCSD(T) specifically requires a restricted reference wavefunction. When this cannot be calculated using a restricted open-shell technique, quasi-restricted orbitals (QRO) can be used. The QROs are formed by taking the natural orbitals of the unrestricted calculation and using those with occupations close to 1 and 2 to construct the ground state determinant, ignoring those with occupations close to zero. [336]

Calculations use a def2-TZVP for the cobalt, nitrogen and halogen atoms and def2-SVP for carbon and hydrogen. The def2 basis set is also a CGTO type. Taking the bromide complex as an example, the basis set described gives a total of 1323 basis functions, which is most likely out of reach for a conventional CCSD(T) treatment (limited to ~1500 basis functions [148]). This is why we chose to use Neese's DLPNO-CCSD(T) technique, which is an efficient approximation that recovers nearly all (99.8%) of the CCSD(T) correltaion energy for larger systems. [154, 155] Both MP2 and DLPNO-CCSD(T) caluclations are considered convereged when RNORM is below 10^{-5} and the change in energy is below 10^{-7}. We use the RI approximation with auxiliary functions optimised for the

Coulomb and exchange integrals (RIJK) in the calculation the reference function. We also use the RI approximation in the MP2 and DLPNO-CCSD(T) calculations, where the auxiliary functions are optimised for correlation calculations (RIC)

Chapter 4

A DFT and MCSCF Study of the $Co_3(dpa)_4Br_2$ Symmetric Form

4.1 Introduction

When considering the question of what is the most stable electronic configuration of the tricobalt EMACs, the vast array of structural and magnetic information summarised in Chapter 1 does not point clearly to the dominance of a single state. In this chapter we will focus on the symmetric structures of the bromide complex, $Co_3(dpa)_4Br_2$. In solution Clérac and co-workers showed the structure has perfect D_4 symmetry, shown in Figure 4.1, exhibiting similar ^1H NMR behaviour to the chloride complex in solution. [37] The NMR spectra show four distinct peaks corresponding to the four protons on the pyridine moieties of the dpa ligands. Further corroboration of this interpretation of the NMR spectra comes from the corresponding spectrum of $Co_3(dpa)_4ClBr$, a contaminant in the $Co_3(dpa)_4Br_2$ solution, which shows eight distinct peaks, split by the different chemical environments at either end of the EMAC and consistent with C_4 symmetry.

In the same work, Clérac *et al.* showed that in the crystalline phase the bromide

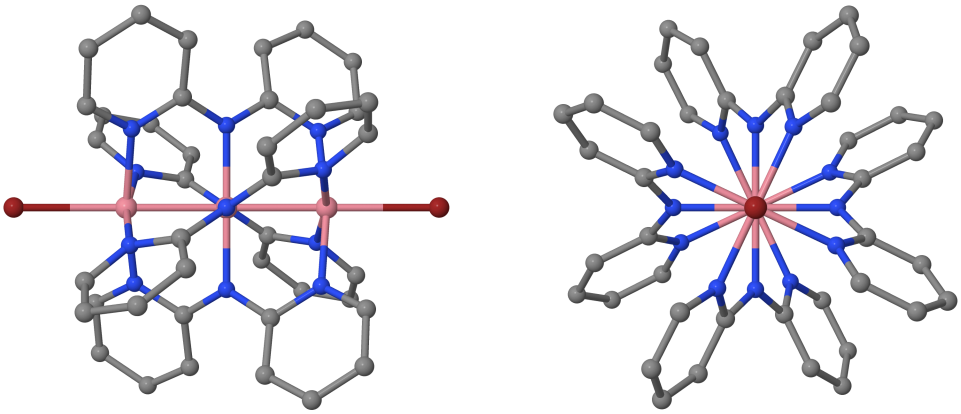

(a) (b)

Figure 4.1: D_4 symmetric $Co_3(dpa)_4Br_2$ structure discovered by Clérac *et al.* [37] viewed down the (a) x-axis and (b) z-axis.

complex maintains a symmetric structure with both the dichloromethane and hexane solvates, $Co_3(dpa)_4Br_2{\cdot}CH_2Cl_2$ and $Co_3(dpa)_4Br_2{\cdot}$Hexane. The temperature dependence of both structures is shown in Figure 4.2. The $Co_3(dpa)_4Br_2{\cdot}CH_2Cl_2$ crystal shows an increase in the Co-Br bond lengths as the temperature is increased, with little change in the Co-Co and terminal Co-N bonds. The only example of a crystal of the chloride complex that shows an increase in the Co-Cl distance is in the $Co_3(dpa)_4Cl_2{\cdot}CH_2Cl_2$ system at low temperatures, although it shortens again at higher temperatures. [35] These systems behave somewhat anomalously: In every other crystal, either symmetric or unsymmetric, the Co-Cl/Br distances always decrease with temperature. This suggests quite clearly that different excited states may be thermally populated in the different crystalline phases. The $Co_3(dpa)_4Br_2{\cdot}$Hexane crystal shows a lengthening of the Co-Co and terminal Co-N bonds and a shortening of the Co-Br bond as the temperature increases. A similar behaviour is observed in the symmetric crystals of the chloride complex: $Co_3(dpa)_4Cl_2{\cdot}$THF, $Co_3(dpa)_4Cl_2{\cdot}$Hexane and $Co_3(dpa)_4Cl_2{\cdot}$Benzene. [36] This behaviour also maps onto the behaviour of the unsymmetric crystals, which see the Co-Co and terminal Co-N distances

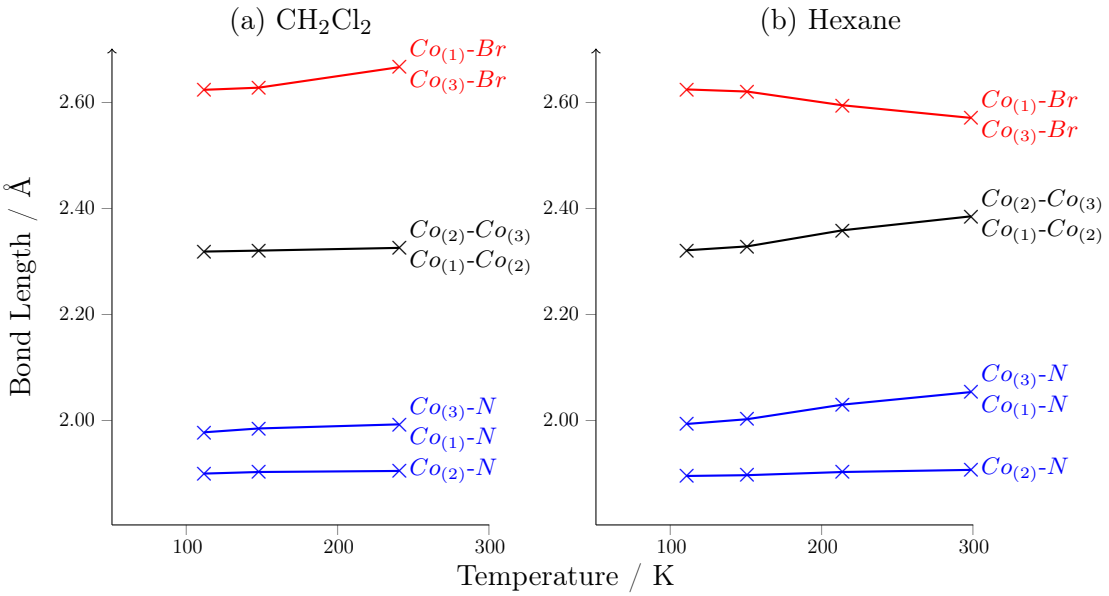

Figure 4.2: Bond lengths for the (a) $Co_3(dpa)_4Br_2{\cdot}CH_2Cl_2$ and (b) $Co_3(dpa)_4Br_2{\cdot}$Hexane crystals from 111 – 240 and 110 – 298 K, respectively. [37]

increase and Co-X distance decrease, but only at one end of the tricobalt chain.

In the initial work Clérac *et al.* only investigated the temperature dependence of the magnetic susceptibility in $Co_3(dpa)_4Br_2{\cdot}CH_2Cl_2$. The curve showed a similar profile to $Co_3(dpa)_4Cl_2{\cdot}CH_2Cl_2$, suggesting a similar spin crossover process occurs in the bromide analogue. As with the chloride, they showed that at low temperatures a LS doublet state dominates the spin equilibrium, with a g value of 2.35, however the HS state multiplicity was undetermined due to a lack of saturation of μ_{eff}. One reason for this is that the work showed the spin crossover process did not begin until a higher temperature compared to the chloride crystal (∼200 vs. 175 K), as well as showing a more gradual transition. [35] Although they do not fit the magnetic data to an ideal spin crossover process, this suggests that the spin crossover temperature will be higher in the bromide complex, and that the HS state should have a greater excitation energy. The work on the chloride crystal showed that assigning the HS state as a quartet or sextet was not straightforward due to the lack of saturation at high temperatures (with the sextet only marginally preferred), and

this is made more difficult for the bromide crystal by the apparent higher spin crossover temperature. In the latest work from Hillard the magnetic data are fit to an ideal spin crossover model from a doublet to a quartet, as described in the Chapter 1. [38] They have done this for all their new crystals and for all those that were previously undetermined. By fitting the data they are able to define a set of thermodynamic parameters, ΔH, ΔS and $T_{\frac{1}{2}}$, for the spin crossover process, where ΔH = 14.9 kJ mol^{-1}, ΔS = 34.5 J K^{-1} mol^{-1} and $T_{\frac{1}{2}}$ = 431 K and ΔH = 8.2 kJ mol^{-1}, ΔS = 40.4 J K^{-1} mol^{-1} and $T_{\frac{1}{2}}$ = 203 K for the $Co_3(dpa)_4Br_2{\cdot}CH_2Cl_2$ and $Co_3(dpa)_4Br_2{\cdot}$Hexane crystals, respectively, confirming the high crossover temperature for $Co_3(dpa)_4Br_2{\cdot}CH_2Cl_2$.

4.2 Aims and Objectives

The fact that the temperature-dependence of the structural data varies dramatically from one compound to another suggests that the three state model presented by McGrady and Pantazis in 2006 is at best a simplification, and it cannot capture the full breadth of behaviour exhibited by the wider family of tricobalt EMACs. [102] The complete set of experimental data suggests that there is a complex relationship between structure, crystalline environment and spin state. Indeed, the recent work from Hillard specifically implicates an excited quartet state that remains symmetric, a feature that was not present in the previous model. [38] The purpose of this chapter is to conduct a wider exploration of the potential energy surface for these Co_3 EMACs, including more possible electronic states that may contribute to the measured structural and magnetic properties under various conditions.

We will first present initial results using DFT with the BP86 functional to optimise the energies and geometries of the electronic states. The original work by McGrady and Pantazis highlighted differences in the single point energies calculated using the B3LYP

and VS98 functionals - in particular unsymmetric states of quartet multiplicity are strongly stabilised relative to the symmetric doublets by hybrid functionals. Given the ongoing discussion of the reliability of density functional theory, [226–233, 239–241, 247, 248, 299–304] we will also consider how functional choice influences the structures of the states and the energetic balance between them. We then conduct the first MCSCF and multi-reference study of the tricobalt system, using CASSCF and CASPT2. Unlike DFT, post-HF treatments do not suffer any functional dependencies in the calculation of spin state splitting energies. Their accuracy depends directly on the user input, specifically on the way the expansion of the multi-configurational wavefunction is truncated, and also on the choice of basis set. This will also provide a further test of DFT beyond comparison with experiment.

This chapter will focus solely on the symmetric structure, which is computed to be the ground state in all previous studies of the analogous chloride complex, at least of the isolated gas-phase molecule at 0 K. [29, 101, 102] The high symmetry allows for tight control of the electronic configuration, and because the solution-phase data indicate a D_4 symmetric structure, a detailed survey of this form logically precedes the investigation of the structures that arise under the influence of the crystalline environment. We will develop a systematic approach to the search for low-lying symmetric excited states, before investigating the unsymmetric structures in Chapters 5 and 6. The initial focus is on the bromide complex as complement to previous work, which has focussed primarily on the chloride analogue, but the work is expanded to include all known halogen complexes, spanning F, Cl, Br and I, in Chapter 7.

4.3 Results and Discussion

4.3.1 DFT Analysis: BP86

Symmetric Ground State

Subject to the constraint of D_4 symmetry (i.e equal Co-Co and terminal Co-N bond lengths), the most stable state of $Co_3(dpa)_4Br_2$ proves to have $^2A_2$ symmetry. The frontier MO diagram is presented in Figure 4.3, below which the optimised Co-Co, Co-N and Co-Br bond lengths are given, which are in excellent agreement with the low-temperature structures of the hexane and dichloromethane solvates (see Table 4.1 page 136). The MO diagram shows the same general features identified in the schematic shown in Chapter 1 (Figure 1.7 page 9). As previously described, the MOs can be considered as the bonding, nonbonding and antibonding combinations of the cobalt d orbitals. The orbitals are also split into separate spin-α and spin-β components due to the presence of a single unpaired electron.

The d_{z^2} (where the z-axis is defined as the Co-Co-Co) orbitals have local σ symmetry with respect to the Co-Co bonds, and transform as a_1 (σ and σ^*) or a_2 (σ^{nb}) within the D_4 point group. The σ orbital (too low in energy to be included in the MO diagram) is doubly occupied, the σ^{nb} ($38a_2$) singly occupied and the σ^* orbital ($41a_1$) is unoccupied. The splitting of the α and β electron energies is most pronounced in the σ^{nb} orbital, as it contains the unpaired electron. Linear combinations of the d_{xz} and d_{yz} orbitals form a set of doubly degenerate orbitals with local π symmetry, all of which transform as e under D_4 symmetry. Only one of the degenerate pairs are shown in the MO diagram, with the other related by a 90° rotation around the Co-Co-Co axis. The π ($61e$), π^{nb} ($60e$) and π^* ($62e$) are all doubly occupied. The bonding orbitals mix with both the dpa ligand orbitals and the nonbonding orbitals of opposite orientation, which raise their energy above the

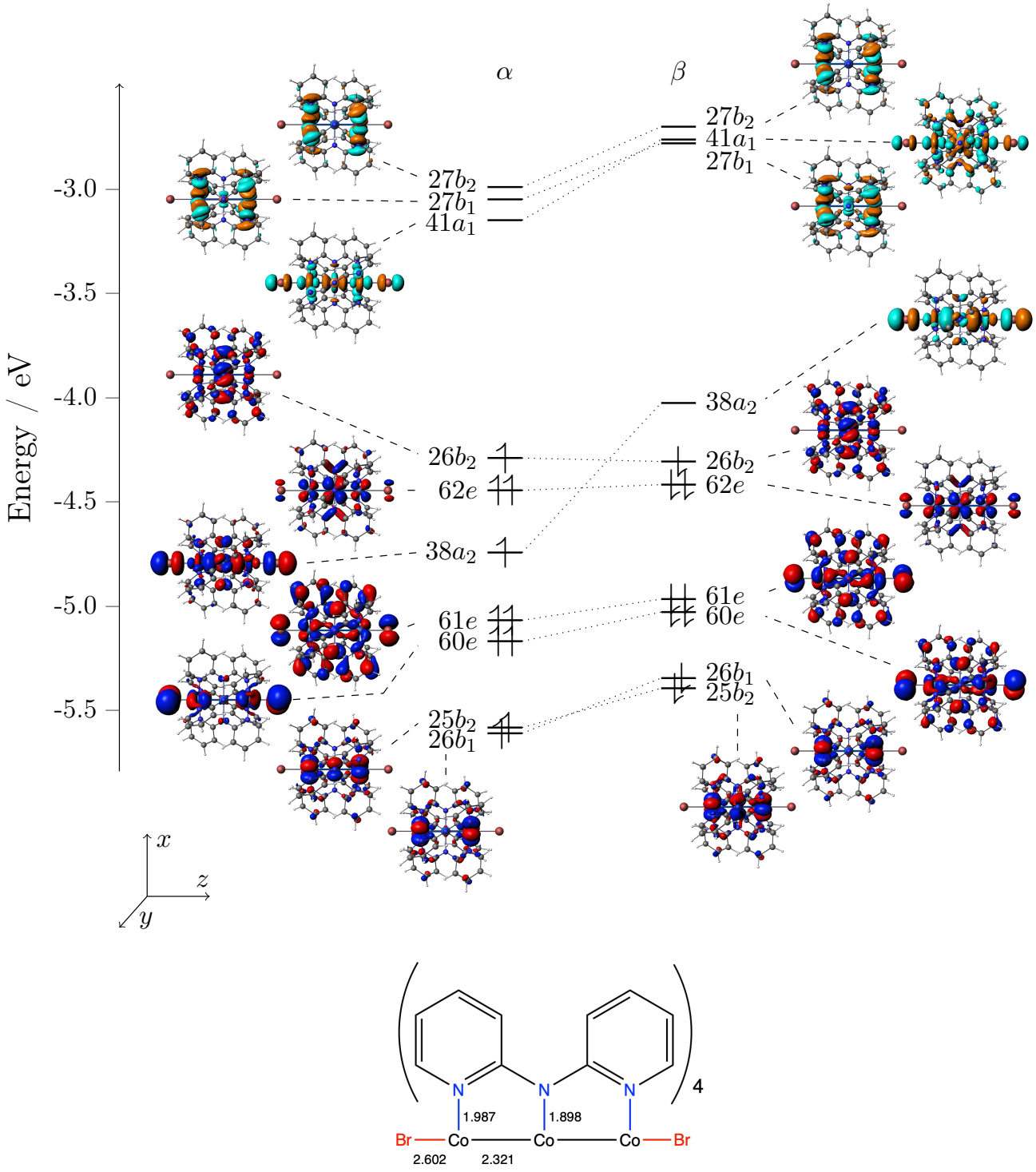

Figure 4.3: MO diagram showing the Kohn-Sham orbital isosurfaces of electron density 0.02 Å^{-1} and schematic structure showing Co-Co, Co-N and Co-Br bond lengths (Å) of the D_4 symmetric bromide complex $^2A_2$ ground state.

nonbonding orbital. There are two distinct types of orbitals with local δ symmetry. The $\delta_{x^2-y^2}$ orbitals (where the x and y axes are defined locally to be aligned along the Co-N bonds on each Co centre) transform as b_1 ($\delta_{x^2-y^2}$ and $\delta^*_{x^2-y^2}$) or b_2 ($\delta^{nb}_{x^2-y^2}$), while the δ_{xy} orbitals transform as b_2 (δ_{xy} and δ^*_{xy}) or b_1 (δ^{nb}_{xy}) under D_4 symmetry. The $\delta_{x^2-y^2}$ ($27b_1$), $\delta^{nb}_{x^2-y^2}$ ($27b_2$) and $\delta^*_{x^2-y^2}$ (too high in energy to be included in the MO diagram) orbitals are all unoccupied. The δ^{nb}_{xy} ($25b_2$), δ^{nb}_{xy} ($26b_1$) and δ^*_{xy} ($26b_2$) are all doubly occupied.

The σ and π orbitals are all delocalised over the tricobalt chain, and have (σ and π) antibonding Co-Br interactions. The weak δ interactions between the cobalt atoms are made weaker still by the helical twist in the dpa ligand, which decreases the orbital overlap and the δ orbitals do not show the delocalisation seen in the σ and π sets. The δ^*_{xy} is localised primarily on the central Co, whilst the $\delta_{x^2-y^2}$ and $\delta^{nb}_{x^2-y^2}$ are localised on the terminal Co. The $\delta_{x^2-y^2}$ orbitals all have strong antibonding Co-N interactions with the dpa ligand of local σ symmetry, while the δ_{xy} have weak Co-N antibonding interactions of local π symmetry. In Chapter 1 we described the importance of the Co-N antibonding interaction in the $\delta_{x^2-y^2}$ orbitals to the experimentally observed variation in the Co-N bond lengths.

Overall the π and δ_{xy} frameworks are fully occupied, and the $\delta_{x^2-y^2}$ completely vacant, and so the Co-Co bonding can be thought of as a three-centre three-electron bond distributed over the σ manifold, precisely as has been described for the chloride analogue.

Symmetric Excited State Configurations

We would expect low-lying excited states to correspond to low energy excitations within the frontier orbitals. The occupied frontier orbitals include the σ^{nb} ($38a_2$), π^* ($62e$) and δ^*_{xy} orbitals ($26b_2$). In the vacant manifold, the σ^* ($41a_1$), $\delta_{x^2-y^2}$ ($27b_1$) and $\delta^{nb}_{x^2-y^2}$ ($27b_2$) orbitals are found approximately 1.5 eV higher in energy. Using the ground-state molecular

orbital array shown in Figure 4.3, we can systematically construct a range of excited configurations that may contribute to the properties of the molecule at higher temperatures. These configurations, which span doublet, quartet, sextet and octet multiplicities, are summarised schematically in Figures 4.4-4.6.

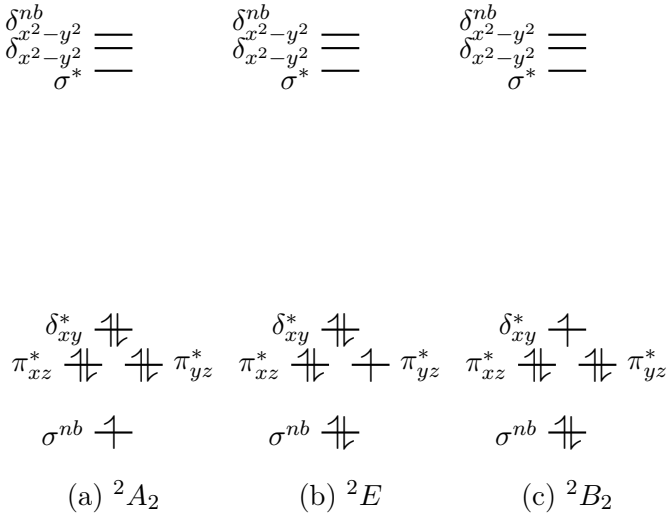

(a) $^2A_2$ (b) ^2E (c) $^2B_2$

Figure 4.4: Frontier electron configurations of the bromide complex (a) $^2A_2$ ground state and predicted low energy doublet states (b) ^2E and (c) $^2B_2$.

Doublet configurations are obtained from the $^2A_2$ ground state by permutation of the unpaired electron between the σ^{nb}, π^* and δ^*_{xy} orbitals. In the ^2E state the unpaired electron is in an orbital of π symmetry, and corresponds to one of the low-lying doublets found by Bénard and Rohmer [101] and the ^2B state presented by McGrady and Pantazis, where C_2 symmetry labels were used rather than D_4. The previous use of C_2 labels was motivated by the fact that any doubly degenerate E state is inevitably subject to a Jahn-Teller distortion which will reduce the symmetry from D_4. However, in practice this distortion is small and does not have a major impact on our findings, so for convenience we retain the labelling according to the irreducible representations of the D_4 point group. In the $^2B_2$ the unpaired electron is in an orbital of δ symmetry, and was also presented in the work of Bénard and Rhomer. It is assumed that any doublet configuration involving

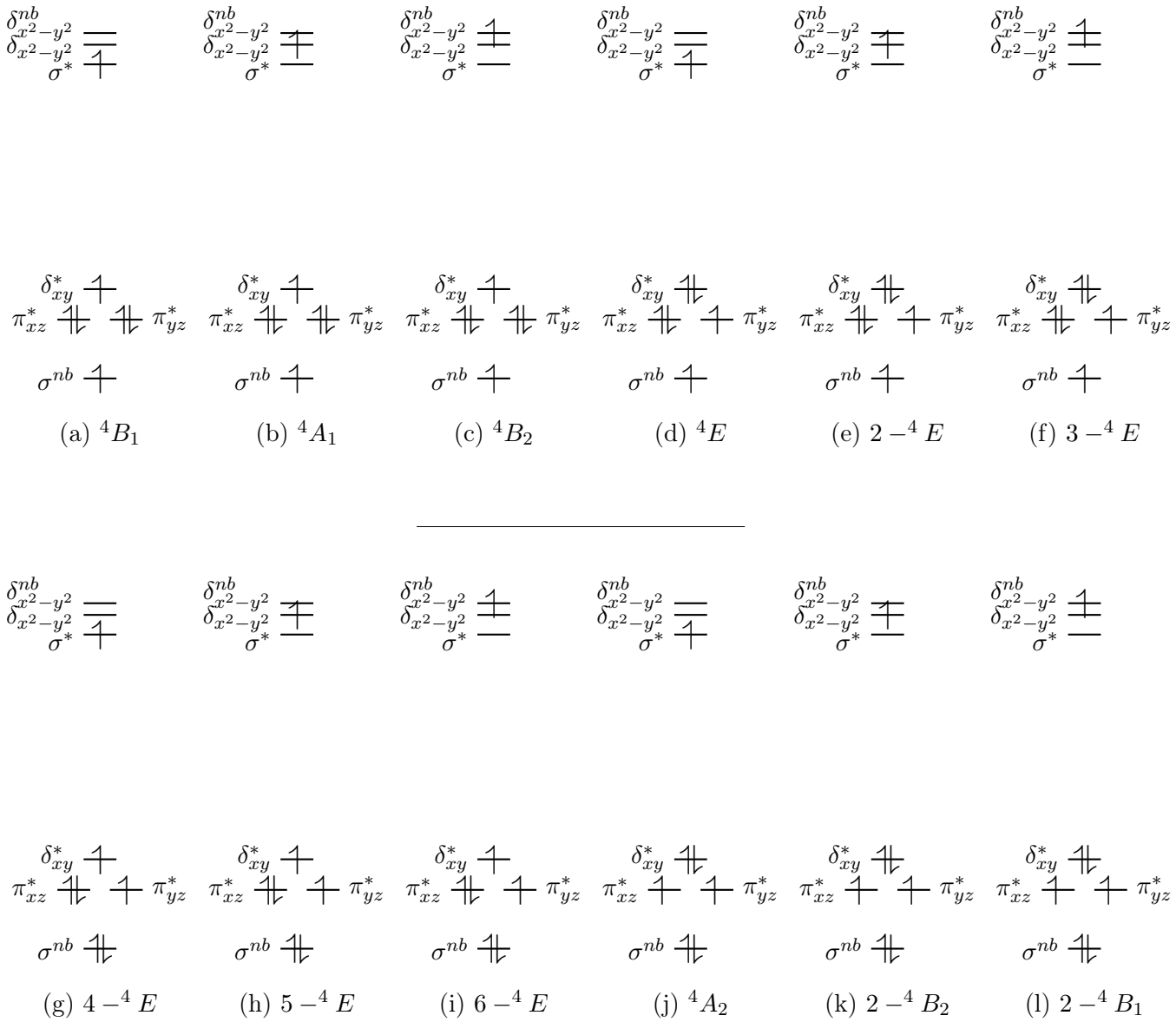

Figure 4.5: Frontier electron configurations of the bromide complex predicted low energy quartet states (a) $^4B_1$, (b) $^4A_1$, (c) $^4B_2$ (d) ^4E, (e) 2-^4E, (f) 3-^4E, (g) 4-^4E, (h) 5-^4E, (i) 6-^4E, (j) $^4A_2$, (k) 2-$^4B_2$ and (l) 2-$^4B_1$.

excitation into the σ^*, $\delta_{x^2-y^2}$ or $\delta^{nb}_{x^2-y^2}$ orbitals would be too high in energy to contribute to the properties under realistic conditions.

Quartet configurations are obtained from the excitation of a β electron into an α hole in either the σ^*, $\delta_{x^2-y^2}$ or $\delta^{nb}_{x^2-y^2}$ orbitals of the doublet configurations. Figures 4.5a-c show excitations from the $^2A_2$ ground state where the δ^*_{xy} electron is excited into each of the high-lying orbitals, and Figures 4.5d-f where the π^* electron is excited. Figures 4.5g-l show

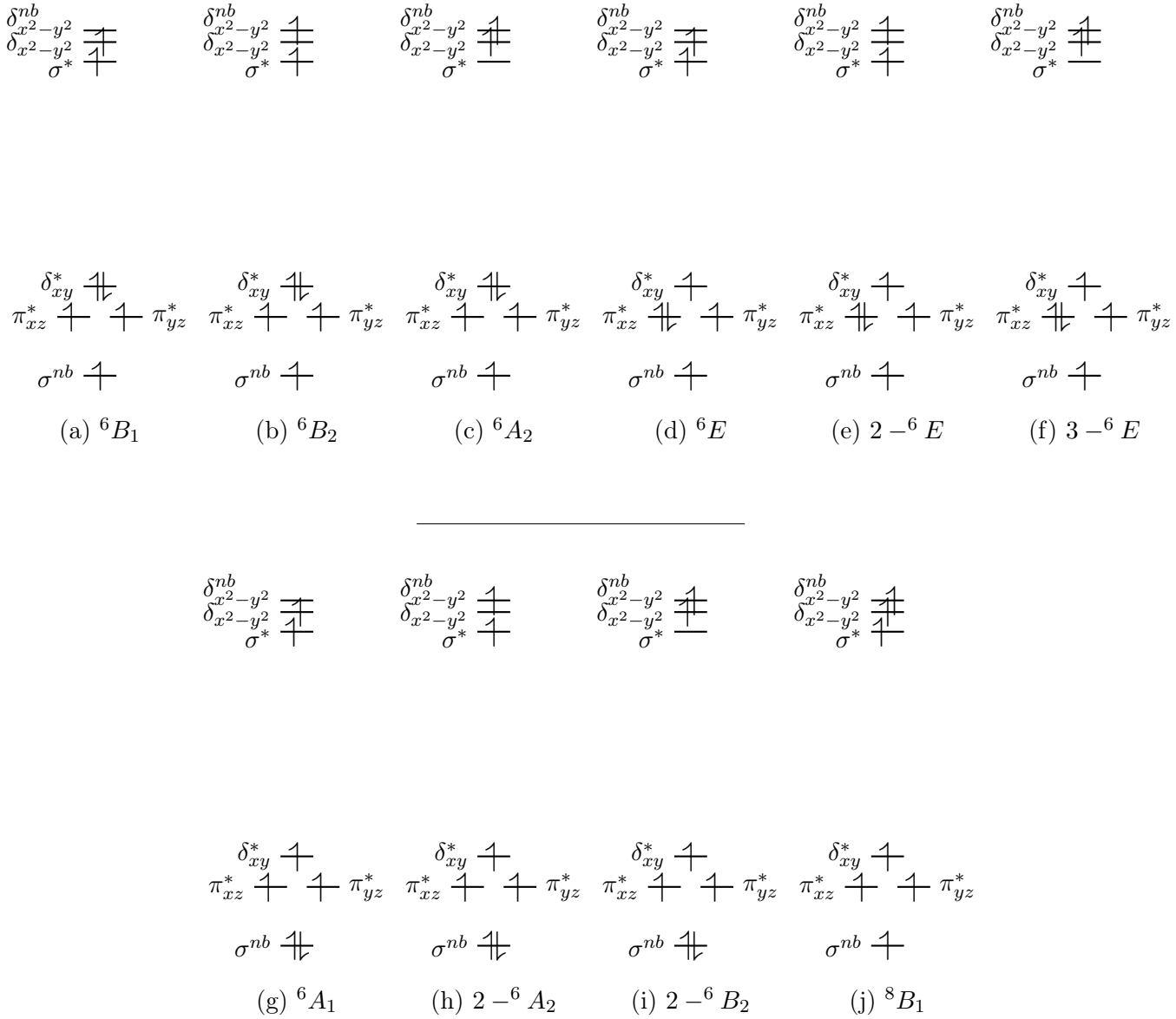

(a) $^6B_1$ (b) $^6B_2$ (c) $^6A_2$ (d) ^6E (e) $2\,{}^6E$ (f) $3\,{}^6E$

(g) $^6A_1$ (h) $2\,{}^6A_2$ (i) $2\,{}^6B_2$ (j) $^8B_1$

Figure 4.6: Frontier electron configurations of the bromide complex predicted low energy sextet and octet states (a) $^6B_1$, (b) $^6B_2$, (c) $^6A_2$, (d) ^6E, (e) 2-^6E, (f) 3-^6E, (g) $^6A_1$, (h) 2-$^6A_2$, (i) 2-$^6B_2$ and (j) $^8B_1$.

excitations from the ^2E state where the δ^*_{xy} or π^* electron is excited. The $^4A_1$ and 2-^4E configurations shown in Figures 4.5b and 4.5e correspond to the ^4A state found by Bénard and Rohmer [29] and the ^4B state found by McGrady and Pantazis, [102] respectively, while the remaining states have not previously been investigated. Sextet configurations are obtained from a further excitation of a β electron into an α hole in either the σ^*, $\delta_{x^2-y^2}$ or $\delta^{nb}_{x^2-y^2}$ orbitals of the quartet configurations. The octet configuration can be obtained

by one final excitation such that there are no β electrons in the frontier space and every α orbital is singly occupied. No sextet or octet states have previously been investigated in the theoretical work.

Excited State Structures

The geometries of each of the configurations shown in Figures 4.4-4.6 have been optimised using the BP86 functional, and the relevant structural data are collected in Table 4.1, alongside the corresponding data for the symmetric bromide crystals (hexane and dichloromethane solvates) at low and high temperatures. Given the symmetric nature of the structures we only report the $Co_{(1)}$-$Co_{(2)}$, $Co_{(1)}$-Br, $Co_{(1)}$-N and $Co_{(2)}$-N bond lengths. The values in parenthesis correspond to the changes in bond length relative to the $^2A_2$ ground state (for the theoretical data) and as the temperature is increased (for the experimental data). The primary purpose of presenting the structural details in this way is so that we can establish which excited states, if thermally populated, could give rise to the temperature-dependent properties observed in the two crystals. Specifically, the fact that in the hexane solvate the Co-Br bond lengths decrease with temperature while in the dichloromethane analogue they increase suggests that different excited states are being populated in the two cases. The trends in bond lengths map logically onto the shapes of the vacant orbitals, and the Co-Br bond lengths are a particularly sensitive reporter of the electronic configuration. For example, in the $^2A_2$ ground state the σ^{nb} orbital, with Co-Br antibonding character, is singly occupied, with Co-Br distances of 2.597 Å. In the other doublets, in contrast, it is doubly occupied and the Co-Br bond length is substantially elongated above 2.7 Å. In contrast, in the 2-^4E and 3-^4E states, while the σ^{nb} orbital remains singly occupied, an electron has been removed from the π^* orbital, which also has substantial Co-Br π^* character. As a result, the Co-Br bond length is even shorter than

in the $^2A_2$ state, at ∼2.5 Å. This trend is most extreme in the $^6A_2$ state, with a Co-Br distance of 2.44 Å, where the σ^{nb} and both components of π^* are singly occupied. At the opposite extreme, the longest Co-Br bond is found in the 4-^4E state (2.904 Å), where the σ^{nb} orbital is doubly occupied and the σ^* orbital is also singly occupied. The Co-Co bond lengths are less sensitive to the electronic configuration due to the constraining effects of the dpa ligands, but nevertheless show some distinct patterns. For example, depopulating the π^* orbital results in a small but distinct contraction (compare $^2A_2$ vs ^2E) while the longest Co-Co bonds come in cases where the σ^* orbital is populated. The terminal Co-N bond lengths are also useful indicators of electronic configuration: where the $\delta_{x^2-y^2}$ and $\delta^{nb}_{x^2-y^2}$ contain no electrons the bonds are in the region of 2.0 Å, while the presence of one or two electrons leads to an elongation to ∼2.06 Å and 2.12 Å, respectively. All of the doublet states have short Co-N bonds, while all the sextet and octet states show a substantial Co-N elongation.

Based on the trends discussed in the previous paragraph, the elongation of the Co-Co and terminal Co-N bonds and the contraction of the Co-Br bonds at elevated temperatures in the $Co_3(dpa)_4Br_2$·Hexane crystal appear consistent with the thermal population of the $^4A_1$ and $^4B_2$ quartet states or the $^6B_1$, $^6B_2$, 3-^6E or 2-$^6B_2$ sextet states. These states all have at least one electron in either of the $\delta_{x^2-y^2}$ or $\delta^{nb}_{x^2-y^2}$, which drives the Co-N elongation. Conversely, the elongation of the Co-Co, Co-N and Co-Br bonds in $Co_3(dpa)_4Br_2$·CH_2Cl_2 are most consistent with the $^4B_1$ and ^4E states, which both have an electron in the σ^* orbital. As we have previously noted the behaviour of the dichloromethane solvate is highly unusual, indicating the crystalline environment created by the solvate plays an important role in tuning the accessibility of the different excited states.

	$Co_{(1)}$-$Co_{(2)}$	$\Delta Co_{(1)}$-$Co_{(2)}$	$Co_{(1)}$-Br	$\Delta Co_{(1)}$-Br	$Co_{(1)}$-N	$\Delta Co_{(1)}$-N	$Co_{(2)}$-N	$\Delta Co_{(2)}$-N
Hexane 110 K	2.319	-	2.623	-	1.991	-	1.893	-
Hexane 298 K	2.383	(0.064)	2.569	(-0.054)	2.051	(0.060)	1.904	(0.012)
CH_2Cl_2 111 K	2.316	-	2.622	-	1.975	-	1.897	-
CH_2Cl_2 240 K	2.323	(0.007)	2.665	(0.043)	1.990	(0.015)	1.902	(0.005)
$^2A_2$	2.320	-	2.597	-	1.985	-	1.896	-
^2E	2.288	(-0.033)	2.732	(0.135)	1.982	(-0.002)	1.909	(0.013)
$^2B_2$	2.327	(0.007)	2.780	(0.183)	1.965	(-0.019)	1.889	(-0.007)
$^4B_1$	2.385	(0.065)	2.710	(0.113)	1.984	(0.000)	1.887	(-0.009)
$^4A_1$	2.363	(0.043)	2.554	(-0.043)	2.041	(0.056)	1.902	(0.006)
$^4B_2$	2.365	(0.045)	2.551	(-0.046)	2.043	(0.058)	1.901	(0.005)
^4E	2.348	(0.027)	2.678	(0.081)	2.000	(0.015)	1.908	(0.012)
2-^4E	2.322	(0.002)	2.517	(-0.080)	2.058	(0.074)	1.916	(0.021)
3-^4E	2.324	(0.004)	2.514	(-0.083)	2.059	(0.075)	1.915	(0.019)
4-^4E	2.338	(0.018)	2.904	(0.307)	1.972	(-0.013)	1.903	(0.007)
5-^4E	2.280	(-0.041)	2.738	(0.141)	1.995	(0.011)	1.978	(0.082)
6-^4E	2.335	(0.014)	2.637	(0.040)	2.042	(0.057)	1.910	(0.014)
$^4A_2$	2.296	(-0.024)	2.851	(0.254)	1.991	(0.007)	1.924	(0.028)
2-$^4B_2$	2.283	(-0.037)	2.603	(0.006)	2.056	(0.071)	1.931	(0.035)
2-$^4B_1$	2.289	(-0.031)	2.596	(-0.001)	2.059	(0.075)	1.927	(0.031)
$^6B_1$	2.342	(0.022)	2.563	(-0.034)	2.078	(0.093)	1.930	(0.034)
$^6B_2$	2.346	(0.025)	2.559	(-0.038)	2.079	(0.095)	1.926	(0.031)
$^6A_2$	2.325	(0.004)	2.441	(-0.155)	2.133	(0.148)	1.931	(0.036)
^6E	2.391	(0.070)	2.595	(-0.002)	2.061	(0.076)	1.911	(0.016)
2-^6E	2.394	(0.074)	2.590	(-0.007)	2.063	(0.079)	1.909	(0.013)
3-^6E	2.374	(0.054)	2.471	(-0.125)	2.118	(0.133)	1.922	(0.026)
$^6A_1$	2.347	(0.027)	2.705	(0.108)	2.051	(0.066)	1.929	(0.033)
2-$^6A_2$	2.358	(0.037)	2.687	(0.090)	2.057	(0.072)	1.921	(0.025)
2-$^6B_2$	2.341	(0.020)	2.529	(-0.068)	2.116	(0.131)	1.932	(0.036)
$^8B_1$	2.402	(0.081)	2.498	(-0.099)	2.138	(0.153)	1.928	(0.033)

Table 4.1: Co-Co, Co-Br and Co-N bond lengths (Å) in $Co_3(dpa)_4Br_2$ for each state optimised using the BP86 functional and the experimental data, including the change in bond length (Δ) with respect to the $^2A_2$ ground state and the low temperature structures.

Excited State Energies

Having considered the structural changes upon excitation to different candidate excited states, we now consider how their energies vary. The experimental magnetic susceptibility data have been fit to an ideal spin crossover into a HS quartet state with ΔH values of 14.9 and 8.2 kJ mol^{-1} (0.155 and 0.085 eV) for the $Co_3(dpa)_4Br_2{\cdot}CH_2Cl_2$ and

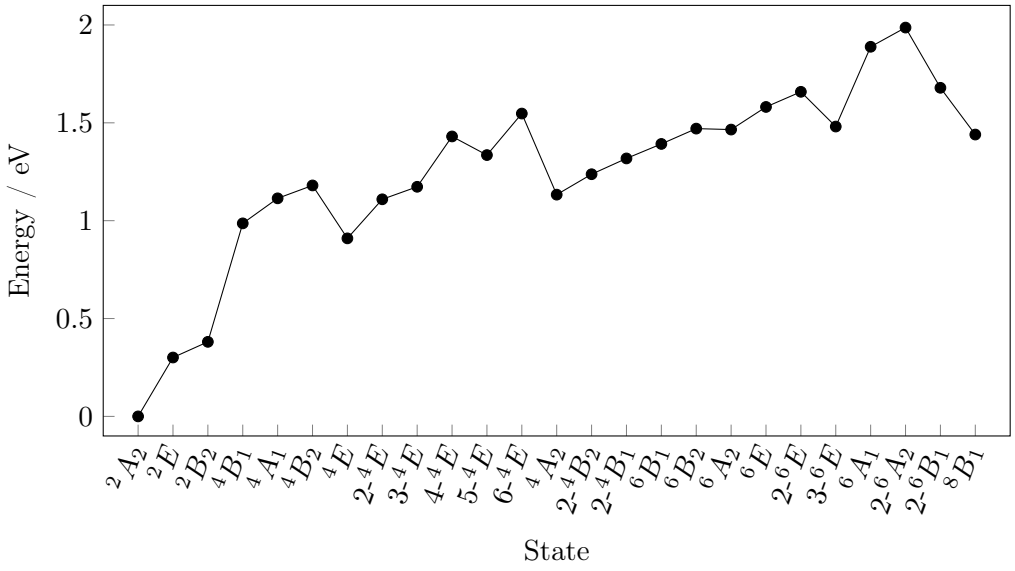

Figure 4.7: Relative energies (eV) to the $^2A_2$ ground state of the bromide complex predicted low-lying doublet, quartet, sextet and octet states detailed in Figures 4.4-4.6 using the BP86 functional.

$Co_3(dpa)_4Br_2$·Hexane crystals, respectively. [38] Figure 4.7 shows calculated excitation energies for each state, all of which are reported relative to the $^2A_2$ ground states. The doublet states generally have the lowest energies, followed by the quartet states and then the sextet and octet states. Moreover, the quartet and sextet states with the σ^* orbital occupied have lower energies than those with the $\delta_{x^2-y^2}$orbital occupied, which are lower still than those with the $\delta^{nb}_{x^2-y^2}$ orbital occupied.

Even the lowest excitation energies are considerably higher than the experimental estimates. In Chapter 1 we described how the crystalline environment can play a pivotal role on the spin state energetics in transition metal complexes. [98, 99, 110–112] This arises from the relative stabilisation and destabilisation of different geometries through crystal packing forces. A Hirshfeld surface analysis specifically showed this to be the case for the tricobalt chloride complexes. [113] The molecular structures of the tricobalt EMACs have only been shown to have D_4 symmetry in solution, whereas in the solid state the structures show greater variation. Even in the structures that remain quite symmetric

through a range of temperatures, some show small divergences in the Co-Co, terminal Co-N and Co-X bonds. This suggests that the symmetry is not enforced, and the unsymmetric distortion could be allowed, just not preferred. By relaxing the symmetry constraint we expect to see a relaxation in the state energies, particularly in the degenerate states of E symmetry, that may effect the relative energies of the excited states. To investigate this we have taken each of the D_4 constrained states and allowed them to relax to their C_2 minima, which allows the Co-Co distances to diverge and the Jahn-Teller distortion to stabilise the E states. As the symmetry is reduced, the number of irreducible representations decreases and we have less control over the electronic configuration. The PES of different states can cross and converge on the same minimum. After the relaxation procedure, we confirm the symmetric nature of eight unique states: $^2A_2$, ^2E, $^4B_1$, ^4E, $^4A_2$, $^6A_2$, 3-^6E and $^8B_1$. All of these states have either no electrons in the $\delta_{x^2-y^2}$ and $\delta^{nb}_{x^2-y^2}$ orbitals, or one electron in both. The previous work from McGrady and Pantazis showed that the occupation of the $\delta_{x^2-y^2}$ orbital is key to the divergence in the Co-N distances and the nature of the unsymmetric tricobalt EMACs, and this will be explored further in the next chapter. For now we maintain our focus on the symmetric states.

4.3.2 DFT Analysis: Functional Dependence

Energies

In the discussion of DFT in Chapter 2 we emphasised the importance of using a variety of functionals to verify result, because whilst most functionals generally do quite well in predicting structures, they often struggle to predict consistent spin state splitting energies, which is of particular importance to this context. In Figure 4.8 below we present the energies of the symmetric states relative to the $^2A_2$ state for the range of functionals: BP86, BLYP, OLYP, OPBE, B3LYP, B3LYP* and SCAN. Even after the relaxation to

C_2 symmetry the symmetric excited states maintained equal Co-Co bonds to within the optimisation thresholds, which corresponds to a D_2 symmetric structure. As such, D_2 symmetry is enforced in the calculations to allow greater control in specifying the electron configuration, however the D_4 naming used in Figures 4.4-4.6 is maintained.

All the GGA functionals agree that the ground state is the $^2A_2$ state, as does the meta-GGA SCAN functional. In general the doublet states have the smallest excitation energies, while the quartet, sextet and octet have increasingly greater excitation energies with the GGA functionals in Figure 4.8. The OPTX exchange functional does stabilise the sextet and octet states for OLYP and OPBE though, which have similar, if not lower, energies to the quartets. The most remarkable feature of the functional results occurs for B3LYP, which actually predicts a $^6A_2$ ground state. As previously discussed, hybrid functionals stabilise HS states due to the inclusion of the exact Hartree-Fock exchange energy in the functional. These results suggest the HS states are overstabilised by B3LYP, as the experimental data unequivocally agree on a doublet ground state. B3LYP*, with 15% Hartree-Fock exchange compared to 20% in B3LYP, does not stabilise the HS states to the same degree, and predicts a $^2A_2$ ground state with a $^6A_2$ first excited state. The SCAN functional predicts the ^2E, ^4E and $^6A_2$ states to have the smallest excitations energies. In general the hybrid and SCAN functionals predict a much larger range of excitations energies, with large differences in the energies of some states. The relative stabilisation of HS states by hybrid functionals can best be seen in the ^2E energies, which lie above the $^6A_2$, ^4E, $^4B_1$ and $^8B_1$ with both B3LYP and B3LYP* whereas all other functionals predict it as the first excited state. As previously discussed, comparing spin state splitting energies across different functionals can often lead to inconsistencies. Nevertheless we can compare the functional dependent energetics of states of the same multiplicity with more confidence. Consistently across all the functionals the ^4E state is the lowest energy quartet

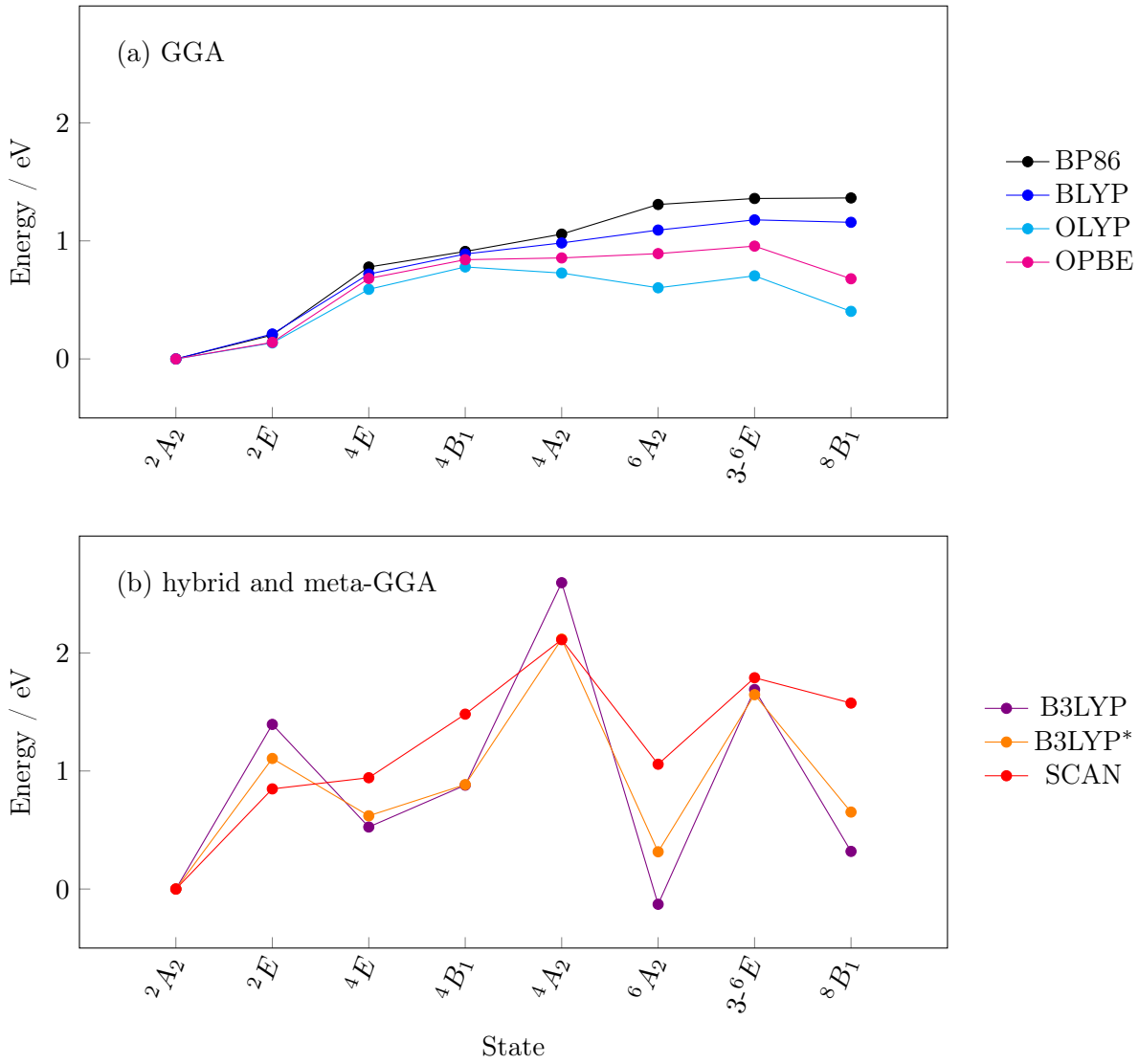

Figure 4.8: Relative energies (eV) to the $^2A_2$ ground state of the bromide complex predicted low-lying symmetric doublet, quartet, sextet and octet states using the (a) GGA (BP86, BLYP, OLYP and OPBE) and (b) hybrid (B3LYP and B3LYP*) and meta-GGA (SCAN) functionals.

state, whilst the $^6A_2$ state is the lowest energy sextet. For all but OLYP the $^4B_1$ state is lower lying than $^4A_2$, quite significantly for the hybrid functionals.

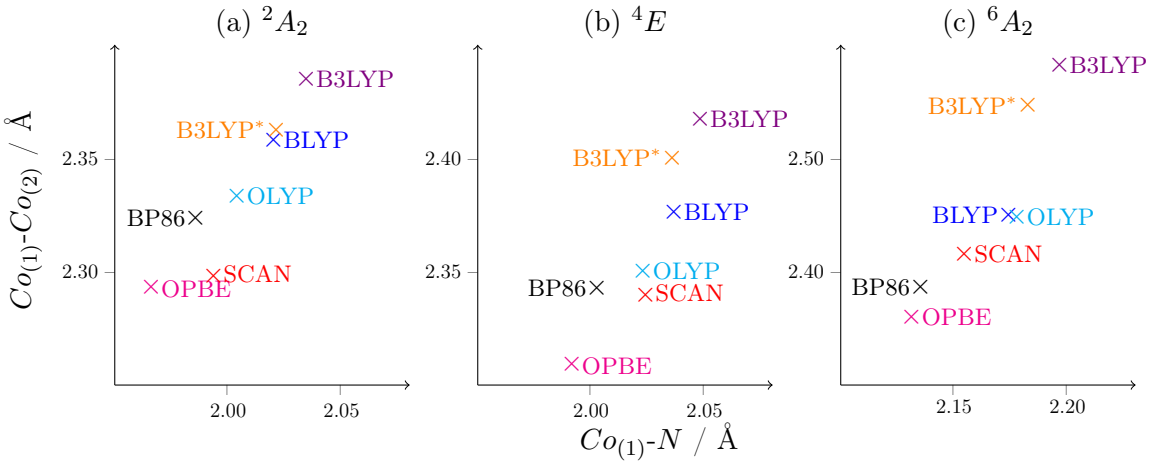

Figure 4.9: Co-Co and terminal Co-N bond lengths for the (a) $^2A_2$, (b) ^4E and (c) $^6A_2$ states using the BP86, BLYP, OLYP, OPBE, B3LYP, B3LYP* and SCAN functionals.

Structures

Further to the excitation energies, we can also compare how the choice of functional affects the optimised structures and wavefunctions. The differences in structure are explored in Figure 4.9. The optimised $Co_{(1)}$-$Co_{(2)}$ and $Co_{(1)}$-N bond lengths of each functional are plotted for the $^2A_2$ ground state, and the ^4E and $^6A_2$ excited states, which were found to be lowest energy unique states consistent with the high temperature experimental symmetric structures. The choice of functional affects the structure of each state similarly, where the data points have the same distribution. Consistently OPBE predicts the shortest bonds, followed by SCAN or BP86, then OLYP, BLYP, B3LYP* and B3LYP.

Wavefunctions

Table 4.2 shows the expectation value of the total spin squared, $\left\langle \hat{S}^2 \right\rangle$, spin contamination, SC, and the cobalt spin densities, ρ, for each state. We measure the spin contamination in the wavefunction using the difference in the unrestricted and exact $\hat{S}^2$ expectation values

given in Equation 2.117 page 79 in Chapter 2.

$$SC = \left\langle \hat{S}^2 \right\rangle_{\text{UHF}} - \left\langle \hat{S}^2 \right\rangle_{\text{Exact}} = N_\beta - \sum_{i,j}^{occupied} \left| \left\langle \psi_i^\alpha \middle| \psi_j^\beta \right\rangle \right|^2 \tag{4.1}$$

The calculated spin densities shown in Table 4.2 correspond to the orbital occupations. For example the $^2A_2$ ground state has the unpaired electron in the σ^{nb} orbital, which is localised on the two terminal cobalt atoms, as is the spin density. The ^4E state has unpaired electrons in the σ^* and π^* orbitals, which are delocalised across the three cobalt atoms, as is the spin density, and the $^6A_2$ state has unpaired electrons in the $\delta_{x^2-y^2}$ and $\delta^{nb}_{x^2-y^2}$ orbitals, which are localised on the terminal cobalt atoms, as is the spin density. The GGA wavefuctions all show similar characteristics, with similarly low levels of spin contamination and cobalt spin densities that indicate a delocalised wavefunction. The hybrid functionals show high levels of spin contamination compared to the GGA functionals. This is to be expected as spin contamination has been shown to be derived from the HF exchange term. [319] We also see an increased localisation of the wavefunction, which can be seen in the larger spin densities. The localisation of the wavefunction also arises from inclusion of the exact HF exchange. The HF exchange term stabilises wavefunctions with unpaired electrons of the same spin (HS states). The term is inversely proportional to the distance between the electrons, and so it is maximised when the unpaired electrons of the same spin are localised. These features are more pronounced for B3LYP due to the larger proportion of Hartree-Fock exchange energy in the exchange correlation functional. The SCAN functional wavefunctions also show similar properties, although they are less prominent than in both the hybrid functionals. High levels of spin contamination are characteristic of antiferromagnetic systems, as the α and β electrons have different spatial wavefunctions, and $\sum_j^{occupied} \left\langle \psi_i^\alpha \middle| \psi_j^\beta \right\rangle \neq 1$. The spin contamination and localisation in

		$\left\langle \hat{\mathbf{S}}^{\mathbf{2}} \right\rangle$	**SC**	ρ **Co**$_{(1)}$	ρ **Co**$_{(2)}$	ρ **Co**$_{(3)}$
$^{\mathbf{2}}\mathbf{A_2}$	**BP86**	0.785	0.035	0.468	-0.140	0.468
	BLYP	0.790	0.040	0.477	-0.159	0.477
	OLYP	0.795	0.045	0.484	-0.162	0.484
	OPBE	0.786	0.036	0.466	-0.128	0.466
	B3LYP	1.250	0.500	0.796	-0.684	0.796
	B3LYP*	1.089	0.339	0.715	-0.548	0.715
	SCAN	1.003	0.253	0.663	-0.404	0.663
$^{\mathbf{4}}\mathbf{E}$	**BP86**	3.778	0.028	0.923	0.941	0.923
	BLYP	3.777	0.027	0.924	0.944	0.924
	OLYP	3.790	0.040	0.959	0.913	0.959
	OPBE	3.793	0.043	0.969	0.866	0.969
	B3LYP	3.775	0.025	0.894	1.149	0.894
	B3LYP*	3.776	0.026	0.876	1.142	0.876
	SCAN	4.031	0.281	0.904	1.159	0.904
$^{\mathbf{6}}\mathbf{A_2}$	**BP86**	8.943	0.193	2.149	-0.089	2.149
	BLYP	8.994	0.244	2.203	-0.227	2.203
	OLYP	9.074	0.324	2.270	-0.357	2.270
	OPBE	8.973	0.223	2.176	-0.114	2.176
	B3LYP	9.584	0.834	2.629	-0.923	2.629
	B3LYP*	9.493	0.743	2.559	-0.849	2.559
	SCAN	9.308	0.558	2.495	-0.698	2.495

Table 4.2: $\left\langle \hat{S}^2 \right\rangle$, spin contamination ($SC$) and cobalt spin densities (ρ) for the $^2A_2$, ^4E and $^6A_2$ states using the BP86 functional ($\left\langle \hat{S}^2 \right\rangle_{\text{Exact}} = 0.75, 3.75$ and 8.75, respectively).

the SCAN and the hybrid wavefunctions suggests antiferromagnetic coupling between the cobalt atoms, rather than the covalent bonding picture suggested by the delocalised GGA wavefunctions.

4.3.3 MCSCF Analysis

Before we present our MCSCF results we first describe two attempts to use two other post-HF treatments, namely MP2 and DLPNO-CCSD(T). MP2 works on both restricted and unrestricted reference wavefunctions, however the DLPNO-CCSD(T) technique currently only works for a restricted reference. We were unable to converge a ROHF solution for the bromide complex. We attempted to use quasi-restricted orbitals from unrestircted

(UHF and UDFT) calculations, but given the system size we were unable to converge the following DLPNO-CCSD(T) calculation using these as a reference at reasonable expense. As such the results presented below are for the chloride complex. Further, again due to the system size, we were unable to converge calculations of any excited chloride states with MP2 or DLPNO-CCSD(T). Either way, the following calculations suggest the use of MP2 or DLPNO-CCSD(T) is not appropriate for the study of the tricobalt EMACs.

The MP2 and DLPNO-CCSD(T) methods were used to calculate the correlation energy of a restricted open shell Hartree-Fock (ROHF) reference wavefunction of the ground state of the chloride complex. Both of these methods are single-reference and use the HF orbitals to generate excited state determinants. No symmetry constraints were imposed on the wavefunction. The HF reference state energy of the chloride complex is -7249.045 Eh. The MP2 correction is -10.757 Eh, and the MP2 corrected wavefunction has 74 orbitals with natural orbital occupation numbers between occupations of 0.02 and 1.98. The DLPNO-CCSD(T) CCSD correction is -10.640 Eh with a further triples correction of -0.457 Eh to give a total correction to the energy of -11.097 Eh. Multi-reference methods are advised when $D_1 < 0.05$, the dominant configuration weight is below 90% and natural orbital occupation numbers lie between 0.05 and 1.95. [282–284, 337] The largest excited state amplitudes are 0.179 and 0.134, which are both large, and the D_1 diagnostic has a value of 0.35, although the T_1 is actually relatively small, with a value of 0.016. As such these results very clearly suggest that a MCSCF or multi-reference approach is needed.

CASSCF and CASPT2

A full geometry optimisation at the CASPT2 level is intractable, but we can explore the shape of the CASPT2 surface by performing single point calculations at the DFT geometries of the different states. We use the BP86 results, which compare well with ex-

periment and show intermediate geometries compared with the other functionals (Figure 4.9). A preliminary CASSCF calculation of the $^2A_2$ ground state of the tricobalt bromide complex was carried out using OpenMolcas. D_2 symmetry is imposed as D_4 is not supported in OpenMolcas. A CAS(3,3) calculation, using the notation CAS(n,m) for an active space with n electrons distributed among m orbitals, gives an active space containing the three sigma orbitals formed by the cobalt d_{z^2} orbitals. The results show significant multi-configurational character. The most significant contribution to the wavefunction comes from the $(\sigma)^2(\sigma^{nb})^u(\sigma^*)^0$ configuration with a weight of 0.597. There are two further significant configurations: $(\sigma)^0(\sigma^{nb})^u(\sigma^*)^2$, with a weight of 0.190 and $(\sigma)^u(\sigma^{nb})^d(\sigma^*)^u$, with a weight of 0.213. The superscript u and d represent the spins (α and β) of an unpaired electron in an orbital. The largest configuration weight of 0.597 is significantly lower than the threshold value of 0.90, and in agreement with the single-reference results we will continue to use a multi-reference approach.

We next turn our attention to the excited states. At the symmetric limit, all the excited states of the tricobalt EMACs discussed in the context of DFT have unpaired electrons in cobalt d orbitals other than those in the CAS(3,3) active space, and it must be expanded. For an accurate comparison of the excited states we need to use a consistent active space across all the states. In principle, we should expand the active space to contain all of the orbitals of the cobalt d manifold, including those with both π and δ symmetry, as well as a correlating d' prime seta and the Co-Br and Co-N bonding orbitals. This would not be possible as the wavefunction would have too many determinants, and as such we try to create a space containing just the Co d orbitals, corresponding to a CAS(21,15) active space. We adopt an approach whereby we introduce a subset of the d orbitals with their d' shell, then remove the d' shell from the active space. We used the RASSCF technique to limit excitations within the π and δ frameworks to doubles only to aid convergence, with

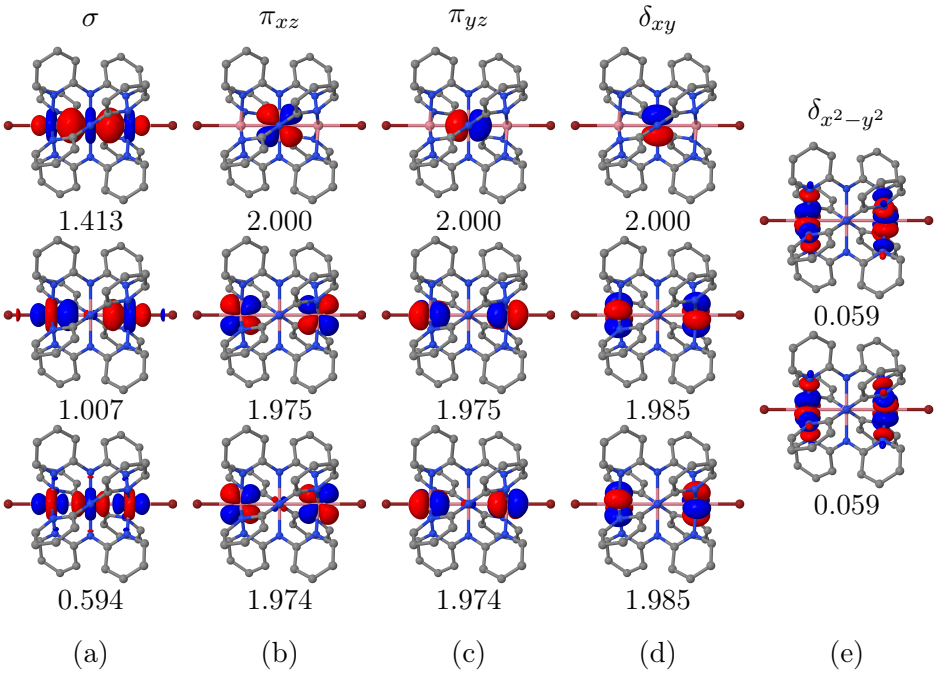

Figure 4.10: CAS(21,14) active space natural orbitals of (a) σ, (b) π_{xz}, (c) π_{yz}, (d) δ_{xy} and (e) $\delta_{x^2-y^2}$ symmetry for $Co_3(dpa)_4Br_2$ with $^2A_2$ ground state natural occupation numbers at the BP86 $^2A_2$ geometry.

the π and δ d orbitals in RAS1, the d' orbitals in RAS3 and the σ framework in RAS2. We begin by introducing the π orbitals formed by the d_{xz} and d_{yz} orbitals, creating a CAS(15,15) space followed by a CAS(15,9) space upon removal of the d' shell. We then introduce the δ orbitals from by the d_{xy} orbitals, creating an initial CAS(21,15) space and then a CAS(21,12) space. Finally we attempt to introduce the δ orbitals from by the $d_{x^2-y^2}$ orbitals, where we use the bonding and antibonding Co-N orbitals rather than the d orbitals with their d' shell. However, we encountered problems in controlling rotations within and out of the active space. In particular the Co-N bonding $\delta^*_{x^2-y^2}$ orbitals would rotate with Co $3p_z$ or Br $3p_z$ orbitals in the inactive space, while the Co-N antibonding orbital on $Co_{(2)}$ would rotate with the σ d' shell. By removing the $\delta^*_{x^2-y^2}$ orbital localised on $Co_{(2)}$ from the active space we were able to obtain a stable CAS(21,14) space, shown in Figure 4.10, containing the full σ, π and δ_{xy} frameworks with the bonding and nonbonding linear combinations of the $d_{x^2-y^2}$ orbitals, localised on the terminal cobalt atoms.

We also observed that the $\delta^*_{x^2-y^2}$ and δ_{xy} orbitals on $Co_{(2)}$ would often mix to create an open-shell singlet state within the subspace of the two orbitals. This leads to an overall doublet state that actually has three unpaired electrons, where two are spin α and one spin β. Such a state does not correspond to any of the DFT results, and we expect it to be a result of the tendency of CASSCF to overstabilise open-shell singlet states. This is discussed in more detail later where we see a similar effect manifest in the $\delta^*_{x^2-y^2}$ and δ_{xy} orbitals on all the Co atoms, which complicates the calculation of excited states. The states of interest will often lie high in energy when calculated with CASSCF, while the low energy states have LS open-shell configurations within δ_{xy} and $\delta^*_{x^2-y^2}$ subspaces. However, we expect a CASPT2 treatment to compensate for this and correct the energetic ordering.

The natural orbitals and their occupations within the $^2A_2$ ground state are shown in Figure 4.10. The occupations of the σ, σ^{nb} and σ^* (1.413, 1.007 and 0.594, respectively) are essentially unchanged from the CAS(3,3) occupations (1.406, 1.000 and 0.594). The work from McGrady and Pantazis suggested that correlation between the δ_{xy} and $\delta_{x^2-y^2}$ orbitals could play an important role in the structural behaviour, but here we see the π orbitals have lower occupations numbers than the d_{xy}, which shows they are also strongly correlated with the $\delta_{x^2-y^2}$. The main configurations all have doubly occupied π and δ_{xy} manifolds and an unoccupied $\delta_{x^2-y^2}$ manifold, $(\pi)^4(\delta_{xy})^2(\pi^{nb})^4(\delta^{nb}_{xy})^2(\pi^*)^4(\delta^*_{xy})^2(\delta_{x^2-y^2})^0(\delta^{nb}_{x^2-y^2})^0$, where $(\pi)^4 = (\pi_{xz})^2(\pi_{yz})^2$. This combines with the three underlying σ configurations with weights of 0.562 for $(\sigma)^2(\sigma^{nb})^u(\sigma^*)^0$, 0.176 for $(\sigma)^0(\sigma^{nb})^u(\sigma^*)^2$ and 0.199 for $(\sigma)^u(\sigma^{nb})^d(\sigma^*)^u$ to make up 94% of the wavefunction. Excitations within the π and δ framework make up the remaining 6%. All the above reflects the complete filling of the π and δ_{xy} orbitals in the ground state, and the metal-metal bonding in the ground state is attributable to the σ manifold, with the formation of a weak three-centre three-electron bond of order $\sim$0.2 between each Co.

	CASSCF	CASPT2	Ref. Wt	σ	π_{xz}	π_{yz}	δ_{xy}	$\delta_{x^2-y^2}$
$^2\mathbf{A_2}$	0.000	0.000	0.286	1.413	2.000	2.000	2.000	0.059
				1.007	1.975	1.975	1.985	0.059
				0.594	1.974	1.974	1.985	
$^2\mathbf{E}$	0.714	0.292	0.273	1.591	1.999	1.862	2.000	0.090
				1.445	1.954	1.635	1.980	0.090
				0.900	1.953	1.521	1.980	
$^4\mathbf{B_1}$	2.206*	-	-	1.880	1.999	1.999	1.125	0.087
				1.062	1.953	1.953	1.945	0.087
				1.058	1.953	1.953	1.947	
$^4\mathbf{A_2}$	1.691*	-	-	1.736	1.778	1.778	2.000	0.163
				1.672	1.634	1.634	1.949	0.163
				1.425	1.560	1.560	1.948	
$^4\mathbf{E}$	1.350*	-	-	1.452	1.996	1.996	2.000	0.156
				1.439	1.910	1.541	1.945	0.156
				1.004	1.909	1.551	1.945	
$^4\mathbf{A_1}$	-0.458	-0.379	0.272	1.381	2.000	2.000	2.000	0.546
				1.004	1.971	1.971	1.510	0.546
				0.623	1.970	1.970	1.509	
2-$^4\mathbf{E}$	-0.257	-0.202*	0.241	1.446	1.998	1.997	2.000	0.531
				1.177	1.634	1.846	1.833	0.528
				0.702	1.629	1.844	1.833	
3-$^6\mathbf{A_2}$	-0.884	-0.605	0.266	1.339	2.000	2.000	2.000	1.034
				1.000	1.966	1.966	1.034	1.034
				0.662	1.966	1.966	1.034	
$^6\mathbf{A_2}$	-0.413	-0.120*	0.186	1.457	1.997	1.997	2.000	1.000
				1.295	1.488	1.513	1.731	1.000
				0.816	1.489	1.515	1.703	
3-$^6\mathbf{E}$	-0.656	-0.216*	0.181	1.491	2.000	1.994	2.000	1.017
				1.069	1.919	1.554	1.291	1.017
				0.728	1.925	1.540	1.455	
$^8\mathbf{B_1}$	-0.076	0.275*	0.045	1.447	1.867	1.867	2.000	1.010
				1.342	1.576	1.576	1.515	1.009
				1.213	1.542	1.542	1.496	

Table 4.3: Relative energies (eV) to the $^2A_2$ state of the bromide complex at the CASSCF and CASPT2 level at the BP86 $^2A_2$ geometry, including CASSCF natural orbital occupation numbers of the CAS(21,14) active space shown in Figure 4.10 and CASPT2 reference weights.
*CASSCF/CASPT2 calculation only moderately converged.

We now use this active space to generate excited state multi-reference wavefunctions for excitations from the π and δ manifold. In all cases the orbitals are not reoptimised ("CI-only" in OpenMolcas). Table 4.3 shows the CASSCF energies (in eV) for states found in the DFT analysis at the BP86 $^2A_2$ ground state geometry, including one new sextet state (3-$^6A_2$), and CASPT2 energies where it has been possible to converge a solution, as well as the natural orbital occupation numbers. All energies are given relative to the $^2A_2$ state at the corresponding level of theory. The positions of the orbital occupation numbers in the table correspond to the layout of the orbitals in Figure 4.10. The weight of the reference state in the PT2 wavefunction are also shown. Reference weights are included as these indicate whether the CASPT2 results are comparable. In general the PT2 reference wavefunction should have a large reference weight, as perturbation treatments only work when the correction is small, however due to the large system size the relatively low weights are not of concern as there are many potential inactive-valence excitations. Problems would arise should any of those individual excitations have a significant weight in the excited state wavefunction, which would lead to a considerably different reference weight, and make comparing the energy with other states unreliable.

Quartet states with a single electron excited into the $\delta_{x^2-y^2}$ framework have lowest energies, actually below the ground state. The occupations show the electron is split between the $\delta_{x^2-y^2}$ and $\delta^{nb}_{x^2-y^2}$ orbitals, as they have very similar energies, and such states were shown to converge on an unsymmetric minimum in the DFT analysis. At slightly higher energies we find quartet states with a singly occupied σ^* orbital, except the occupations do not correspond to the DFT results, having seven unpaired electrons. As mentioned earlier, such open-shell singlets are overstabilised by CASSCF. On each terminal Co, the δ_{xy} electron pair is split between the δ_{xy} and $\delta_{x^2-y^2}$ orbitals. If we examine the configurations contributing to the multi-configurational wavefunction, we see

that these states are stabilised for two reasons. Firstly, the δ_{xy} electrons use the vacant $\delta_{x^2-y^2}$ orbitals to correlate their motion, with the $\delta_{x^2-y^2}$ orbitals acting like a d'_{xy} shell. Secondly we notice the δ_{xy} electrons both have the same spin, as do the $\delta_{x^2-y^2}$ electrons, but opposite to the δ_{xy} electrons, which maximises the exchange energy as the same spin electrons are closer to each other. These states therefore have low CASSCF energies. The states with orbital occupations that correspond to those found in the DFT analysis, namely the $^4B_1$, $^4A_2$ and ^4E, are all found to have large excitation energies at the CASSCF level. For example the state corresponding to the $^4B_1$ occupations is not found until the 133rd state. When we optimise a high energy state with OpenMolcas we need to optimise all the lower energy states too. Calculations of the $^4B_1$, $^4A_2$ and ^4E states require calculating expansion coefficients for a large number of states, and we were only able to converge CASSCF energies moderately. Higher energy states become increasingly poorly described by the reference CASSCF wavefunction, and as such we were unable to converge a solution for the CASPT2 correction for any of the high energy quartet states.

The CASSCF energies of the remaining sextet and octet states also lie below that of the $^2A_2$ state, which was found to be the ground state for all density functionals expect B3LYP. In particular the new 3-$^6A_2$ state has CASSCF and CASPT2 energies that are significantly lower than the $^2A_2$ state: -0.884 and -0.605 eV, respectively. The 3-$^6A_2$ state was not found using DFT, and contains four unpaired electrons in the bonding and nonbonding δ_{xy} and $\delta_{x^2-y^2}$ orbitals localised on the terminal Co atoms. Within the σ framework the electronic configuration can be considered the same as the $^2A_2$ state, with σ, σ^{nb} and σ^* natural orbital occupation numbers of 1.339, 1.000 and 0.662, respectively. Given the highly multiconfigurational character of all the excited states, and the fact that the experimental work all unequivocally suggests a doublet ground state, these results suggest that the active space may be too restrictive to properly describe the electron

correlation fully.

4.4 Conclusions

In this chapter we present the first investigation into the tricobalt bromide EMAC, focussing on symmetric structures with equal Co-Co distances. We undertake a detailed analysis the ground state and of a multitude excited states. The spin state splitting energies show a strong dependence on the methodology used, and indicate the spin crossover is finely balanced. The DFT structures give the best correlation with the experiment, and are perhaps the most useful tool in predicting the underlying electronic structure. This is particularly apparent when you consider the significant impact the crystalline environment has on the behaviour. The $^2A_2$ ground state is described by a three-centre three-electron bond with a D_4 symmetric structure that matches the experimental solution and low temperature crystal structures. This corresponds to the picture presented for the chloride complex by McGrady and Pantazis. [102] Two HS states emerge as the best candidates to explain the observed structural behaviour associated with the spin crossover in the symmetric crystals: population of the symmetric ^4E, with elongated Co-Br bonds, is most consistent with the behaviour of $Co_3(dpa)_4Cl_2{\cdot}CH_2Cl_2$; while population of the symmetric $^6A_2$, with elongated Co-N bonds at both terminal Co atoms, is most consistent with the behaviour of $Co_3(dpa)_4Cl_2{\cdot}$Hexane. This is the first sextet state configuration to be associated with the behaviour of any of tricobalt EMAC system, and the quartet state is the first symmetric quartet state to be identified. In the next chapter we focus on unsymmetric structures. We return to the results of this chapter in Chapters 7 and 8, where we use the $^2A_2$, ^4E and $^6A_2$ states in an analysis of the symmetric-unsymmetric transition in Chapter 7 and extend the study to the fluoride, chloride and iodide complexes in Chapter 8.

Chapter 5

A DFT and MCSCF Study of the $Co_3(dpa)_4Br_2$ Unsymmetric Form

5.1 Introduction

In the solid state the tricobalt EMACs exhibit varying degrees of asymmetry, which arise through the divergence of both the Co-Co and Co-N bonds. In the previous chapter we discussed the behaviour and properties of the symmetric (D_4 and D_2) form of the $Co_3(dpa)_4Br_2$ EMACs. In this chapter, we follow the same protocol to investigate the unsymmetric (C_2) form. Whilst there is consensus in the experimental and theoretical work that the gas-phase ground states of the isolated tricobalt EMACs adopt the symmetric structure, a number of examples of unsymmetric forms are known in the crystallographic literature. For example, whilst the tricobalt bromide complex has a symmetric structure in the $Co_3(dpa)_4Br_2{\cdot}CH_2Cl_2$ and $Co_3(dpa)_4Br_2$·Hexane crystals, the $Co_3(dpa)_4Br_2$·1.75Toluene·0.5Hexane solvate is highly unsymmetric over a wide range of temperatures (Figures 5.1a-b). [37] An unsymmetric structure can also emerge at elevated temperatures, even when the low-temperature structure is symmetric, as shown by the

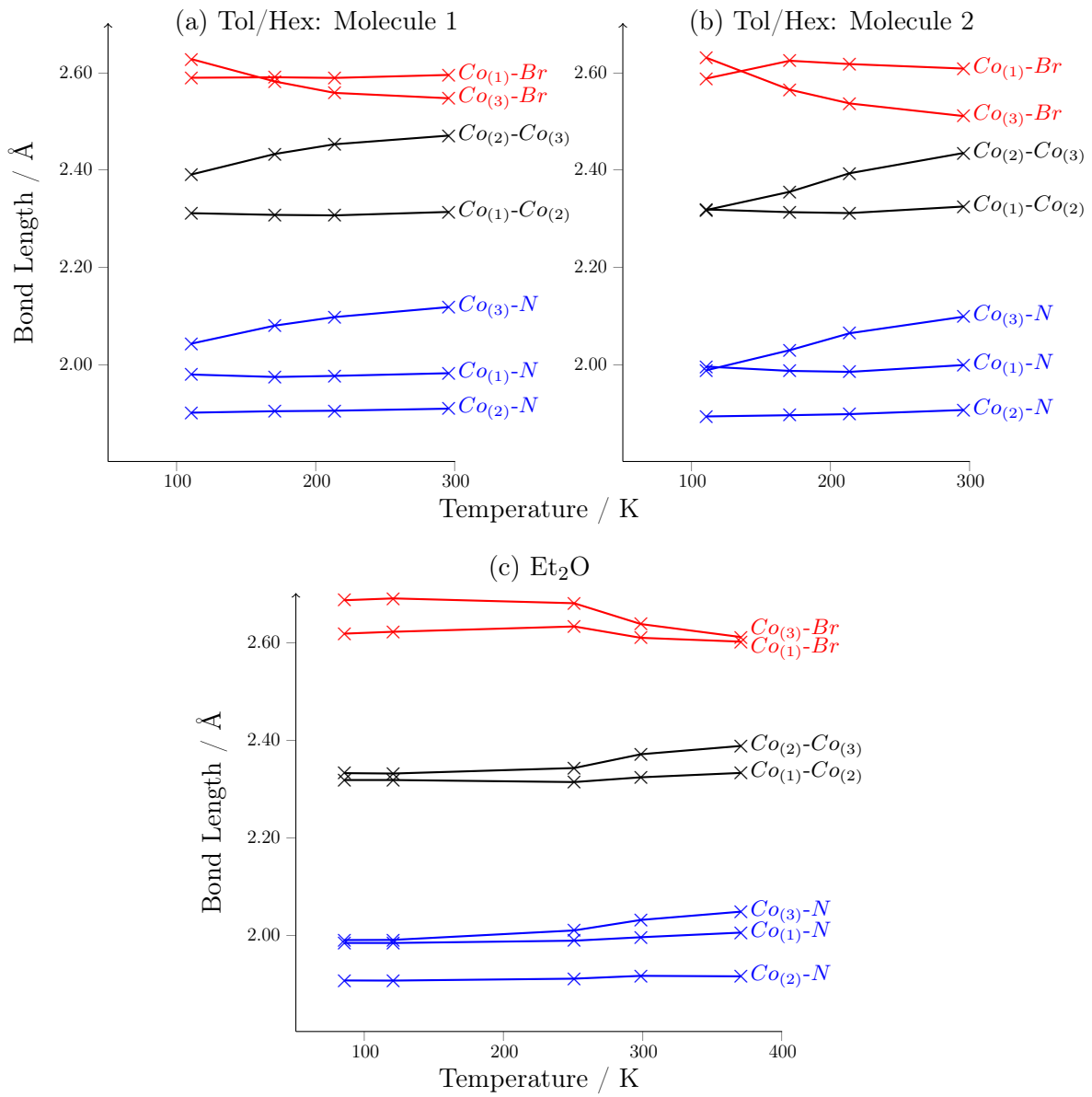

Figure 5.1: Bond lengths for the $Co_3(dpa)_4Br_2$·0.175Toluene·0.5Hexane crystal molecules (a) 1 and (b) 2 from 110 – 298 K and the (c) $Co_3(dpa)_4Br_2$·Et_2O crystal from 85 - 350 K. [37, 38]

Hillard group in the $Co_3(dpa)_4Br_2$·Et_2O crystal (Figure 5.1c). [38] Both unsymmetric crystals show an increase in the effective magnetic moment with temperature indicating a spin crossover occurs. In the most recent work Hillard *et al.* fit the magnetic data to an ideal spin equilibrium model between a LS doublet and HS quartet state. They were able to extract the thermodynamic parameters of the spin crossover process, where ΔH = 13.3 kJ mol^{-1}, ΔS = 40.9 J K^{-1} mol^{-1} and $T_{\frac{1}{2}}$ = 325 K and ΔH = 8.0

kJ mol^{-1}, ΔS = 33.2 J K^{-1} mol^{-1} and $T_{\frac{1}{2}}$ = 241 K for the $Co_3(dpa)_4Br_2 \cdot Et_2O$ and $Co_3(dpa)_4Br_2 \cdot 1.75Toluene \cdot 0.5Hexane$ crystals, respectively.

The nature of the unsymmetric structure suggests the dissociation of the Co_3 unit into an isolated Co centre and a Co_2 dimer. Compared to the D_4-symmetric structure, the asymmetry arises through changes in both the Co-Co and Co-N bonds: the divergence of the Co-Co distance leads to a C_4 symmetric structure while a Jahn-Teller distortion in the Co-N bonds can lead to a D_2 symmetric structure, as discussed in the previous chapter. When both occur simultaneously, the structure has C_2 symmetry. The previous study from McGrady and Pantazis showed how the asymmetry effected the composition of the molecular orbitals in the chloride complex: the D_2 relaxation lifted the degeneracy in the π orbitals of e symmetry in the D_4 point group, while the C_4 relaxation led to a localisation of the orbitals onto either the cobalt dimer or the isolated cobalt centre. [102] This picture corresponds with the experimental work, which explained the spin crossover behaviour as a localised transition at the more isolated terminal cobalt in the unsymmetric crystals. [26] However, McGrady and Pantazis noted that this localisation should only be considered as a first approximation, and there was significant mixing evident between the two sides of the tricobalt chain. Their work explored the origin of the distortion in the context of $Co_3(dpa)_4Cl_2$, and they argued that the lowest energy structure at the unsymmetric limit had ^{4}B symmetry (in the C_2 point group). They described the ^4B bonding as a diamagnetic cobalt dimer with a single sigma bond coupled to an isolated high spin cobalt with three unpaired electrons in localised d_{z^2}, d_{yz} and $d_{x^2-y^2}$ orbitals.

5.2 Aims and Objectives

In this chapter we adopt a similar approach to Chapter 4, beginning with a search for the HS quartet ground state in the unsymmetric limit. Starting from the calculated unsymmetric

Kohn-Sham orbitals we undertake a systematic search for low-lying states by permuting the configuration. We again use a combination of DFT, CASSCF and CASPT2. Combined with the results in Chapter 4 we aim to clarify which states are relevant at both the symmetric and the unsymmetric limits.

5.3 Results and Discussion

5.3.1 DFT Analysis: BP86

Unsymmetric Ground State

The unsymmetric ^4B state of the chloride complex found by McGrady and Pantazis has a formal correspondence with the occupied orbitals the 2-^4E state found in the previous chapter. [102] We also showed in the previous chapter that the 2-^4E state does not remain symmetric when we relaxed the D_4 symmetry constraint, and was not included in the latter part of the discussion. We now return to this point, and conduct a formal search for the ^4B state of the bromide complex. Given the correspondence of the ^4B and 2-^4E electronic structures, we attempt to optimise the ^4B state by starting at the D_4 symmetric 2-^4E structure and relaxing the symmetry constraint to locate the unsymmetric C_4 and C_2 minima. We note here a technical point, that ADF does not support the non-Abelian C_4 point group and all calculations described as 'C_4-symmetric" were in fact performed using the lower C_2 sub-group. In order to maintain the 4-fold rotational symmetry, the electron density in degenerate E states was distributed evenly over the two components of the degenerate e orbitals using the FON protocol. This corresponds to occupation numbers of 0.5 for the two spin-β components. The evolution of the energies and optimized structures of the 2-^4E state as the symmetry is reduced from D_4 to C_4 and then C_2 is shown in Figure 5.2. As we showed in Chapter 4, the D_4 symmetric form has long terminal cobalt-

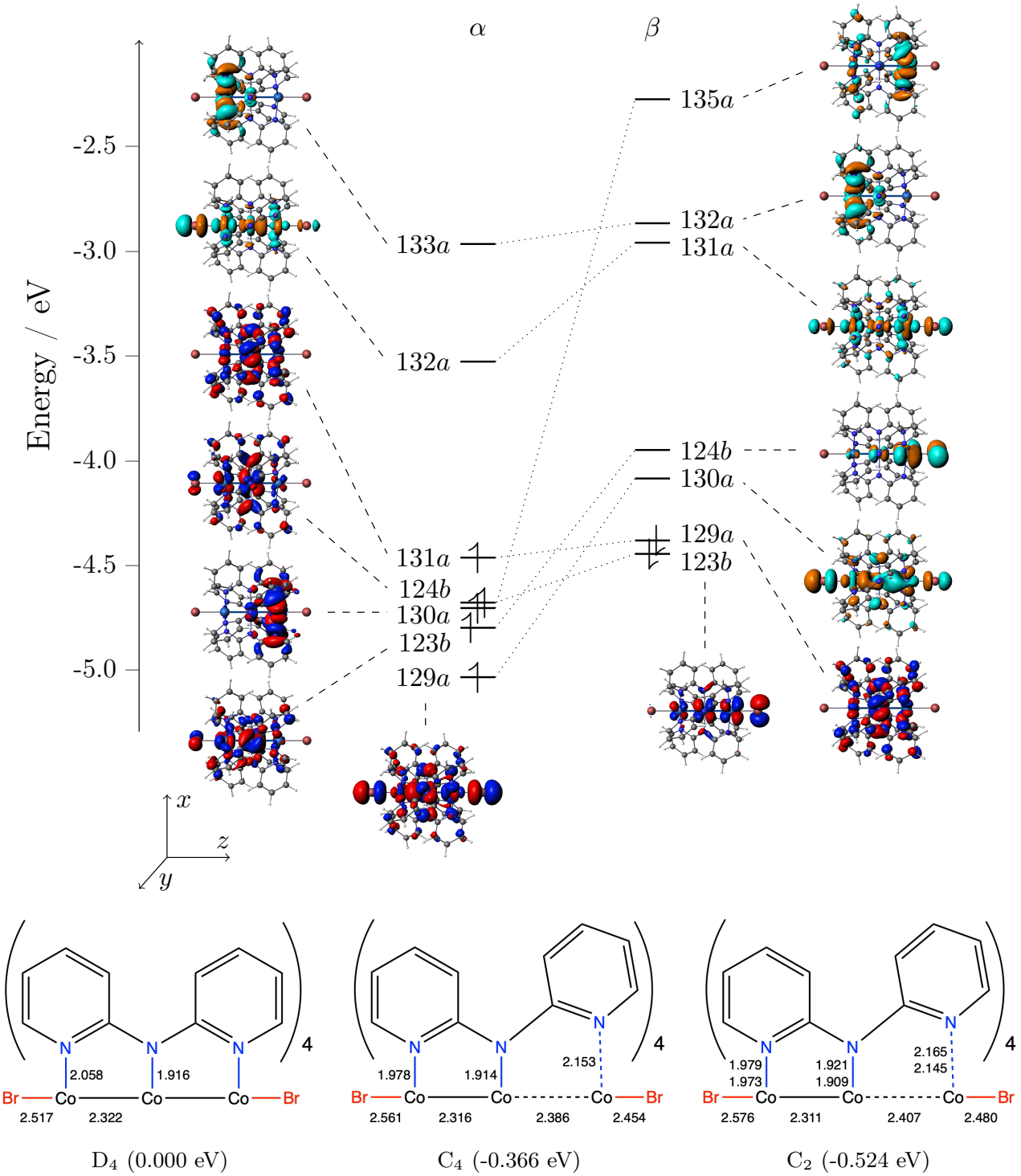

Figure 5.2: MO diagram showing the Kohn-Sham orbital isosurfaces of electron density 0.02 Å^{-1} and schematic structures showing Co-Co, Co-N and Co-Br bond lengths (Å) of the bromide complex ^4B state constrained to D_4, C_4 and C_2 point group symmetry, with energies relative to the D_4 value.

nitrogen bonds (2.058 Å) and the tricobalt chain remains symmetric. When the symmetry constraint is relaxed to C_4 the energy is stabilised by 0.366 eV, and the unsymmetric nature of the Co_3 chain is evident with ΔCo-Co = 0.070 Å, while the Co-Br bond is shorter at the isolated Co centre. The most striking difference compared to the symmetric structure comes in the terminal Co-N bond lengths, which differ by 0.175 Å at the two ends of the molecule, where the cobalt atom with the long Co-N bonds in an unsymmetric structure is defined as $Co_{(3)}$. The other terminal cobalt will be identified as $Co_{(1)}$ and the central cobalt as $Co_{(2)}$. Lifting the symmetry constraint further to C_2 the Jahn-Teller distortion takes effect on the Co-N bonds, seeing two distinct distances at each Co, as well as in the Co-Co-Co chain, seeing a slight increase in the asymmetry. Although the magnitude of both distortions is very small, the energy is stabilised by a further 0.158 eV. In the remainder of this chapter we will use C_2 symmetry for the geometry optimisations. All energies and structures should be assumed to have relaxed to their C_2 minimum and states will be labelled according to C_2 symmetry.

Figure 5.2 also shows the optimised Kohn-Sham orbitals of the C_2 structure. The orbitals are labelled according to the irreducible representations of the C_2 point group. The σ and δ orbitals all transform as a in C_2, and the π as b. The descent in symmetry leads to mixing between orbitals that had different symmetries in the D_4-symmetric form. The most dramatic change in energy caused by this mixing is seen in the $\delta_{x^2-y^2}$ orbitals. When constrained to D_4 symmetry the terminal $d_{x^2-y^2}$ orbitals combine in- and out-of-phase with equal terminal cobalt densities, as seen in orbitals $27b_1$ and $27b_2$ in Chapter 4 Figure 4.3 page 129. In C_2 (and C_4) symmetry both transform as a (b), and the two orbitals mix such that they localise on opposite cobalt centres, as seen in orbitals $130a$ and $133a$ in Figure 5.2. This mixing can only occur when the symmetry in the tricobalt chain is broken. This is a second-order Jahn-Teller effect, which occurs in systems with near degeneracies, in this

case, due to the similar energies of the $27b_1$ and $27b_2$ orbitals in the D_4 limit. This will be explored further in Chapter 6 where we discuss the transition between the symmetric and unsymmetric limits. In the ^4B state the occupied orbital is localised on $Co_{(3)}$ ($130a$) and the unoccupied on $Co_{(1)}$ ($133a$) in the ^4B state. This localisation means the elongation of the Co-N distances associated with the occupation of the $\delta_{x^2-y^2}$ orbitals only occurs at $Co_{(3)}$. The third $\delta_{x^2-y^2}$ is localised on $Co_{(2)}$, and is also unoccupied lying much higher in energy (not shown in the MO diagram). A similar localisation can be seen in the δ_{xy} orbitals, where only the high energy δ_{xy} orbital (localised on the central $Co_{(2)}$) lies in the frontier orbital energy region ($131a$). The localisation can also be seen in the σ and π orbitals, although to a lesser extent. Reducing the symmetry to C_2 also causes a distinct (first-order) Jahn-Teller splitting of the degenerate components of the π orbitals (123b and 124b). The stronger Co-Co σ and π interactions mean the orbitals retain some delocalised character in the unsymmetric limit, especially in the σ manifold, but in general we can separate the orbitals into a set localised primarily on the isolated cobalt and a set localised on the dimer, as originally proposed by Peng *et al.* and shown for the chloride complex by McGrady and Pantazis. [26, 102] This picture is a convenient way to think of the orbitals in the unsymmetric limit, where the Co_2 dimer orbitals are the σ, π and δ bonding and antibonding combinations of each pair of d-orbitals and the orbitals on the isolated cobalt are localised pure d-orbitals. The unpaired electrons in the ^{4}B state are all in orbitals localised on the terminal $Co_{(3)}$: the $d_{x^2-y^2}$, d_{z^2} and d_{yz}. Together they are responsible for the experimentally predicted localised high-spin cobalt. The remaining d_{xy} and d_{xz} orbitals are doubly occupied, while the dimer has a $(\sigma)^2(\pi)^4(\delta_{xy})^2(\delta^*_{xy})^2(\pi^*)^4$ configuration. The following schematic MO diagram shows this separation of the orbitals and the ^4B electronic configuration, and will be used in this work to define new configurations in Figures 5.4-5.6 as we search for new unsymmetric excited states.

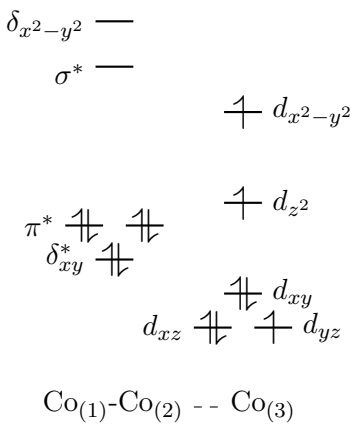

Figure 5.3: Schematic MO diagram and electronic configuration of the unsymmetric ^4B state, split into σ, π and δ orbitals on a $Co_{(1)}$-$Co_{(2)}$ dimer coupled to pure d orbitals on an isolated $Co_{(3)}$.

Unsymmetric Excited State Configurations

Following the pattern established in Chapter 4, we will now use the Kohn-Sham orbitals shown in Figure 5.2 as a framework to explore possible low-lying excited states. The low symmetry presents a technical problem, in that some of the excited states at the unsymmetric limit will correlate with more stable structures in the symmetric limit. Whilst it is possible to impose high symmetry (D_4), it is not possible to prevent a low-symmetry structure from converging to a more symmetric one (where the point group of the low-symmetry structure is a sub-group of the high-symmetry alternative). Thus we cannot impose C_2 symmetry in the same way as we can impose D_4 symmetry. A second limitation imposed by the low (C_2) symmetry is that there are fewer irreducible representations (a and b) compared to the D_4 point group (a_1, a_2, b_1, b_2 and e). Therefore if we are to consider a number of possible configurations, it is inevitable that some will be non-aufbau. Non-aufbau configurations present a computational problem, in that it is very difficult to converge the SCF orbital optimisation. Typically, the occupied and virtual orbitals cross at some point in the process, causing an electron to oscillate between them. A similar phenomenon can occur for systems with near degeneracies at the Fermi level,

where the HOMO and LUMO alternate during the SCF cycle leading to failed convergence, while Jahn-Teller type distortions are a physical manifestation of an attempt to lift such degeneracies. This problem is avoided if the orbitals that cross transform as different representations of the point group in question, and so by specifying the occupancy of each representation of the point group, we can converge on non-aufbau configurations only when the configuration within each representation is itself aufbau.

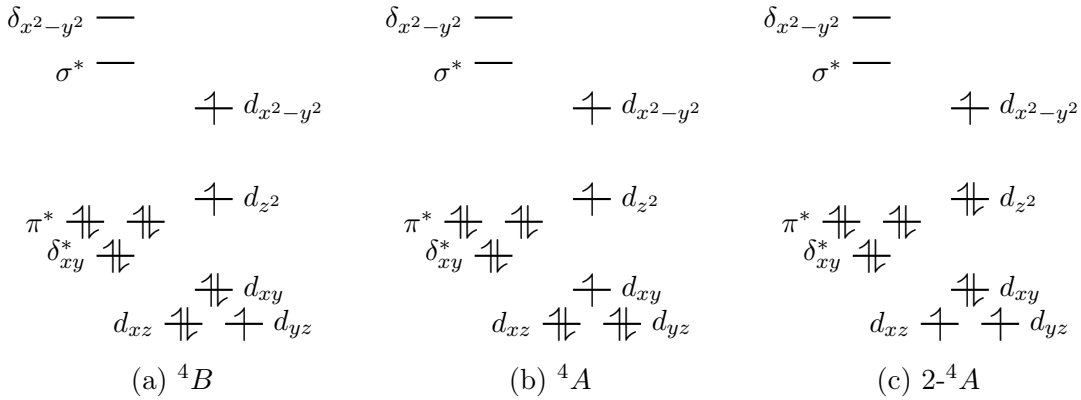

Figure 5.4: Unsymmetric frontier electron configurations of the bromide complex predicted low energy quartet states (a) ^4B, (b) ^4A and (c) 2-^4A.

We consider first the potential low-lying quartet states that can arise from the redistribution of electrons within the frontier orbitals of the ^4B configuration shown in Figures 5.2 and 5.3. This amounts to the permutation of two unpaired electrons within the d_{xz}, d_{yz}, d_{xy} and d_{z^2} orbitals, where we assume configurations with a doubly occupied $d_{x^2-y^2}$ orbital or with any occupation of the σ^* or $\delta_{x^2-y^2}$ orbitals would be too high in energy. In the ^4A state the unpaired electrons are in the d_{xy} and d_{z^2} orbitals, which corresponds to the unsymmetric ^4A state found by Bénard and Rohmer and also McGrady and Pantazis, [29, 102] whilst in a second quartet of A symmetry not previously investigated, 2-^4A, the unpaired electrons are in the d_{xz} and d_{yz} orbitals. The state in which the unpaired electrons are in the d_{yz} and d_{z^2} orbitals would be a non-aufbau configuration because both orbitals d_{xy} and d_{z^2} have a symmetry, so we have been unable to converge

on this configuration.

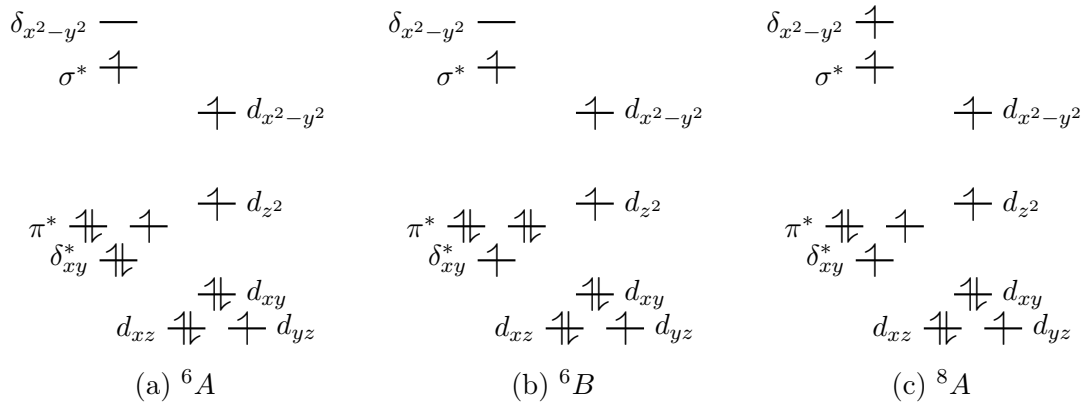

Figure 5.5: Unsymmetric frontier electron configurations of the bromide complex predicted low energy sextet and octet states (a) ^6A, (b) ^6B and (c) ^8A.

Sextet configurations are obtained from the excitation of a β electron into an α hole in the ^4B configuration. In the quantitative MO diagram in Figure 5.2 we see that there are only two frontier β electrons available, in the π^*_{xz} and δ^*_{xy} orbitals, and exciting each leads to the ^6A and ^6B configurations, respectively. The electron must be excited into the σ^* alpha hole, as the $\delta_{x^2-y^2}$ orbital has the same symmetry (a), and such a configuration would be non-aufbau. An octet configuration arises from the promotion of the remaining β electron into the $\delta_{x^2-y^2}$ α hole.

At the opposite extreme, four distinct doublet states can be accessed by taking a

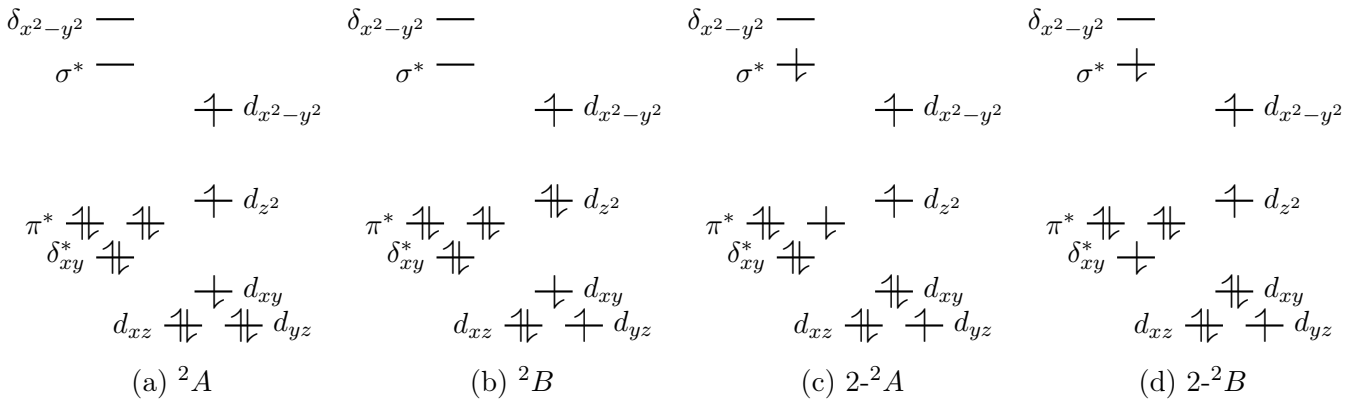

Figure 5.6: Unsymmetric frontier electron configurations of the bromide complex predicted low energy doublet states (a) ^2A, (b) ^2B, (c) 2-^2A and (d) 2-^2B.

single electron from the spin-α manifold of the ^4B state to the spin-β manifold. The d_{yz} and d_{z^2} β holes lie lowest in energy on the isolated cobalt atom, and exciting the d_{xy} α electron into each gives the ^2A and ^2B configurations, respectively. We can also consider excitations on the Co_2 dimer, were we can excite the π^*_{xy} α electron into the σ^* β hole to give the 2-^2A configuration, which corresponds to the unsymmetric doublet (also called 2-^2A) found by McGrady *et al.*, or we can excite the δ^*_{xy} α electron instead to give the 2-^2B configuration.

Excited State Structures

As we did for the predicted low-lying symmetric states, the geometries of each of the configurations shown in Figures 5.4-5.6 have been optimised using the BP86 functional, and the relevant structural data are collected in Table 5.1, alongside the corresponding data for the unsymmetric bromide crystals (toluene/hexane and diethyl ether solvates) at low and high temperatures. Here we report the $Co_{(1)}$-$Co_{(2)}$, $Co_{(2)}$-$Co_{(3)}$, $Co_{(1)}$-Br, $Co_{(3)}$-Br, $Co_{(1)}$-N, $Co_{(2)}$-N and $Co_{(3)}$-N bond lengths to fully describe the asymmetry in the structures. The values in parenthesis correspond to the changes in bond length relative to the D_4 symmetric $^2A_2$ ground state (for the theoretical data) and as the temperature is increased (for the experimental data). In the case of the Co-N bond lengths we report the average value of the Co-N distances on each cobalt atom. In the calculations two distinct distances are allowed by the C_2 point group, while the experimental data shows up to four different distances. In practice, the differences in these bond lengths are small ($\sim$0.02 Å).

We now examine the structural patterns to establish which states most closely correspond to the high temperature unsymmetric crystal structures, and are therefore likely to become thermally populated during the spin-crossover. To facilitate this comparison, in Figure 5.7 we plot the Co-Co, Co-Br and terminal Co-N bond lengths against each other

	$Co_{(1)}$-$Co_{(2)}$	$\Delta Co_{(1)}$-$Co_{(2)}$	$Co_{(2)}$-$Co_{(3)}$	$\Delta Co_{(2)}$-$Co_{(3)}$	$Co_{(1)}$-Br	$\Delta Co_{(1)}$-Br	$Co_{(3)}$-Br	$\Delta Co_{(3)}$-Br
Tol/Hex: 1 110 K	2.310	-	2.389	-	2.588	-	2.626	-
Tol/Hex: 1 295 K	2.312	(0.003)	2.469	(0.080)	2.594	(0.006)	2.546	(-0.080)
Tol/Hex: 2 110 K	2.317	-	2.316	-	2.586	-	2.629	-
Tol/Hex: 2 295 K	2.323	(0.006)	2.433	(0.117)	2.607	(0.020)	2.509	(-0.120)
Et2O 85 K	2.316	-	2.330	-	2.617	-	2.685	-
Et2O 298 K	2.322	(0.006)	2.369	(0.039)	2.608	(-0.009)	2.636	(-0.049)
^{2}A	2.322	(0.001)	2.326	(0.006)	2.616	(0.019)	2.592	(-0.005)
^{2}B	2.284	(-0.036)	2.290	(-0.030)	2.746	(0.149)	2.718	(0.121)
2-^{2}A	2.300	(-0.021)	2.415	(0.095)	2.693	(0.096)	2.483	(-0.114)
2-^{2}B	2.358	(0.038)	2.308	(-0.013)	2.633	(0.036)	2.504	(-0.093)
^{4}B	2.311	(-0.009)	2.407	(0.086)	2.576	(-0.021)	2.480	(-0.117)
^{4}A	2.312	(-0.008)	2.420	(0.100)	2.587	(-0.01)	2.508	(-0.089)
2-^{4}A	2.340	(0.020)	2.308	(-0.012)	2.656	(0.059)	2.498	(-0.099)
^{6}A	2.422	(0.102)	2.279	(-0.042)	2.674	(0.077)	2.470	(-0.127)
^{6}B	2.404	(0.083)	2.397	(0.077)	2.704	(0.107)	2.499	(-0.098)
^{8}A	2.413	(0.092)	2.420	(0.100)	2.499	(-0.098)	2.496	(-0.101)

	$Co_{(1)}$-N	$\Delta Co_{(1)}$-N	$Co_{(2)}$-N	$\Delta Co_{(2)}$-N	$Co_{(3)}$-N	$\Delta Co_{(3)}$-N
Tol/Hex: 1 110 K	1.979	-	1.900	-	2.042	-
Tol/Hex: 1 K	1.981	(0.003)	1.909	(0.008)	2.117	(0.075)
Tol/Hex: 2 K	1.995	-	1.893	-	1.987	-
Tol/Hex: 2 K	1.998	(0.003)	1.906	(0.013)	2.097	(0.010)
Et_2O 85 K	1.982	-	1.905	-	1.988	-
Et_2O 298 K	1.994	(0.012)	1.914	(0.01)	2.029	(0.041)
^{2}A	1.985	(0.001)	1.898	(0.002)	1.988	(0.003)
^{2}B	1.980	(-0.005)	1.909	(0.013)	1.985	(0.001)
2-^{2}A	1.987	(0.002)	1.920	(0.024)	2.160	(0.176)
2-^{2}B	1.985	(0.001)	1.912	(0.016)	2.094	(0.110)
^{4}B	1.976	(-0.009)	1.915	(0.019)	2.155	(0.171)
^{4}A	1.974	(-0.010)	1.908	(0.012)	2.131	(0.146)
2-^{4}A	1.972	(-0.012)	1.924	(0.028)	2.167	(0.182)
^{6}A	1.983	(-0.001)	1.926	(0.030)	2.178	(0.193)
^{6}B	1.975	(-0.010)	1.907	(0.012)	2.156	(0.171)
^{8}A	2.140	(0.155)	1.925	(0.030)	2.143	(0.158)

Table 5.1: Co-Co, Co-Br and Co-N bond lengths (Å) in $Co_3(dpa)_4Br_2$ for each state optimised using the BP86 functional and the experimental data, including the change in bond length (Δ) with respect to the $^2A_2$ ground state and the low temperature structures.

(e.g. $Co_{(1)}$-$Co_{(2)}$ vs. $Co_{(2)}$-$Co_{(3)}$). The diagonal highlighted in the graphs shows where the Co-Co bonds, terminal Co-N and Co-Br bonds are equal, and so the further a state is from the diagonal, the higher the degree of asymmetry in the structure. The Co-N bond lengths highlight the unsymmetric nature of many states, with elongated $Co_{(3)}$-N and contracted $Co_{(1)}$-N distances in the 2-^2A, 2-^2B, ^4B, ^4A, 2-^4A, ^6A and ^6B states, consistent with occupied $d_{x^2-y^2}$ and unoccupied $\delta_{x^2-y^2}$ orbitals. The Co-N bonds do not help to elucidate which of the unsymmetric states correlate best with the experimental structures. In contrast the Co-Co and Co-Br bonds show several states that have structures inconsistent with

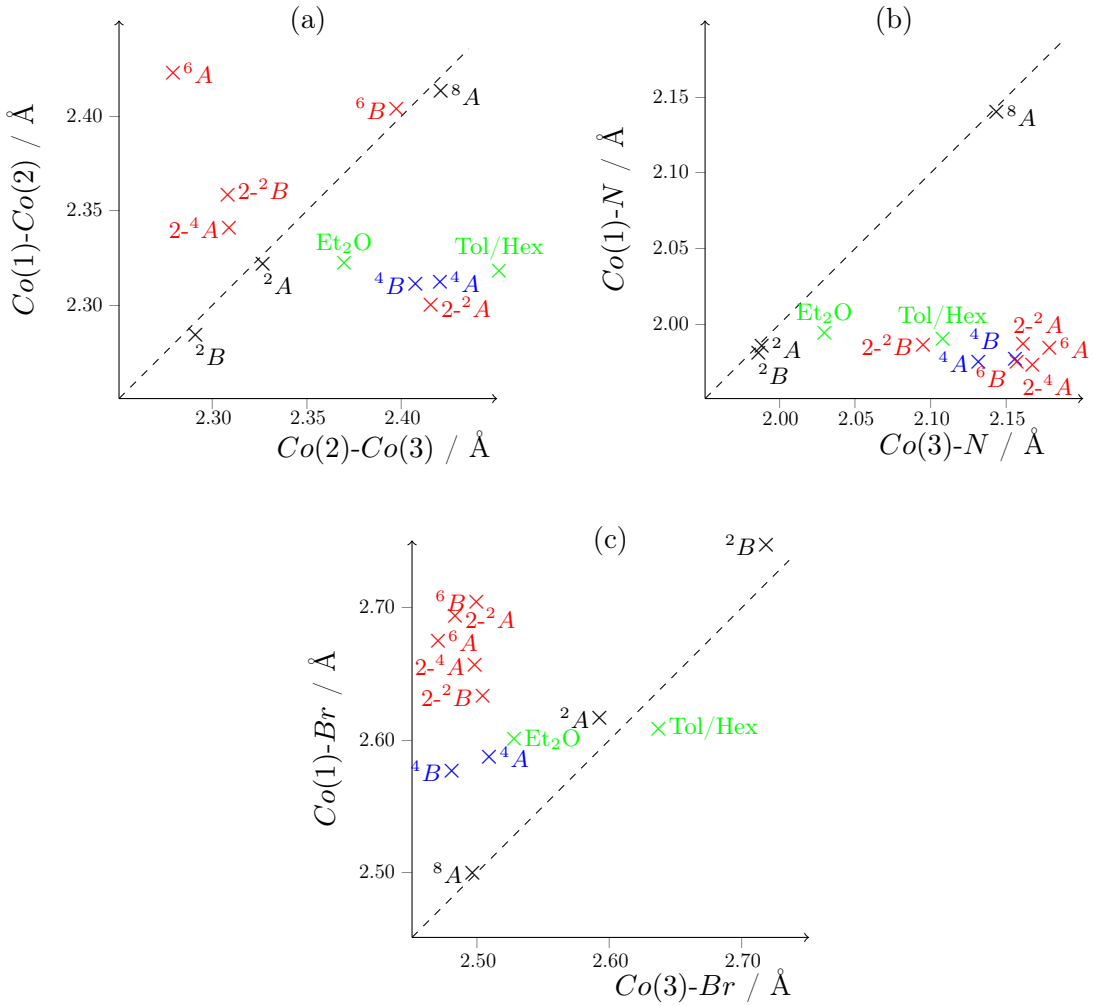

Figure 5.7: (a) Co-Co, (b) Co-Br and (c) terminal Co-N bond lengths for the predicted low-lying unsymmetric states detailed in Figures 5.4-5.6 using the BP86 functional and for the toluene/hexane and diethyl ether solvate crystal structures at 295 K and 298 K, respectively.

experiment. The states that consistently match the experimental structures are plotted in blue, while the states that show inconsistent distances in at least one Co-Co, Co-N or Co-Br bonds are plotted in red. Only the ^4A and ^4B states are consistent with experiment over all three sets of bonds. The Co-Co bonds show that the 2-^2B, 2-^4A and ^6B states have almost symmetric Co-Co-Co chains, where the $Co_{(1)}$-$Co_{(2)}$ is actually slightly longer than the $Co_{(2)}$-$Co_{(3)}$ bond. This feature is even more pronounced in the ^6A state, where the $Co_{(1)}$-$Co_{(2)}$ bond is significantly longer than $Co_{(2)}$-$Co_{(3)}$. The effect could be associated with the σ^* orbital, which we expect to lengthen the $Co_{(1)}$-$Co_{(2)}$ distance. It is occupied in the 2-^2B, ^6B and ^6A states, however this does not explain the behaviour of the 2-^4A state in which it is unoccupied. Examining the Co-Br bonds we notice that all the states have much shorter $Co_{(3)}$-Br bonds than the experimental structures. Instead we focus on the $Co_{(1)}$-Br bond, which is significantly longer in the 2-^2A state than experiment, as are the 2-^4A and sextet states. This could again be explained by the occupied σ^* orbital, which is Co-Br antibonding, although the 2-^2A state does not show the $Co_{(1)}$-$Co_{(2)}$ elongation seen in the other states with occupied σ^* (2-^2B, ^6B and ^6A).

Unlike in the symmetric (D_4) limit, where the mixing between orbitals is restricted by the symmetry, we cannot straightforwardly associate changes in the structure to the predicted electronic configurations. The σ^* occupation detailed in the previous paragraph highlight this, but the effect is most evident in the equilibrium structures of the ^2A, ^2B and ^8A states. The three states lie on the symmetric diagonal for the Co-Co, terminal Co-N and Co-Br bonds and converge on a symmetric geometry during the optimisation, and so they are not viable candidates for the ground state in the unsymmetric limit. They are plotted in black to differentiate from the unsymmetric structures. Examining the bond lengths shown in Table 5.1 shows that each state relaxes to a geometry almost identical to the $^2A_2$, ^2E and $^8B_1$ structures in D_4 symmetry, respectively. The optimised orbitals

of these symmetric states bare little resemblance to those of the ^4B state, where mixing and PES crossing leads to orbitals that more closely resemble the symmetric framework described in Chapter 4.

	$\langle \hat{\mathbf{S}}^{\mathbf{2}} \rangle$	**SC**	**Q Co$_{(1)}$**	**Q Co$_{(2)}$**	**Q Co$_{(3)}$**	**ρ Co$_{(1)}$**	**ρ Co$_{(2)}$**	**ρ Co$_{(3)}$**
^{2}A	0.785	0.035	0.429	1.012	0.422	0.467	-0.140	0.468
^{2}B	0.757	0.007	0.441	1.023	0.431	0.297	0.431	0.316
2-^{2}A	2.337	1.587	0.469	1.004	0.415	-0.832	-0.620	2.235
2-^{2}B	1.776	1.026	0.381	1.014	0.449	0.601	-0.458	0.553
^{4}B	3.800	0.050	0.454	0.990	0.431	0.188	0.031	2.314
^{4}A	3.818	0.068	0.454	1.003	0.420	0.345	-0.054	2.174
2-^{4}A	4.081	0.331	0.423	0.993	0.466	-0.344	0.630	2.387
^{6}A	8.787	0.037	0.416	0.987	0.477	0. 913	1.056	2.437
^{6}B	8.795	0.045	0.437	0.995	0.476	0.854	0.955	2.433
^{8}A	15.811	0.061	0.453	0.981	0.450	2.428	1.025	2.429

Table 5.2: $\langle \hat{S}^2 \rangle$, spin contamination ($SC$) and cobalt charge (Q) and spin densities (ρ) for the predicted low-lying unsymmetric states detailed in Figures 5.4-5.6 using the BP86 functional.

Excited State Wavefunctions

The spin density distributions (ρ), shown in Table 5.2, confirm the qualitative picture of bonding set out in Figure 5.3 for the ^4B state. In particular the value of ρ(Co$_{(1)}$, Co$_{(2)}$, Co$_{(3)}$) = (0.188, 0.031, 2.314) corresponds to a high-spin Co$_{(3)}$ coupled to a diamagnetic Co$_{(1)}$-Co$_{(2)}$ dimer, where the low spin densities on Co$_{(1)}$ and Co$_{(2)}$ are indicative of a covalent interaction. The charge density distributions (Q) do not suggest any electron transfer between the cobalt atoms, and the spin crossover is localised on the Co$_{(3)}$. Similarly large Co$_{(3)}$ spin density is apparent in the ^4A and 2-^4A states. In the ^6A and ^6B cases, the large spin on the isolated Co is now accompanied by substantial spin density localised on the Co$_2$ unit (Co$_{(1)}$-Co$_{(2)}$). We can interpret this as being indicative of a high-spin Co(II) centre, ferromagnetically coupled to a Co$_2$ unit in a locally triplet excited state. Conversely, the 2-^2A state corresponds to a high-spin Co(II) centre antiferromagnetically coupled to a

Co_2 unit in a local spin triplet state where $\rho(Co_{(1)}, Co_{(2)}, Co_{(3)})$ = (-0.832, -0.620, +2.235). The high $\left\langle \hat{S}^2 \right\rangle$ value of 2.337 is indicative of substantial spin contamination, typical of an antiferromagnetic state.

Excited State Energies

The energies of the low-lying states described in the previous section are summarised in Figure 5.8, relative to the energy of the ^4B state described previously. As previously discussed, we cannot impose a symmetry restriction on the system in such a way to ensure the structure remains unsymmetric during a geometry optimisation. By using single point calculations we can instead impose a geometry, and enforce an unsymmetric structure in states that would otherwise converge to a symmetric structure if allowed to relax. In Figure 5.8, we therefore present the single point energies (green curve) of each state at the unsymmetric ^4B geometry (Figure 5.2 page 156) alongside the corresponding energies of each state at their optimised geometry (black curve) in Figure 5.8. All calculations are performed with the BP86 functional.

Of these excited state configurations, the lowest lying single point energy is the ^2A state, only 0.035 eV above the ^4B state, while the 2-^4A and ^4A and states lie at 0.042 and 0.177 eV, respectively. The ^2E and 2-^2A states lie at 0.227 and 0.397 eV, while the 2-^2B and both sextets, ^6B and ^6A, lie above 0.5 eV. The 8A state has a much higher excitation energy of 1.416 eV. If we compare this manifold of states to the symmetric case discussed in Chapter 4, we note that the excitation energies are generally much lower. In D_4 symmetry with the BP86 functional, only the low-lying doublets (^2E and $^2B_2$ states), had excitation energies below 0.381 eV, while the quartet, sextet and octet states all had excitation energies between 0.910 eV and 1.987 eV. Considering the excited state energies after they are allowed to relax to their respective minima, the most striking feature of

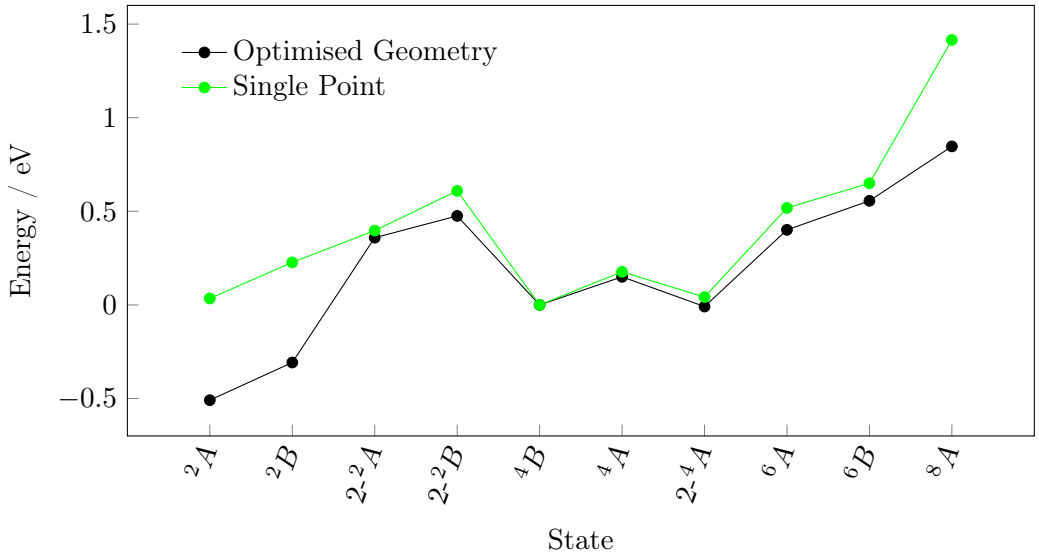

Figure 5.8: Relative energies (eV) to the ^4B ground state of the bromide complex predicted low-lying doublet, quartet, sextet and octet states detailed in Figures 5.4-5.6 at the ^4B geometry (green) and at the optimised geometry of each state (black) using the BP86 functional.

Figure 5.8 is that the ^2A and ^2B states are significantly stabilised, and in fact now lie 0.509 eV and 0.308 eV lower than the ^4B state. A similar stabilisation is seen in the ^8A state, although it is still high-lying at the relaxed geometry. The common feature of these states is that they all relax to a symmetric structure, and the configurations are therefore intrinsically incompatible with an unsymmetric structure. In all other cases, the relaxation energy is much smaller, and indeed the optimised structural data show that all other states remain unsymmetric in their local minima.

5.3.2 DFT Analysis: Functional Dependence

Energies

As we showed in Chapter 4, it is important to check DFT results are consistent using multiple functionals. In Figure 5.9 we present the energies of all the unsymmetric states optimised with the BP86, BLYP, OLYP, OPBE, B3LYP, B3LYP* and SCAN functionals, excluding the symmetric ^2A, ^2B and ^8A from the results. In general the spin state energies

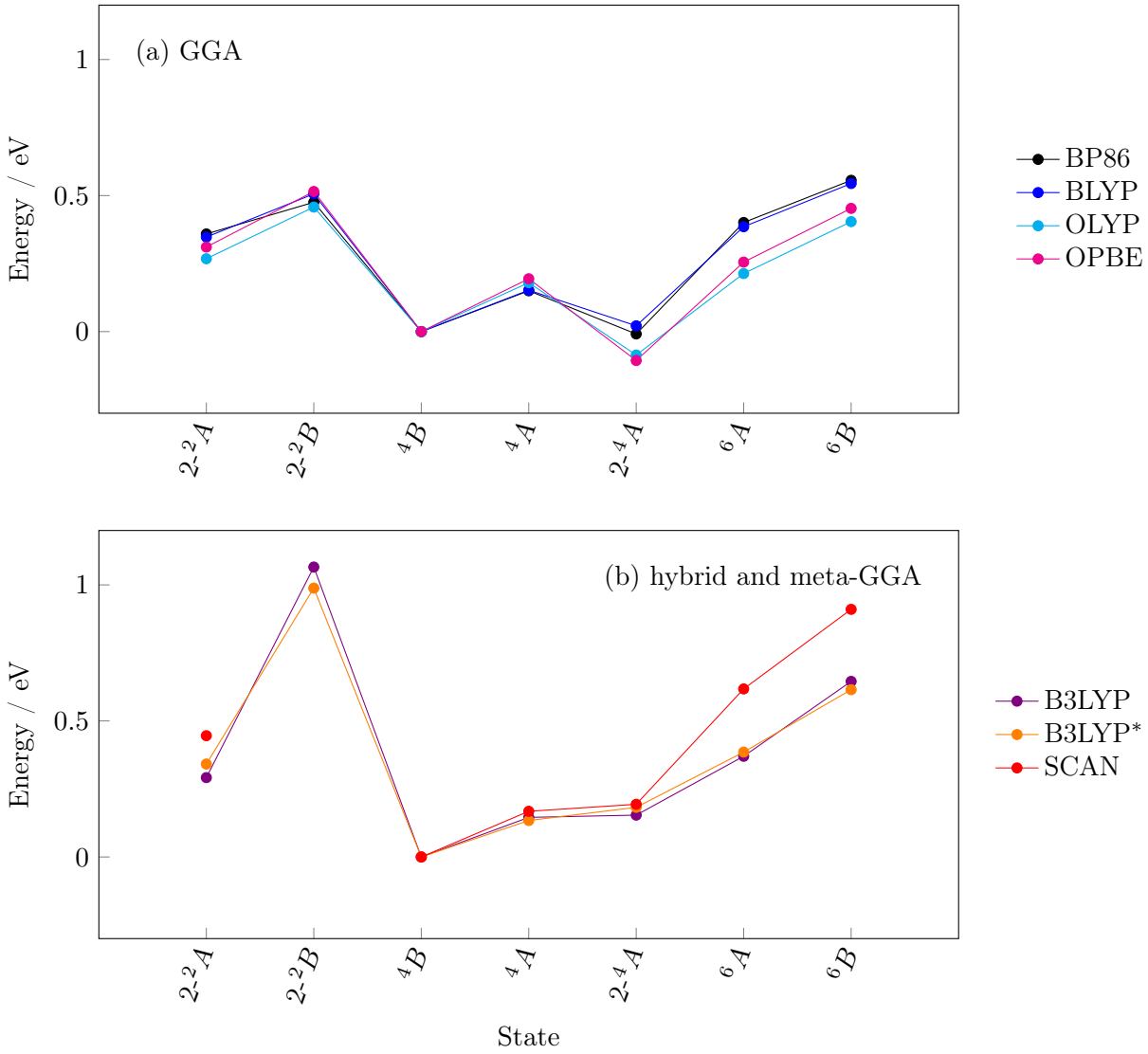

Figure 5.9: Relative energies (eV) to the ^4B state of the bromide complex predicted low-lying unsymmetric doublet, quartet, sextet states using the (a) GGA (BP86, BLYP, OLYP and OPBE) and (b) hybrid (B3LYP and B3LYP*) and meta-GGA (SCAN) functionals.

are predicted more consistently by the different functionals compared to the symmetric limit, with the exception of the 2-^2B state which is predicted to have a much higher relative energy by the hybrids. However, as the spin state energies all lie much closer together, the functionals do not agree on the ground state. The BP86, OLYP and OPBE functionals all predict the 2-^4A state to have the lowest energy, whilst the B3LYP, B3LYP* and SCAN functionals predict the ^4B state to be the most stable. BLYP is the only GGA functional to agree with the hybrid and SCAN results, although the 2-^4A energy is only

0.021 eV above the ^4B. In fact, all the quartet states lie very close in energy for all the functionals. For the remaining states the GGA functionals show lower excitation energies in general, which are all quite similar for the 2-^2A, 2-^2B, ^6A and ^6B states. The most obvious difference is the stabilisation of the 2-^4A and sextet states (∼0.2 eV) by the OPTX exchange functional in OLYP and OPBE. The hybrid and SCAN functionals predict a similar energetic ordering of the four states: 2-$^2A \approx {}^6A < {}^6B < 2\text{-}^2B$. Here we note that we were not able to converge the 2-^2B state using SCAN.

Structures and Wavefunctions

We will now examine the effect of the functional choice on the structure and wavefunction at the unsymmetric limit. Figure 5.10 depicts the Co-Co and terminal Co-N bonds of the ^4B state for the range of functionals. The distribution of the data points representing each functional is very similar to those in Figure 4.9 in the previous chapter, where OPBE and SCAN give the shortest bonds, followed by BP86, OLYP, BLYP B3LYP* and B3LYP. The spin densities also show similar behaviour to the symmetric limit across the range

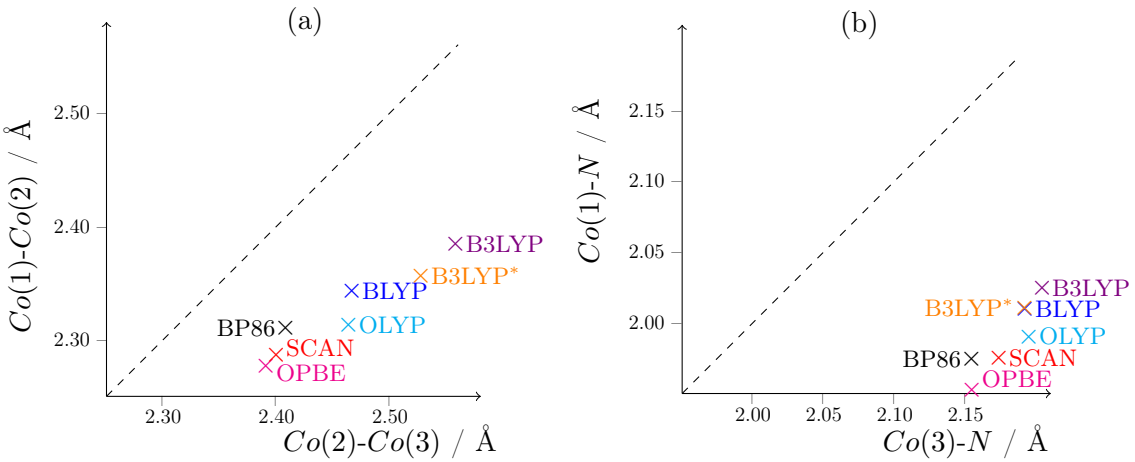

Figure 5.10: (a) Co-Co and (b) terminal Co-N bond lengths for ^4B state using the BP86, BLYP, OLYP, OPBE, B3LYP, B3LYP* and SCAN functionals.

of functionals, shown in Table 5.3. The GGA functionals all predict the same bonding picture for the ^4B state, with a covalently bonded Co_2 dimer coupled to an isolated high-spin $Co_{(3)}$. The hybrid and SCAN functionals, however, show an antiferromagnetically exchange coupled Co_2 unit which is in turn antiferromagnetically coupled to the isolated high-spin $Co_{(3)}$. This is reflected in the larger spin contamination. They also show an increased localisation of the wavefunction, with higher spin densities on all cobalt atoms increasing SCAN $<$ B3LYP* $<$ B3LYP.

^{4}**B**	$\left\langle \hat{\mathbf{S}}^{\mathbf{2}} \right\rangle$	**SC**	ρ **Co**$_{(1)}$	ρ **Co**$_{(2)}$	ρ **Co**$_{(3)}$
BP86	3.800	0.050	0.188	0.032	2.309
BLYP	3.799	0.049	0.188	-0.002	2.332
OLYP	3.835	0.085	0.069	0.065	2.397
OPBE	3.837	0.087	0.073	0.094	2.375
B3LYP	4.373	0.623	0.775	-0.776	2.629
B3LYP*	4.201	0.451	0.660	-0.637	2.565
SCAN	3.997	0.247	0.534	-0.437	2.523

Table 5.3: $\left\langle \hat{S}^2 \right\rangle$, spin contamination ($SC$) and cobalt spin densities (ρ) for the ^4B state using the using the BP86, BLYP, OLYP, OPBE, B3LYP, B3LYP* and SCAN functionals.

5.3.3 MCSCF Analysis

CASSCF and CASPT2

We now describe an unsymmetric CASSCF reference wavefunction that corresponds to the symmetric CAS(21,14) active space generated for the symmetric ground state. The BP86 optimised ^4B structure is used throughout for the following calculations. C_2 symmetry is imposed and the wavefunction optimised for a ^4B configuration using OpenMolcas. In D_2 symmetry the π orbitals are split between the b_2 and b_3 representations. In C_2 they all belong to the b representation. When we optimise just the lower of the two ^4B configurations, the π_{xz} orbitals rotate with the inactive space to bring in orbitals that correlate with the hole in the $Co_{(3)}$ d_{yz} orbital. To overcome this issue we run the same

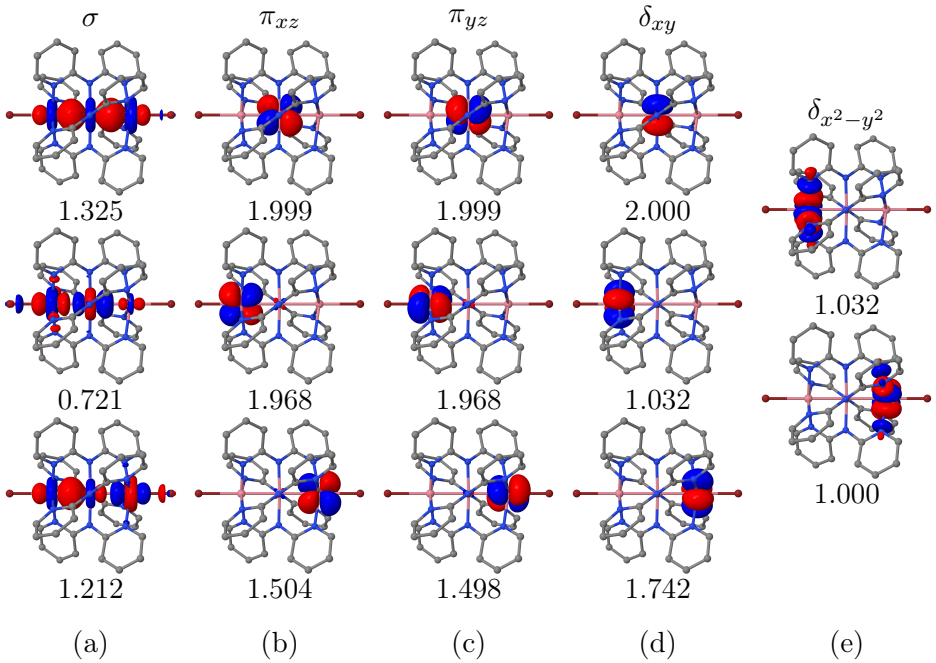

Figure 5.11: CAS(21,14) active space natural orbitals of (a) σ, (b) π_{xz}, (c) π_{yz}, (d) δ_{xy} and (e) $\delta_{x^2-y^2}$ symmetry for $Co_3(dpa)_4Br_2$ with ^4B state averaged natural occupation numbers at the BP86 ^4B geometry.

calculation using a state-averaged (SA-CASSCF) calculation, [338] averaging over the first two states, the second of which is only slightly higher in energy due to the Jahn-Teller distortion, and has the $Co_{(3)}$ d_{xz} orbital singly occupied, fixing it in the active space. The natural orbitals of the resulting SA-CAS(21,14) calculation are presented in Figure 5.11 with the state-averaged natural occupation numbers. The orbitals in the top two rows are those localised on the dimer, and the orbitals on the bottom row are those localised on the isolated cobalt.

The π and δ orbitals are localised on each of the individual Co atoms, compared to the DFT results which show significant mixing. The σ^* orbital is localised primarily on the Co_2 dimer, while the σ and $Co_{(3)}$ d_{z^2} orbitals are significantly mixed. The orbital with greater d_{z^2} character has a lower occupation number and shows an antibonding interaction between the $Co_{(2)}$ and $Co_{(3)}$ atoms. The orbital with greater σ character has a larger occupation number and a bonding interaction between the $Co_{(2)}$ and $Co_{(3)}$ atoms.

Co_2 Dimer Configuration	Lone Co Configuration	Weight
$(\sigma)^2(\pi)^4(\delta_{xy})^2(\delta^*_{xy})^2(\pi^*)^4(\delta^*_{x^2-y^2})^0(\sigma^*)^0$	$(d_{xz})^2(d_{yz})^1(d_{xy})^2(d_{z^2})^1(d_{x^2-y^2})^1$	0.15573
$(\sigma)^2(\pi)^4(\delta_{xy})^2(\delta^*_{xy})^2(\pi^*)^4(\delta^*_{x^2-y^2})^0(\sigma^*)^0$	$(d_{xz})^1(d_{yz})^2(d_{xy})^2(d_{z^2})^1(d_{x^2-y^2})^1$	0.14934
$(\sigma)^u(\pi)^4(\delta_{xy})^2(\delta^*_{xy})^2(\pi^*)^4(\delta^*_{x^2-y^2})^0(\sigma^*)^0$	$(d_{xz})^2(d_{yz})^1(d_{xy})^2(d_{z^2})^2(d_{x^2-y^2})^1$	0.09003
$(\sigma)^u(\pi)^4(\delta_{xy})^2(\delta^*_{xy})^2(\pi^*)^4(\delta^*_{x^2-y^2})^0(\sigma^*)^0$	$(d_{xz})^1(d_{yz})^2(d_{xy})^2(d_{z^2})^2(d_{x^2-y^2})^1$	0.08647
$(\sigma)^2(\pi)^4(\delta_{xy})^2(\delta^*_{xy})^2(\pi^*)^4(\delta^*_{x^2-y^2})^0(\sigma^*)^0$	$(d_{xz})^2(d_{yz})^1(d_{xy})^1(d_{z^2})^2(d_{x^2-y^2})^1$	0.082
$(\sigma)^2(\pi)^4(\delta_{xy})^2(\delta^*_{xy})^2(\pi^*)^4(\delta^*_{x^2-y^2})^0(\sigma^*)^0$	$(d_{xz})^1(d_{yz})^2(d_{xy})^1(d_{z^2})^2(d_{x^2-y^2})^1$	0.08018
$(\sigma)^0(\pi)^4(\delta_{xy})^2(\delta^*_{xy})^2(\pi^*)^4(\delta^*_{x^2-y^2})^0(\sigma^*)^2$	$(d_{xz})^2(d_{yz})^1(d_{xy})^2(d_{z^2})^1(d_{x^2-y^2})^1$	0.05372
$(\sigma)^0(\pi)^4(\delta_{xy})^2(\delta^*_{xy})^2(\pi^*)^4(\delta^*_{x^2-y^2})^0(\sigma^*)^2$	$(d_{xz})^1(d_{yz})^2(d_{xy})^2(d_{z^2})^1(d_{x^2-y^2})^1$	0.05154
$(\sigma)^1(\pi)^4(\delta_{xy})^2(\delta^*_{xy})^2(\pi^*)^4(\delta^*_{x^2-y^2})^0(\sigma^*)^2$	$(d_{xz})^2(d_{yz})^1(d_{xy})^2(d_{z^2})^0(d_{x^2-y^2})^1$	0.04887
$(\sigma)^1(\pi)^4(\delta_{xy})^2(\delta^*_{xy})^2(\pi^*)^4(\delta^*_{x^2-y^2})^0(\sigma^*)^2$	$(d_{xz})^1(d_{yz})^2(d_{xy})^2(d_{z^2})^0(d_{x^2-y^2})^1$	0.04691

Table 5.4: Principal configurations and their weights for the ^4B state within the CAS(21,14) active space shown in Figure 5.11.

The natural occupation numbers show that the configuration actually has an electron pair split between the $Co_{(1)}$ d_{xy} and $Co_{(1)}$ $d_{x^2-y^2}$ orbitals. This effect was seen in the excited quartet states of the symmetric structure, where an open-shell singlet was formed in the subspace spanned by the $\delta^*_{x^2-y^2}$ and δ_{xy} orbitals of several states. Such configurations are overstabilised by CASSCF, and because the states with doubly occupied $\delta^*_{x^2-y^2}$ orbitals were so high in energy, we were unable to perform a CASPT2 calculation. Fortunately, in the unsymmetric limit the configurations that corresponds to the ^4B states with a doubly occupied $Co_{(1)}$ d_{xy} orbital are lower in energy. They are the fifth (singly occupied d_{yz}) and sixth (singly occupied d_{xz}) excited states in the CAS(21,14) active space shown in Figure 5.11 (employing CIONLY to prevent the SCF cycle and fix the orbitals). The multi-configurational expansion of the fifth excited state shows several determinants contributing to the wavefunction. The highest weight orbitals that compose ∼85% of the CASSCF wavefunction are detailed in Table 5.4 for the fifth state. The majority of the configurations have a $(\pi)^4(\delta_{xy})^2(\delta^*_{xy})^2(\pi^*)^4(\delta^*_{x^2-y^2})^0$ Co_2 dimer electronic structure and a $(d_{xz})^2(d_{yz})^1(d_{xy})^2(d_{z^2})^1(d_{x^2-y^2})^1$ electronic structure on the isolated Co. As we saw in the ground state, the multi-configurational character can mainly be attributed to correlation within the σ framework. Correlation between the dimer σ and $Co_{(3)}$ d_{z^2} orbital in the

third and fourth largest weight configurations actually sees the transfer of an electron from the dimer to the isolated cobalt. We see correlation between the $Co_{(3)}$ d_{xy} β electron to the $Co_{(3)}$ d_{z^2} orbitals in the fifth and sixth largest weight configurations, and between the dimer σ and σ^* orbitals and the $Co_{(1)}$ d_{xy} and σ^* orbitals in the remaining configurations. The unpaired electron in the π framework switches between the π_{yz} and π_{xz} in every other configuration. The weights of the configurations with the unpaired electron in the π_{yz} are always slightly greater. The sixth excited state shows the same pattern except the configurations with the unpaired electron in the π_{xz} orbital have the greater weight.

We now use the CAS(21,14) active space to generate excited state multi-reference wavefunctions in the unsymmetric limit, as we did in the symmetric limit. Table 5.5 shows the CASSCF and, where possible, CASPT2 energies, reference weights and the natural orbital occupation numbers for states found by the DFT analysis, and some new states identified with the CASSCF calculations. The positions of the orbital occupation numbers in the table corresponds to the layout of the orbitals in Figure 5.11. At the CASSCF level the ^4B state with an open-shell configuration within the $Co_{(1)}$ d_{xy} and $Co_{(1)}$ $d_{x^2-y^2}$ orbitals (labelled OS in Table 5.5) has a lower energy than the state with paired $Co_{(1)}$ d_{xy} electrons. Unlike in the symmetric limit, however, the state with paired $Co_{(1)}$ d_{xy} electrons is sufficiently low-lying that we are able to perform a CASPT2 calculation on both states. The second-order correction reorders the energies and the ^4B state with a doubly occupied $Co_{(1)}$ d_{xy} orbital has the lower energy. CASSCF also predicts the ^4A state to lie below the ^4B, but again the CASPT2 correction reorders the states, although they still have very similar energies separated by only 0.048 eV at the CASPT2 level. At both CASSCF and CASPT2 levels the ^4A and ^4B states lie lower than the 2-^4A. The ^2A configuration that most resembles the ground state has a large excitation energy at both CASSCF and CASPT2 levels. At the symmetric limit the ground state had equal occupations of the δ_{xy}^{nb}

	CASSCF	CASPT2	Ref. Wt	σ	π_{xz}	π_{yz}	δ_{xy}	$\delta_{x^2-y^2}$
^{4}B	0.000	0.000	0.283	1.398	1.999	2.000	2.000	0.056
				0.609	1.976	1.976	1.985	1.000
				1.001	2.000	1.001	1.998	
^{4}B (OS)	-0.313	0.005	0.286	1.283	1.998	2.000	2.000	1.032
				0.718	1.968	1.968	1.032	1.000
				1.003	2.000	1.002	1.997	
^{4}A	-0.100	0.048	0.282	1.397	2.000	2.000	2.000	0.057
				0.609	1.976	1.976	1.985	1.061
				1.001	1.939	1.939	1.061	
2-^{4}A	0.293	0.260	0.288	1.984	1.991	1.991	2.000	0.057
				0.624	1.976	1.976	1.985	1.000
				1.400	1.009	1.009	1.998	
^{2}A	1.251	1.161	0.246	1.396	2.000	1.999	2.000	0.057
				0.613	1.975	1.975	1.985	0.115
				1.016	1.952	1.950	1.967	
^{6}A	0.783	-	-	1.637	1.764	1.743	2.000	0.061
				1.040	1.956	1.959	1.984	1.001
				1.426	1.253	1.276	1.899	
2-^{6}A	-0.470	-	-	1.307	2.000	2.000	2.000	1.032
				0.694	1.968	1.968	1.032	1.061
				1.000	1.939	1.939	1.061	
3-^{6}A	-0.050	-	-	1.286	1.995	1.999	2.000	1.000
				0.753	1.958	1.061	1.940	1.000
				1.025	1.983	1.003	1.997	
^{6}B	0.783	-	-	1.004	1.149	2.000	2.000	0.066
				1.852	1.971	1.896	1.982	1.058
				1.085	1.881	1.941	1.116	
2-^{6}B	-0.158	0.185	0.243	1.281	1.996	2.000	2.000	1.000
				0.730	1.013	1.991	1.986	1.061
				1.004	1.939	1.939	1.061	

Table 5.5: Relative energies (eV) to the ^4B state of the bromide complex at the CASSCF and CASPT2 level at the BP86 ^4B geometry, including CASSCF natural orbital occupation numbers of the CAS(21,14) active space shown in Figure 5.11 and CASPT2 reference weights.

and δ^*_{xy}, as both orbitals correlated into the $\delta_{x^2-y^2}$ set equally. The same was true of the π^{nb} and π^* orbitals. In the unsymmetric limit the d_{xy}, d_{xz} and d_{yz} on the isolated cobalt with long Co-N distances all have lower occupations than the corresponding δ^*_{xy} and π^* orbitals localised on $\mathrm{Co}_{(1)}$, while the $d_{x^2-y^2}$ on $\mathrm{Co}_{(3)}$ has greater occupation than the $\delta^*_{x^2-y^2}$ localised on $\mathrm{Co}_{(1)}$. This highlights the importance of the occupation of the $d^*_{x^2-y^2}$ orbital to the unsymmetric behaviour. The sextet states suffer from similar problems to the doublet states in the symmetric limit, where the low energy states do not have configurations with an electron excited into the σ^* orbital, instead exciting into the $\delta^*_{x^2-y^2}$ orbital localised on $\mathrm{Co}_{(1)}$. The occupations that most resemble the ^6A and ^6B states show similar occupation numbers, differing by an electron transfer between the d_{xy} and d_{xz} orbitals. Their energies are almost identical, separated by only 0.0006 eV, but high-lying compared to the quartets and other sextets. The predicted lowest energy sextet state, 2-^6A with singly occupied δ^*_{xy} and $\delta^*_{x^2-y^2}$ orbitals, corresponds to the open-shell ^4B state but with aligned spins. The second lowest energy state, 2-^6B, is related to 2-^6A by the transfer of a π^*_{xz} electron into the δ^*_{xy} orbital, and the final sextet, 3-^6A, related to 2-^6B by the transfer of a d_{xz} electron into the d_{xy}. Because the lower symmetry creates a greater number of determinants, we found the CASPT2 calculation of these sextets to be intractable.

5.4 Conclusions

In this chapter we consider a range of unsymmetric excited states, in extension of the work in the previous chapter on the symmetric states. Only by doing so can we hope to understand the full breadth of behaviours exhibited in the experimental work, which shows many crystals with varying degrees of asymmetry. Two unsymmetric quartet states stand out from the structural analysis, where the population of either the ^4B or ^4A states would be consistent with experiment. The elongation of both the $\mathrm{Co}_{(2)}$-$\mathrm{Co}_{(3)}$ and $\mathrm{Co}_{(3)}$-N bonds

whilst maintaining short $Co_{(1)}$-$Co_{(2)}$ and $Co_{(1)}$-N distances in both states is consistent with the behaviour of both the $Co_3(dpa)_4Cl_2 \cdot Et_2O$ and $Co_3(dpa)_4Cl_2 \cdot 1.75Toluene \cdot 0.5Hexane$ crystals. Again, the DFT structures seem to be most useful for the prediction the electronic structure. The calculated spin state splitting energies highlight the intricate nature of the spin crossover process. DFT predicts either a ^4B or $2-^4A$ ground state in the unsymmetric limit. MCSCF predicts the ^4A state to be the ground state, while the CASPT2 correction reorders the energies to predict a ^4B state. Results at both the symmetric and unsymmetric limits are consistent with the behaviour of the chloride complex. The DFT and CASSCF results also confirm the importance of the $\delta^*_{x^2-y^2}$ framework in the symmetric-unsymmetric transition, as seen in the previous theoretical work from McGrady and Pantazis. [102] This will be explored in more detail in the following chapter, where we take the ^4B state forward with the $^2A_2$, ^4E and $^6A_2$ states identified in the previous chapter to analyse the underlying mechanisms by which the structure distorts.

Chapter 6

The Symmetric-Unsymmetric Transition of $Co_3(dpa)_4Br_2$

6.1 Introduction

In the previous two chapters we have explored the electronic structures of the symmetric and unsymmetric limits available to the tricobalt EMACs. However, the vast majority of the available crystal structures fall between these two limits. In this chapter, we discuss two different models that could account for these observations, one based on a continuously variable doublet potential surface, modelled using fractional occupation number DFT, the other assuming an equilibrium between distinct LS and HS forms. The experimental and theoretical work shows the crystalline environment has a strong influence on the structure and properties of the EMACs. In the latest experimental work from the Hillard group, various crystal structures have been categorised as either symmetric or unsymmetric based on their low temperature structure, but these structures are in fact strongly temperature dependent. [38] Crystals of the bromide complex that are symmetric at low temperatures either remain symmetric as the temperature increases (hexane

and dichloromethane solvates) or, alternatively, develop an increased degree of asymmetry (diethyl ether and toluene/hexane solvates). In all cases, crystals that have an unsymmetric structure at low temperatures undergo an increase in the degree of asymmetry as the temperature increases. Hillard *et al.* present the temperature dependent structures of the $Co_3(dpa)_4Cl_2{\cdot}Et_2O$ and $Co_3(dpa)_4Cl_2{\cdot}2CH_2Cl_2$ crystals side by side, showing a convergence of the high-temperature $Co_3(dpa)_4Cl_2{\cdot}Et_2O$ structure with the low-temperature $Co_3(dpa)_4Cl_2{\cdot}2CH_2Cl_2$ structure, shown in the Introduction (Figure 1.18). This suggests that the structures of the different crystals are fundamentally linked, with a consistent mechanism driving the symmetric-unsymmetric transition where the crystalline environment and temperature govern the extent to which each crystal structure distorts. Examining the experimental data for the bromine crystal shows a similar relationship exists between the $Co_3(dpa)_4Br_2{\cdot}Et_2O$ and $Co_3(dpa)_4Cl_2{\cdot}1.75$Toluene$\cdot 0.5$Hexane crystals, shown in Figure 6.1. There are two crystallographically independent EMAC molecules in $Co_3(dpa)_4Cl_2{\cdot}1.75$Toluene$\cdot 0.5$Hexane, and the one defined as Molecule 1 is shown. Understanding the change in the electronic structures of the various states at a range of geometries will be key to understanding the behaviour of the different crystals.

In the theoretical work from McGrady and Pantazis on the chloride complex, a model to describe the change in structure was developed based on a continuous, flat doublet potential energy surface that linked the symmetric and unsymmetric limits. [102] Starting at an unsymmetric geometry, they identified a ^2B (using C_2 symmetry) state 0.31 eV above the ^4B state (single point energy), which, when optimised, relaxed to a symmetric minimum. The smooth convergence of the doublet in the unsymmetric limit to a symmetric minimum prompted the authors to suggest that it connects the symmetric and unsymmetric limits of the tricobalt EMAC, as described by the schematic PES diagram shown in the Introduction (Figure 1.22). The ground state and ^2B minima lie in the

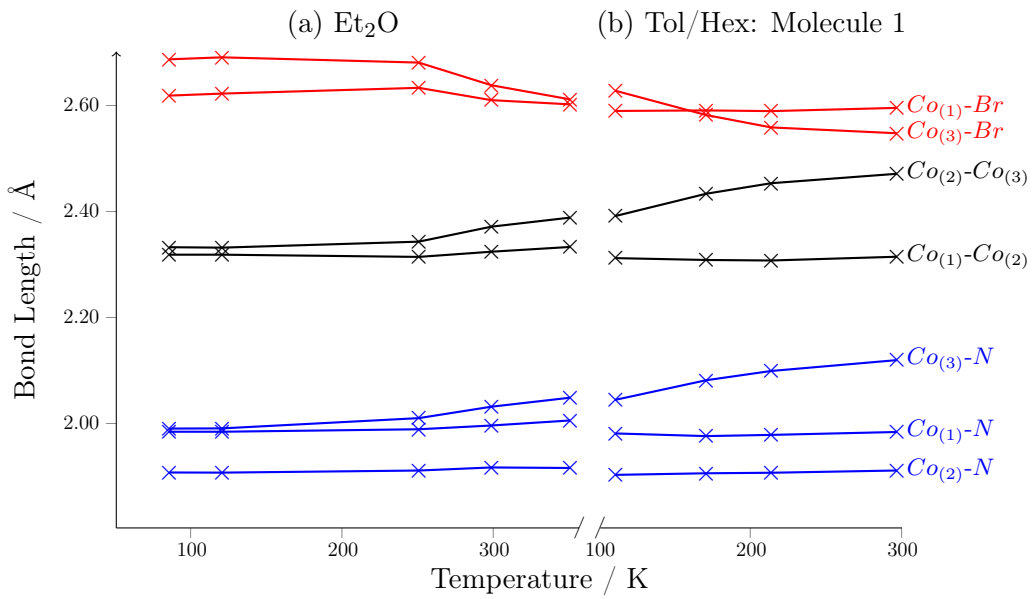

Figure 6.1: Bond lengths for the (a) $Co_3(dpa)_4Br_2{\cdot}Et_2O$ crystal from 85 - 350 K and (b) $Co_3(dpa)_4Br_2{\cdot}0.175Toluene{\cdot}0.5Hexane$ crystal Molecule 1 from 110 – 298 K. [37, 38]

symmetric limit, while the ^4B minima is located in the unsymmetric limit. The model supposes that the ^2B surface is flat in the symmetric-unsymmetric distortion coordinate, lying close in energy to the ground state in the symmetric limit and to the ^4B state in the unsymmetric limit. The ^2B PES bridges the high energy region between the LS ground state and the HS ^4B excited state, which are responsible for the observed magnetic behaviour. As the molecule explores the flat PES and becomes more unsymmetric, the spin crossover is facilitated and this results in the variation in the predicted spin crossover temperatures of the different crystals. They relate the electronic structure of the ^2B in the symmetric and unsymmetric limits by the transfer of an electron from the δ_{xy} to the $\delta_{x^2-y^2}$ orbital. They model the symmetric-unsymmetric transition using FON-DFT by continuously varying the population of the δ_{xy} and $\delta_{x^2-y^2}$ α orbitals between occupations of (2,0) and (1,1) that are characteristic of the two limits. The changes in the optimised structures with increasing fractional occupation mapped onto the changes observed in the experimental structures with increasing temperature. In particular, as the $\delta_{x^2-y^2}$

occupation is increased the Co-N distances increase at one of the terminal Co atoms and the structure develops an asymmetric Co-Co-Co chain. This will be described in more detail using the bromide complex in this chapter.

6.2 Aims and Objectives

In this Chapter, we aim to explore the origins of the temperature-dependent behaviours of the bromide complex. To begin we will evaluate the FON model presented by McGrady and Pantazis in the context of the symmetric-unsymmetric transition. In Chapter 5 we showed that the ^2B state relaxed to a symmetric minimum in the same way described by McGrady *et al.* for the chloride complex, and as such we expect to see a similar behaviour for the bromide. We also showed the same behaviour for the $2A$ state, which relaxed to the ground state structure and configuration. This suggests that we can apply the FON analysis to the ground state and it should also be able to provide a low energy pathway connecting the symmetric and unsymmetric limits. Indeed, the early work from Bénard and Rohmer predicted a flat PES for the ground state. [101] The single point energies of the ^2A and ^2B states calculated at the unsymmetric ^4B geometry in Chapter 5 showed they lie 0.035 and 0.227 eV above the ^4B state, respectively, which suggests that the ^2A state may provide a lower energy pathway to the unsymmetric limit. By optimising structures at different fractional occupations we will explore how the geometries evolve, which is pivotal to understanding the range of structures that are present in the crystals of different solvates. By performing single point calculations for other configurations at these intermediate geometries, we can quantify the schematic PES that was presented in the original paper.

In the second part of the chapter we will evaluate the spin equilibrium model used in the experimental work to fit the magnetic data. We will develop a similar model,

based on the structural evolution rather than the development of the effective magnetic moment during the spin crossover. In a spin crossover process the LS and HS states exist in equilibrium, and the effective magnetic moment is derived from the thermal population of the spin states under a Boltzmann regime. Similarly the structure at a given temperature would also correspond to the population-weighted average of the LS and HS structures. The apparently continuous variation in structural parameters then arises from the continuous variation in the ratio of the LS and HS populations. Using the optimised values of the thermodynamic parameters ΔH and $T_{\frac{1}{2}}$ calculated for each crystal in the experimental work, we can investigate how the X-ray crystal structure would appear under the influence of a thermal population of the excited state. We will be able to use this model to investigate both symmetric and unsymmetric crystals, not just the symmetric-unsymmetric transition. Comparing with the experimental X-ray data and the fractional occupation structures will allow us to determine to what degree the structural variation may be accounted for by the spin crossover in contrast to the continuous doublet surface model proposed by McGrady and Pantazis.

6.3 Results and Discussion

6.3.1 Fractional Occupation Number Model

The electronic structures of the unsymmetric ^2A and ^2B states depicted in Chapter 5 (Figures 5.6a-b page 161) do not appear to bare much resemblance to the electronic configurations of the symmetric $^2A_2$ and ^2E states on which they converge, depicted in Chapter 4 (Figures 4.4a-b page 131). McGrady and Pantazis attribute the convergence of both states to the singly occupied d_{xy} and $d_{x^2-y^2}$ orbitals in the unsymmetric limit, where the two orbitals contain electrons of opposite spin. In contrast, in the symmetric limit the δ_{xy}

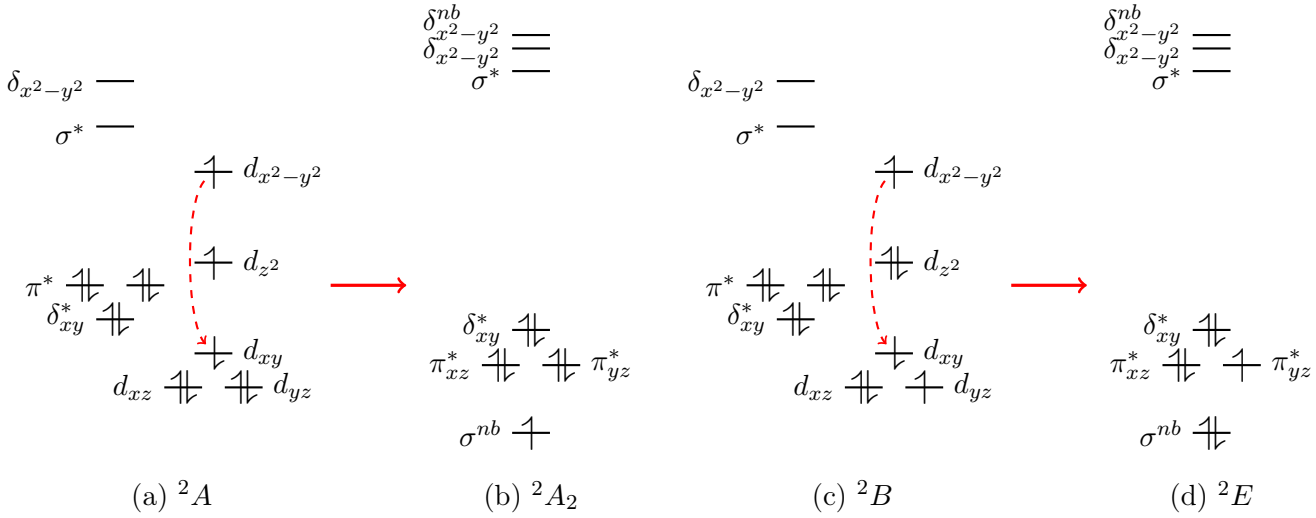

Figure 6.2: Relationship between the (a) unsymmetric ^2A and (b) symmetric $^2A_2$ electronic configurations and the (c) unsymmetric ^2B and (d) symmetric ^2E electronic configurations

framework is fully occupied, and the $\delta_{x^2-y^2}$ completely vacant. In effect, the transition from unsymmetric to symmetric limits is marked by the transfer of a single α electron from the $d_{x^2-y^2}$ orbital to the d_{xy}, as shown in Figure 6.2. The population of the $d_{x^2-y^2}$ and d_{xy} α orbitals has a strong influence on the structure, and in particular on the length of $Co_{(3)}$-N bonds. At the unsymmetric geometry the single occupation of the $d_{x^2-y^2}$ orbital leads to a long $Co_{(3)}$-N bond but during the geometry optimisation, the electron is transferred back to the d_{xy} orbital, leading to the symmetric electronic structure. Given we are exploring the symmetric-unsymmetric transition in this chapter, we will be using C_2 symmetry in all the calculations, and so we will continue to use the C_2 point group to name the electronic states going forward, as we did in Chapter 5.

Applying the same reasoning to the opposite (symmetric-unsymmetric) transition, we can drive the symmetric ^2A and ^2B structures towards an unsymmetric geometry by transferring the δ_{xy} α electron into the vacant $\delta_{x^2-y^2}$ orbital. Figure 6.3 depicts the evolution of the Co-Co (black), Co-Br (red) and Co-N (blue) bond lengths as a function of the fractional occupation of the $\delta_{x^2-y^2}$ orbital. The dependence of all structural parameters

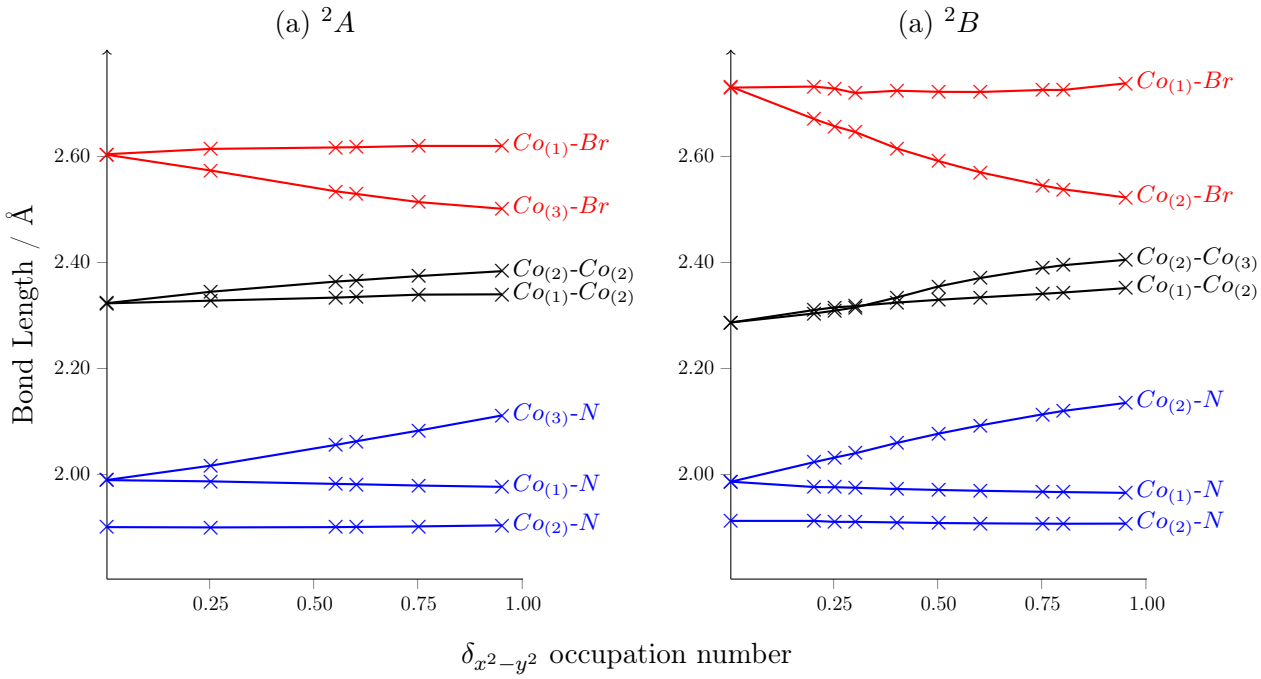

Figure 6.3: Co-Co, Co-Br and Co-N bond lengths for (a) ^2A and (b) ^2B of the the bromide complex with a range of $\delta_{x^2-y^2}$ fractional occupation numbers between the limits of 0 and 1, using the BP86 functional.

on the fractional occupation of the $\delta_{x^2-y^2}$ orbital in the ^2A and ^2B states bare a striking resemblance to the changes driven by the temperature in unsymmetric bromide crystals of the diethyl ether and toluene/hexane solvates, and those of the chloride complex in the previous theoretical work. There is a distinct shift towards an unsymmetric geometry as the fractional occupation increases, with divergences in the Co-Co terminal Co-N bond lengths. The only difference between the model being applied to the ^2A and ^2B states is the length of the Co-Br distances. They are greater in the ^2B state due to the doubly occupied σ^{nb} orbital, which has Co-Br antibonding character and is only singly occupied in the ^2A state. Still, in both models the $Co_{(1)}$-Br bond length remains unaffected by the fractional occupation of the $\delta_{x^2-y^2}$ orbital, but the $Co_{(3)}$-Br contracts as the fractional occupation increases.

As described in Chapter 5, the asymmetry is driven by a second-order Jahn-Teller instability. At symmetric geometries the $\delta_{x^2-y^2}$ and $\delta^{nb}_{x^2-y^2}$ orbitals are delocalised over

both terminal cobalt atoms, as in- and out-of-phase combinations of the terminal $d_{x^2-y^2}$ orbitals. The weak δ interactions and the large separation of the terminal Co atoms means that both orbitals have very similar energies. In the ground state both orbitals are vacant. In an excited state, if one were to become occupied it would create a near-degeneracy, where the occupied orbital lies just below the vacant one. To lower the energy of the occupied orbital the two can mix, however this can only occur once the centre of symmetry is removed. This centre of symmetry exists at the central cobalt in the symmetric Co-Co-Co chain, so to break this symmetry the chain distorts towards an unsymmetric structure. Thus a configuration with a single electron in one of the two linear combinations of $\delta_{x^2-y^2}$ will inevitably lead to an unsymmetric structure. Once it does distort, the mixing between the two linear combinations localises the electron on one side or the other. To maximise the exchange energy it becomes favourable for the other unpaired electrons to localise on the same cobalt, and the previously delocalised system is now better described by a Co_2 dimer and isolated $Co_{(3)}$ centre in the unsymmetric limit. Even at low $\delta_{x^2-y^2}$ fractional occupation number, we see a significant localisation of the orbital to $Co_{(3)}$, and as this occupation increases the $Co_{(3)}$-N distances increase along with the divergence of the Co-Co bonds. In both fractional occupation models, the structures are perfectly symmetric at low $\delta_{x^2-y^2}$ occupations while in many of the experimental structures some degree of asymmetry remains even at the lowest accessible temperatures. This is the only experimental feature not reproduced by the fractional occupation model, and it may, therefore, arise from crystal packing effects not replicated by the theoretical calculations on the isolated molecule. The same inconsistency is present for the experimental and theoretical chloride structures at different temperatures and $\delta_{x^2-y^2}$ occupations described.

6.3.2 Potential Energy Surfaces

McGrady and Pantazis presented a schematic PES diagram for the triocobalt chloride EMAC in their earlier theoretical work. [102] Having modelled the structural evolution of the doublet surfaces of the bromide complex using fractional occupation number DFT, we now have a range of optimised geometries between the symmetric and unsymmetric limits. We now use these intermediate geometries in order to quantify the PES of three states for the bromide complex. Specifically, we compute the single point energies of the ^2A, ^2B and ^4B states described in Chapter 5: these are plotted in Figure 6.4 using the structures obtained from FON model with the ^2A and ^2B states shown in Figure 6.3. Single point energies at the ^2A and ^4B geometries are also given in Figure 6.4a and at the ^2B and ^4B geometries in Figure 6.4b. All energies are given relative to the minimum energy of the ^2A ground state. The x coordinate is an internal distortion coordinate, IDC, that we define to represent the asymmetry in the structure by the following equation.

$$IDC = \sqrt{(\Delta\text{Co-Co})^2 + (\Delta\text{Co-N})^2} \tag{6.1}$$

The previous work from McGrady *et al.* argued that the conical intersection of the ^2A and ^4B states would be found at high energy, as their minima are located in very different regions of conformation space. They described the ^2B PES as unique in allowing the EMAC to short-circuit the high-energy region, explaining the apparently continuous variation in the experimental structural data. The results shown in Figure 6.4 show that the ^2B surface does indeed provide a low energy pathway between the symmetric to the unsymmetric limits. However, they also indicate that the ^2A surface behaves similarly. At the unsymmteric limit both states have low excitation energies relative to the ^4B state, and the PES of both decrease smoothly to their symmetric minima. Moreover, the results

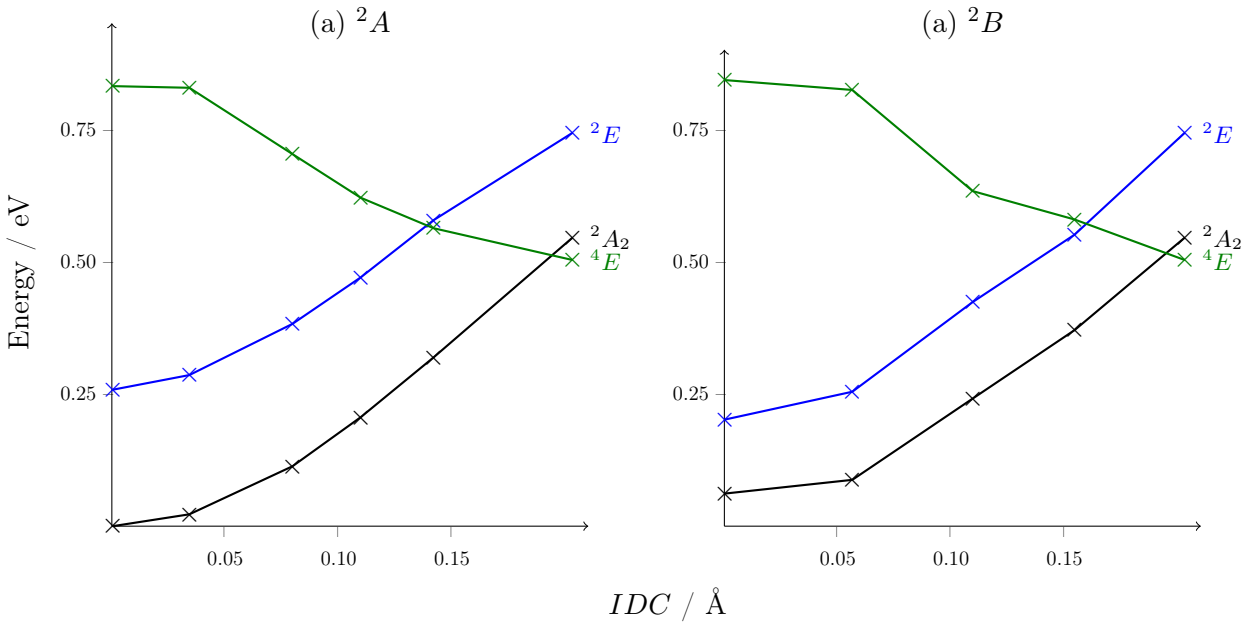

Figure 6.4: Relative single point energies (eV) to the ^2A ground state for the ^2A, ^2B and ^4B configurations at the geometries of the the bromide complex (a) ^2A and (b) ^2B states with a range of $\delta_{x^2-y^2}$ fractional occupation numbers between the limits of 0 and 1, using the BP86 functional.

show that the ^2A surface provides a lower energy pathway to connect the symmetric and unsymmetric limits. Unlike the doublet surfaces, the energy of the ^4B state state is lowest in the unsymmetric limit and increases as the structure becomes more symmetric. The results also shows that the ^4B surface flattens out in the symmetric limit. Examining the occupied MOs shows that in the symmetric limit the three unpaired electrons are in the σ^{nb}, π^* and σ^* orbitals, which corresponds the ^4E state presented in Chapter 4, but as the structure becomes more unsymmetric the σ^* electron transfers to the $\delta_{x^2-y^2}$ orbital. This indicates the crossing of the PES of ^4E and ^4B states as the structure distorts and the $\delta_{x^2-y^2}$ orbital localises on the terminal $Co_{(3)}$ and lowers in energy below the σ^*. The energies of all the states converge as the structure distorts. When the structure has a more symmetric geometry the states are ordered $^2A < {}^2B < {}^4B$, whilst at the ^4B geometry the states are ordered $^4B < {}^2A < {}^2B$.

6.3.3 Spin Equilibrium Model

The results presented thus far investigate how the structure changes on the doublet potential energy surfaces, and the fractional occupation structures do indeed closely parallel the experimental structural data. As described in the introduction, an alternative model to rationalise the experimental structural data involves the thermal population of an excited state. In the following section, we will consider how the structure would appear as a result of the spin crossover process and the increasing population of the symmetric and unsymmetric HS states found in Chapters 4 and 5. We have already shown in this work that the LS doublet ground state and the HS excited states have different structures. The variation in the fraction of the LS and HS states would lead to variations in the measured X-ray structure, which represents the average atomic positions in the crystal. The geometry at any given temperature is then determined by the thermal population of the HS excited state in a Boltzmann regime.

We now develop a model based on the spin equilibrium process to reflect this. The derivation is equivalent to the one used for the spin crossover model used in the experimental work, the result of which is given by Equation 1.4 page 30 in Chapter 1, and follows the method described in Kahn's Molecular Magnetism. [85] Rather than the magnetic susceptibility, the central variable in the following derivation will be the molecular structure, $\mathbf{R}$, which is used to represents the atomic coordinates, as we did in the Theoretical Techniques. The structure at a given temperature, $\mathbf{R}^T$, is given by the weighted average of the LS and HS structures, $\mathbf{R}^{LS}$ and $\mathbf{R}^{HS}$, using x to represent the fraction of HS molecules.

$$\mathbf{R}^T = x\,\mathbf{R}^{HS} + (1-x)\,\mathbf{R}^{LS} \tag{6.2}$$

During an equilibrium process, the quantity under consideration is the Gibbs free energy,

G, which for a system of LS and HS molecules is given by the weighted average of their respective free energies.

$$G = x\,G^{HS} + \,(1-x)\,G^{LS} \tag{6.3}$$

In any mixed system another term is needed. The entropy of mixing, S_{mix}, accounts for the many ways in which the HS and LS molecules can be ordered.

$$S_{mix} = -R[x\,ln(x) + (1-x)\,ln(1-x)] \tag{6.4}$$

Incorporating the mixing entropy into the Gibbs free energy and taking the partial derivative with respect to x allows us to see how the free energy changes with the fraction of HS molecules.

$$G = x\,G^{HS} + \,(1-x)\,G^{LS} - TS_{mix} \tag{6.5}$$

$$\frac{\partial G}{\partial x} = G^{HS} - G^{LS} + RT\left[ln(x) + 1 - \frac{1}{1-x} - ln(1-x) + \frac{x}{1-x}\right] \tag{6.6}$$

$$\frac{\partial G}{\partial x} = G^{HS} - G^{LS} + RT\left[ln(x) + \frac{1-x}{1-x} - \frac{1}{1-x} - ln(1-x) + \frac{x}{1-x}\right] \tag{6.7}$$

$$\frac{\partial G}{\partial x} = G^{HS} - G^{LS} + RT\,ln\left(\frac{x}{1-x}\right) \tag{6.8}$$

Here we notice that $G^{HS} - G^{LS}$ is the difference in the Gibbs free energy, ΔG, between the HS and LS states. ΔG is often given at temperature T using the enthalpy, ΔH, and entropy, ΔS, differences between the two states (where the mixing entropy is not considered). ΔG can also be given by the ratio of the LS and HS concentrations at equilibrium, K_c.

$$G^{HS} - G^{LS} = \Delta G = \Delta H - T\Delta S \tag{6.9}$$

$$\Delta G = -RTln\left(\frac{[HS]}{[LS]}\right) = -RTln(K_c) \tag{6.10}$$

At the critical temperature the enthalpy and entropy terms cancel out, such that $\Delta G = 0$. At this point exactly half the molecules are HS and half are LS, $[HS] = [LS]$ and $K_c = 1$. The temperature at which this occurs, $T_{\frac{1}{2}}$, is how we define the spin crossover temperature.

$$T_{\frac{1}{2}} = \frac{\Delta H}{\Delta S} \tag{6.11}$$

The condition for equilibrium in the mixed system is defined by the minimum in the free energy, where $\frac{\partial G}{\partial x} = 0$, and at this point we can relate x to ΔG.

$$-ln\left(\frac{x}{1-x}\right) = ln\left(\frac{1-x}{x}\right) = \frac{\Delta G}{RT} = \frac{\Delta H}{RT} - \frac{\Delta S}{R} \tag{6.12}$$

Rearranging for the HS fraction, x can be defined at any temperature in terms of the enthalpy difference between the LS and HS states and the spin crossover temperature.

$$ln\left(\frac{1-x}{x}\right) = \frac{\Delta H}{R}\left[\frac{1}{T} - \frac{\Delta S}{\Delta H}\right] \tag{6.13}$$

$$\left(\frac{1-x}{x}\right) = \exp\left(\frac{\Delta H}{R}\left[\frac{1}{T} - \frac{1}{T_{1/2}}\right]\right) \tag{6.14}$$

$$1 - x = x\exp\left(\frac{\Delta H}{R}\left[\frac{1}{T} - \frac{1}{T_{1/2}}\right]\right) \tag{6.15}$$

$$x\left(\exp\left(\frac{\Delta H}{R}\left[\frac{1}{T} - \frac{1}{T_{1/2}}\right]\right) + 1\right) = 1 \tag{6.16}$$

$$x = \frac{1}{\exp\left(\frac{\Delta H}{R}\left[\frac{1}{T} - \frac{1}{T_{1/2}}\right]\right) + 1} \tag{6.17}$$

This result for x can then be used in the original definition of the temperature dependent structure, $\mathbf{R}^T$ (Equation 6.2 page 188).

$$\mathbf{R}^T = x\,\mathbf{R}^{HS} + (1-x)\,\mathbf{R}^{LS} = x\,(\mathbf{R}^{HS} - \mathbf{R}^{LS}) + \mathbf{R}^{LS} \tag{6.18}$$

$$\mathbf{R}^{T} = \frac{(\mathbf{R}^{HS} - \mathbf{R}^{LS})}{\exp\left(\frac{\Delta H}{R}\left[\frac{1}{T} - \frac{1}{T_{1/2}}\right]\right) + 1} + \mathbf{R}^{LS} \tag{6.19}$$

Equation 6.19 predicts the structure at a given temperature as a function of the LS and HS structures, using the thermodynamic parameters ΔH and $T_{\frac{1}{2}}$. In the experimental work these thermodynamic parameters were extracted from the magnetic data using a least squares fitting to an idealised spin crossover process. Using the extracted parameters in Equation 6.19 allows us to approximate the HS fraction. To define the temperature dependent structure we also need to define the LS and HS structures, $\mathbf{R}^{LS}$ and $\mathbf{R}^{HS}$. We will use the D_4 symmetric $^2A_2$ ground state geometry described in Chapter 4 as the LS structure, which corresponds with all the experimental low-temperature symmetric crystal structures. The previous chapters showed a variety of HS states with structures that correspond to the various experimental high-temperature crystal structures. Using the specific thermodynamic parameters for each crystal and the HS state that best matches the observed high temperature structure we can predict how the structure develops over the experimental temperature range. In the unsymmetric $Co_3(dpa)_4Br_2{\cdot}Et_2O$ and $Co_3(dpa)_4Br_2{\cdot}1.75Toluene{\cdot}0.5Hexane$ crystals the HS state should have an unsymmetric structure, where the ^4B state provides the closest match to the experimental data. In the symmetric $Co_3(dpa)_4Br_2{\cdot}CH_2Cl_2$ and $Co_3(dpa)_4Br_2{\cdot}Hexane$ crystals the HS state should have a symmetric structure. In Chapter 4 we concluded a spin crossover into the ^4E state is most consistent with the structural changes of the dichloromethane solvate, in particular the observed Co-Br elongation. For the hexane solvate a spin crossover into the $^6A_2$ state was shown to be most consistent with the structural behaviour, showing an elongation of the Co-Co distances and of the Co-N distances at both terminal Co atoms.

We first evaluate the unsymmetric crystal structures using the ^4B state optimised

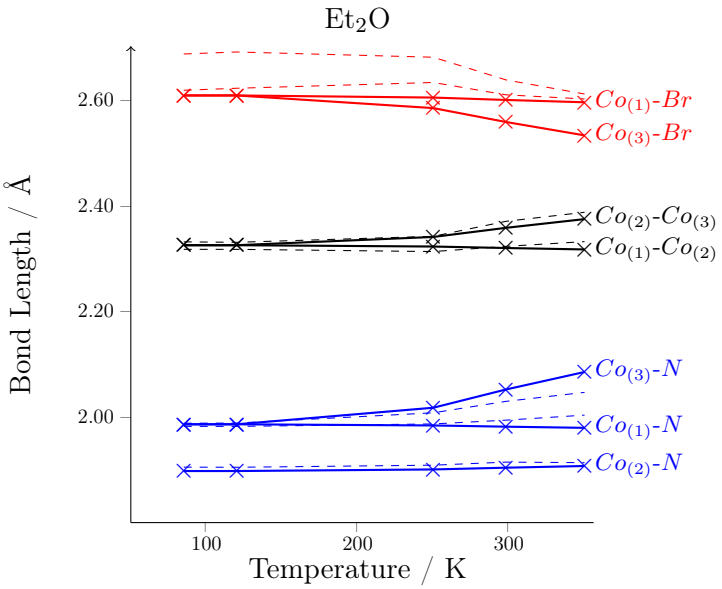

Figure 6.5: Co-Co, Co-Br and Co-N bond lengths for the $Co_3(dpa)_4Br_2{\cdot}Et_2O$ crystal predicted by the spin equilibrium model using Equation 6.19 with a ^4B HS structure (solid lines) and experimental values (dashed lines) from 85 - 350 K. [37, 38]

geometry as $\mathbf{R}^{HS}$ with the $^2A_2$ ground state geometry as $\mathbf{R}^{LS}$ to predict the structure at a range of temperatures using Equation 6.19. The optimised thermodynamic parameters of the unsymmetric $Co_3(dpa)_4Br_2{\cdot}Et_2O$ crystal were found to be $\Delta H = 13.3$ kJ mol^{-1} and $T_{\frac{1}{2}} = 325$ K. [38] In Figure 6.5 we plot values that correspond to the temperatures at which the experimental structures were determined using the solid lines, and the original experimental data with the dashed lines. The model predicts Co-Co bonds that coincide with the experimental structure very closely, showing a divergence of $Co_{(1)}$-$Co_{(2)}$ and $Co_{(2)}$-$Co_{(3)}$ at higher temperatures. The predicted Co-N bond lengths also show a similar profile to the experimental data, however the divergence of $Co_{(1)}$-N and $Co_{(3)}$-N is more exaggerated than the experiment. The $Co_{(1)}$-Br distances also corresponds with experiment, and although the predicted $Co_{(3)}$-Br bond lengths are slightly shorter than the experimental values, they do contract as the temperature increases, as observed in the experiment.

We next turn our attention to the symmetric crystal structures, starting with $Co_3(dpa)_4Br_2{\cdot}$Hexane. In both previous crystals we used the unsymmetric ^4B structure as

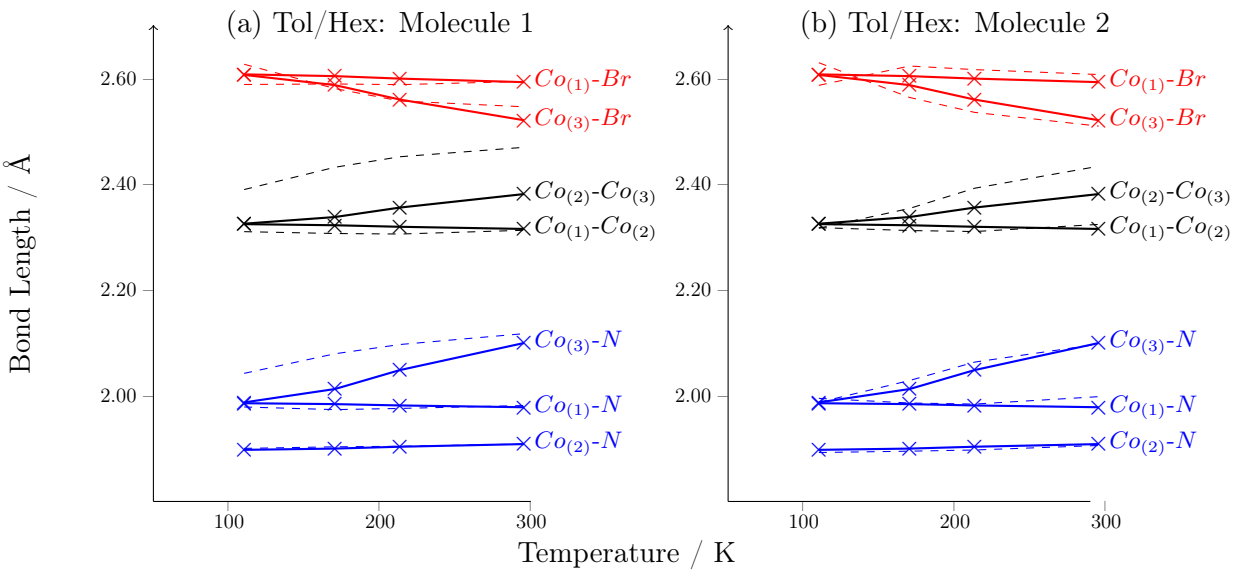

Figure 6.6: Co-Co, Co-Br and Co-N bond lengths for the $Co_3(dpa)_4Br_2$·1.75Toluene·0.5Hexane crystal (a) Molecule 1 and (b) Molecule 2 predicted by the spin equilibrium model using Equation 6.19 with a ^4B HS structure (solid lines) and experimental values (dashed lines) from 110 - 298 K. [37, 38]

$\mathbf{R}^{HS}$ to model the change in structure with temperature using Equation 6.19. In Chapter 4 we showed that the symmetric $^6A_2$ state best corresponds with the high temperature structure of $Co_3(dpa)_4Br_2$·Hexane. As such we use the optimised geometry of the $^6A_2$ state as $\mathbf{R}^{HS}$, again in combination with the $^2A_2$ ground state geometry as $\mathbf{R}^{LS}$ to model the temperature dependent structure. The extracted thermodynamic parameters for $Co_3(dpa)_4Br_2$·Hexane are $\Delta H = 8.2$ kJ mol^{-1} and $T_{\frac{1}{2}} = 203$ K. [37, 38] It should be noted that these values are from fitting the magnetic data to spin crossover process into a quartet state, and the values for a spin crossover into a sextet state would likely be different (e.g higher $T_{\frac{1}{2}}$). The changes in the bond lengths plotted in Figure 6.7 correspond to the experimental data, showing an elongation of the Co-Co and terminal Co-N distances and a contraction of the Co-Br distances. As we saw for $Co_3(dpa)_4Br_2$·Et_2O the Co-Co distance correspond with the experiment very closely, whilst the predicted terminal Co-N (and Co-Br) are longer than the experiment. This would again suggest the crystal packing forces restrict the Co-N elongation, whilst the internal Co_3 chain can distort more freely.

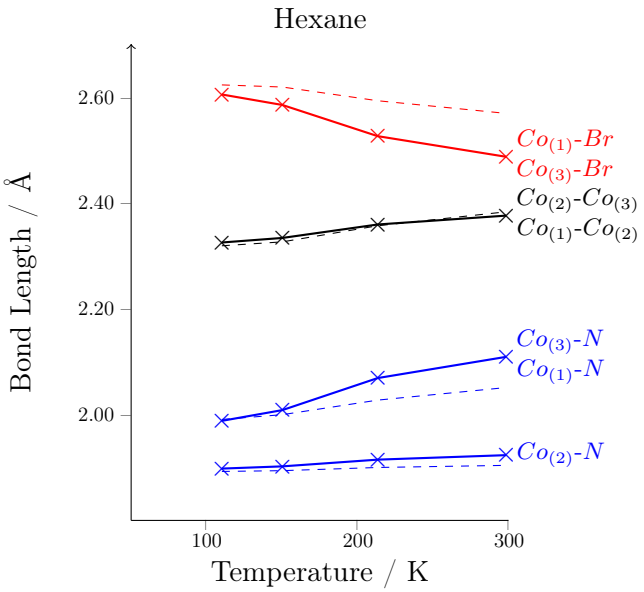

Figure 6.7: Co-Co, Co-Br and Co-N bond lengths for the $Co_3(dpa)_4Br_2$·Hexane crystal predicted by the spin equilibrium model using Equation 6.19 with a $^6A_2$ HS state (solid lines) and experimental values (dashed lines) from 110 - 298 K. [37, 38]

The behaviour of the $Co_3(dpa)_4Br_2{\cdot}CH_2Cl_2$ crystal structure is unusual compared to the other EMACs, showing an elongation in the Co-Br bonds and a very high spin crossover temperature. The HS state that is most consistent with this observation is the symmetric ^4E state described in Chapter 4, which has an occupied σ^* orbital and corresponding long Co-Br bonds due to the antibonding Co-Br interactions in the σ framework. For this final bromide crystal we use the optimised geometry of the ^4E state as $\mathbf{R}^{HS}$ with the $^2A_2$ ground state geometry as $\mathbf{R}^{LS}$ in the spin equilibrium model goverened by Equation 6.19. The spin crossover temperature was shown to be particularly high, and the thermodynamic parameters of the $Co_3(dpa)_4Br_2{\cdot}CH_2Cl_2$ crystal are $\Delta H = 14.9$ kJ mol^{-1} and $T_{\frac{1}{2}} = 431$ K. [37, 38] In Figure 6.8 the structures predicted by the spin equilibrium model show almost no variation over the entire temperature range. This does not correlate with the experimental data, where a significant elongation in the Co-Br distances is observed. Given the very high spin crossover temperature, we attribute the behaviour of the model structure to the low population of the HS state even at elevated temperatures, which

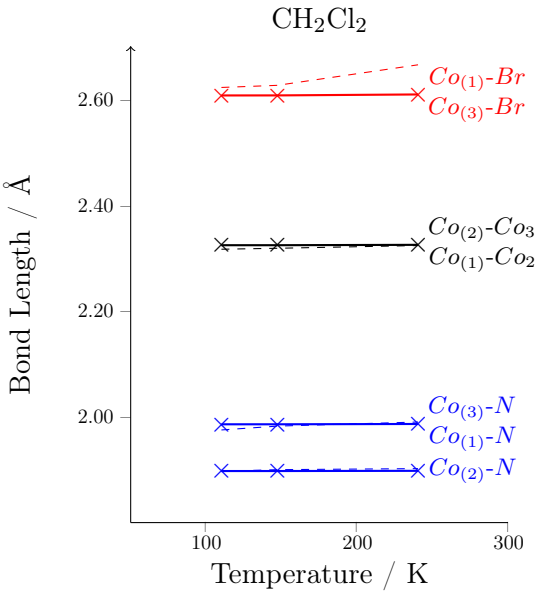

Figure 6.8: Co-Co, Co-Br and Co-N bond lengths for the $Co_3(dpa)_4Br_2{\cdot}CH_2Cl_2$ crystal predicted by the spin equilibrium model using Equation 6.19 with a ^4E HS state (solid lines) and experimental values (dashed lines) from 111 - 240 K [37, 38]

cannot effect any observable change in the structure. This suggests that the observed structural variation must arise from the population of an alternative LS doublet state. Both the $2E$ and $^2B_2$ states presented in Chapter 4 show an elongation of the Co-Br bonds due to an excitation into the σ^{nb} orbital, which is only singly occupied in the $^2A_2$ ground state. The population of either of these states would not affect the molecular magnetism, but could still influence the structure. In the analysis of the two-step spin crossover in the $[Co_3(dpa)_4Cl_2]^+$ cation, the low-temperature regime is described by such an excitation. [86, 118] In the cation, however, this corresponded to a singlet-triplet transition and could be observed in the magnetic behaviour. The low-temperature structural variation showed an elongation of the Co-Cl bonds (see Figure 1.20 in the Introduction), as we see in the Co-Br bonds in $Co_3(dpa)_4Br_2{\cdot}CH_2Cl_2$. We are unable to use our spin equilibrium model to describe the variation in structure due to the population of a LS state as there are no corresponding thermodynamic parameters to model this transition.

6.4 Conclusions

In this chapter we have presented two models by which the EMAC structure can transition between the symmetric and unsymmetric limits observed experimentally. The first builds on the previous work of McGrady and Pantazis, extending their FON model to the tricobalt bromide complex. [102] The second is a model that we have developed to predict the temperature dependent structure of a spin crossover complex as the thermally weighted average of the LS and HS structures. We have described a second-order Jahn-Teller instability in states with a singly occupied $\delta_{x^2-y^2}$ orbital, which breaks the symmetry in the Co_3 chain and localises the $\delta_{x^2-y^2}$ onto the more isolated $Co_{(3)}$ atom. The FON model uses the fractional occupation of the $\delta_{x^2-y^2}$ orbital in two low-energy symmetric doublet states to instigate a distortion towards an unsymmetric structure with little energetic cost. These results explain the observed low temperature unsymmetric structures and their low spin crossover temperatures as the LS and HS PES converge as the structure becomes more unsymmetric. They also show that symmetric-unsymmetric distortion is intimately linked to the single occupation of the $\delta_{x^2-y^2}$ framework. The spin crossover model uses the thermal population of the unsymmetric ^4B state to describe the continuous distortion between the symmetric and unsymmetric limits in the X-ray crystal structures of $Co_3(dpa)_4Br_2{\cdot}Et_2O$ and $Co_3(dpa)_4Br_2{\cdot}1.75Toluene{\cdot}0.5Hexane$. These results highlight the important role of the crystalline environment, and suggest that some may stabilise unsymmetric geometries and facilitate the spin crossover into the unsymmetric HS state. The spin crossover model has also been used to describe the structural evolution of those crystal structures that remain symmetric over a range of temperatures. The results indicate the thermal population of a symmetric HS $^6A_2$ state in $Co_3(dpa)_4Br_2{\cdot}Hexane$, while the population of a LS doublet state is most consistent with the behaviour of $Co_3(dpa)_4Br_2{\cdot}CH_2Cl_2$, which has a

particularly high spin crossover temperature and shows little HS population, even at high temperatures. In the following chapter we take forward the symmetric $^2A_2$, ^4E and $^6A_2$ and unsymmetric ^4B states identified in the previous chapters as we consider the fluoride, chloride and iodide analogues.

Chapter 7

Influence of the Axial Ligand on $Co_3(dpa)_4X_2$ [X = F, Cl, Br, I]

7.1 Introduction

Chapters 4-6 presented a detailed study of the tricobalt bromide EMAC. The structural and magnetic behaviour were described in terms of a spin crossover process and two low-lying doublet states with flexible structures. The doublet potential energy surfaces provide a low energy pathway for the structure to distort, which allows the crystalline environment to take significant effect on the experimental properties. This is most apparent in the crystals of the same complex but with different solvates having different structures and spin crossover temperatures. Recently the Hillard group has, for the first time, synthesised crystals of the fluoride and iodide analogues of the chloride and bromide EMACs described in the previous chapters. [38] This presents an opportunity to extend the chemical range of our analysis of the electronic structure. A single crystal with a fluoride ligand suitable for X-ray diffraction was found, with a dichloromethane solvate, $Co_3(dpa)_4F_2{\cdot}2CH_2Cl_2$. In addition, two distinct crystals with iodide terminal ligands were found, with either 1,2-

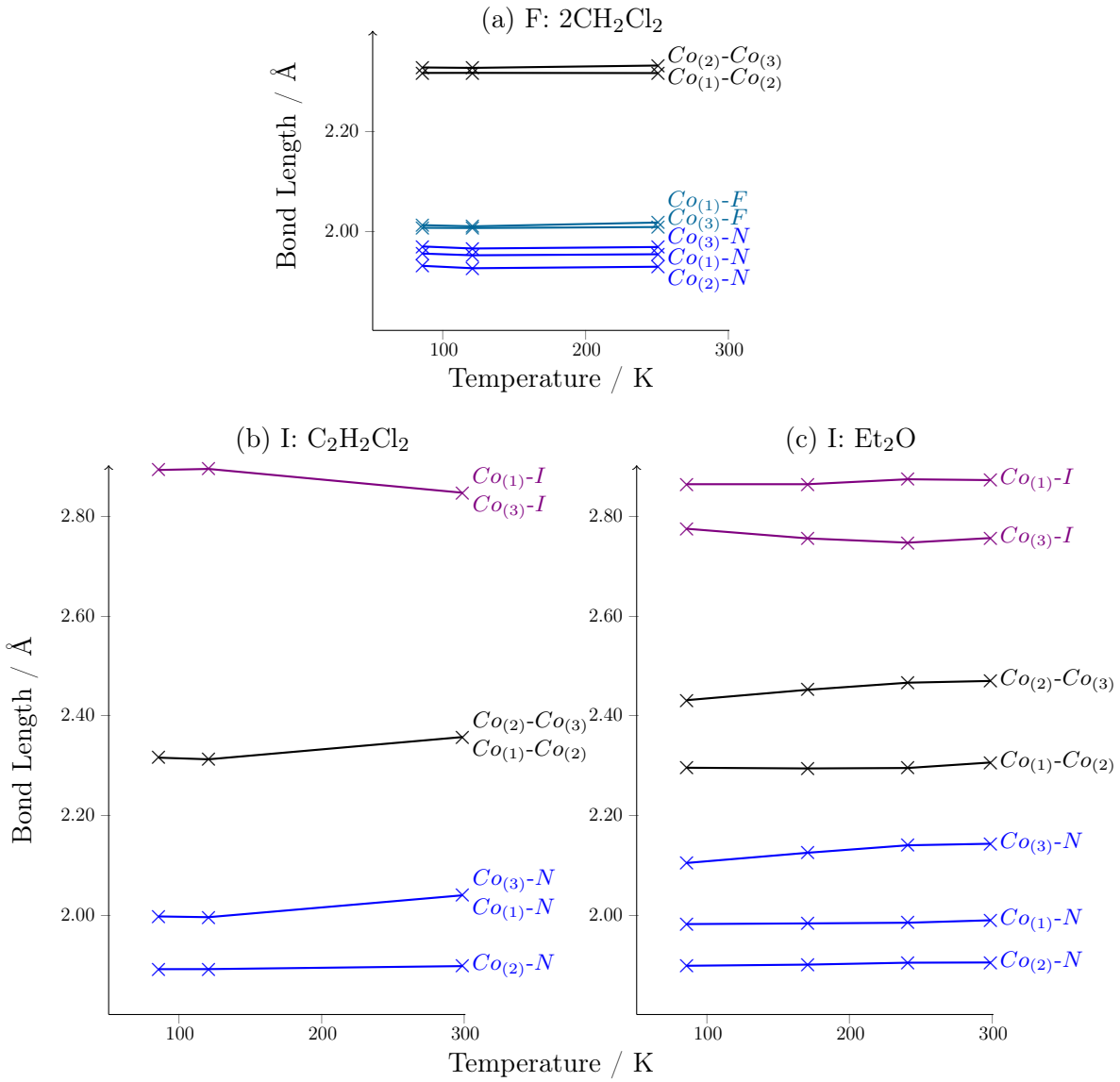

Figure 7.1: Bond lengths for the (a) $Co_3(dpa)_4F_2{\cdot}2CH_2Cl_2$ crystal from 85 – 250 K, (b) $Co_3(dpa)_4I_2{\cdot}C_2H_4Cl_2$ crystal and (c) $Co_3(dpa)_4I_2{\cdot}Et_2O$ from 85 – 298 K. [38]

dichloroethane or diethyl ether as the solvate, $Co_3(dpa)_4I_2{\cdot}C_2H_4Cl_2$ and $Co_3(dpa)_4I_2{\cdot}Et_2O$.

$Co_3(dpa)_4F_2{\cdot}2CH_2Cl_2$ proves to adopt a symmetric structure at low temperatures but begins to show a small increase in the degree of asymmetry at higher temperatures, with a difference of 0.015 Å in the Co-Co bonds. $Co_3(dpa)_4I_2{\cdot}C_2H_4Cl_2$ is also symmetric at low temperatures and remains perfectly symmetric at high temperatures, where both Co-Co and terminal Co-N bonds lengthen while the Co-I bonds contract; similar behaviour was noted for $Co_3(dpa)_4Br_2{\cdot}$Hexane. $Co_3(dpa)_4I_2{\cdot}Et_2O$, in contrast, has a very unsymmetric

structure at low temperatures, which shows relatively little change as the temperature is increased, although there is a slight increase in the degree of asymmetry; similar to the behaviour of $Co_3(dpa)_4Br_2$·1.75Toluene·0.5Hexane. By fitting the temperature dependence of the magnetic susceptibilities of all three compounds, as well as a number of others that had previously been reported in the literature, Hillard and co-workers were able to extract thermodynamic parameters associated with the spin crossover behaviour for a wide range of crystals. Their work suggests that the axial ligand plays an important role in the spin crossover process and structural behaviour. The different crystals show a range of spin crossover temperatures and enthalpy changes, with a general trend that the spin-crossover temperature decreases in the order F > Cl > Br > I. Previous studies have shown that Cr_3 [32–34] complexes favour symmetric geometries with strong field axial ligands and unsymmetric geometries with weak field axial ligands, while Co_3 complexes all show a symmetric structure with a range of strong field ligands. [116, 117] Hillard *et al.* suggest that this could explain the structures of $Co_3(dpa)_4X_2$ with halide axial ligands, where only a symmetric structure is found for the strongest field fluoride complex, whilst the weaker field iodide complex with a diethyl ether solvate exhibits the highest degree of asymmetry in any of the low temperatures structures. In the unsymmetric crystals they are able to associate the structure to the spin crossover temperature in the chloride and bromide complexes, showing that the larger the degree of asymmetry at high temperatures the lower the spin crossover temperature.

7.2 Aims and Objectives

In this chapter we will extend the analysis developed in Chapters 4-6 to the fluoride, chloride and iodide complexes. Using DFT we will investigate how the change in axial ligand effects the electronic structure of the $Co_3(dpa)_4X_2$ EMACs, and in turn their structural

and magnetic properties. We will evaluate the results presented in the recent experimental work, in particular looking at the interrelation between the axial ligand, spin crossover process and structural behaviour.

7.3 Results and Discussion

7.3.1 Spin State Splitting Analysis

Initial results follow the approach taken in Chapter 4. The D_4 symmetric $^2A_2$ state was found for the complexes of each halide and the symmetric excited states were defined using excitations within that framework, as described in Figures 4.4-4.6 of Chapter 4 (pages 131-133). For each halide, the energy of each state is given relative to the $^2A_2$ state in Figure 7.2. The excitation energies of each halide complex follow the same general pattern as the bromide ligand. The $^2A_2$ state proves to be the ground state for every halide, with the other doublet states having the lowest excitation energies followed by the quartets, sextets and the octet. For almost every state the axial halide ligand affects the excitation

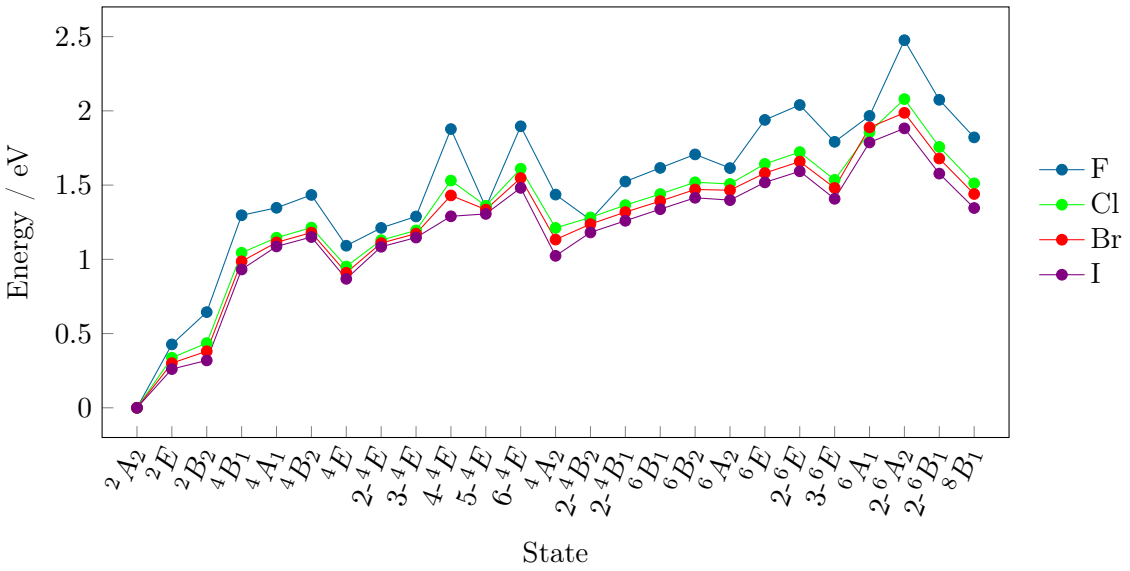

Figure 7.2: Relative energies (eV) to the $^2A_2$ ground state of the predicted low-lying doublet, quartet, sextet and octet states detailed in Chapter 4 Figures 4.4-4.6 (pages 131-133) for the fluoride, chloride, bromide and iodide complexes using the BP86 functional.

energy in the same way: as group VII is descended, the excitation energy relative to the $^2A_2$ ground state decreases in the order F > Cl > Br > I. The F-Cl energy separation is particularly large, while the Cl-Br and Br-I separations are much smaller. This correlates with the experimental spin-crossover temperatures. The only exceptions to this general observation are apparent in the 2-$^4B_2$, 5-^4E, $^6A_2$ and $^6A_1$ states shown in Figure 7.2, where the fluoride complex has an uncharacteristically low energy, the origin of which will be discussed in the next section where we evaluate the structures and wavefunctions of the D_4 symmetric BP86 results. First we will examine the spin state splitting energies when the symmetry constraint is relaxed and look at their functional dependence.

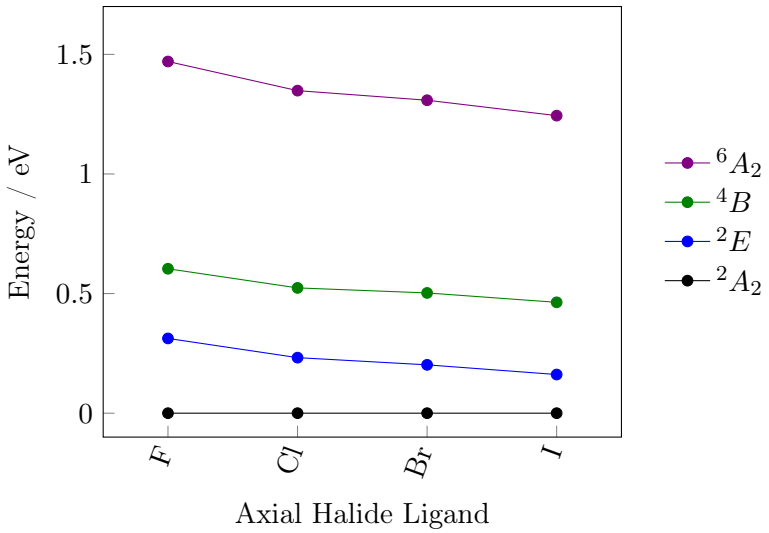

Figure 7.3: Relative energies (eV) to the $^2A_2$ ground state of the ^2E, $^6A_2$ and ^4B states of the fluoride, chloride, bromide and iodide complexes using the BP86 functional.

The energy range in Figure 7.2 is quite large, and the differences in spin state splitting energies of the F, Cl, Br and I complexes are difficult to elucidate. To aid the comparison of the different axial ligands we will focus on the low energy states of the bromide complex identified in Chapters 4-6, namely the $^2A_2$, ^2E and $^6A_2$ symmetric states and the ^4B unsymmetric state. The corresponding BP86 energies are shown in Figure 7.3, relative to the $^2A_2$ ground state, where the symmetric and unsymmetric states have have

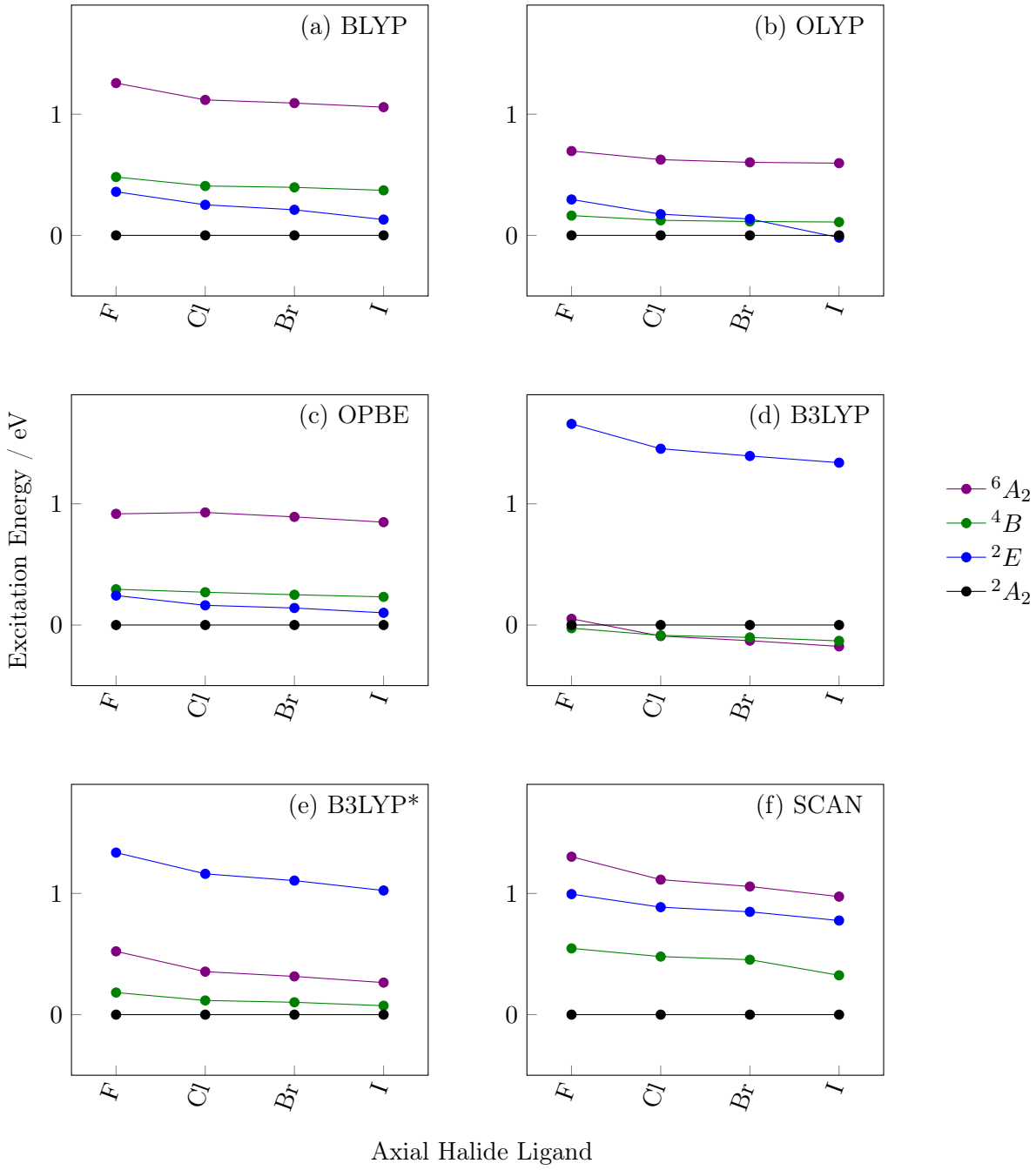

Figure 7.4: Relative energies (eV) to the $^2A_2$ ground state of the ^2E, $^6A_2$ and ^4B states of the fluoride, chloride, bromide and iodide complexes using the GGA ((a) BLYP, (b) OLYP and (c) OPBE) hybrid ((d) B3LYP and (e) B3LYP*) and meta-GGA ((f) SCAN) functionals.

been allowed to relax to their D_2 and C_2 symmetric minima, respectively. We also explore the spin state splitting energies for the BLYP, OLYP, OPBE, B3LYP, B3LYP* and SCAN functionals in Figure 7.4. The results show many of the same features seen in the previous chapters when exploring the functional dependence, for example the stabilisation of HS states by hybrid functionals, which again highlights the delicately balanced spin crossover. Comparing the complexes of the different halides, all the functionals show the same pattern as BP86: a decreasing energy in all states relative to $^2A_2$ descending the group F > Cl > Br > I.

7.3.2 Structure and Wavefunction Analysis

We now explore the characteristics of the structure and wavefunction of the D_4 symmetric $^2A_2$ ground state for each of the halide complexes. As we did in Chapter 4, because the structure is symmetric we only include the $Co_{(1)}$-$Co_{(2)}$, $Co_{(1)}$-X, $Co_{(1)}$-N and $Co_{(2)}$-N bond lengths, the $Co_{(1)}$, $Co_{(2)}$ and $X_{(1)}$ charge densities and the $Co_{(1)}$ and $Co_{(2)}$ spin densities, where $X_{(1)}$ is defined as the halide bonded to $Co_{(1)}$. The corresponding $Co_{(3)}$ and $X_{(2)}$ values are identical to the $Co_{(1)}$ and $X_{(1)}$ values. The spin densities reflect the three-centre three-electron bond delocalised over the sigma framework in all the complexes. As we saw for the energies, the Cl, Br and I complexes are closely related and show similar values for the bond lengths, charge and spin densities. There are, however, some subtle but significant differences in the fluoride complex. The terminal Co-N bonds are ∼0.03 Å shorter than the other halide complexes, and the terminal Co charge and spin densities are larger. Conversely, the central Co-N bonds are slightly longer (0.02 Å) in the fluoride complex, and the $Co_{(2)}$ charge and spin densities smaller. The charge density of the F atom is also greater than the other halides, and the fluoride complexes all have a greater total positive charge spread between the three cobalt atoms.

		$Co_{(1)}$-$Co_{(2)}$	$Co_{(1)}$-X	$Co_{(1)}$-N	$Co_{(2)}$-N	Q $Co_{(1)}$	Q $Co_{(2)}$	Q $X_{(1)}$	ρ $Co_{(1)}$	ρ $Co_{(2)}$
$^2A_2$	**F**	2.318	1.976	1.950	1.915	0.669	0.877	-0.630	0.506	-0.117
	Cl	2.323	2.418	1.980	1.898	0.433	0.993	-0.548	0.479	-0.137
	Br	2.320	2.597	1.985	1.896	0.426	1.020	-0.551	0.462	-0.136
	I	2.315	2.889	1.988	1.893	0.380	1.011	-0.432	0.428	-0.132
2-$^4B_2$	**F**	2.235	2.235	1.975	2.027	0.643	0.815	-0.636	0.440	1.887
	Cl	2.284	2.284	2.049	1.935	0.415	0.979	-0.550	1.155	0.572
	Br	2.283	2.283	2.056	1.931	0.407	1.005	-0.552	1.158	0.561
	I	2.274	2.274	2.062	1.927	0.361	1.002	-0.434	1.155	0.560

Table 7.1: Co-Co, Co-Br and Co-N bond lengths (Å) and cobalt and halide charge densities (Q) and cobalt spin densities (ρ) for the $^2A_2$ and 2-$^4B_2$ states for the fluoride, chloride, bromide and iodide complexes using the BP86 functional.

These results can be explained in the context of *s*-*d* mixing, originally described by Orgel in 1958. [339] In TM complexes the 4*s* orbitals have radial wavefunctions with a greater electron density at larger radii than the 3*d* orbitals. The 4*s* orbitals, therefore, have a larger overlap with the ligand orbitals and are strongly repelled by the ligand electron density. They tend to be omitted from the discussion of TM complexes as they are considered too high in energy, but this is an oversimplification. Orgel suggested that in linear complexes, when the molecular symmetry allows it, the 4*s* and $3d_{z^2}$ orbitals hybridise as shown in Figure 7.5. This results in a $3d_{z^2}$ orbital with a much larger electron density in the xy-plane. In the tricobalt EMACs we have only really discussed the Co-N bonding in terms of the $3d_{x^2-y^2}$ orbitals, but the 4*s* and $3d_{z^2}$ hybridisation means there is also some significant bonding to the hybrid orbital.

In the experimental work Hillard has suggested that the structural behaviour of the complexes of different halides may be explained by the strength of the halide ligand field, citing literature that shows stronger field axial ligands favour symmetric structures in Cr_3 and Co_3 complexes. [32–34, 38, 116, 117] The fluoride anion is considered to have a stronger ligand field compared to Cl, Br and I because of the weaker π donation. In

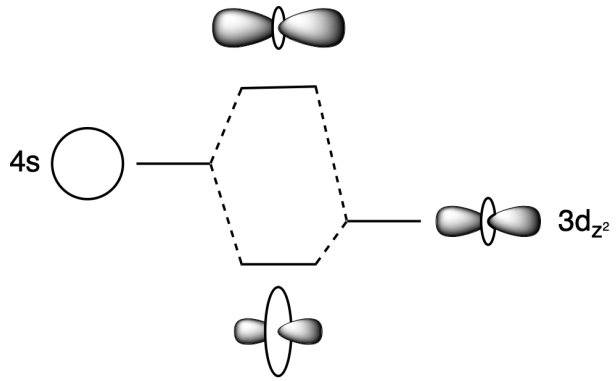

Figure 7.5: Schematic MO diagram showing the *s*-*d* hybridisation described by Orgel. [339]

an octahedral complex π donation raises the energy of the t_{2g} orbitals and decreases Δ_{oct}. Our results suggest that it is not the ligand field that plays the important role, but in fact the weaker σ donation of the fluoride anion. In octahedral complexes this leads to lower energy e_g orbitals, which in turn have weaker interactions with the higher energy $4s$ orbitals and show a lesser degree of *s*-*d* hybridisation. The weaker F donation is evident in the charge densities of the Co_3 EMACs, where the F atom has a greater (negative) charge density than the other halides, whilst the terminal Co atoms have a greater (positive) charge density. The charge densities of all the other halides decrease down the group F > Cl > Br > I, highlighting the greater donation into the Co_3 framework. The corresponding terminal Co d_{z^2} orbitals therefore have a lower energy, hybridise to a lesser extent and have a lower electron density in the xy-plane. The lesser electron density compared to the other halides leads to a weaker repulsion of the equatorial dpa ligands, and this can be seen in the contracted terminal Co-N distances. The opposite effect can be seen on the central Co, which has stronger interactions with the terminal Co atoms in the fluoride complex, a smaller charge density, greater degree of *s*-*d* hybridisation and elongated $Co_{(2)}$-N distances. The shorter terminal Co-N distances lead to an increase in the energy of the terminal Co $d_{x^2-y^2}$ orbitals, which increases the energy needed for the spin crossover process, as can be seen in the high $T_{\frac{1}{2}}$. In contrast, the longer central Co-N distances decrease the energy

of the central Co $d_{x^2-y^2}$.

In the earlier discussion of the BP86 D_4 results we noted the abnormal F energies in the 2-$^4B_2$, 5-^4E, $^6A_2$ and $^6A_1$ states, and we now examine the structure and wavefunction of the the 2-$^4B_2$ state, detailed in Table 7.1. The corresponding electron configuration shown in Chapter 4 (Figure 4.5k page 132) has a single electron in the $\delta_{x^2-y^2}$ orbital, which is of b_1 symmetry in the D_4 point group. Indeed, all of the four states highlighted previously have in common the fact that an orbital of b_1 symmetry is singly occupied. In the heavier halides (Cl, Br, I), this orbital is formed from a linear combination of the two terminal $d_{x^2-y^2}$ orbitals, and as a result their structures tend to feature elongated terminal Co-N bonds (e.g. 2.059 Å for the bromide complex) and large terminal Co spin densities (1.158 for the bromide complex). The central Co-N bonds are, in contrast, short (1.927 Å) and the spin density at the central Co small (0.561). In the fluoride complex the opposite picture emerges. The terminal Co-N bonds are short (1.975 Å), and the terminal cobalt spin densities low (0.440). On the other hand, the central Co-N bonds are long (2.027 Å) and the spin density at the central Co high (1.887). All of the above are consistent with the occupation of the $\delta^*_{x^2-y^2}$ orbital, also of b_1 symmetry, which is localised on the central $Co_{(2)}$ atom. In Chapter 4 excitations into the $\delta^*_{x^2-y^2}$ orbital were not considered for the bromide complex as it lay too high in energy. These results indicate a reversal of the order of the high-lying $\delta_{x^2-y^2}$ orbitals in these states for the fluoride complex, and suggest a distinct difference in the bonding compared to the heavier halides.

7.3.3 Re-evaluation of the Structure-Spin Crossover Relationship

In the preceding discussion we have explored the effect of the axial ligand on the spin state splitting energies and the EMAC structure. Both reflect the spin crossover and structural properties observed experimentally. In this final section we will discuss the link

between between the structure and the spin crossover. In the experimental work Hillard *et al.* calculated the thermodynamic parameters (ΔH and $T_{\frac{1}{2}}$) for the entire collection of Co_3 spin crossover complexes by fitting the magnetic data to an ideal spin crossover from a doublet to a quartet. Their analysis showed that the unsymmetric structures can be related to the spin crossover temperature, where the higher the degree of asymmetry in the structure at the high temperature limit, the lower the spin crossover temperature. In our work we have shown that the ^4B state has a structure that is consistent with the experimental unsymmetric structures. We have also identified a $^6A_2$ that is consistent with the high temperature symmetric structures. The electronic structures of the two states can be related. In the quartet the spin crossover process is consistent with a localised transition at a single terminal cobalt atom, while in the sextet the transition occurs at both terminal cobalt atoms. Their structures can also be related, where the Co-Co and Co-N bonds of the spin crossover Co atoms elongate in both states. In the ^4B state this leads to the unsymmetric structure, where only one set of Co-Co and Co-N distances increase. In the $^6A_2$ state both Co-Co distances increase, as do the Co-N bonds at both terminal Co. Rather than using the asymmetry as a measure to relate the structure to the spin crossover, we instead suggest using the average Co-Co and Co-N distances such that the spin crossover into both symmetric and unsymmetric HS states can be considered.

In Figure 7.6 we plot the average Co-Co and terminal Co-N distances, Co-Co(avg) and Co-N(avg), against the spin crossover temperature, just as Hillard *et al.* did using ΔCo-Co. A regression analysis of both gave regression coefficients of $R^2 = 0.847$ and 0.895 for the average Co-Co and Co-N distances, respectively. The results show a very strong correlation between the structure and the spin crossover temperature. The crystalline environment clearly plays a pivotal role in the spin crossover. In the crystals of some solvates there is a clear bias towards an unsymmetric structure. This would correspond to a

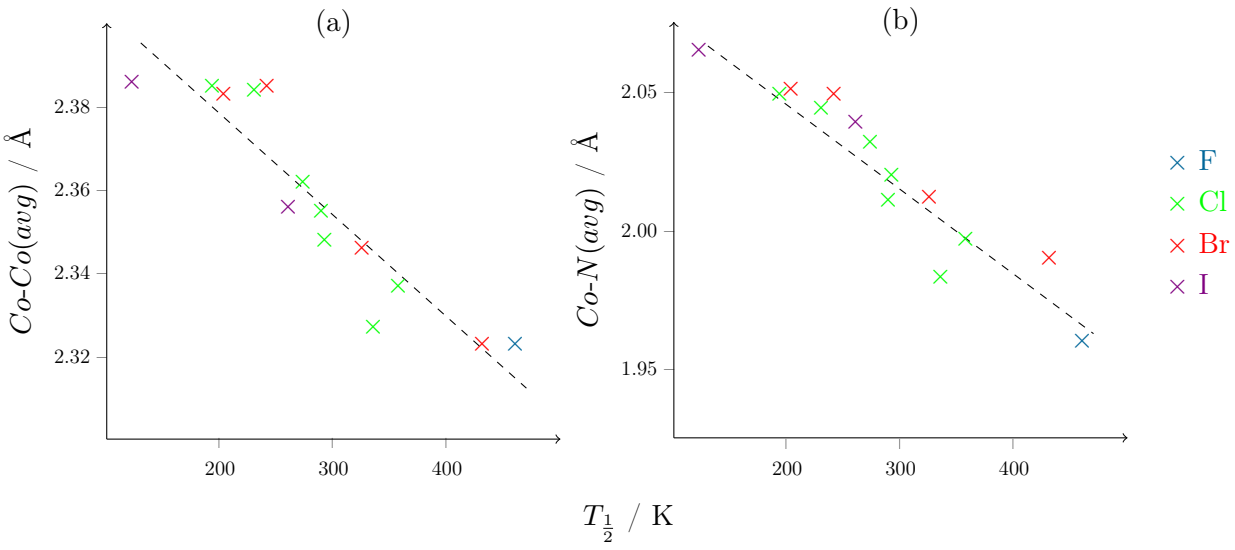

Figure 7.6: Collected high temperature average (a) Co-Co and (b) terminal Co-N bond lengths vs. spin crossover temperatures for entire experimental work. [35–38]

situation where the crystal packing forces are less strong at one end of the EMAC molecule, and the spin transition occurs at a lower temperature at that end. The transition to the sextet is prohibited by the strong packing forces at the other end. Such packing forces were explicitly shown in the unsymmetric $Co_3(dpa)_4Cl_2{\cdot}2CH_2Cl_2$ crystal by a Hirshfeld surface analysis, which showed a spin crossover into a quartet. [35, 113] In the crystals that maintain a symmetric structure, there may be equal crystal packing forces at both ends, as the Hirshfeld surface analysis showed for $Co_3(dpa)_4Cl_2{\cdot}CH_2Cl_2$, where the spin crossover behaviour was best modelled using a high spin sextet. [35, 113] This suggests that the spin crossover may occur preferentially into the sextet state when an unsymmetric HS state is not stabilised by the crystalline environment. This is mirrored by the spin crossover in solution, which is again best fit to a HS sextet, and gives the clearest indication of what would occur with no packing forces. [75] In the full set of experimental data there does not appear to be an exact trend saying the spin crossover of the unsymmetric structures occurs at lower temperature, for example the symmetric $Co_3(dpa)_4Br_2{\cdot}$Hexane and unsymmetric $Co_3(dpa)_4Br_2{\cdot}Et_2O$ have respective spin crossover temperatures of 203

and 325 K. The average Co-Co and terminal Co-N distances of the high temperature structures are therefore likely give an indication of the crystal packing forces, where those that restrict the elongation also limit the spin crossover.

7.4 Conclusions

In this chapter we have extended our study of the tricobalt bromide EMAC to the complexes of the other halide axial ligands: fluoride, chloride and iodide. Analysis of the spin state splitting energies using a range of DFT functionals show that the relative energies of the excited state all decrease going down group VII: F > Cl > Br > I. This corresponds to the results presented in the experimental work, which show decreasing spin crossover temperatures down the group. We show that the strength of the σ donation plays a defining role in the structure of the EMACs, rather than the ligand field strength. The structure of the fluoride complex is described in the context of its weak σ donation. This leads to shorter terminal Co-N distances and longer central Co-N distances compared to the complexes of the heavier halides. The shorter Co-N distances cause an increase in the energy of the bonding and nonbonding $\delta_{x^2-y^2}$ orbitals localised on the terminal Co atoms, which corresponds with the high HS state excitation energies in $Co_3(dpa)_2F_2$. We also present an analysis of the experimental structures and spin crossover, and show a strong correlation between the average Co-Co and terminal Co-N distances and spin crossover temperatures. These results suggest that the spin crossover is strongly dependent on the crystal packing forces, which not only effects the spin crossover temperature, but also the relative stabilities of the HS states, in particular the symmetric $^6A_2$ and unsymmetric ^4B. The spin transition will occur into the sextet state preferentially, but the energies are so finely balanced that a crystalline environment that stabilises unsymmetric states will force the spin transition to occur into the quartet.

Chapter 8

Conclusions

The work presented in this thesis focuses on understanding the varied behaviours observed in the tricobalt EMACs using a combination of DFT and MCSCF approaches. The experimental literature contains a wide range of solution- and crystalline-phase structural and magnetic behaviours that depend on both temperature and the crystalline environment (or lack thereof). In both the solution and solid state the tricobalt EMACs exhibit distinct spin crossover behaviour, and structures vary between a symmetric and unsymmetric limit, defined by having either equal or unequal Co-Co bonds. Understanding the structure-function relationships that govern these properties necessitated a thorough investigation of the ground and excited electronic states over the range of experimentally observed structures.

In the symmetric limit we identify the global ground state, $^2A_2$, which is described by a three-centre three-electron bond within the σ manifold containing the bonding, nonbonding and antibonding linear combinations of the cobalt d_{z^2} orbitals. We consider a broad spectrum of excited states that are optimised at the DFT level and found to retain the symmetric Co_3 core. Excitations within the ground state frontier orbitals correspond to low energy HS excited states that could become thermally populated during the spin

crossover. Of these, a symmetric sextet state, $^6A_2$, is found to correspond to the experimental magnetic and structural behaviours seen in solution and in the crystal structures that remain symmetric in the observed temperature range. The sextet state is described by two terminal HS Co atoms, with two unpaired electrons in the π^* orbitals and a single unpaired electron in each of the σ^{nb}, $\delta_{x^2-y^2}$ and $\delta^{nb}_{x^2-y^2}$ orbitals. The spin state splitting is finely balanced, with the crystalline environment playing an important role in the relative energies, and evidence of the population of other excited states, a LS ^2E or $^2B_2$, is also found in the experimental symmetric crystal structures.

In the unsymmetric limit we identify a local ground state, ^4B, which is described by a diamagnetic Co_2 dimer coupled to an isolated HS Co. Its electronic structure is related to the sextet state found in the symmetric limit, where only one of the terminal Co atoms undergoes a spin transition. The dimer unit has a consistent electronic structure through the observed temperature range, consistent with the formation of a single σ bond. The isolated Co exists in a HS state, with three unpaired electrons in the d_{yz}, d_{z^2} and $d_{x^2-y^2}$ orbitals localised on the isolated cobalt. The single occupation of the $d_{x^2-y^2}$ framework is paramount to the unsymmetric nature of the high temperature crystal structures. A second-order Jahn-Teller distortion drives the asymmetry and localises the orbitals on the isolated cobalt. The strong antibonding Co-N interactions means its occupation elongates the Co-N bonds, consistent with the experimental observations of the unsymmetric crystal structures at high temperatures.

CASSCF results showed significant multiconfigurational character in both the symmetric and unsymmetric limits. Even in the symmetric limit the ground state shows a considerable occupation of the two $\delta_{x^2-y^2}$ orbitals. In the unsymmetric limit the occupation of the $d_{x^2-y^2}$ orbital localised on the isolated cobalt is increased compared to the $\delta_{x^2-y^2}$ occupations in the symmetric limit, whilst the occupation of the $d_{x^2-y^2}$ orbital

localised on terminal cobalt of the dimer is essentially the same as those of the $\delta_{x^2-y^2}$ orbitals in the symmetric limit. A FON-DFT model showed that gradually increasing the $\delta_{x^2-y^2}$ occupation of two symmetric doublet states, ^2A and ^2B, leads to low energy distortions in the structure towards the unsymmetric limit. A second model developed in this thesis predicts the temperature dependent structure using an ideal spin crossover process by taking the thermally weighted average of the LS symmetric ground state with either a symmetric HS excited state or an unsymmetric HS excited state, governed by Boltzmann regime. Combined, the results of both models explain the range of observed structural phenomena, including both the symmetric and unsymmetric crystals and the low temperature unsymmetric structures. They also confirm the importance of the crystalline environment, which can stabilise symmetric or unsymmetric structures and reorder the spin state energies. Crystal packing forces can restrict the distortions associated with the population of either the HS $^6A_2$ or ^4B states. Crystals that allow the distortion at one end of the EMAC preferentially have structures that become unsymmetric as the ^4B state is stabilised, whilst crystals which do not impart a bias in the EMAC have structures that remain symmetric. The fact that either can become populated again reflects the proximity and sensitivity of both HS state energies.

The choice of axial ligand is also shown to influence the structure and spin state energies of the tricobalt EMACs. The experimental work showed decreasing spin crossover temperatures F $>$ Cl $>$ Br $>$ I and the spin state splitting energies of all the states reflect this observation, also decreasing down the group VII halides. The experimental structures are found to correlate with the spin crossover temperatures over the whole range of complexes with different structures and axial halide ligands. The high temperature structure indicates the strength of the crystal packing forces, where large distortions in the structure correspond to weaker packing forces and lower spin crossover temperatures.

Looking forward, their are many avenues by which this work could be extended. Firstly, we could investigate the fluoride, chloride and iodide complexes with the MCSCF methods described in this work, and maybe also include DMRG or FCIQMC to test the active space further. In addition we could also extend the DFT work to higher level functionals. Now that we have identified the states that best correlate with experiment, the work would be more focussed and more time could be spent on each state. This could also include a proper treatment of relativistic effects, and the frozen core approximation could be lifted. In collaboration with the Hillard group we could re-examine the magnetic data for the symmetric crystals into which we predict a spin crossover into a HS sextet state, for example $Co_3(dpa)_4Cl_2$·Hexane. Fitting the magnetic data to a spin crossover from a doublet to a sextet would generate more accurate enthalpy differences and spin crossover temperatures for the spin equilibrium model. Further, the spin equilibrium model could actually be extended theoretically. Normal mode frequencies could be used to calculate the enthalpies and entropies for the ground and excited states. The thermodynamic parameteres could also be calculated at specific temperatures, and a purely theoretical temperature dependent structure predicted. This would also be able to predict the influence of LS state occupations, for example in the $Co_3(dpa)_4Cl_2$·CH_2Cl_2 crystal.

Bibliography

[1] J. A. Bertrand, F. A. Cotton, W. A. Dollase, *Journal of the American Chemical Society* **1963**, *85*, 1349–1350.

[2] F. A. Cotton, T. E. Haas, *Inorganic Chemistry* **1964**, *3*, 10–17.

[3] F. A. Cotton, N. F. Curtis, C. B. Harris, B. F. G. Johnson, S. J. Lippard, J. T. Mague, W. R. Robinson, J. S. Wood, *Science* **1964**, *145*, 1305–1307.

[4] D. Lawton, R. Mason, *Journal of the American Chemical Society* **1965**, *87*, 921–922.

[5] F. A. Cotton, W. K. Bratton, *Journal of the American Chemical Society* **1965**, *87*, 921–921.

[6] M. H. Chisholm, F. A. Cotton, *Accounts of Chemical Research* **1978**, *11*, 356–362.

[7] W.-Z. Chen, F. A. Cotton, N. S. Dalal, C. A. Murillo, C. M. Ramsey, T. Ren, X. Wang, *Journal of the American Chemical Society* **2005**, *127*, 12691–12696.

[8] F. A. Cotton, C. Lin, C. A. Murillo, *Inorganic Chemistry* **2000**, *39*, 4574–4578.

[9] J. F. Berry, F. A. Cotton, P. Huang, C. A. Murillo, X. Wang, *Dalton Transactions* **2005**, 3713–3715.

[10] J. F. Berry, E. Bill, E. Bothe, F. A. Cotton, N. S. Dalal, S. A. Ibragimov, N. Kaur, C. Y. Liu, C. A. Murillo, S. Nellutla, J. M. North, D. Villagrán, *Journal of the American Chemical Society* **2007**, *129*, 1393–1401.

[11] T. Nguyen, A. D. Sutton, M. Brynda, J. C. Fettinger, G. J. Long, P. P. Power, *Science* **2005**, *310*, 844–847.

[12] K. A. Kreisel, G. P. A. Yap, O. Dmitrenko, C. R. Landis, K. H. Theopold, *Journal of the American Chemical Society* **2007**, *129*, 14162–14163.

[13] Y.-C. Tsai, C.-W. Hsu, J.-S. K. Yu, G.-H. Lee, Y. Wang, T.-S. Kuo, *Angewandte Chemie International Edition* **2008**, *47*, 7250–7253.

[14] T. J. Hurley, M. A. Robinson, *Inorganic Chemistry* **1968**, *7*, 33–38.

[15] S. Aduldecha, B. Hathaway, *Journal of the Chemical Society Dalton Transactions* **1991**, 993–998.

[16] P. Kiehl, M.-M. Rohmer, M. Bénard, *Inorganic Chemistry* **2004**, *43*, 3151–3158.

[17] Z. Tabookht, X. López, C. de Graaf, *The Journal of Physical Chemistry A* **2010**, *114*, 2028–2037.

[18] L.-P. Wu, P. Field, T. Morrissey, C. Murphy, P. Nagle, B. Hathaway, C. Simmons, P. Thornton, *Journal of the Chemical Society Dalton Transactions* **1990**, 3835–3840.

[19] G. J. Pyrka, M. El-Mekki, A. A. Pinkerton, *Journal of the Chemical Society Chemical Communications* **1991**, 84–85.

[20] M. Bénard, J. F. Berry, F. A. Cotton, C. Gaudin, X. López, C. A. Murillo, M.-M. Rohmer, *Inorganic Chemistry* **2006**, *45*, 3932–3940.

[21] J.-T. Sheu, C.-C. Lin, I. Chao, C.-C. Wang, S.-M. Peng, *Chemical Communications* **1996**, 315–316.

[22] C.-K. Kuo, I. P.-C. Liu, C.-Y. Yeh, C.-H. Chou, T.-B. Tsao, G.-H. Lee, S.-M. Peng, *Chemistry – A European Journal* **2007**, *13*, 1442–1451.

[23] G.-C. Huang, I. P.-C. Liu, J.-H. Kuo, Y.-L. Huang, C.-Y. Yeh, G.-H. Lee, S.-M. Peng, *Dalton Transactions* **2009**, 2623–2629.

[24] M. Spivak, V. Arcisauskaite, X. López, J. E. McGrady, C. de Graaf, *Dalton Transactions* **2017**, *46*, 6202–6211.

[25] F. A. Cotton, L. M. Daniels, C. A. Murillo, I. Pascual, *Journal of the American Chemical Society* **1997**, *119*, 10223–10224.

[26] E.-C. Yang, M.-C. Cheng, M.-S. Tsai, S.-M. Peng, *Journal of the Chemical Society Chemical Communications* **1994**, 2377–2378.

[27] F. A. Cotton, L. M. Daniels, G. T. Jordan IV, *Chemical Communications* **1997**, 421–422.

[28] N. Benbellat, M.-M. Rohmer, M. Bénard, *Chemical Communications* **2001**, 2368–2369.

[29] M.-M. Rohmer, A. Strich, M. Bénard, J.-P. Malrieu, *Journal of the American Chemical Society* **2001**, *123*, 9126–9134.

[30] M.-M. Rohmer, M. Bénard, *Chemical Society Reviews* **2001**, *30*, 340–354.

[31] S. Shaik, A. Shurki, D. Danovich, P. C. Hiberty, *Chemical Reviews* **2001**, *101*, 1501–1540.

[32] F. A. Cotton, L. M. Daniels, C. A. Murillo, I. Pascual, *Inorganic Chemistry Communications* **1998**, *1*, 1–3.

[33] R. Clérac, F. A. Cotton, L. M. Daniels, K. R. Dunbar, C. A. Murillo, I. Pascual, *Inorganic Chemistry* **2000**, *39*, 748–751.

[34] J. F. Berry, F. A. Cotton, T. Lu, C. A. Murillo, B. K. Roberts, X. Wang, *Journal of the American Chemical Society* **2004**, *126*, 7082–7096.

[35] R. Clérac, F. A. Cotton, L. M. Daniels, K. R. Dunbar, K. Kirschbaum, C. A. Murillo, A. A. Pinkerton, A. J. Schultz, X. Wang, *Journal of the American Chemical Society* **2000**, *122*, 6226–6236.

[36] R. Clérac, F. A. Cotton, L. M. Daniels, K. R. Dunbar, C. A. Murillo, X. Wang, *Inorganic Chemistry* **2001**, *40*, 1256–1264.

[37] R. Clérac, F. A. Cotton, L. M. Daniels, K. R. Dunbar, C. A. Murillo, X. Wang, *Journal of the Chemical Society Dalton Transactions* **2001**, 386–391.

[38] A. Srinivasan, X. Wang, R. Clérac, M. Rouzières, L. R. Falvello, J. E. McGrady, E. A. Hillard, *Dalton Transactions* **2018**, *47*, 16798–16806.

[39] R. H. Ismayilov, W.-Z. Wang, G.-H. Lee, C.-Y. Yeh, S.-A. Hua, Y. Song, M.-M. Rohmer, M. Bénard, S.-M. Peng, *Angewandte Chemie International Edition* **2011**, *50*, 2045–2048.

[40] F. A. Cotton, L. M. Daniels, C. A. Murillo, *Chemical Communications* **1998**, 39–40.

[41] F. A. Cotton, L. M. Daniels, T. Lu, C. A. Murillo, X. Wang, *Journal of the Chemical Society Dalton Transactions* **1999**, 517–518.

[42] H.-C. Chang, J.-T. Li, C.-C. Wang, T.-W. Lin, H.-C. Lee, G.-H. Lee, S.-M. Peng, *European Journal of Inorganic Chemistry* **1999**, *1999*, 1243–1251.

[43] F. A. Cotton, L. M. Daniels, C. A. Murillo, X. Wang, C. A. Murillo, *Chemical Communications* **1999**, 2461–2462.

[44] Y.-H. Chen, C.-C. Lee, C.-C. Wang, G.-H. Lee, S.-Y. Lai, F.-Y. Li, C.-Y. Mou, S.-M. Peng, *Chemical Communications* **1999**, 1667–1668.

[45] S.-J. Shieh, C.-C. Chou, G.-H. Lee, C.-C. Wang, S.-M. Peng, *Angewandte Chemie International Edition in English* **1997**, *36*, 56–59.

[46] C.-Y. Yeh, C.-H. Chou, K.-C. Pan, C.-C. Wang, G.-H. Lee, Y. O. Su, S.-M. Peng, *Journal of the Chemical Society Dalton Transactions* **2002**, 2670–2677.

[47] C.-H. Chien, J.-C. Chang, C.-Y. Yeh, G.-H. Lee, J.-M. Fang, S.-M. Peng, *Dalton Transactions* **2006**, 2106–2113.

[48] S.-Y. Lai, T.-W. Lin, Y.-H. Chen, C.-C. Wang, G.-H. Lee, M.-h. Yang, M.-k. Leung, S.-M. Peng, *Journal of the American Chemical Society* **1999**, *121*, 250–251.

[49] J. F. Berry, F. A. Cotton, P. Lei, T. Lu, C. A. Murillo, *Inorganic Chemistry* **2003**, *42*, 3534–3539.

[50] C.-C. Wang, W.-C. Lo, C.-C. Chou, G.-H. Lee, J.-M. Chen, S.-M. Peng, *Inorganic Chemistry* **1998**, *37*, 4059–4065.

[51] C.-H. Chien, J.-C. Chang, C.-Y. Yeh, G.-H. Lee, J.-M. Fang, Y. Song, S.-M. Peng, *Dalton Transactions* **2006**, 3249–3256.

[52] S.-Y. Lai, C.-C. Wang, Y.-H. Chen, C.-C. Lee, Y.-H. Liu, S.-M. Peng, *Journal of the Chinese Chemical Society* **1999**, *46*, 477–485.

[53] S.-M. Peng, C.-C. Wang, Y.-L. Jang, Y.-H. Chen, F.-Y. Li, C.-Y. Mou, M.-K. Leung, *Journal of Magnetism and Magnetic Materials* **2000**, *209*, 80–83.

[54] P.-J. Chen, M. Sigrist, E.-C. Horng, G.-M. Lin, G.-H. Lee, C.-h. Chen, S.-M. Peng, *Chemical Communications* **2017**, *53*, 4673–4676.

[55] M. Nippe, J. F. Berry, *Journal of the American Chemical Society* **2007**, *129*, 12684–12685.

[56] M.-M. Rohmer, I. P.-C. Liu, J.-C. Lin, M.-J. Chiu, C.-H. Lee, G.-H. Lee, M. Bénard, X. López, S.-M. Peng, *Angewandte Chemie International Edition* **2007**, *46*, 3533–3536.

[57] I. P.-C. Liu, G.-H. Lee, S.-M. Peng, M. Bénard, M.-M. Rohmer, *Inorganic Chemistry* **2007**, *46*, 9602–9608.

[58] L.-C. Yu, G.-H. Lee, M. Sigrist, T.-S. Lin, S.-M. Peng, *European Journal of Inorganic Chemistry* **2016**, *2016*, 4250–4256.

[59] W.-C. Chang, C.-W. Chang, M. Sigrist, S.-A. Hua, T.-J. Liu, G.-H. Lee, B.-Y. Jin, C.-h. Chen, S.-M. Peng, *Chemical Communications* **2017**, *53*, 8886–8889.

[60] G.-C. Huang, M. Bénard, M.-M. Rohmer, L.-A. Li, M.-J. Chiu, C.-Y. Yeh, G.-H. Lee, S.-M. Peng, *European Journal of Inorganic Chemistry* **2008**, *2008*, 1767–1777.

[61] M. Nippe, E. Victor, J. F. Berry, *European Journal of Inorganic Chemistry* **2008**, *2008*, 5569–5572.

[62] M. Nippe, E. Bill, J. F. Berry, *Inorganic Chemistry* **2011**, *50*, 7650–7661.

[63] D. W. Brogden, J. H. Christian, N. S. Dalal, J. F. Berry, *Inorganica Chimica Acta* **2015**, *424*, 241–247.

[64] D. Aydin-Cantürk, H. Nuss, *Zeitschrift für anorganische und allgemeine Chemie* **2011**, *637*, 543–546.

[65] Y. Turov, J. F. Berry, *Dalton Transactions* **2012**, *41*, 8153–8161.

[66] M. Nippe, Y. Turov, J. F. Berry, *Inorganic Chemistry* **2011**, *50*, 10592–10599.

[67] D. W. Brogden, J. F. Berry, *Inorganic Chemistry* **2014**, *53*, 11354–11356.

[68] M.-C. Cheng, S.-A. Hua, Q. Lv, M. Sigrist, G.-H. Lee, Y.-C. Liu, M.-H. Chiang, S.-M. Peng, *Dalton Transactions* **2018**, *47*, 1422–1434.

[69] M. Nippe, G. H. Timmer, J. F. Berry, *Chemical Communications* **2009**, 4357–4359.

[70] M.-C. Cheng, C.-L. Mai, C.-Y. Yeh, G.-H. Lee, S.-M. Peng, *Chemical Communications* **2013**, *49*, 7938–7940.

[71] M.-J. Huang, S.-A. Hua, M.-D. Fu, G.-C. Huang, C. Yin, C.-H. Ko, C.-K. Kuo, C.-H. Hsu, G.-H. Lee, K.-Y. Ho, C.-H. Wang, Y.-W. Yang, I.-C. Chen, S.-M. Peng, C.-h. Chen, *Chemistry – A European Journal* **2014**, *20*, 4526–4531.

[72] G. Parkin, *Accounts of Chemical Research* **1992**, *25*, 455–460.

[73] G. Parkin, *Chemical Reviews* **1993**, *93*, 887–911.

[74] F. A. Cotton, L. M. Daniels, Jordan, C. A. Murillo, *Journal of the American Chemical Society* **1997**, *119*, 10377–10381.

[75] F. A. Cotton, C. A. Murillo, X. Wang, *Inorganic Chemistry* **1999**, *38*, 6294–6297.

[76] F. A. Cotton, C. A. Murillo, X. Wang, *Journal of the Chemical Society Dalton Transactions* **1999**, 3327–3328.

[77] F. A. Cotton, R. Poli, *Inorganic Chemistry* **1987**, *26*, 3652–3653.

[78] L. P. He, C. L. Yao, M. Naris, J. C. Lee, J. D. Korp, J. L. Bear, *Inorganic Chemistry* **1992**, *31*, 620–625.

[79] A. Earnshaw, *Introduction to Magnetochemistry*, Elsevier Science, **2013**.

[80] P. Gütlich, H. Goodwin, Y. Garcia, *Spin Crossover in Transition Metal Compounds I*, Springer, **2004**.

[81] S. Mebs, B. Braun, R. Kositzki, C. Limberg, M. Haumann, *Inorganic Chemistry* **2015**, *54*, 11606–11624.

[82] G. S. Matouzenko, J.-F. Létard, S. Lecocq, A. Bousseksou, L. Capes, L. Salmon, M. Perrin, O. Kahn, A. Collet, *European Journal of Inorganic Chemistry* **2001**, *2001*, 2935–2945.

[83] J. A. Real, H. Bolvin, A. Bousseksou, A. Dworkin, O. Kahn, F. Varret, J. Zarembowitch, *Journal of the American Chemical Society* **1992**, *114*, 4650–4658.

[84] C. M. Harris, T. N. Lockyer, R. L. Martin, H. R. H. Patil, E. Sinn, *Australian Journal of Chemistry* **1969**, *22*, 2105–2116.

[85] O. Kahn, *Molecular Magnetism*, VCH, **1993**.

[86] R. Clérac, F. A. Cotton, K. R. Dunbar, T. Lu, C. A. Murillo, X. Wang, *Journal of the American Chemical Society* **2000**, *122*, 2272–2278.

[87] I. G. Dance, M. Gerloch, J. Lewis, F. S. Stephens, F. Lions, *Nature* **1966**, *210*, 298.

[88] P. Gütlich, H. Goodwin, M. Boillot, Y. Garcia, *Spin Crossover in Transition Metal Compounds II*, Springer, **2004**.

[89] I. Krivokapic, M. Zerara, M. L. Daku, A. Vargas, C. Enachescu, C. Ambrus, P. Tregenna-Piggott, N. Amstutz, E. Krausz, A. Hauser, *Coordination Chemistry Reviews* **2007**, *251*, 364–378.

[90] U. Beckmann, S. Brooker, *Coordination Chemistry Reviews* **2003**, *245*, 17–29.

[91] K. S. Murray, *European Journal of Inorganic Chemistry* **2008**, *2008*, 3101–3121.

[92] D. Schweinfurth, S. Demeshko, S. Hohloch, M. Steinmetz, J. G. Brandenburg, S. Dechert, F. Meyer, S. Grimme, B. Sarkar, *Inorganic Chemistry* **2014**, *53*, 8203–8212.

[93] P. Gütlich, Y. Garcia, H. A. Goodwin, *Chemical Society Reviews* **2000**, *29*, 419–427.

[94] J. A. Real, A. B. Gaspar, M. C. Muñoz, *Dalton Transactions* **2005**, 2062–2079.

[95] O. Sato, J. Tao, Y.-Z. Zhang, *Angewandte Chemie International Edition* **2007**, *46*, 2152–2187.

[96] S. V. Larionov, *Russian Journal of Coordination Chemistry* **2008**, *34*, 237–250.

[97] P. Gamez, J. S. Costa, M. Quesada, G. Aromí, *Dalton Transactions* **2009**, 7845–7853.

[98] M. A. Halcrow, *Chemical Society Reviews* **2011**, *40*, 4119–4142.

[99] J. Tao, R.-J. Wei, R.-B. Huang, L.-S. Zheng, *Chemical Society Reviews* **2012**, *41*, 703–737.

[100] P. Gütlich, A. B. Gaspar, Y. Garcia, *Beilstein Journal of Organic Chemistry* **2013**, *9*, 342–391.

[101] M.-M. Rohmer, M. Bénard, *Journal of the American Chemical Society* **1998**, *120*, 9372–9373.

[102] D. A. Pantazis, J. E. McGrady, *Journal of the American Chemical Society* **2006**, *128*, 4128–4135.

[103] J. C. Slater, J. B. Mann, T. M. Wilson, J. H. Wood, *Physical Review* **1969**, *184*, 672–694.

[104] F. W. Averill, G. S. Painter, *Physical Review B* **1992**, *46*, 2498–2502.

[105] S. G. Wang, W. H. E. Schwarz, *The Journal of Chemical Physics* **1996**, *105*, 4641–4648.

[106] D. Cremer, M. Filatov, V. Polo, E. Kraka, S. Shaik, *International Journal of Molecular Sciences* **2002**, *3*, 604–638.

[107] J.-D. Chai, *The Journal of Chemical Physics* **2012**, *136*, 154104.

[108] H. Laqua, J. Kussmann, C. Ochsenfeld, *The Journal of Chemical Physics* **2018**, *148*, 121101.

[109] H. B. Buergi, J. D. Dunitz, *Accounts of Chemical Research* **1983**, *16*, 153–161.

[110] G. S. Matouzenko, A. Bousseksou, S. Lecocq, P. J. van Koningsbruggen, M. Perrin, O. Kahn, A. Collet, *Inorganic Chemistry* **1997**, *36*, 5869–5879.

[111] G. Lemercier, N. Bréfuel, S. Shova, J. A. Wolny, F. Dahan, M. Verelst, H. Paulsen, A. X. Trautwein, J.-P. Tuchagues, *Chemistry – A European Journal* **2006**, *12*, 7421–7432.

[112] C. Bartual-Murgui, R. Diego, S. Vela, S. J. Teat, O. Roubeau, G. Aromí, *Inorganic Chemistry* **2018**, *57*, 11019–11026.

[113] R. D. Poulsen, J. Overgaard, A. Schulman, C. Østergaard, C. A. Murillo, M. A. Spackman, B. B. Iversen, *Journal of the American Chemical Society* **2009**, *131*, 7580–7591.

[114] N. K. Hansen, P. Coppens, *Acta Crystallographica Section A* **1978**, *34*, 909–921.

[115] M. A. Spackman, D. Jayatilaka, *CrystEngComm* **2009**, *11*, 19–32.

[116] R. Clérac, F. A. Cotton, S. P. Jeffery, C. A. Murillo, X. Wang, *Inorganic Chemistry* **2001**, *40*, 1265–1270.

[117] R. Clérac, F. A. Cotton, K. R. Dunbar, T. Lu, C. A. Murillo, X. Wang, *Inorganic Chemistry* **2000**, *39*, 3065–3070.

[118] D. A. Pantazis, C. A. Murillo, J. E. McGrady, *Dalton Transactions* **2008**, 608–614.

[119] C. A. Mack, *IEEE Transactions on Semiconductor Manufacturing* **2011**, *24*, 202–207.

[120] G. E. Moore, *IEEE Solid-State Circuits Society Newsletter* **2006**, *11*, 33–35.

[121] M. Lundstrom, *Science* **2003**, *299*, 210–211.

[122] N. S. Kim, T. Austin, D. Baauw, T. Mudge, K. Flautner, J. S. Hu, M. J. Irwin, M. Kandemir, V. Narayanan, *Computer* **2003**, *36*, 68–75.

[123] J. R. Heath, *Frontiers of Engineering: Reports on Leading-Edge Engineering from the 2003 NAE Symposium on Frontiers of Engineering*, National Academies Press, **2004**.

[124] S.-Y. Lin, I.-W. P. Chen, C.-h. Chen, M.-H. Hsieh, C.-Y. Yeh, T.-W. Lin, Y.-H. Chen, S.-M. Peng, *The Journal of Physical Chemistry B* **2004**, *108*, 959–964.

[125] C. Yin, G.-C. Huang, C.-K. Kuo, M.-D. Fu, H.-C. Lu, J.-H. Ke, K.-N. Shih, Y.-L. Huang, G.-H. Lee, C.-Y. Yeh, C.-h. Chen, S.-M. Peng, *Journal of the American Chemical Society* **2008**, *130*, 10090–10092.

[126] K.-N. Shih, M.-J. Huang, H.-C. Lu, M.-D. Fu, C.-K. Kuo, G.-C. Huang, G.-H. Lee, C.-h. Chen, S.-M. Peng, *Chemical Communications* **2010**, *46*, 1338–1340.

[127] V. P. Georgiev, J. E. McGrady, *Journal of the American Chemical Society* **2011**, *133*, 12590–12599.

[128] D.-H. Chae, J. F. Berry, S. Jung, F. A. Cotton, C. A. Murillo, Z. Yao, *Nano Letters* **2006**, *6*, 165–168.

[129] V. P. Georgiev, J. E. McGrady, *Inorganic Chemistry* **2010**, *49*, 5591–5597.

[130] T. Weng, D. DeBrincat, V. Arcisauskaite, J. E. McGrady, *Inorganic Chemistry Frontiers* **2014**, *1*, 468–477.

[131] E. Schrödinger, *Annalen der Physik* **1926**, *384*, 361–376.

[132] D. Griffiths, *Introduction to Quantum Mechanics*, Cambridge University Press, **2017**.

[133] A. Szabo, N. Ostlund, *Modern Quantum Chemistry: Introduction to Advanced Electronic Structure Theory*, Dover Publications, **1996**.

[134] D. R. Hartree, *Mathematical Proceedings of the Cambridge Philosophical Society* **1928**, *24*, 89–110.

[135] M. Born, R. Oppenheimer, *Annalen der Physik* **1927**, *389*, 457–484.

[136] G. Gräff, H. Kalinowsky, J. Traut, *Zeitschrift für Physik A Atoms and Nuclei* **1980**, *297*, 35–39.

[137] R. P. Feynman, *Physical Review* **1939**, *56*, 340–343.

[138] C. Cramer, *Essentials of Computational Chemistry: Theories and Models*, Wiley, **2013**.

[139] F. Jensen, *Introduction to Computational Chemistry*, Wiley, **2016**.

[140] P. Atkins, R. Friedman, *Molecular Quantum Mechanics*, OUP Oxford, **2011**.

[141] J. Simons, *An Introduction to Theoretical Chemistry*, Cambridge University Press, **2003**.

[142] A. Wallis, D. L. S. McElwain, H. O. Pritchard, *International Journal of Quantum Chemistry* **1969**, *3*, 711–722.

[143] P. A. M. Dirac, *Mathematical Proceedings of the Cambridge Philosophical Society* **1939**, *35*, 416–418.

[144] J. C. Slater, *Physical Review* **1929**, *34*, 1293–1322.

[145] P. Dirac, *The Principles of Quantum Mechanics*, Clarendon Press, **1958**.

[146] C. C. J. Roothaan, *Reviews of Modern Physics* **1951**, *23*, 69–89.

[147] G. G. Hall, *Proceedings of the Royal Society of London. Series A. Mathematical and Physical Sciences* **1951**, *205*, 541–552.

[148] T. Janowski, P. Pulay, *Journal of Chemical Theory and Computation* **2008**, *4*, 1585–1592.

[149] P. Pulay, *Chemical Physics Letters* **1983**, *100*, 151–154.

[150] S. Sæbø, P. Pulay, *Chemical Physics Letters* **1985**, *113*, 13–18.

[151] F. Neese, F. Wennmohs, A. Hansen, *The Journal of Chemical Physics* **2009**, *130*, 114108.

[152] F. Neese, A. Hansen, D. G. Liakos, *The Journal of Chemical Physics* **2009**, *131*, 064103.

[153] C. Riplinger, F. Neese, *The Journal of Chemical Physics* **2013**, *138*, 034106.

[154] C. Riplinger, P. Pinski, U. Becker, E. F. Valeev, F. Neese, *The Journal of Chemical Physics* **2016**, *144*, 024109.

[155] Y. Guo, C. Riplinger, U. Becker, D. G. Liakos, Y. Minenkov, L. Cavallo, F. Neese, *The Journal of Chemical Physics* **2018**, *148*, 011101.

[156] P. E. M. Siegbahn, A. Heiberg, B. O. Roos, B. Levy, *Physica Scripta* **1980**, *21*, 323–327.

[157] B. O. Roos, P. R. Taylor, P. E. M. Siegbahn, *Chemical Physics* **1980**, *48*, 157–173.

[158] P. E. M. Siegbahn, J. Almlöf, A. Heiberg, B. O. Roos, *The Journal of Chemical Physics* **1981**, *74*, 2384–2396.

[159] K. Andersson, P.-Å. Malmqvist, B. O. Roos, *The Journal of Chemical Physics* **1992**, *96*, 1218–1226.

[160] L. H. Thomas, *Mathematical Proceedings of the Cambridge Philosophical Society* **1927**, *23*, 542–548.

[161] E. Fermi, *Rendiconti Accademia Lincei* **1927**, *6*, 5.

[162] R. Parr, Y. Weitao, *Density-Functional Theory of Atoms and Molecules*, Oxford University Press, **1994**.

[163] W. Koch, M. Holthausen, *A Chemist's Guide to Density Functional Theory*, Wiley, **2015**.

[164] P. Hohenberg, W. Kohn, *Physical Review* **1964**, *136*, 864–871.

[165] W. Kohn, L. J. Sham, *Physical Review* **1965**, *140*, 1133–1138.

[166] D. M. Ceperley, B. J. Alder, *Physical Review Letters* **1980**, *45*, 566–569.

[167] D. C. Langreth, M. J. Mehl, *Physical Review B* **1983**, *28*, 1809–1834.

[168] R. Haunschild, A. Barth, W. Marx, *Journal of Cheminformatics* **2016**, *8*, 52.

[169] A. D. Becke, *The Journal of Chemical Physics* **1986**, *84*, 4524–4529.

[170] J. P. Perdew, W. Yue, *Physical Review B* **1986**, *33*, 8800–8802.

[171] A. D. Becke, *Physical Review A* **1988**, *38*, 3098–3100.

[172] N. C. Handy, A. J. Cohen, *Molecular Physics* **2001**, *99*, 403–412.

[173] J. P. Perdew, *Physical Review B* **1986**, *33*, 8822–8824.

[174] C. Lee, W. Yang, R. G. Parr, *Physical Review B* **1988**, *37*, 785–789.

[175] J. P. Perdew, J. A. Chevary, S. H. Vosko, K. A. Jackson, M. R. Pederson, D. J. Singh, C. Fiolhais, *Physical Review B* **1992**, *46*, 6671–6687.

[176] J. P. Perdew, K. Burke, M. Ernzerhof, *Physical Review Letters* **1996**, *77*, 3865–3868.

[177] J. P. Perdew, K. Burke, Y. Wang, *Physical Review B* **1996**, *54*, 16533–16539.

[178] J. Tao, J. P. Perdew, V. N. Staroverov, G. E. Scuseria, *Physical Review Letters* **2003**, *91*, 146401.

[179] J. Sun, A. Ruzsinszky, J. P. Perdew, *Physical Review Letters* **2015**, *115*, 036402.

[180] A. D. Becke, *The Journal of Chemical Physics* **1992**, *96*, 2155–2160.

[181] A. D. Becke, *The Journal of Chemical Physics* **1992**, *97*, 9173–9177.

[182] A. D. Becke, *The Journal of Chemical Physics* **1993**, *98*, 5648–5652.

[183] S. H. Vosko, L. Wilk, M. Nusair, *Canadian Journal of Physics* **1980**, *58*, 1200–1211.

[184] P. J. Stephens, F. J. Devlin, C. F. Chabalowski, M. J. Frisch, *The Journal of Physical Chemistry* **1994**, *98*, 11623–11627.

[185] Y. Zhao, B. J. Lynch, D. G. Truhlar, *The Journal of Physical Chemistry A* **2004**, *108*, 4786–4791.

[186] S. Grimme, *The Journal of Chemical Physics* **2006**, *124*, 034108.

[187] J. C. Slater, *Physical Review* **1930**, *36*, 57–64.

[188] S. F. Boys, *Proceedings of the Royal Society of London. Series A. Mathematical and Physical Sciences* **1950**, *200*, 542–554.

[189] W. J. Hehre, R. F. Stewart, J. A. Pople, *The Journal of Chemical Physics* **1969**, *51*, 2657–2664.

[190] J. S. Binkley, J. A. Pople, W. J. Hehre, *Journal of the American Chemical Society* **1980**, *102*, 939–947.

[191] M. S. Gordon, J. S. Binkley, J. A. Pople, W. J. Pietro, W. J. Hehre, *Journal of the American Chemical Society* **1982**, *104*, 2797–2803.

[192] R. Ditchfield, W. J. Hehre, J. A. Pople, *The Journal of Chemical Physics* **1971**, *54*, 724–728.

[193] W. J. Hehre, R. Ditchfield, J. A. Pople, *The Journal of Chemical Physics* **1972**, *56*, 2257–2261.

[194] P. C. Hariharan, J. A. Pople, *Theoretica Chimica Acta* **1973**, *28*, 213–222.

[195] M. M. Francl, W. J. Pietro, W. J. Hehre, J. S. Binkley, M. S. Gordon, D. J. DeFrees, J. A. Pople, *The Journal of Chemical Physics* **1982**, *77*, 3654–3665.

[196] R. Krishnan, J. S. Binkley, R. Seeger, J. A. Pople, *The Journal of Chemical Physics* **1980**, *72*, 650–654.

[197] T. Clark, J. Chandrasekhar, G. W. Spitznagel, P. v. R. Schleyer, *Journal of Computational Chemistry* **1983**, *4*, 294–301.

[198] M. J. Frisch, J. A. Pople, J. S. Binkley, *The Journal of Chemical Physics* **1984**, *80*, 3265–3269.

[199] F. Weigend, R. Ahlrichs, *Physical Chemistry Chemical Physics* **2005**, *7*, 3297–3305.

[200] F. Weigend, *Physical Chemistry Chemical Physics* **2006**, *8*, 1057–1065.

[201] F. Weigend, *Journal of Computational Chemistry* **2008**, *29*, 167–175.

[202] A. Hellweg, C. Hättig, S. Höfener, W. Klopper, *Theoretical Chemistry Accounts* **2007**, *117*, 587–597.

[203] J. Almlöf, P. R. Taylor, *The Journal of Chemical Physics* **1987**, *86*, 4070–4077.

[204] T. H. Dunning, *The Journal of Chemical Physics* **1989**, *90*, 1007–1023.

[205] D. E. Woon, T. H. Dunning, *The Journal of Chemical Physics* **1993**, *98*, 1358–1371.

[206] D. E. Woon, T. H. Dunning, *The Journal of Chemical Physics* **1994**, *100*, 2975–2988.

[207] A. K. Wilson, D. E. Woon, K. A. Peterson, T. H. Dunning, *The Journal of Chemical Physics* **1999**, *110*, 7667–7676.

[208] P.-O. Widmark, P.-Å. Malmqvist, B. O. Roos, *Theoretica Chimica Acta* **1990**, *77*, 291–306.

[209] P.-O. Widmark, B. J. Persson, B. O. Roos, *Theoretica Chimica Acta* **1991**, *79*, 419–432.

[210] R. Pou-Amérigo, M. Merchán, I. Nebot-Gil, P.-O. Widmark, B. O. Roos, *Theoretica Chimica Acta* **1995**, *92*, 149–181.

[211] K. Pierloot, B. Dumez, P.-O. Widmark, B. O. Roos, *Theoretica Chimica Acta* **1995**, *90*, 87–114.

[212] B. O. Roos, R. Lindh, P.-Å. Malmqvist, V. Veryazov, P.-O. Widmark, *The Journal of Physical Chemistry A* **2004**, *108*, 2851–2858.

[213] B. O. Roos, V. Veryazov, P.-O. Widmark, *Theoretical Chemistry Accounts* **2004**, *111*, 345–351.

[214] B. O. Roos, R. Lindh, P.-Å. Malmqvist, V. Veryazov, P.-O. Widmark, *The Journal of Physical Chemistry A* **2005**, *109*, 6575–6579.

[215] B. O. Roos, R. Lindh, P.-Å. Malmqvist, V. Veryazov, P.-O. Widmark, *Chemical Physics Letters* **2005**, *409*, 295–299.

[216] B. O. Roos, R. Lindh, P.-Å. Malmqvist, V. Veryazov, P.-O. Widmark, A. C. Borin, *The Journal of Physical Chemistry A* **2008**, *112*, 11431–11435.

[217] P.-O. Widmark, J. P. Zobel, V. P. Vysotskiy, T. Tsuchiya, V. Veryazov, *The Journal of Chemical Physics* **2018**, *149*, 194102.

[218] R. S. Mulliken, *The Journal of Chemical Physics* **1955**, *23*, 1833–1840.

[219] R. S. Mulliken, *The Journal of Chemical Physics* **1962**, *36*, 3428–3439.

[220] T. Kar, L. Behera, A. Sannigrahi, *Chemical Physics Letters* **1989**, *163*, 157–164.

[221] P. Löwdin, *The Journal of Chemical Physics* **1950**, *18*, 365–375.

[222] P. Löwdin, *Advances in Quantum Chemistry*, Academic Press, **1970**.

[223] R. F. W. Bader, *Accounts of Chemical Research* **1985**, *18*, 9–15.

[224] F. Martin, H. Zipse, *Journal of Computational Chemistry* **2005**, *26*, 97–105.

[225] J. Rigby, E. I. Izgorodina, *Physical Chemistry Chemical Physics* **2013**, *15*, 1632–1646.

[226] M. Swart, A. R. Groenhof, A. W. Ehlers, K. Lammertsma, *The Journal of Physical Chemistry A* **2004**, *108*, 5479–5483.

[227] M. Swart, *Journal of Chemical Theory and Computation* **2008**, *4*, 2057–2066.

[228] W.-M. Hoe, A. J. Cohen, N. C. Handy, *Chemical Physics Letters* **2001**, *341*, 319–328.

[229] K. Pierloot, S. Vancoillie, *The Journal of Chemical Physics* **2008**, *128*, 034104.

[230] N. C. Handy, A. J. Cohen, *Molecular Physics* **2001**, *99*, 607–615.

[231] M. Reiher, O. Salomon, B. Artur Hess, *Theoretical Chemistry Accounts* **2001**, *107*, 48–55.

[232] O. Salomon, M. Reiher, B. A. Hess, *The Journal of Chemical Physics* **2002**, *117*, 4729–4737.

[233] N. Kaltsoyanis, J. McGrady, *Principles and Applications of Density Functional Theory in Inorganic Chemistry I*, Springer, **2004**.

[234] P. Gütlich, H. Goodwin, Y. Garcia, *Spin Crossover in Transition Metal Compounds III*, Springer, **2004**.

[235] H. Paulsen, V. Schünemann, J. A. Wolny, *European Journal of Inorganic Chemistry* **2013**, *2013*, 628–641.

[236] S. Vela, M. Fumanal, J. Ribas-Arino, V. Robert, *Physical Chemistry Chemical Physics* **2015**, *17*, 16306–16314.

[237] M. Fumanal, F. Jiménez-Grávalos, J. Ribas-Arino, S. Vela, *Inorganic Chemistry* **2017**, *56*, 4474–4483.

[238] C. Daniel, *Coordination Chemistry Reviews* **2003**, *238-239*, 143–166.

[239] J. N. Harvey, *Annual Reports Section "C" (Physical Chemistry)* **2006**, *102*, 203–226.

[240] M. M. Quintal, A. Karton, M. A. Iron, A. D. Boese, J. M. L. Martin, *The Journal of Physical Chemistry A* **2006**, *110*, 709–716.

[241] C. J. Cramer, D. G. Truhlar, *Physical Chemistry Chemical Physics* **2009**, *11*, 10757–10816.

[242] F. Furche, J. P. Perdew, *The Journal of Chemical Physics* **2006**, *124*, 044103.

[243] M. Bühl, H. Kabrede, *Journal of Chemical Theory and Computation* **2006**, *2*, 1282–1290.

[244] M. Bühl, C. Reimann, D. A. Pantazis, T. Bredow, F. Neese, *Journal of Chemical Theory and Computation* **2008**, *4*, 1449–1459.

[245] F. Neese, T. Schwabe, S. Grimme, *The Journal of Chemical Physics* **2007**, *126*, 124115.

[246] F. Neese, *Coordination Chemistry Reviews* **2009**, *253*, 526–563.

[247] S. M. Tekarli, M. L. Drummond, T. G. Williams, T. R. Cundari, A. K. Wilson, *The Journal of Physical Chemistry A* **2009**, *113*, 8607–8614.

[248] W. Zhang, D. G. Truhlar, M. Tang, *Journal of Chemical Theory and Computation* **2013**, *9*, 3965–3977.

[249] R. Peverati, D. G. Truhlar, *Philosophical Transactions of the Royal Society A: Mathematical Physical and Engineering Sciences* **2014**, *372*, 20120476.

[250] E. R. Johnson, A. D. Becke, *The Journal of Chemical Physics* **2017**, *146*, 211105.

[251] J. P. Perdew, K. Schmidt, *AIP Conference Proceedings* **2001**, *577*, 1–20.

[252] A. J. Cohen, P. Mori-Sánchez, W. Yang, *Chemical Reviews* **2012**, *112*, 289–320.

[253] M. Ekholm, D. Gambino, H. J. M. Jönsson, F. Tasnádi, B. Alling, I. A. Abrikosov, *Physical Review B* **2018**, *98*, 094413.

[254] M. Swart, *Inorganica Chimica Acta* **2007**, *360*, 179–189.

[255] M. Radoń, *Physical Chemistry Chemical Physics* **2014**, *16*, 14479–14488.

[256] B. Pinter, A. Chankisjijev, P. Geerlings, J. N. Harvey, F. De Proft, *Chemistry – A European Journal* **2018**, *24*, 5281–5292.

[257] N. A. Bandeira, Z. Tabookht, C. de Graaf, X. López, *Comptes Rendus Chimie* **2012**, *15*, 163–169.

[258] X. López, M.-M. Rohmer, M. Bénard, *Journal of Molecular Structure* **2008**, *890*, 18–23.

[259] I. P.-C. Liu, M. Bénard, H. Hasanov, I.-W. P. Chen, W.-H. Tseng, M.-D. Fu, M.-M. Rohmer, C.-h. Chen, G.-H. Lee, S.-M. Peng, *Chemistry – A European Journal* **2007**, *13*, 8667–8677.

[260] Y. Kitagawa, T. Matsui, Y. Nakanishi, Y. Shigeta, T. Kawakami, M. Okumura, K. Yamaguchi, *Dalton Transactions* **2013**, *42*, 16200–16208.

[261] A. Fouqueau, S. Mer, M. E. Casida, L. M. Lawson Daku, A. Hauser, T. Mineva, F. Neese, *The Journal of Chemical Physics* **2004**, *120*, 9473–9486.

[262] A. Fouqueau, M. E. Casida, L. M. L. Daku, A. Hauser, F. Neese, *The Journal of Chemical Physics* **2005**, *122*, 044110.

[263] K. Pierloot, S. Vancoillie, *The Journal of Chemical Physics* **2006**, *125*, 124303.

[264] S. Vancoillie, H. Zhao, M. Radoń, K. Pierloot, *Journal of Chemical Theory and Computation* **2010**, *6*, 576–582.

[265] M. Radoń, *Physical Chemistry Chemical Physics* **2019**, *21*, 4854–4870.

[266] K. Pierloot, *Molecular Physics* **2003**, *101*, 2083–2094.

[267] Y.-K. Choe, T. Nakajima, K. Hirao, R. Lindh, *The Journal of Chemical Physics* **1999**, *111*, 3837–3845.

[268] M. Radoń, E. Broclawik, K. Pierloot, *The Journal of Physical Chemistry B* **2010**, *114*, 1518–1528.

[269] M. Radoń, K. Pierloot, *The Journal of Physical Chemistry A* **2008**, *112*, 11824–11832.

[270] L. González, D. Escudero, L. Serrano-Andrés, *ChemPhysChem* **2012**, *13*, 28–51.

[271] S. Niu, M. B. Hall, *Chemical Reviews* **2000**, *100*, 353–406.

[272] L. M. Lawson Daku, F. Aquilante, T. W. Robinson, A. Hauser, *Journal of Chemical Theory and Computation* **2012**, *8*, 4216–4231.

[273] M. Radoń, *Journal of Chemical Theory and Computation* **2014**, *10*, 2306–2321.

[274] Y. Minenkov, E. Chermak, L. Cavallo, *Journal of Chemical Theory and Computation* **2015**, *11*, 4664–4676.

[275] B. O. Roos, *Collection of Czechoslovak Chemical Communications* **2003**, *68*, 265–274.

[276] M. Brynda, L. Gagliardi, P.-O. Widmark, P. P. Power, B. O. Roos, *Angewandte Chemie International Edition* **2006**, *45*, 3804–3807.

[277] L. Gagliardi, B. O. Roos, *Nature* **2005**, *433*, 848–851.

[278] B. O. Roos, P.-Å. Malmqvist, L. Gagliardi, *Journal of the American Chemical Society* **2006**, *128*, 17000–17006.

[279] B. Vlaisavljevich, P. Miró, C. J. Cramer, L. Gagliardi, I. Infante, S. T. Liddle, *Chemistry – A European Journal* **2011**, *17*, 8424–8433.

[280] F. Aquilante, J. Autschbach, R. K. Carlson, L. F. Chibotaru, M. G. Delcey, L. De Vico, I. Fdez. Galván, N. Ferré, L. M. Frutos, L. Gagliardi, M. Garavelli, A. Giussani, C. E. Hoyer, G. Li Manni, H. Lischka, D. Ma, P. Å. Malmqvist, T. Müller, A. Nenov, M. Olivucci, T. B. Pedersen, D. Peng, F. Plasser, B. Pritchard, M. Reiher, I. Rivalta, I. Schapiro, J. Segarra-Martí, M. Stenrup, D. G. Truhlar, L. Ungur, A. Valentini, S. Vancoillie, V. Veryazov, V. P. Vysotskiy, O. Weingart, F. Zapata, R. Lindh, *Journal of Computational Chemistry* **2016**, *37*, 506–541.

[281] K. Andersson, B. O. Roos, *Chemical Physics Letters* **1992**, *191*, 507–514.

[282] O. Wiest, Y. Wu, *Computational Organometallic Chemistry*, Springer Berlin Heidelberg, **2012**.

[283] B. O. Roos, K. Andersson, M. P. Fülscher, P.-Å. Malmqvist, L. Serrano-Andrés, K. Pierloot, M. Merchán in *Advances in Chemical Physics*, John Wiley & Sons, Ltd, **2007**, Chapter 05, pp. 219–331.

[284] V. Veryazov, P. Å. Malmqvist, B. O. Roos, *International Journal of Quantum Chemistry* **2011**, *111*, 3329–3338.

[285] C. J. Stein, V. von Burg, M. Reiher, *Journal of Chemical Theory and Computation* **2016**, *12*, 3764–3773.

[286] G. Ghigo, B. O. Roos, P.-Å. Malmqvist, *Chemical Physics Letters* **2004**, *396*, 142–149.

[287] M. Kepenekian, V. Robert, B. Le Guennic, *The Journal of Chemical Physics* **2009**, *131*, 114702.

[288] K. Pierloot, Q. M. Phung, A. Domingo, *Journal of Chemical Theory and Computation* **2017**, *13*, 537–553.

[289] F. Aquilante, L. De Vico, N. Ferré, G. Ghigo, P.-Å. Malmqvist, P. Neogrády, T. B. Pedersen, M. Pitoňák, M. Reiher, B. O. Roos, L. Serrano-Andrés, M. Urban, V. Veryazov, R. Lindh, *Journal of Computational Chemistry* **2010**, *31*, 224–247.

[290] V. Sauri, L. Serrano-Andrés, A. R. M. Shahi, L. Gagliardi, S. Vancoillie, K. Pierloot, *Journal of Chemical Theory and Computation* **2011**, *7*, 153–168.

[291] C. J. Stein, M. Reiher, *Journal of Chemical Theory and Computation* **2016**, *12*, 1760–1771.

[292] S. R. White, *Physical Review Letters* **1992**, *69*, 2863–2866.

[293] S. R. White, *Physical Review B* **1993**, *48*, 10345–10356.

[294] G. K.-L. Chan, S. Sharma, *Annual Review of Physical Chemistry* **2011**, *62*, 465–481.

[295] K. H. Marti, M. Reiher, *Physical Chemistry Chemical Physics* **2011**, *13*, 6750–6759.

[296] T. Yanai, Y. Kurashige, W. Mizukami, J. Chalupský, T. N. Lan, M. Saitow, *International Journal of Quantum Chemistry* **2015**, *115*, 283–299.

[297] D. Cleland, G. H. Booth, A. Alavi, *The Journal of Chemical Physics* **2010**, *132*, 041103.

[298] G. Li Manni, A. Alavi, *The Journal of Physical Chemistry A* **2018**, *122*, 4935–4947.

[299] P. E. M. Siegbahn, *Journal of Biological Inorganic Chemistry* **2006**, *11*, 695–701.

[300] A. Ghosh, *Journal of Biological Inorganic Chemistry* **2006**, *11*, 712–724.

[301] K. Yang, R. Peverati, D. G. Truhlar, R. Valero, *The Journal of Chemical Physics* **2011**, *135*, 044118.

[302] M. Isegawa, R. Peverati, D. G. Truhlar, *The Journal of Chemical Physics* **2012**, *137*, 244104.

[303] S. Hammes-Schiffer, *Science* **2017**, *355*, 28–29.

[304] M. G. Medvedev, I. S. Bushmarinov, J. Sun, J. P. Perdew, K. A. Lyssenko, *Science* **2017**, *355*, 49–52.

[305] E. J. Baerends, T. Ziegler, A. J. Atkins, J. Autschbach, D. Bashford, O. Baseggio, A. Bérces, F. M. Bickelhaupt, C. Bo, P. M. Boerritger, L. Cavallo, C. Daul, D. P. Chong, D. V. Chulhai, L. Deng, R. M. Dickson, J. M. Dieterich, D. E. Ellis, M. van Faassen, A. Ghysels, A. Giammona, S. J. A. van Gisbergen, A. Goez, A. W. Götz, S. Gusarov, F. E. Harris, P. van den Hoek, Z. Hu, C. R. Jacob, H. Jacobsen, L. Jensen, L. Joubert, J. W. Kaminski, G. van Kessel, C. König, F. Kootstra, A. Kovalenko, M. Krykunov, E. van Lenthe, D. A. McCormack, A. Michalak, M. Mitoraj, S. M. Morton, J. Neugebauer, V. P. Nicu, L. Noodleman, V. P. Osinga, S. Patchkovskii, M. Pavanello, C. A. Peeples, P. H. T. Philipsen, D. Post, C. C. Pye, H. Ramanantoanina, P. Ramos, W. Ravenek, J. I. Rodríguez, P. Ros, R. Rüger, P. R. T. Schipper, D. Schlüns, H. van Schoot, G. Schreckenbach, J. S. Seldenthuis, M. Seth, J. G. Snijders, M. Solà, S. M., M. Swart, D. Swerhone, G. te Velde, V. Tognetti, P. Vernooijs, L. Versluis, L. Visscher, O. Visser, F. Wang, T. A. Wesolowski, E. M. van Wezenbeek, G. Wiesenekker, S. K. Wolff, T. K. Woo, A. L. Yakovlev, ADF2017, SCM, Theoretical Chemistry, Vrije Universiteit, Amsterdam, The Netherlands, https://www.scm.com.

[306] G. te Velde, F. M. Bickelhaupt, E. J. Baerends, C. Fonseca Guerra, S. J. A. van Gisbergen, J. G. Snijders, T. Ziegler, *Journal of Computational Chemistry* **2001**, *22*, 931–967.

[307] C. F. Guerra, J. Snijders, G. t. te Velde, E. J. Baerends, *Theoretical Chemistry Accounts* **1998**, *99*, 391–403.

[308] L. Versluis, T. Ziegler, *The Journal of Chemical Physics* **1988**, *88*, 322–328.

[309] L. Versluis, *The Determination of molecular structures by the HFS- method (Unpublished doctoral thesis)*, University of Calgary, **1989**.

[310] L. Fan, T. Ziegler, *The Journal of Chemical Physics* **1991**, *95*, 7401–7408.

[311] L. Fan, T. Ziegler, *The Journal of Chemical Physics* **1992**, *96*, 9005–9012.

[312] L. Fan, T. Ziegler, *Journal of the American Chemical Society* **1992**, *114*, 10890–10897.

[313] A. Bérces, R. M. Dickson, L. Fan, H. Jacobsen, D. Swerhone, T. Ziegler, *Computer Physics Communications* **1997**, *100*, 247–262.

[314] H. Jacobsen, A. Bérces, D. P. Swerhone, T. Ziegler, *Computer Physics Communications* **1997**, *100*, 263–276.

[315] S. K. Wolff, *International Journal of Quantum Chemistry* **2005**, *104*, 645–659.

[316] D. Young, *Computational Chemistry: A Practical Guide for Applying Techniques to Real World Problems*, Wiley, **2004**.

[317] J. P. Perdew, A. Savin, K. Burke, *Physical Review A* **1995**, *51*, 4531–4541.

[318] J. Wang, A. D. Becke, V. H. Smith, *The Journal of Chemical Physics* **1995**, *102*, 3477–3480.

[319] J. Baker, A. Scheiner, J. Andzelm, *Chemical Physics Letters* **1993**, *216*, 380–388.

[320] J. Gräfenstein, D. Cremer, *Molecular Physics* **2001**, *99*, 981–989.

[321] A. J. Cohen, D. J. Tozer, N. C. Handy, *The Journal of Chemical Physics* **2007**, *126*, 214104.

[322] M. A. Watson, N. C. Handy, A. J. Cohen, *The Journal of Chemical Physics* **2003**, *119*, 6475–6481.

[323] E. van Lenthe, E. J. Baerends, J. G. Snijders, *The Journal of Chemical Physics* **1993**, *99*, 4597–4610.

[324] E. van Lenthe, E. J. Baerends, J. G. Snijders, *The Journal of Chemical Physics* **1994**, *101*, 9783–9792.

[325] E. van Lenthe, A. Ehlers, E.-J. Baerends, *The Journal of Chemical Physics* **1999**, *110*, 8943–8953.

[326] E. van Lenthe, J. G. Snijders, E. J. Baerends, *The Journal of Chemical Physics* **1996**, *105*, 6505–6516.

[327] E. van Lenthe, R. van Leeuwen, E. J. Baerends, J. G. Snijders, *International Journal of Quantum Chemistry* **1996**, *57*, 281–293.

[328] E. van Lenthe, E. J. Baerends, *Journal of Computational Chemistry* **2003**, *24*, 1142–1156.

[329] I. Fdez. Galván, M. Vacher, A. Alavi, C. Angeli, F. Aquilante, J. Autschbach, J. J. Bao, S. I. Bokarev, N. A. Bogdanov, R. K. Carlson, L. F. Chibotaru, J. Creutzberg, N. Dattani, M. G. Delcey, S. S. Dong, A. Dreuw, L. Freitag, L. M. Frutos, L. Gagliardi, F. Gendron, A. Giussani, L. González, G. Grell, M. Guo, C. E. Hoyer, M. Johansson, S. Keller, S. Knecht, G. Kovačević, E. Källman, G. Li Manni, M. Lundberg, Y. Ma, S. Mai, J. P. Malhado, P. Å. Malmqvist, P. Marquetand, S. A. Mewes, J. Norell, M. Olivucci, M. Oppel, Q. M. Phung, K. Pierloot, F. Plasser,

M. Reiher, A. M. Sand, I. Schapiro, P. Sharma, C. J. Stein, L. K. Sørensen, D. G. Truhlar, M. Ugandi, L. Ungur, A. Valentini, S. Vancoillie, V. Veryazov, O. Weser, T. A. Wesołowski, P.-O. Widmark, S. Wouters, A. Zech, J. P. Zobel, R. Lindh, *Journal of Chemical Theory and Computation* **2019**, *15*, 5925–5964.

[330] B. O. Roos, *International Journal of Quantum Chemistry* **1980**, *18*, 175–189.

[331] E. R. Davidson, *Journal of Computational Physics* **1975**, *17*, 87–94.

[332] M. Reiher, A. Wolf, *The Journal of Chemical Physics* **2004**, *121*, 2037–2047.

[333] I. Røeggen, T. Johansen, *The Journal of Chemical Physics* **2008**, *128*, 194107.

[334] P.-O. Löwdin, *Physical Review* **1955**, *97*, 1474–1489.

[335] F. Neese, *WIREs Computational Molecular Science* **2012**, *2*, 73–78.

[336] F. Neese, *Journal of the American Chemical Society* **2006**, *128*, 10213–10222.

[337] C. L. Janssen, I. M. Nielsen, *Chemical Physics Letters* **1998**, *290*, 423–430.

[338] J. Finley, P.-Å. Malmqvist, B. O. Roos, L. Serrano-Andrés, *Chemical Physics Letters* **1998**, *288*, 299–306.

[339] L. E. Orgel, *Journal of the Chemical Society* **1958**, 4186–4190.